UNIVERSITY OF
BIRMINGHAM

A STUDY OF FLOW STRUCTURES IN A TWO-STAGE CHANNEL USING FIELD DATA, A PHYSICAL MODEL AND NUMERICAL MODELLING

by

BUDI GUNAWAN

A thesis submitted to
The University of Birmingham
for the degree of
DOCTOR OF PHILOSOPHY

Department of Civil Engineering
School of Engineering
The University of Birmingham
March 2010

ABSTRACT

This thesis consists of two main elements: the analysis of field measurements of velocity and resistance in a river, undertaken over a three year period, and numerical modelling of open channel flow. An Acoustic Doppler Current Profiler (ADCP) was used to measure the spatial distribution of velocity in two cross sections of a small meandering river (River Blackwater, Hampshire) during inbank, bankfull and overbank flow conditions. The same reach of the river had been previously studied over a number of years, as well as investigated on a 1:5 scale physical model, making it possible to compare the flow structure in the river and in the physical model.

A new measurement procedure and data processing methodology were developed for ADCP measurements, suitable for use in times of flood. Methods for orientating the measured velocity data and reducing the velocity fluctuations in the data, due to their instantaneous random nature, are described. The post processed data has been verified against 300s time-averaged velocity data at several locations along the cross sections, and also against ADV measurements obtained under the same flow conditions. The approach of averaging several transect data together has successfully reduced the noise in the ADCP velocity data. The field data indicates incremental rises in U_d with rising water level, while the opposite is true for the physical model data. Key similarities and differences between the secondary flow patterns in the river and model have been identified.

The discharge capacity of the main river channel is significantly reduced during summer months, due to seasonal growth in vegetation, reaching a minimum in August. The gradient of the stage-discharge rating curve for summer months can be seven times larger than that for the winter months. The falling limbs of the rating curve have a higher discharge capacity than the rising limbs for summer months (June/July to October/November). An attempt was made to predict the stage-discharge relationship for overbank flow conditions using a quasi 2D RANS model, SKM (Shiono and Knight Method). SKM is shown to be capable of simulating the lateral distribution of the depth-averaged streamwise velocity in the river and physical model with reasonable accuracy, subject to appropriate choice of three calibration parameters.

The research shows that the ADCP has a great potential for obtaining accurate 3D velocity data in rivers during flood events, and that the SKM is a useful modelling tool. The importance of taking into account the effect of vegetation when undertaking engineering design has been demonstrated.

ACKNOWLEDGEMENTS

First and foremost, I wish to express my sincere gratitude to Dr. Mark Sterling and Emeritus Professor Donald W. Knight for providing me with the opportunity to carry out this research, for undertaking the role of thesis supervisors and for always providing me with useful and constructive input throughout the project. Their guidance over the past three or more years has been invaluable as part of the development of my professional career

I would like to thank the research team members, Dr. Mark Sterling, Professor Donald W. Knight, Professor Koji Shiono, Dr. Ponnambalam Rameshwaran, Dr. Xin Sun, Dr. Xiaonan Tang, Professor Jim H. Chandler, Professor Nigel G. Wright and Professor Robert H.J. Sellin, for their collaboration in this project. Special thanks go to the Environment Agency (UK) for allowing me to access their data.

I am grateful to the Engineering and Physical Sciences Research Council (UK) and the University of Birmingham (UK) who provide me with financial support throughout my PhD study.

In the last three years, I have had valuable discussions with Dr. Daniel Brown, Dr. Jennifer Chlebek, Mr. Francesco Dorigatti, Mr. Charlie Hendrawan, Dr. Rudi Merola, Dr. Soroosh Sharifi and Mr. Benoit Terrier. In no particular order, I would like to thank them for their generosity. I would also like to thank Mr. Mike Vanderstam, chief technician from the hydraulics laboratory, for his involvement in the modifications to the ADCP and for assistance in installing staff gauges in the River Blackwater.

For their never-ending support, love and patience, I would like to thank my Mom, Dad, Sister and my lovely fiancée, Jocelin.

LIST OF CONTENTS

CHAPTER 3: EXPERIMENTAL SITE AND PREVIOUS RESEARCH ONTHE RIVER BLACKWATER

CHAPTER 4: INSTRUMENTATION AND METHODOLOGY

CHAPTER 5: FLOW STRUCTURES IN THE RIVER BLACKWATER

CHAPTER 6: ANALYSIS OF DISCHARGE AND RESISTANCE COEFFICIENTS RELATING TO THE RIVER BLACKWATER

CHAPTER 7: NUMERICAL MODELLING OF FLOW IN THE RIVER BLACKWATER

CHAPTER 8: CONCLUSIONS AND RECOMMENDATIONS

LIST OF FIGURES

CHAPTER 1: INTRODUCTION

CHAPTER 2: LITERATURE REVIEW

CHAPTER 3: EXPERIMENTAL SITE AND PREVIOUS RESEARCH ONTHE RIVER BLACKWATER

CHAPTER 4: INSTRUMENTATION AND METHODOLOGY

CHAPTER 5: FLOW STRUCTURES IN THE RIVER BLACKWATER

CHAPTER 6: ANALYSIS OF DISCHARGE AND RESISTANCE COEFFICIENTS RELATING TO THE RIVER BLACKWATER

CHAPTER 7: NUMERICAL MODELLING OF FLOW IN THE RIVER BLACKWATER

LIST OF TABLES

CHAPTER 4: INSTRUMENTATION AND METHODOLOGY

CHAPTER 5: FLOW STRUCTURES IN THE RIVER BLACKWATER

CHAPTER 6: ANALYSIS OF DISCHARGE AND RESISTANCE COEFFICIENTS RELATING TO THE RIVER BLACKWATER

CHAPTER 7: NUMERICAL MODELLING OF FLOW IN THE RIVER BLACKWATER

LIST OF NOTATIONS

A	cross section area	(m^2)
A	constant	
a	constant	
B	constant	
B_s	water surface width	(m)
C	speed of sound	(ms^{-1})
C_{shore}	edge shape coefficient, 0.3535 for triangular and 0.91 for rectangular	
D	minimum distance	(m)
D	the diameter of the pipe	(m)
D_{50}	the size at which half of the individual stones (by weight) are smaller than the specified diameter	(m)
DL	distance from left bank	(m)
D_r	relative depth	(m)
d_i	distance of point i to the interpolation point	(m)
d_m	depth of the first or the last segment	(m)
ds	differential area	(m)
dt	differential time	(s)
dz	vertical differential depth	(m)
E	Exponent for inverse distance weighting interpolation	
f	Darcy-Weisbach friction factor	
F	Force	(N)
F_i	Force in the i direction	(N)
F_D	Doppler Shift frequency	(Hz)
F_S	frequency of sound source when everything is still	(Hz)
Fr	Froude number	
$\vec{F}_{net}$	Force balance	(N)
g	gravitational acceleration	(ms^{-2})
g_x	gravitational acceleration in the x direction	(ms^{-2})
H	flow depth in the main channel	(m)
H_m	hydraulic mean depth in the main channel	(m)

H_{max}	maximum stage	(m)
h	flow depth in the floodplain	(m)
h_f	head loss due to friction	(m)
h_m	hydraulic mean depth in the floodplain	(m)
k	unit vector in the vertical direction	
k_s	Nikuradse's equivalent roughness	(m)
k_u	ratio between Q_{ADCP} and $Q_{LS\text{-}PIV}$	
l	mixing length	(m)
L	distance from the shore to the first or the last segment specified by user	(m)
L	length of the pipe	(m)
n	Manning's coefficient	($m^{-1/3}s$)
n	global open channel resistance coefficient (based on Manning's n)	($m^{-1/3}s$)
n_b	base value of n for floodplain's natural bare soil surface (the true Manning's n value)	($m^{-1/3}s$)
n_1	correction factor for the effect of the surface irregularities on the floodplain	($m^{-1/3}s$)
n_2	used to describe resistance due to variation in shape and size of a river channel and hence not applicable to the wide floodplain region - set to zero in the current work	($m^{-1/3}s$)
n_3	value for obstructions on floodplain (e.g. hedges, fences, buildings)	($m^{-1/3}s$)
n_4	value for average vegetation cover on floodplain	($m^{-1/3}s$)
m_5	correction factor for sinuosity of floodplain outer limits, equal to 1.0 if the floodplain banks are straight and the flow on the floodplain is assumed parallel with these, and 1.3 if strongly sinuous	
$\bar{n}$	a unit vector normal to ds at a general point	
N	number of data considered for IDW interpolation at each interpolation point	
μT	a unit for magnetic flux density	($kgA^{-1}s^{-2}$)
R	hydraulic radius	(m)
R^2	coefficient of determination	
R_e	Reynolds number	
S_o	channel bed slope	
S_w	water surface slope	
Q_{ADCP}	discharge obtained from ADCP measurement	(m^3s^{-1})
$Q_{LS\text{-}PIV}$	discharge approximated from LS-PIV water surface velocity	(m^3s^{-1})

Q_T	total river discharge	(m^3s^{-1})
Q_{max}	maximum discharge	(m^3s^{-1})
$\overline{Q}$	mean discharge of a set of transects	(m^3s^{-1})
Q_{CS}	cross section discharge, determined using the methodology outlined in chapter 4	(m^3s^{-1})
ΔQ	difference between the discharge of a transect and the mean discharge of a set of transects from one cross section measurement	(m^3s^{-1})
T	total cross section traverse time	(s)
T	temperature	(^oC)
U	average streamwise velocity with respect to averaging time	(ms^{-1})
U_d	depth-averaged streamwise velocity	(ms^{-1})
U_s	water surface velocity measured using LS-PIV	(ms^{-1})
u	streamwise velocity	(ms^{-1})
u'	streamwise velocity fluctuations	(ms^{-1})
u_{max}	maximum streamwise velocity	(ms^{-1})
u_*	shear velocity	(ms^{-1})
V	average lateral velocity with respect to averaging time	(ms^{-1})
V_d	depth-averaged lateral velocity	(ms^{-1})
V_i	the sum of velocity components normal to the element sides	(ms^{-1})
V_{SO}	relative velocity between sound source and observer	(ms^{-1})
$\overline{V_b}$	mean vessel-velocity vector	(ms^{-1})
$\overline{V_f}$	mean water-velocity vector	(ms^{-1})
V_m	mean water velocity in the first or the last segment	(ms^{-1})
v	lateral velocity	(ms^{-1})
v'	lateral velocity fluctuations	(ms^{-1})
W	average vertical velocity with respect to averaging time	(ms^{-1})
W_d	depth-averaged vertical velocity	(ms^{-1})
w	lateral velocity	(ms^{-1})
w'	vertical velocity fluctuations	(ms^{-1})
w_i	weighting parameter point i to the interpolation point	(m^{-2})
y	lateral distance	(m)
z	distance to the channel bed	(m)

z_0	roughness length	(m)

Greek symbols

α	angle between the velocity vector and the transducer beam	(^{o})
Γ	secondary flow parameter	
Δx	the spatial separation of the sampling points	(m)
ε_t	eddy viscosity	(m^2s^{-1})
ε_{yx}	depth-averaged eddy viscosity	(m^2s^{-1})
η	coefficient used in the analytical solution of the SKM	
η	Kolmogorov microscale	(m)
κ	von Karman's constant	
λ	dimensionless eddy viscosity	
ξ	coefficient used in the analytical solution of the SKM	
μ	dynamic viscosity	(Nsm^{-2})
ν	kinematic viscosity	(m^2s^{-1})
ρ	fluid density	(kgm^{-3})
τ	laterally averaged boundary shear stress	(Nm^{-2})
τ_b	bed shear stress	(Nm^{-2})
τ_o	boundary shear stress	(Nm^{-2})
τ_w	wall shear stress	(Nm^{-2})
ϑ	angle between water velocity and boat velocity	(^{o})
ω	coefficient used in the analytical solution of the SKM	

LIST OF ABBREVIATIONS

DNS	Direct numerical simulation
DTM	Digital Terrain Model
EA	Environment Agency
EG	Electromagnetic gauge
FCF	Flood Channel Facility (UK)
LES	Large eddy simulations
RANS	Reynolds-averaged Navier Stokes Equation
RMSE	Root Mean Squared Error
SKM	Shiono and Knight Method
SM	Stationary measurements
TA	Transect averaging
TIN	Triangular Irregular Network

1 INTRODUCTION

1.1 Research background

Flooding has been one of the most significant natural disasters around the world. Floods and hydrological-related disasters have occurred more than any other types of natural disasters worldwide. Annually, they have also affected the life of more than 100 million people and caused damages worth more than US$ 19 billion between 2000 and 2007 (see Figure 1.1). In the UK context, flooding is not a new issue either. A recent independent report (Pitt, 2008) indicates that the year 2007 was the wettest summer in the UK, causing 13 deaths, 7,000 people to be rescued and 55,000 properties to be flooded. It was also reported that almost half a million people were left without mains water or electricity, the largest loss of essential services since World War II. The estimated cost for the insurance industry was over £3 billion, making the summer flood of 2007 in the UK to be the most costly in the world that year. The social and economic impacts caused by floods and other weather catastrophes have been increasing over the last 58 years (see Figure 1.2), and further increase is expected in the future due to climate change.

In order to respond to the future flood-related challenges in the UK, the government Foresight 'Flood and Coastal Defence Project' (Foresight, 2010) aims to produce a long term (30 - 100 years) vision of flood and coastal defence in the whole of the UK that is robust, takes account of the many uncertainties, and can be used as a basis to inform policy and its delivery. One of the key issues related to this is the uncertainty in determining discharges in rivers during flood, an issue that was also ranked as a key research area by another recent government report (Defra, 2002). Accurate determination of discharge (volume of water flowing per second) during floods may lead to an improvement in the accuracy of flood risk mapping, and thereby potentially decrease the loss due to flooding.

The practice of mapping the risk of flooding is usually undertaken by means of numerical modelling. In this context, typical numerical models try to model the interaction between the flow parameters, such as stage (the depth of flow) and discharge, and the factors that affect the flow itself, for a given set of boundary conditions at the inlet and outlet of the reach being modelled. The flow in a river is affected by the resistance, turbulence, the drag forces caused by any emergent or submerged vegetation and any hydraulic structures present. All of these physical effects are often represented

by a so called “calibration parameters”. As suggested from the name, calibration parameters require a specific calibration process in order to produce accurate results. The role of measurement data becomes important at this point since the calibration process requires verification that is done by assessing the closeness of the numerical model results to the measured data.

Among the numerical models available is the Shiono & Knight method (SKM) (Shiono and Knight, 1988; 1991). The SKM has been shown to be capable of predicting the lateral distribution of streamwise velocity in open channel with a good accuracy, and is relatively easy to use when compared to full 2D or 3D models. For these reasons, it has been adopted by the UK’s Environment Agency for use within the recently developed ‘Conveyance Estimation System and Afflux Estimation System’ (CES-AES) software (McGahey, 2006; Flow Database at the University of Birmingham, 2009).

A particularly important aspect that needs to be taken into account when modelling flood events is the overbank flow features, which are far more complex than those occurring during inbank flow conditions. Recent laboratory research on floodplain hydrodynamics has shown that flow resistance is caused by high levels of turbulence, large planform or horizontal eddies and secondary flow in the vicinity of main channel/floodplain boundaries in straight channels (Shiono & Knight, 1991; Ervine *et al.*, 2000; Ikeda, 2001; Spooner & Shiono, 2003; Abril & Knight, 2004). The flow in two-stage meandering channels is even more complex, due to the complex system of secondary flow cells driven by turbulence, centrifugal forces and floodplain flows entering the main channel at the cross-over (Shiono & Muto, 1998; Ervine *et. al*., 1993). Furthermore, the existence of vegetation in the main channel and floodplain cannot be ignored as they may significantly affect the flow also. In order to accurately predict the stage in natural rivers, it is therefore imperative to understand these complex flow features which may exist, measure the relevant parameters and then to correctly represent these flow features in the model.

Field data availability is clearly crucial for understanding the complex flow mechanism in rivers during overbank flow conditions. The challenge posed in measuring field data, apart from its high operational cost and safety concerns, is the considerable difficulty in obtaining reliable data during flood events, since conventional measurement instruments, such as propeller, electromagnetic flowmeter or floats, are generally not designed to operate under such extreme conditions. Furthermore, given the unpredictability of floods, it is often difficult to predict exactly when and where flood will occur and as a result, it may require years in order to obtain flood data.

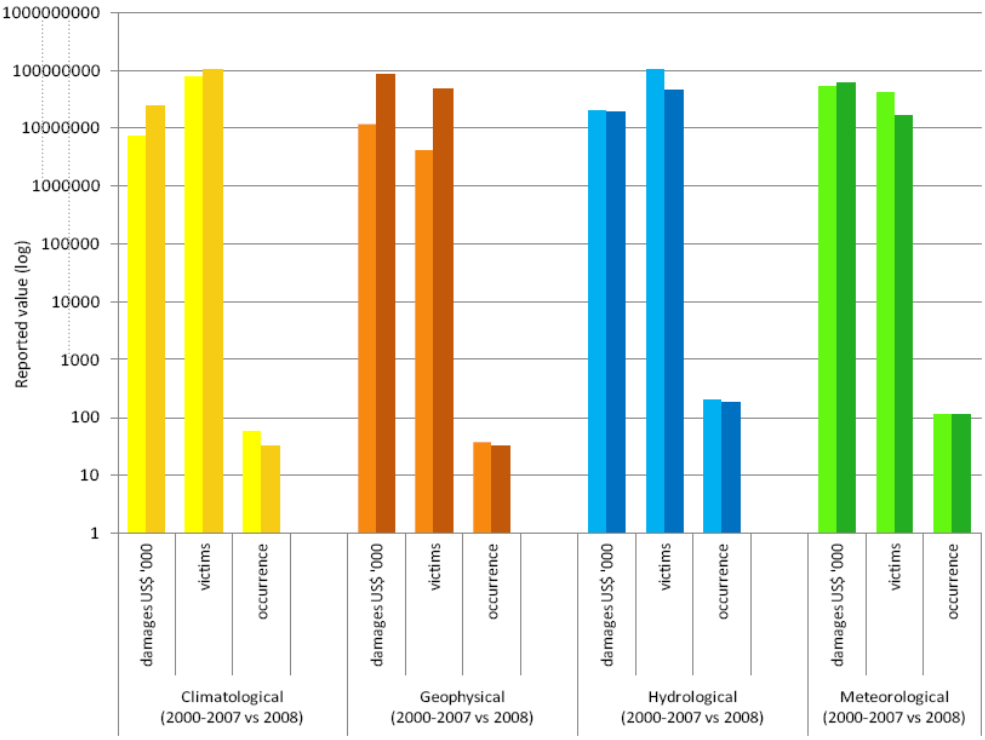

Figure 1.1 Natural disasters impacts by disaster sub-group: 2008 versus 2000-2007 annual average (Rodriguez *et al.*, 2009)

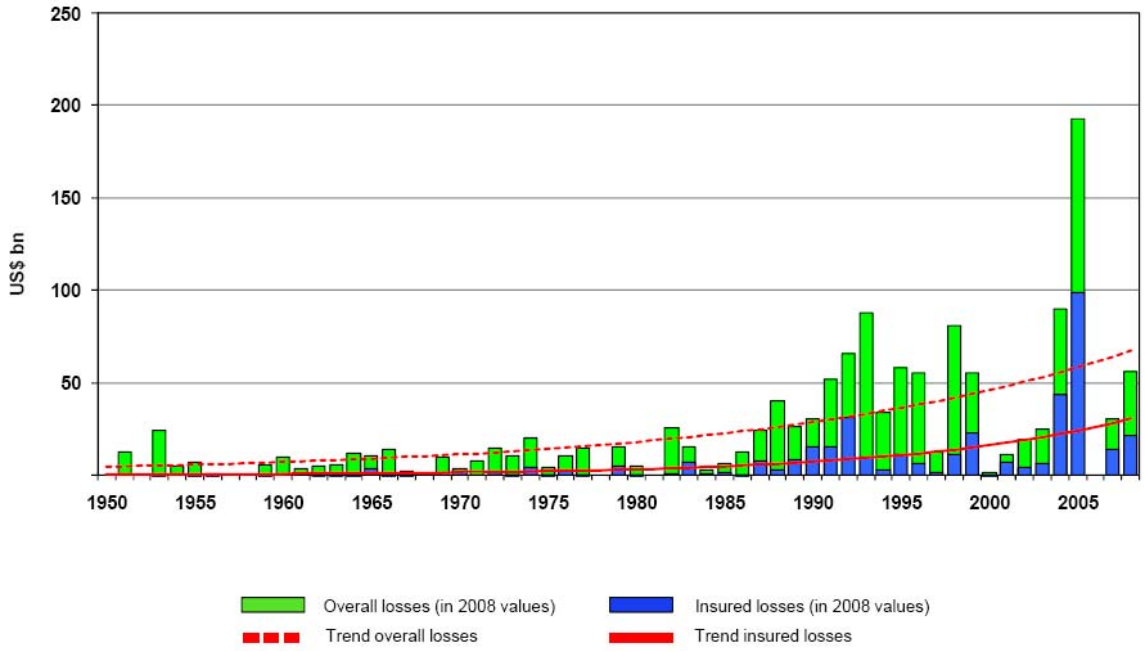

Figure 1.2 Great weather catastrophes 1950-2008 (Munich RE, 2009)

More advanced measurement method, Acoustic Doppler Velocimeter (ADV), has been used to measure the flow in the field during overbank flow conditions (Babaeyan-Koopaei *et al.*, 2002). Since ADV measures velocity point by point, obtaining data for the whole river cross section is virtually impossible. Another drawback related to ADV measurement is the lack of a heading sensor on the ADV. Except when such a sensor is integrated into the ADV, manual projection is required in order to orientate the velocity, at each measurement point, to the desired direction, e.g. streamwise and lateral. If care is not taken in this process, significant errors may occur.

Another advanced measurement method is that based on the Acoustic Doppler Current Profiler (ADCP), which has been used to measure velocity on large rivers (Muste *et al.*, 2004a; Szupiany *et al.*, 2007, Le Coz *et al.*, 2007). The ADCP is capable of measuring the spatial distribution of velocity over a river cross section within a reasonably short time. However, the velocity measured using an ADCP can fluctuate significantly. Despite having great potential for studying the flow in rivers, standardised procedures for ADCP measurements in rivers are currently lacking (Muste *et al.*, 2004a; Szupiany *et al.*, 2007). Recently, the Commission for Hydrology (CHy) of the World Meteorological Organization (WMO) identified the need to assess the performance of flow measurement instruments and techniques in response to the dramatic changes in hydrometric instrumentation, and to compute associated discharge measurement uncertainties (WMO, 2004). A proposal, and an implementation project, is currently being considered. The issues that are addressed in this research concern the measurement of velocity in a small river using an ADCP, and the adaptations required for measuring in a river with such a relatively small scale.

Another important feature of this research is that it enables comparisons to be made between field, laboratory and numerical modelling data. A 500m reach of the River Blackwater, Hampshire, UK, is used as a test site. Detailed velocity measurements have also been undertaken on a 1:5 scale physical model of the same Blackwater reach, built within the UK Flood Channel Facility (Lambert and Sellin, 1996; Naish and Sellin, 1996). The same reach of the River Blackwater was also studied at full scale using discharge data obtained from an electromagnetic flow gauge by Sellin and van Beesten (2002 and 2004). This research fills some of the gaps left by the previous research by providing further detailed velocity, turbulence and resistance data for the River Blackwater.

1.2 Aim and objectives of the work

The overall aim of this work was to examine the flow characteristics which occur in a small reach of a doubly meandering compound channel during inbank, bankfull and overbank conditions.

The objectives of this research can be specified as:

1. To undertake a comprehensive set of flow measurements in a straight and meandering sections of the River Blackwater, during inbank, bankfull and overbank flow conditions, using an Acoustic Doppler Current Profiler.
2. To undertake necessary modifications of the ADCP and the data processing methodology in order to obtain reliable velocity data.
3. To analyse the flow structures in the river and to compare it with that in the River Blackwater 1:5 scale physical model.
4. To study the behaviour of the slope, stage, discharge and resistance in the River Blackwater.
5. To investigate the effect of seasonal variation on the flow in the River Blackwater.
6. To undertake numerical modelling for the River Blackwater and the small scale physical model of the River Blackwater, and to seek a relationship between values of the calibration parameters used in the simulation and the measurement data.
7. To attempt to obtain stage-discharge rating curves in the river using simple interpolation methods and a numerical model (SKM).
8. To explore the feasibility of using the combination of ADCP data and LS-PIV data (Large Scale Particle Image Velocimetry) for measuring the discharge in rivers.

It should be noted that the LS-PIV data used in this thesis were measured and processed by the research group from Loughborough University. The ADV data used in this thesis were obtained and processed by the research group from the Centre for Ecology and Hydrology and the author.

1.3 Layout of thesis

In order to deliver the objectives of this research, the following thesis structure was adopted:

Chapter 1 provides an introduction and the motivation for the research.

Chapter 2 reviews the previous research undertaken in the field of open channel hydraulics that is relevant to the current work. The chapter emphasizes three main components: flow mechanisms, numerical modelling and the technology behind ADCP velocity measurements in rivers.

Chapter 3 is concerned with the experimental site and previous work undertaken on the river and its small scale physical model.

Chapter 4 provides details of the ADCP, ADCP modifications, the methodologies used for ADCP measurement and data processing, and some of the key characteristics of the measured ADCP data obtained from the River Blackwater.

Chapter 5 investigates the inbank, bankfull and overbank flow structures in the River Blackwater and compares them with the flow structures measured in the physical model.

Chapter 6 analyses the water slope, stage-discharge relationship and the resistance coefficients in the River Blackwater. The effects of seasonal variation on the discharge capacity, resistance coefficient and the shape of the stage-discharge rating curve are also examined. In addition, the feasibility of using a combination of LS-PIV and ADCP data for estimating discharge is also assessed.

Chapter 7 consists of numerical modelling of the flow in the river and physical model using SKM. Data from both the physical simulations and field work are used in order to gain an insight into the calibration of the model.

Chapter 8 summarises the key findings of the research and examines their implications in a broader context. In addition, recommendations for future work are also presented.

1.4 Publication of research

Some of the work presented in this thesis has already been published and or has been submitted to journals and conference proceedings:

1. Dawadi, P., Gunawan, B., Sterling, M, Wright, N. G. and Rameshwaran, P. (2010) The importance of quantifying vegetation when modelling to the flow in a small river. Submitted to Journal Water Management. Proceedings of the Institution of Civil Engineers.
2. Gunawan, B., Sterling, M., Tang, X. and Knight, D.W. (2010) Measuring and modelling flow structures in a small river. International Conference on Fluvial Hydraulics, Braunschweig, Germany, September 8-10, 2010 (abstract accepted).
3. Gunawan, B., Sterling, M. and Knight, D.W. (2009) Using an Acoustic Doppler Current Profiler in a small river. (CIWEM) Water and Environment Journal (in press for printing, published online on 12/5/2009/DOI: 10.1111/j.1747-6593.2009.00170.x).
4. Gunawan, B., Sun, X., Sterling, M., Knight, D.W., Shiono, K., Chandler, J., Rameshwaran, P., Wright, N.G, Sellin, R.H.J, Tang, X. and Fujita, I. (2008) An integrated and novel approach to estimating the conveyance capacity of the River Blackwater. Proceeding of the Eight International Conference on Hydro-science and Engineering, Nagoya, Japan, September 8-12, 2008.

The remaining unpublished sections are being prepared for submission to journal publications:

1. Sun, X., Gunawan, B., Sterling, M., Shiono, K., Rameshwaran, P., Knight, D.W., Tang, X., Chandler, J., Fujita, I. (2010) The application of LS-PIV, ADCP and ADV to a small river.
2. Gunawan, B., Sterling, M. and Knight, D.W. (2010) Effect of seasonal variation on the stage-discharge rating curve of a small river.
3. Gunawan, B., Sterling, M., Knight, D.W. and Rameshwaran, P. (2010) Three-dimensional flow structures in a river during inbank, bankfull and overbank flow conditions.
4. Gunawan, B., Sterling, M. and Knight, D.W. (2010) Stage discharge rating curve extension using simple interpolation methods and numerical modelling.
5. Sharifi, S., Gunawan, B., Sterling, M. and Knight, D.W. (2010) Application of an evolutionary algorithm for modelling the flow in a river.

2 LITERATURE REVIEW

2.1 Introduction

This chapter provides an overview of the previous research undertaken in the field of open channel hydraulics that is relevant to the current work. Three main components inherent in this PhD project, flow mechanisms, numerical modelling and Acoustic Doppler Current Profiler velocity measurement in rivers, are covered in this chapter. The chapter starts with a description of some of the dominant flow structures which are often found in rivers (2.2). It continues with a section on the governing equations required to model the velocity distribution in rivers numerically (2.3). A section is devoted to the background for predicting stage and discharge in open channel using SKM (2.4). The chapter closes with a brief review on velocity and discharge measurements in rivers using Acoustic Doppler Current Profilers (ADCPs) (2.5). The details on how an ADCP system works and the standard methodology used to process its data are covered in Chapter 4.

2.2 Flow structure in open channel

The structure of flow in open channels is highly dependent on the regime of the flow, i.e. laminar or turbulent, as well as the existence of vortices at various length scales, acting toward all three directions, typically generated by high shear between fluid layers or between the fluid and its boundaries. Such vortices are a form of energy transfer that converts part of the kinetic energy of the flow into heat via viscosity. The common types of vortices that develop in open channel flow are due to surface roughness, the anisotropy of turbulent velocity fluctuations in the *y* and *z* directions, leading to secondary flows and high velocity gradients between the main channel and floodplain, leading to planform vortices at this interface (Figure 2.1). Each of these components is described briefly in the following sections.

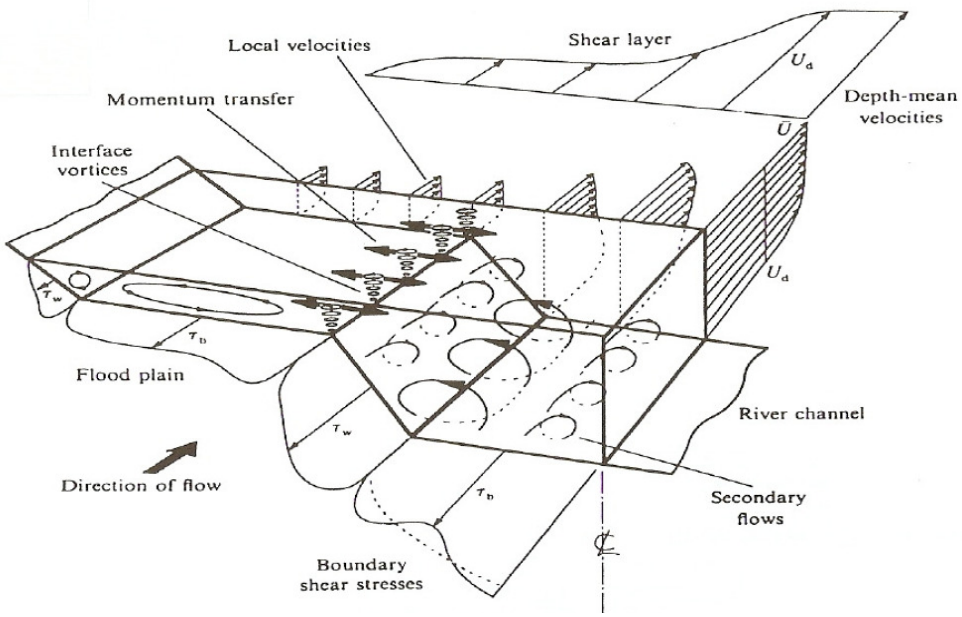

Figure 2.1 Flow mechanisms associated with straight overbank flow in a two-stage channel (Shiono & Knight, 1990).

2.2.1 Turbulence in open channel flow

The behaviour of open channel flow is strongly governed by the effect of viscosity and gravity relative to the inertial forces of the flow (Chow, 1959). When the viscous forces are strong relative to the inertial force, the flow is said to be laminar, whereas when the viscous forces are weak relative to the inertial forces, the flow is said to be turbulent (see Reynolds number explanation below). In laminar flow, fluids appear to move in a definite path and infinitesimally thin layers of fluid seem to slide over adjacent layers. In contrast to this, turbulent flow is characterised with irregularity that makes a deterministic approach to turbulence problems impossible, instead, one relies on statistical methods (Tennekes and Lumley, 1972). Other characteristics of turbulent flow are as follows (Tennekes and Lumley, 1972; Davidson, 2004; Tsinober, 2001):

1. Three dimensional vorticity fluctuations

   Turbulence is rotational and three dimensional. The random vorticity fluctuations that characterise turbulence are maintained by the process of vortices lengthening (vortex stretching).
2. Continuum

   Turbulence is a continuum phenomenon, governed by the equations of fluid mechanics. Even the smallest scales occurring in a turbulent flow are larger than any molecular length scale.

3. Diffusive

   Turbulence causes rapid mixing and increased rates of momentum, heat and mass transfer.

4. Dissipative

   Turbulence energy dissipates through viscosity. Thus, turbulence requires energy in order to maintain its form.

5. Turbulence flows are flows

   Turbulence is not a feature of fluids but of fluid flows. Most of the dynamics of turbulence are the same in all fluids, whether they are liquids or gases, if the Reynolds number of the turbulence is large enough.

The transition from laminar to turbulent flow was first pointed out by Osborne Reynolds in 1883 (Davidson, 2004) when he examined flow inside a pipe. He argued that the transition between laminar and turbulent flow was controlled by a parameter which has a value of UD/v, now called the Reynolds number (Re), where D is the pipe diameter, U is the mean flow in the pipe and v is the kinematic viscosity of the fluid flowing through the pipe. When cross sectional area (A) and wetted perimeter (P) are calculated for pipes, then substituted to the equation $R = A/P$, it can be shown that R is equivalent to ¼ D. Reynolds suggested that the instability that initiates turbulence might require a perturbation of a certain magnitude, for a given value of Re. Chow (1959) reported that the flow in an open channel changes from laminar to turbulence at a critical value of Re that ranges from 500 to 12500. However, a laminar flow with Re value up to 9×10^4 has been achieved for pipe flow, with a special inlet conditions to minimise disturbances (Davidson, 2004).

Tennekes and Lumley (1972) state that the transition from laminar to turbulent flow is commonly initiated by a primary instability mechanism that produces secondary motions, which are generally three dimensional and become unstable themselves. In other cases, turbulence originates from an instability that causes vortices which subsequently become unstable. In open channel flow, such vortices generally occur due to the high velocity gradients and feature on a variety of length scales. High velocity gradients are generally induced by geometry changes of the boundary such as the presence of floodplains, vegetation, structures, pools and riffles. Unstable vortices eventually break up or evolve into smaller eddies as a result of stretching due to the velocity gradients and interaction with the boundaries. The smaller eddies continue to break up or evolve into even smaller eddies and so on until it dissipates through viscosity (Richardson's energy cascade concept, Davidson, 2004). Such vortices may be formed from translational kinetic energy which no longer contributes to the

streamwise channel conveyance as its form is transferred to rotational kinetic energy (McGahey, 2006).

2.2.2 Boundary shear

As a fluid passes over a solid boundary, a shear force acts in between the fluid and the boundary in the opposite direction to the flow. The boundary shear generates resistance to the flow and therefore, reduces the fluid velocity. The reduction of velocity becomes less perceptible as the distance from the boundary increases. Fully developed turbulent flow over a smooth surface comprises of a viscous sub layer and a turbulent boundary layer (Schlichting and Gersten, 2000). A viscous sub layer is a thin layer where the viscous force is dominant and the velocity in this layer is often considered as having a linear distribution. Thus, the shear stress (τ_b) in the viscous sub layer for two dimensional flow can be expressed as:

$$\tau_b = \mu\left(\frac{\partial u}{\partial z}\right) \tag{2.1}$$

with μ = dynamic viscosity, u = streamwise velocity and z = distance to the channel bed.

Integrating (2.1) over the depth yields:

$$\frac{u}{u_*} = \frac{u_* z}{\nu} \tag{2.2}$$

with

$$u_* = \sqrt{\frac{\tau_b}{\rho}}$$

A comparison with experimental data indicates that (2.2.) is only valid for $z^+ = u_* z / \nu < 5$ (Nezu, 2005). As z^+ becomes larger, the velocity profile tends to follow a logarithmic distribution. Prandtl proposed his mixing length theory for $z^+ > 70$ (Schlichting and Gersten, 2000) to obtain:

$$\tau_b = \rho l^2 \left(\frac{\partial u}{\partial z}\right)^2 \tag{2.3}$$

The mixing length (l) is equal to the von Karman constant (often expressed as κ) multiplied by the depth of the flow for near wall region (Schlichting and Gersten, 2000). After integration (2.3) becomes:

$$u^+ = A\ln(z) + C = A\ln(\frac{z}{z_0}) \tag{2.4}$$

with $u^+ = u / u_*$

The parameter z_0 is often called a roughness length and its value depends on the condition of the wall. Using a dimensional argument (Schlichting, 1979), it is possible to show that:

$$z_0 \propto \frac{\nu}{u_*} = \beta \frac{\nu}{u_*} \tag{2.5}$$

Thus, equation (2.4) can be rewritten as:

$$u^+ = A\ln z^+ + B \tag{2.6}$$

The values for parameters κ (=1/A) and B were often adopted from Nikuradse experimental result (Nezu and Nakagawa, 1993), i.e. 0.4 and 5.5 respectively. The velocity distribution in the buffer zone (a region between log law layer and viscous sub layer) cannot be expressed by either equation (2.2) or (2.6), as it is affected by both viscous and turbulent forces. Based on Nikuradse's (1933) experimental results on resistance, (2.6) can be written as (Chow, 1959; Nezu and Nakagawa, 1993):

$$u^+ = 5.75\log\left(\frac{9u_*H}{\nu}\right) \quad \text{(for } k_s^+ < 5 \text{ or smooth boundary)} \tag{2.7}$$

$$u^+ = 5.75\log\left(\frac{30H}{k_s}\right) \quad \text{(for } k_s^+ > 70 \text{ or rough boundary)} \tag{2.8}$$

With $k_s^+ = k_s / (\nu / u_*)$ and k_s = Nikuradse's equivalent sand roughness.

Equations (2.7) and (2.8) are known as Prandtl's universal law for smooth and rough turbulent flow respectively. Alternatively, a power law has also been proposed to represent the velocity distribution in the form of (Barenblatt, 1993; Schlichting, 1979):

$$u^+ = a(z^+)^m \tag{2.9}$$

The parameters *a* and *m* are the coefficient and exponent of the power law. Chen (1991) suggested a range of 1/12 to 3/12 for the exponent while Schlichting (1979) showed that the exponent varies with *Re* and suggested exponent value in the range of 1/10 to 1/6 for $4 \times 10^3 < Re < 3.24 \times 10^6$.

The velocity distribution described by the log or the power law has a maximum value on the surface. However, this is often not the case in reality due to the velocity dip phenomenon (see Section 2.2.3). In order to take the velocity dip into account, a wake function, dependent on *z* and *H*, is often added to the log law (Coles, 1956; Nezu and Rodi, 1986). Other methods have been proposed which take such features into account, e.g. the entropy method (Chiu, 1987), however, this is beyond the scope of the current work.

2.2.3 Longitudinal vortices/secondary flow

Studies of the secondary circulation in open channel flow have been carried out for more than 100 years. Nezu *et al*. (1993) reported that Stearns (1883) and Moeller (1883) observed a velocity dip, a condition where the maximum velocity appeared below the water surface, in narrow rivers. They presumed that this was due to the appearance of a pair of counter-rotating secondary currents that flow from the banks toward the centre along the free surface and turn downward in the middle of the channel. Prandtl first postulated the existence of such secondary currents to explain the isovel distortions of the streamwise velocity he observed in a straight non-circular duct flow as early as 1926 (Perkins, 1970). He envisaged a system of longitudinal spirals in the flow that is caused by velocity fluctuations tangential to the isovels, larger than those perpendicular to the isovels, which induced a centrifugal acceleration in these regions. This type of flow is often known as the Prandtl's secondary flow of the second kind, as a tribute to Ludwig Prandtl. Einstein and Li (1958) proposed the mathematical formulation of Prandtl's secondary flow of the second kind and confirmed that this type of flow is mainly caused by the anisotropy of the turbulence intensities in the lateral and the vertical directions, which tend to occur at solid boundaries and the free surface. The magnitude of

the Prandtl's secondary flow of the second kind is typically 2-3% of the primary mean velocity (Tominaga *et al.*, 1989). Secondary flow can also be generated as a result of mean flow skewing (Perkins, 1970), that resulting in centrifugal forces acting on the fluid. This is termed Prandtl's secondary flow of the first kind. Such flow generally occurs in river bends or in regions where the cross sectional area changes.

The existence of these secondary current affects the primary flow and, therefore, conveyance. The velocity gradient of the secondary flow also affects the lateral distribution of boundary shear stress (Knight and Shiono, 1996) and pattern of isovels (Knight and Patel, 1985). As a direct result of this, it also affects the spanwise distribution of the sediment concentration (Vanoni, 1946) and the three-dimensional configurations of river bed (Nezu *et al.* 1993; Karcz, 1966; Culbertson, 1967; Allen, 1985).

Bathurst *et al.* (2002) investigated overbank deposition patterns in straight and meandering channels on the UK FCF at HR Wallingford, UK. Experiments were undertaken for two relative depth (Dr) values in the straight channel (0.26 and 0.44) and one relative depth value for the meandering case (0.27). For the straight channel, it was found that deposition occurred in the form of a berm along the channel bank and little sediment was transferred onto the floodplain. The berms consisted of a train of small dunes migrating along the bank in the direction of the flow with widths corresponded to the widths over which main channel water was dispersed by mixing at the channel-floodplain interface. A different pattern of deposition was found for the meandering channel, i.e., deposition was not limited to the near-bank area but took place across the entire floodplain tongue (i.e., the floodplain on the side of the inner main channel bank) between successive meanders. Maximum deposition occurred on the downstream side of the meander tongue. In the area upstream of the tongue, the velocities were too strong for deposition to occur.

Tominaga *et al.* (1989) carried out measurements of the secondary currents using hot film anemometry in rectangular and trapezoidal channels with smooth surfaces. They found that the maximum value of the secondary current velocity for the smooth surface, for both types of channel, is nearly equal to 1.5%U_{max}. Tominaga *et al.* (1989) also conducted a measurement in a rectangular channel with rough walls (roughened with glass beads with 12mm diameter). They found out that the maximum value of the secondary current velocity for the rough rectangular channel was higher than those for the smooth channels, if expressed in terms of the maximum streamwise velocity, i.e.

2%U_{max}. In the rectangular channel, the secondary currents flow toward the side wall along the horizontal plane at about *y/H* = 0.6. This created a pair of vortices, one above another, that are termed the free-surface vortex and the bottom vortex (Figure 2.2a). The secondary currents patterns for the trapezoidal channel are different from those for the rectangular channel and depend on the angle of the sidewall (Figure 2.2b).

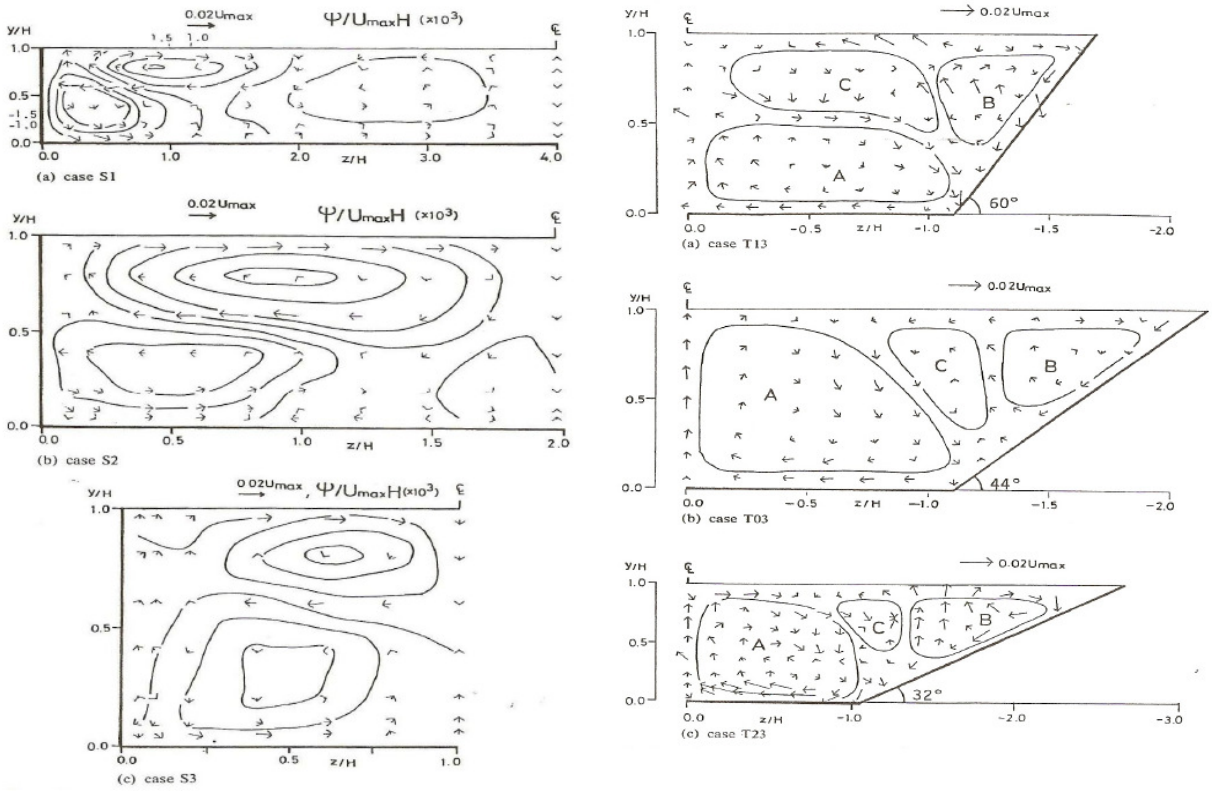

(a) Rectangular channel - various water depths. (b) Trapezoidal channel - various sidewall angles.

Figure 2.2 Secondary flow vectors in rectangular channel with various water depths (Tominaga *et al.*, 1989).

Nezu *et al*. (1993) conducted a measurement of secondary flow in a man-made river with a river width and depth values of 17.5m and 2.2m respectively. The measurement location was categorised as a wide channel as its aspect ratio (*B/H*) is greater than 5. The water discharge in the river was kept constant at 14m^3s^{-1} by a weir upstream of the measurement location. Two sets of specially designed electromagnetic flow meters mounted on a traversing mechanism were used to measure the 3D velocity at 270 chosen points. Two instrument configurations were used: (1) 3 minutes measurement with a sampling frequency of 100Hz and (2) 7 minutes measurement with a sampling frequency of 40Hz. Based on these results, Nezu *et al*. (1993) interpreted several sets of secondary cells along the river as shown in Figure 2.3. However, different possibilities of secondary flow cell

distribution can also be interpreted from these measurement results. The maximum value of secondary currents was reported to be below 4% of the maximum streamwise velocity. Unfortunately, no details relating to the straightness of the reach were given.

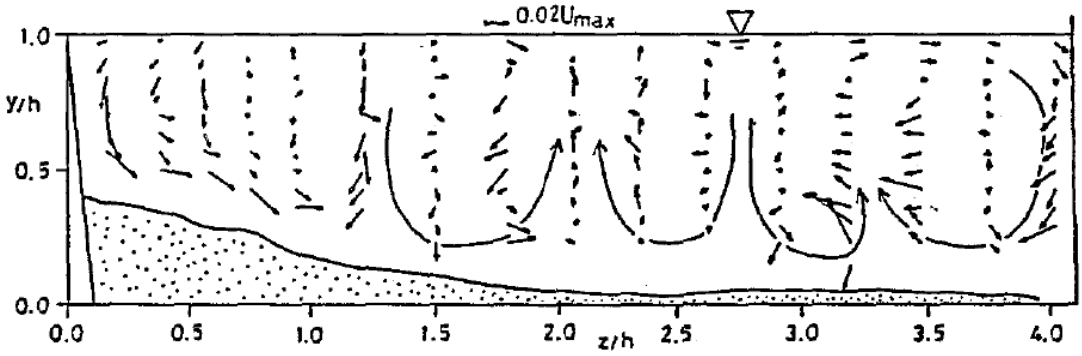

Figure 2.3 Interpretation of the secondary flow cells direction from data obtained using two electromagnetic current meters (Nezu *et al.*, 1993).

Secondary flow can also be triggered by the interaction between the flows in the main channel and the flow in the floodplain in a meandering compound channel. During overbank conditions, the floodplain flow in such a channel could be tangential to the streamwise velocity direction in the main channel. Ervine, *et al.* (1993) reported that the interaction between floodplain and main channel flow in such conditions will generate a large scale secondary cell, which grows in width along the cross-over length and then decays rapidly (Figure 2.4). In relation to this, Shiono and Muto (1998) reported that the floodplain flow tends to be more tangential to the main channel flow with increasing relative depth (D_r = (H-h)/H) as shown in Figure 2.5. At D_r = 0.15, the flow in the floodplain suddenly deviated and was forced to follow the main channel streamwise direction. At D_r = 0.25, the deviation of the floodplain flow was much less than that for D_r = 0.15 and only occurred near the entrance and exit of each bend. At D_r = 0.5, no characteristics of interaction between the main channel flow and floodplain flow could be observed and the streamlines of water surface were almost wholly aligned with longitudinal direction (the direction from left to right in Figure 2.4).

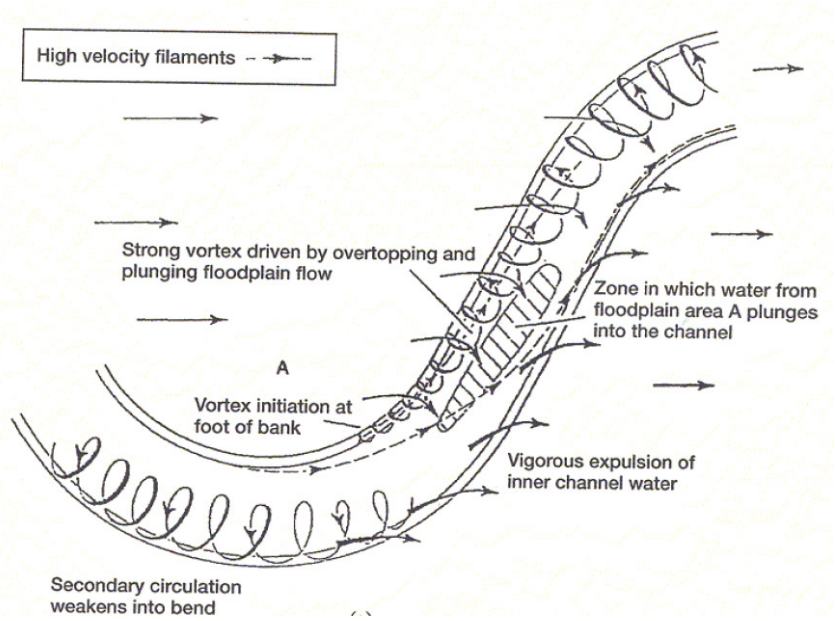

Figure 2.4 Flow structures in a flooded meandering channel (Ervine *et al.*, 1993).

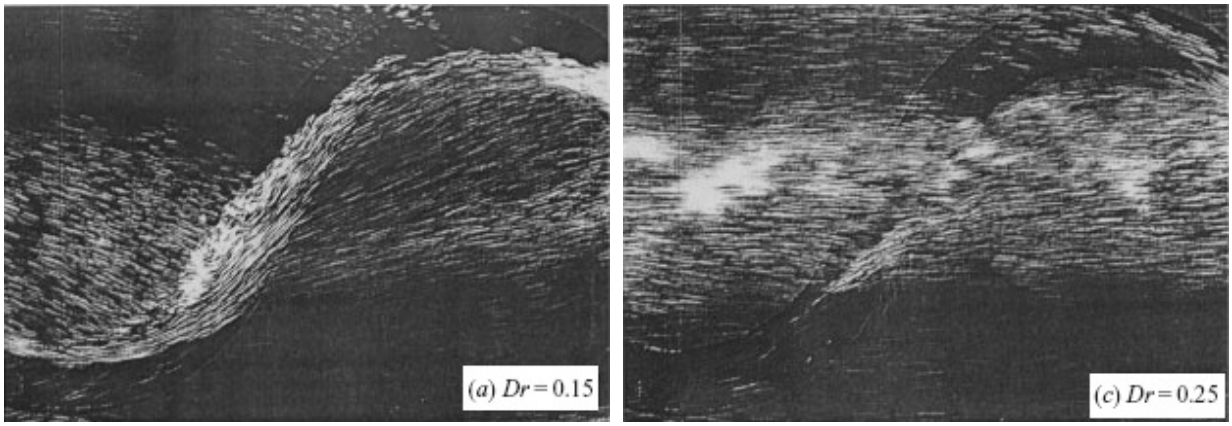

Figure 2.5 Flow visualization on water surface with sawdust (Shiono & Muto, 1998).

Willets and Rameshwaran (1996) conducted laboratory experiments to determine the flow structures present in a meandering two-stage channel. They used two channel cross section configurations: trapezoidal and natural channels. The natural bed was created by feeding the channel with material at the upstream end of the flume under to ensure an equilibrium transport rate. Once this was achieved, the bed surface was fixed to prevent further evolution of the bed topography. Three water depth configurations were examined, i.e. for D_r = 0, 0.25 and 0.35. It was found that once the flow goes overbank the rate of increase of discharge with respect to depth is greater in the case of the natural channel compared to the trapezoidal channel. Willets and Rameshwaran suggested that this increase caused less energy dissipation at the interface between the floodplain and the main channel. This suggestion was supported by an increase in the magnitude

of the secondary flow circulation in the trapezoidal channel than in the natural channel. It was shown that for a right hand bend, the primary secondary circulation cell is anticlockwise for inbank flow, but clockwise for overbank flow. This reversal of direction was reported to be driven by the momentum exchange with the flow coming off the floodplain in the cross-over region where the channel and floodplain flows are oblique in plan. It was also reported that the location of the maximum streamwise velocity relocated to the inner meander bend with rising water depth.

2.2.4 Planform vortices

Sellin (1964) reported the presence of horizontal vortices with vertical axes at a highly-sheared region between the main channel and floodplain (Figure 2.6). This feature was identified from the flow in a 4.6m long compound channel, and visualised by scattering aluminium powder. Similarly, large horizontal planform vortices were also observed in rivers during overbank flow conditions such as that in River Tone, Japan, during the 1981 flood (Figure 2.7). Ikeda *et al*. (2001), as reported by Knight *et al.* (2009), examined the behaviour of these large planform vortices in half trapezoidal compound channel with 1.2m width and 12m length at various depths. They observed similar patterns of large planform vortices, as shown in Figure 2.8a, as those observed in the River Tone during the 1981 flood for a relative depth (D_r) value of 0.180. The geometry of the vortices is unsymmetrical, with a lower free surface elevation at the centre of the vortex (Knight *et al.,* 2009). The geometry of the vortices is stretched in the streamwise direction. Thus, they are a major influence on the instantaneous value of velocity in the lateral direction. For a relative depth value of 0.344, the periodic planform vortices were replaced by active intermittent boils (Figure 2.8b). It was also reported that the intermittent boils become stronger as the depth ratio increases.

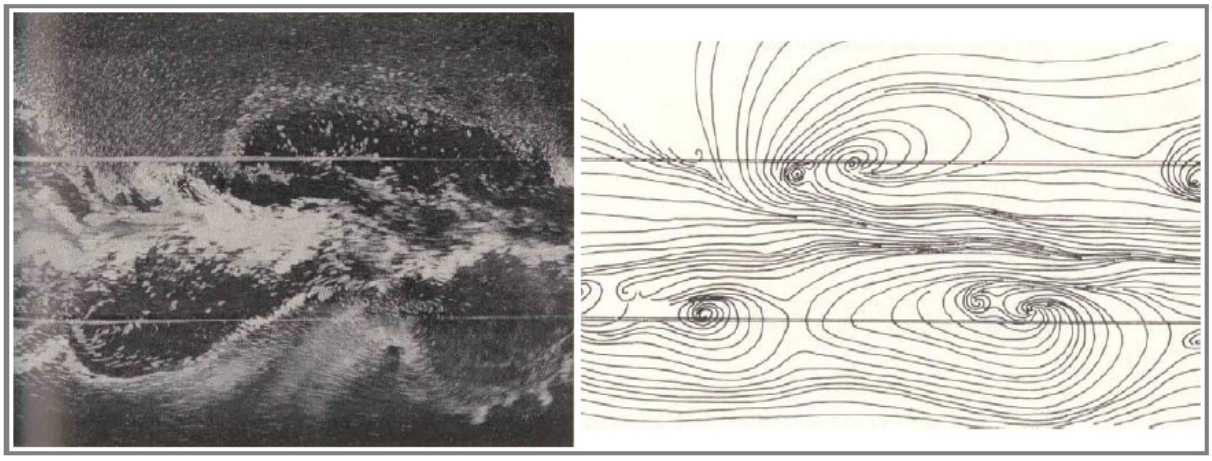

(a) velocity visualisation (b) streamlines

Figure 2.6 Surface (a) velocity patterns and (b) streamlines relative to the moving camera (Sellin, 1964).

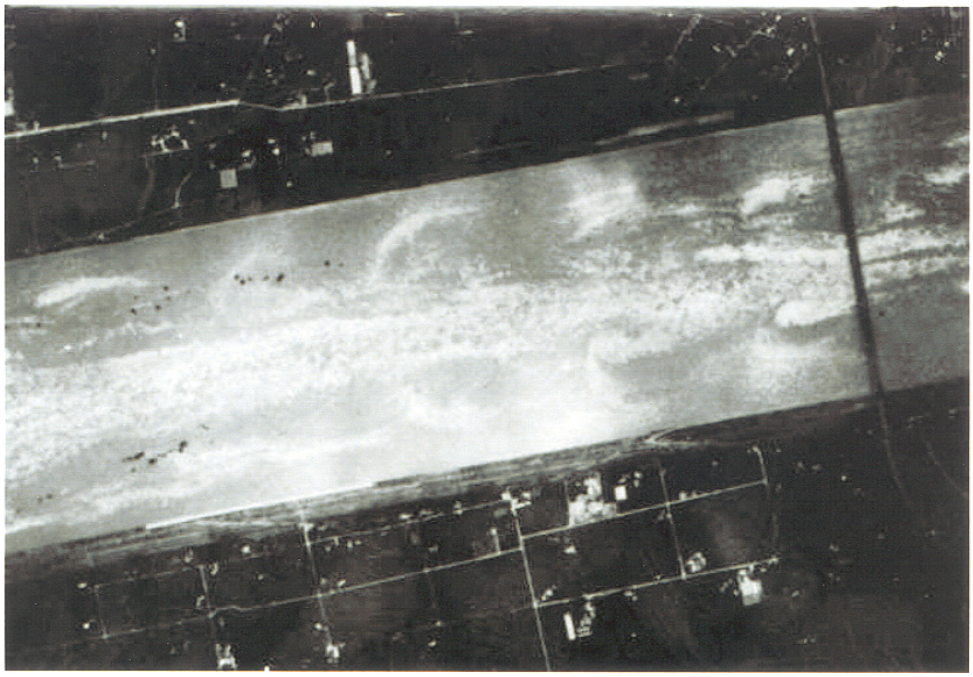

Figure 2.7 Horizontal vortices observed in the River Tone, Japan, during the 1981 flood. The flow is from left to right. (Courtesy of the Ministry of Construction of Japan).

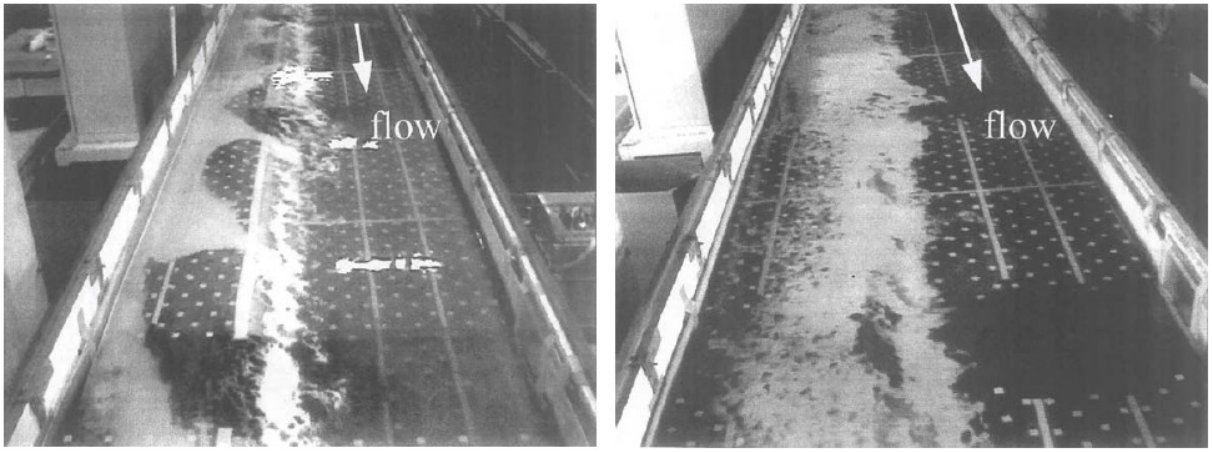

(a) $(H\text{-}h)/H = 0.180$ (b) $(H\text{-}h)/H = 0.344$

Figure 2.8 Visualisation of the free surface in a straight two-stage channel at a relative depth of (a) 0.180 and (b) 0.344 (Ikeda *et al.*, 2001).

2.3 Governing equations

A certain degree of simplification is required when trying to interpret the physics of the flow in rivers mathematically. In order to know the limitations of a numerical model, it is crucial to understand the simplifications or assumptions that have been adopted. This section aims to provide an

understanding of the mathematical concepts used in developing the Shiono and Knight Method (SKM).

2.3.1 The differential equation of linear momentum

The governing equations of fluid flow are based on the conservation laws of mass and momentum. Newton's second law states that the acceleration of a body is proportional and in the same direction of the net force acting on that body. Expressed as a differential equation, this can be written as:

$$F = \frac{d(mv)}{dt} \tag{2.10}$$

The force balance on a rectangular element of fluid in Cartesian coordinates with edges *dx*, *dy*, *dz*, assuming only gravity, pressure and viscous forces acting on the element, can be written as (Davidson 2004, White 1999):

$$\rho \delta V \frac{DV_i}{Dt} = \rho g \delta V - (\nabla p)\delta V + viscousforces \tag{2.11}$$

with: $\delta V = dxdydz$

$$\nabla p = \frac{dp_x}{dx} + \frac{dp_y}{dy} + \frac{dp_z}{dz}$$

V_i = the sum of velocity components normal to the element sides

In other words, (2.11) states that the mass of the fluid particle times its acceleration is equal to the sum of body forces acting on the particle, net pressure acting on the lump sum and any viscous forces arising from viscous stresses.

The viscous forces acting on the fluid particle should be defined in order to complete equation (2.11). The stresses arising due to viscosity will consist of shear and normal stresses as shown in Figure 2.9. For simplicity, the normal stresses are expressed as τ rather than the more commonly used notation σ. The stress is acting on the plane perpendicular to the axis mentioned by the first letter of the

subscript. The second letter of the subscript indicates the direction of the stress on that plane. Stresses that are acting on the *x* direction are illustrated in Figure 2.10.

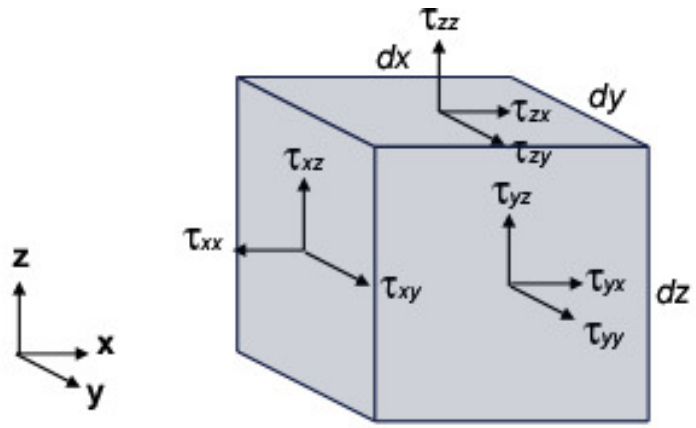

Figure 2.9. Notation for stresses.

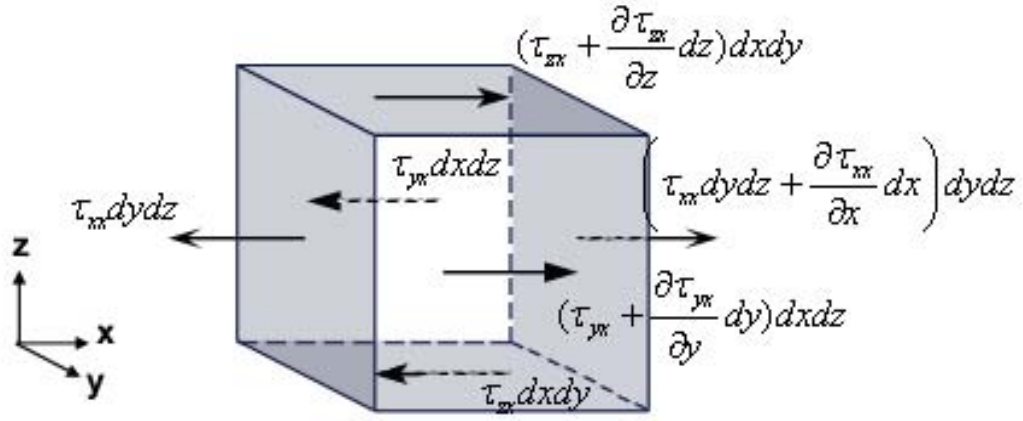

Figure 2.10 Stresses acting on *x* direction.

Based on Figure 2.10, the net force in the *x* direction can be expressed as:

$$dF_x = \left(\frac{\partial \tau_{xx}}{\partial x} + \frac{\partial \tau_{yx}}{\partial y} + \frac{\partial \tau_{zx}}{\partial z} \right) \delta V \tag{2.12}$$

Equation (2.12) can be written in the abbreviated form:

$$dF_x = \frac{\partial \tau_{jx}}{\partial x_j} \delta V \tag{2.13}$$

Similar expressions can be used for forces acting in any perpendicular directions, so that:

$$dF_i = \frac{\partial \tau_{ji}}{\partial x_j} \delta V \tag{2.14}$$

Substituting the viscous force terms in (2.11) with (2.14) and expressing the resulting equation in per unit volume yields:

$$\rho \frac{DV}{Dt} = \rho g - \nabla p + \frac{\partial \tau_{ji}}{\partial x_j} \tag{2.15}$$

For Newtonian fluid, e.g. water, the viscous stresses can be assumed as being proportional to the element strain rates and the coefficient of viscosity (Newton's law of viscosity):

$$\tau_{ij} = \rho \nu \left(\frac{\partial u_i}{\partial x_j} + \frac{\partial u_j}{\partial x_i} \right) \tag{2.16}$$

Substituting (2.15) to (2.16) yields

$$\rho \frac{DV}{Dt} = \rho g - \nabla p + \nu \nabla^2 V \tag{2.17}$$

The equation (2.17) is known as the Navier-Stokes equation (Davidson, 2004).

2.3.2 One dimensional form of the Navier-Stokes equation

When fluid particles are moving along the *x* direction only, (2.17) is reduced to:

$$\rho \frac{Du}{Dt} = \rho g_x - \frac{\partial p}{\partial x} + \frac{\partial \tau_{xx}}{\partial x} + \frac{\partial \tau_{yx}}{\partial y} + \frac{\partial \tau_{zx}}{\partial z} \tag{2.18}$$

Convective derivatives and conservation of mass are used in order to simplify (2.18) into a more usable term. Stokes introduced the convective derivative ($D(.)/Dt$), a term used to express rate of change in *Lagrangian* approach. The convective derivative Du/Dt observes the rate of change of fluid particle acceleration as it moves around. It should not be confused with $\partial u/\partial t$, an *Eulerian* approach, that observes the rate of change of particle acceleration at one fixed point. The chain rule can be used to express the term Du/Dt with:

$$\frac{Du}{Dt} = \frac{\partial u}{\partial t} + \frac{\partial u}{\partial x}\frac{\partial x}{\partial t} + \frac{\partial u}{\partial y}\frac{\partial y}{\partial t} + \frac{\partial u}{\partial z}\frac{\partial z}{\partial t} = \frac{\partial u}{\partial t} + u\frac{\partial u}{\partial x} + v\frac{\partial u}{\partial y} + w\frac{\partial u}{\partial z} \tag{2.19}$$

Expanding (2.19) with product rule yields:

$$\frac{Du}{Dt} = \frac{\partial u}{\partial t} + \frac{\partial uu}{\partial x} + \frac{\partial uv}{\partial y} + \frac{\partial uw}{\partial z} - u\left(\frac{\partial u}{\partial x} + \frac{\partial v}{\partial y} + \frac{\partial w}{\partial z}\right) \tag{2.20}$$

Conservation of mass (continuity equation) can be expressed as:

$$\frac{\partial \rho}{\partial t} + \frac{\partial(\rho u)}{\partial x} + \frac{\partial(\rho v)}{\partial y} + \frac{\partial(\rho w)}{\partial z} = 0 \tag{2.21}$$

Since generally the fluid in an open channel flow can be assumed to be incompressible, (2.21) becomes:

$$\frac{\partial u}{\partial x} + \frac{\partial v}{\partial y} + \frac{\partial w}{\partial z} = 0 \tag{2.22}$$

Substituting (2.22) to (2.21) yields:

$$\frac{Du}{Dt} = \frac{\partial u}{\partial t} + \frac{\partial uu}{\partial x} + \frac{\partial uv}{\partial y} + \frac{\partial uw}{\partial z} \tag{2.23}$$

Substituting (2.23) to (2.18) yields:

$$\rho\left(\frac{\partial u}{\partial t}+\frac{\partial uu}{\partial x}+\frac{\partial uv}{\partial y}+\frac{\partial uw}{\partial z}\right)=\rho g_x-\frac{\partial p}{\partial x}+\frac{\partial \tau_{xx}}{\partial x}+\frac{\partial \tau_{yx}}{\partial y}+\frac{\partial \tau_{zx}}{\partial z} \tag{2.24}$$

If the flow is assumed to be uniform with parallel streamlines and no curvature, then there are no changes of velocity and normal stress in the *x* direction. The pressure gradient term can be assumed as zero since generally the pressure can be assumed as hydrostatic. Thus, (2.24) becomes:

$$\rho\left(\frac{\partial uv}{\partial y}+\frac{\partial uw}{\partial z}\right)=\rho g_x+\frac{\partial \tau_{yx}}{\partial y}+\frac{\partial \tau_{zx}}{\partial z} \tag{2.25}$$

Substituting (2.16) into (2.25) yields:

$$\rho\left(\frac{\partial uv}{\partial y}+\frac{\partial uw}{\partial z}\right)=\rho g_x+\rho\nu\frac{\partial^2 u}{\partial y^2}+\rho\nu\frac{\partial^2 u}{\partial z^2} \tag{2.26}$$

In summary, these assumptions are used to derive (2.26):

1. The fluid flows only in the *x* direction.
2. The fluid is incompressible (density of fluids is constant).
3. Newtonian fluid (linear relationship between stress and the rate of strain).
4. Flow is steady uniform in the *x* direction (changes of velocity in the *x* direction are zero).

2.3.3 Reynolds-averaged Navier-Stokes equation

One of the characteristics of turbulence is the apparent randomness of velocity fluctuation over time, however, the statistical properties of turbulence are not random. The instantaneous velocity (u) can be expressed as the sum of time averaged velocity (U) and fluctuating component (u') (Figure 2.11). The value of u' become stable at a constant value when averaged over a certain period of time.

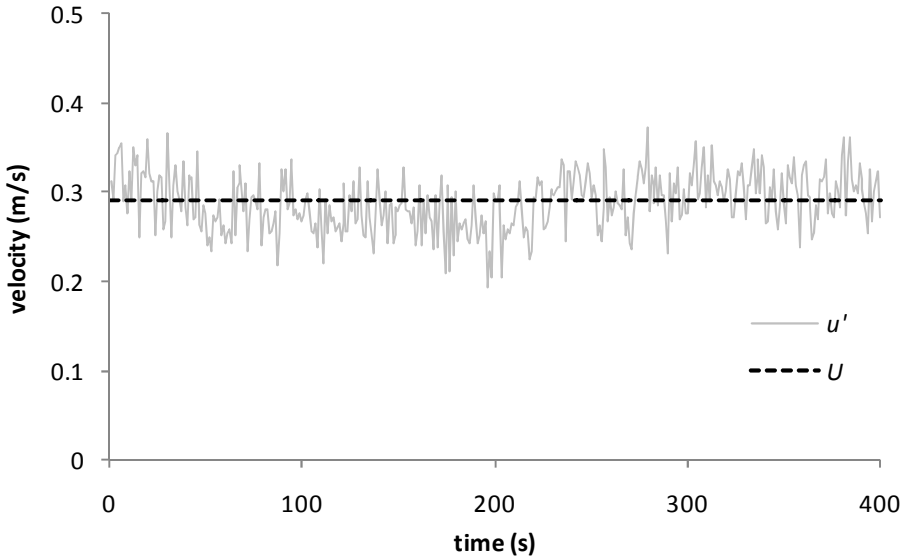

Figure 2.11 Definition of instantaneous velocity, mean velocity and fluctuating component.

Substituting u with the sum of U and u' to (2.26) yields:

$$\rho\left(\frac{\partial(U+u')(V+v')}{\partial y}+\frac{\partial(U+u')(W+w')}{\partial z}\right)=\rho g_x+\frac{\partial}{\partial y}\left(\rho\nu\frac{\partial(U+u')}{\partial y}\right)+\frac{\partial}{\partial z}\left(\rho\nu\frac{\partial(U+u')}{\partial z}\right) \qquad (2.27)$$

Equation (2.27) can be expanded to:

$$\rho\left(\frac{\partial UV}{\partial y}+\frac{\partial Uv'}{\partial y}+\frac{\partial u'V}{\partial y}+\frac{\partial u'v'}{\partial y}+\frac{\partial UW}{\partial z}+\frac{\partial Uw'}{\partial z}+\frac{\partial u'W}{\partial z}+\frac{\partial u'w'}{\partial z}\right)$$
$$=\rho g_x+\rho\nu\left(\frac{\partial^2U}{\partial y^2}+\frac{\partial^2u'}{\partial y^2}+\frac{\partial^2U}{\partial z^2}+\frac{\partial^2u'}{\partial z^2}\right) \qquad (2.28)$$

When averaged over an adequately long interval so that $\overline{u'}=\overline{v'}=\overline{w'}=0$ and $\overline{u'v'}$ & $\overline{u'w'}\neq 0$, (2.28) becomes:

$$\rho\left(\frac{\partial UV}{\partial y}+\frac{\partial UW}{\partial z}+\frac{\partial\overline{u'v'}}{\partial y}+\frac{\partial\overline{u'w'}}{\partial z}\right)=\rho g_x+\rho\nu\left(\frac{\partial^2U}{\partial y^2}+\frac{\partial^2U}{\partial z^2}\right) \qquad (2.29)$$

Rearranging of (2.29) gives:

$$\rho\left(\frac{\partial UV}{\partial y}+\frac{\partial UW}{\partial z}\right)=\rho g_x+\frac{\partial}{\partial y}\left(\rho\nu\frac{\partial U}{\partial y}-\rho\overline{u'v'}\right)+\frac{\partial}{\partial z}\left(\rho\nu\frac{\partial U}{\partial z}-\rho\overline{u'w'}\right) \tag{2.30}$$

The two terms $-\rho\overline{u'v'}$ and $-\rho\overline{u'w'}$ are referred as the Reynolds stresses. The shear stresses in the *x* direction are redefined as:

$$\tau_{yx}=\rho\upsilon\frac{\partial U}{\partial y}-\rho\overline{u'v'} \tag{2.31}$$

$$\tau_{zx}=\rho\upsilon\frac{\partial U}{\partial z}-\rho\overline{u'w'} \tag{2.32}$$

2.3.4 Solving the RANS - equations

The appearance of the Reynolds stresses makes turbulence a difficult problem to solve since there are more unknowns than equations, i.e. termed the closure problem. The widely used approach to solving the Navier-Stokes equation is to use a turbulence model. It is possible to solve the equation using a direct numerical simulation (DNS) where all the scales of the eddies are directly computed (Davidson, 2004). One of the benefits of using DNS lies in the fact that the initial conditions of the simulation can be controlled in a way which is just not possible in the laboratory (Davidson, 2004), e.g. setting the initial *Re* value. However, DNS require a vast number of sampling points since the spatial separation of the sampling points (Δx) cannot be greater than the Kolmogorov microscale (η - the approximate size of the smallest eddies). Thus, it requires high computational resources and time. This is the major drawback of DNS at the moment. Another approach is to use the large eddy simulations (LES). The mean flow and the large energy-containing eddies are computed in LES, but the small scale eddies are modelled. This is particularly useful if the main interest is in the large scales. The success of LES rests on the energy cascade concept, i.e. that the energy of the larger eddies travels down to the smaller eddies, not in the reverse direction (Davidson, 2004). Most engineering purposes do not require the detail of the turbulent fluctuations, and only the effects of the turbulence on the mean flow are usually sought (Versteeg and Malasekera, 1995). They are often adequately represented using a turbulence model. Thus, turbulence models alone are often used as they are likely to be more economical to run compared to DNS and LES. Unfortunately, even though turbulence models have improved recently, up to the point where they can be used in design,

they tend to work only for specific problems. Hence, physical model studies or full scale measurements are often required to verify the numerical model results.

Turbulence models are generally classified according to the number of transport equations they use. Examples of turbulence models are: eddy viscosity model, mixing length model, one equation models, two equation models, Reynolds stress equation models (Nezu and Nakagawa, 1993). The SKM employs the Boussinesq eddy viscosity concept in order to account the effect of the Reynolds stresses on the mean flow. Boussinesq introduced additional viscosity (ε_t) to account the effect of turbulence mixing momentum (τ_{xy}^R) in the one dimensional form as:

$$\tau_{xy} + \tau_{xy}^R = \rho(\nu + \varepsilon_t)\frac{\partial U}{\partial z} \tag{2.33}$$

Therefore, the role of turbulence in the eddy viscosity concept is to add the effective viscosity from ν to $\nu + \varepsilon_t$, which yields additional momentum caused by turbulence mixing, as characterised by τ_{xy}^R. In the three dimensional form, τ_{xy}^R becomes (Davidson, 2004):

$$\tau_{xy}^R = -\rho\overline{u_i' u_j'} = \rho\varepsilon_t\left[\frac{\partial U_i}{\partial x_j} + \frac{\partial U_j}{\partial x_i}\right] - \frac{\rho}{3}\overline{u_k' u_k'}\,\delta_{ij} \tag{2.34}$$

The eddy viscosity in (2.34) is a scalar measure and hence, its values are the same for all stress components (isotropic) (Nezu and Nakagawa, 1993). As a result, it does not produce any turbulence driven secondary motion. A more refined model is required in order to represent the effect of the turbulence driven secondary flow. Prandtl was the first person to suggest a means of calculating the eddy viscosity, using his mixing length concept, written as:

$$\varepsilon_t = l^2\left|\frac{\partial U}{\partial z}\right| \tag{2.35}$$

The parameter *l* is the Prandlt mixing length, the size of the large eddies, which has to be chosen appropriately, often by experiments. Furthermore, in open channel flow the distribution of eddy viscosity over the depth has been found in some cases to be parabolic (see Nezu and Nakagawa,

1993). Readers interested in a more detailed review of turbulence models are directed to Davidson (2004), Nezu and Nakagawa (1993), ASCE Task Committee on Turbulence Models in Hydraulic Computations (1998a, 1998b, 1998c, 1998d and 1998e), Versteeg and Malasekera (1995).

2.4 Stage – discharge prediction in rivers using SKM

This section describes the background of the Shiono and Knight Method (SKM), which will be used for modelling the flow in the River Blackwater, both in the physical model and in the actual river. A brief description of resistance coefficients and their application in predicting discharges in open channels, using simple modelling techniques, is also presented. An understanding of the concept of resistance coefficients is important for applying the SKM.

2.4.1 Resistance coefficients

As water flows, resistance is encountered by the bulk of water due to its interaction with the boundary. Such resistance clearly affects the velocity distribution. Attempts to quantify the resistance in open channel flow have been made as early as 1768 when Antoine Chezy was given the task of designing a canal for the Paris water supply (Henderson, 1966). He postulated that:

$$u = C\sqrt{RS_0} \tag{2.36}$$

with *C* denotes the Chezy coefficient.

The Chezy coefficient may be expected to depend on the Reynolds number, boundary roughness and the shape of the cross section. Its values vary from $30 m^{1/2} s^{-1}$ for a rough channel to $90 m^{1/2} s^{-1}$ for a smooth channel (White, 1999).

Darcy (1857) and Weisbach (1845) suggested a different approach to compute the resistance coefficient in pipe, in the form:

$$f = h_f \frac{D}{L} \frac{2g}{u^2} \tag{2.37}$$

where h_f is the head loss due to friction, f is the Darcy-Weisbach friction factor, L is the length of the pipe and D is the diameter of the pipe. When applied to open channel flow, D becomes $4R$ (Chow, 1959).

One of the most famous, and still currently in use, is Manning's equation, and his coefficient, n, which suggests that C increases approximately as the sixth root of the channel size:

$$C \approx \frac{R^{1/6}}{n} \tag{2.38}$$

The parameter n is called Manning's roughness parameter. Substituting this relation into (2.36) yields:

$$u = \frac{1}{n} R^{2/3} S^{1/2} \tag{2.39}$$

Comprehensive lists on the n values for different materials can be found in Chow (1959) and White (1999).

Furthermore, Colebrook and White (1937) developed a formula to calculate the f by combining experimental results of studies of laminar and turbulent flow in pipes. Prandtl and Nikuradse established the relationship between f and Re based on their works on smooth and artificially roughened pipes and suggesting three turbulent zones (Chlebek, 2009):

1. Smooth turbulence zone where f is a function of Re:

$$\frac{1}{\sqrt{f}} = 2\log\frac{\mathrm{Re}\sqrt{f}}{2.51} \tag{2. 40}$$

2. Transition zone where f is a function of Re and k/D

3. Rough turbulence zone where f is a function of k/D:

$$\frac{1}{\sqrt{f}} = 2\log\frac{3.7\,D}{k} \tag{2.41}$$

Colebrook and White (1937) combined (2.40) and (2.41) to yield the Colebrook-White equation:

$$\frac{1}{\sqrt{f}} = -2\log\frac{2.51}{\mathrm{Re}\sqrt{f}} + \frac{k}{3.7\,D} \tag{2.42}$$

When applied to open channel flow, *D* becomes *4R* (see Section 2.2.1).

In order to simplify the relationship between shear stress and friction factor, it is often assumed that $\tau = \rho g R S_f$. Substituting this into equation (2.37) yields:

$$\tau = \left(\frac{f}{8}\right)\rho u^2 \tag{2.43}$$

When using (2.43), care needs to be taken to distinguish between global (for the whole cross sectional area), zonal (for each sub area) and local friction factors since their values are likely to be different.

2.4.2 Simple modelling techniques

The Chezy and Manning's equations have often been used for the calculation of discharge in open channel, e.g. the single channel method (SCM). The SCM is a simple method that treats the channel as a single cross section. The discharge of an open channel is calculated by simply integrating the velocity over the cross sectional area of the channel. In rivers where the material of the bed changes laterally, this method is clearly not representing the physics correctly, as the lateral variation of roughness is represented only by one single value. Furthermore, there is no additional term to take into account the longitudinal and planform vortices.

Another simple method for estimating discharge is the divided channel method (DCM). The DCM divides the channel into a number of zones that have similar characteristics. The discharge in each zone is computed using either the Chezy or Manning's equations and added together in order to obtain the total discharge of the cross section. This method is an improvement from the SCM, as it

provides a means to represent the lateral variation of roughness over the cross section. However, this method usually overestimates the total flow within the cross section as the momentum exchange between the divisions is not accounted for (Chlebek, 2009).

2.4.3 Shiono & Knight Method (SKM)

2.4.3.1 Governing equations, boundary conditions and solutions

The Shiono & Knight Method (SKM) is a quasi two-dimensional mathematical model that takes into account the secondary flow in rivers (Shiono & Knight 1988, 1991). The model is capable of predicting the lateral variations of depth-averaged velocity and boundary shear stress. The SKM has been able to predict stage discharge relationship in straight channels with good accuracy (Shiono & Knight, 1988; 1991; Knight, 1989; Knight *et al*., 1989). The recently developed UK 'Conveyance and Afflux Estimation System' software has adopted the SKM as its main engine (CES, 2010) (see also Knight, *et al*., 2010; McGahey, 2006; McGahey *et al*., 2006; 2008). The momentum equation of the SKM is based on the Navier-Stokes equation described previously. Thus, the Navier-Stokes equation for flow in the *x* direction can be written as:

$$\rho\left(\frac{\partial UV}{\partial y}+\frac{\partial UW}{\partial z}\right)=\rho g_x+\frac{\partial \tau_{yx}}{\partial y}+\frac{\partial \tau_{zx}}{\partial z} \tag{2.44}$$

Body force due to the mass of the fluid only act in the *x* direction, thus $g_x = g\sin\theta = gS_o$. The depth–averaged form of (2.44) can be written as:

$$\frac{\partial H(\rho UV)_d}{\partial y}=\rho g S_o H+\left(\int_{z_0}^{z_s}\frac{\partial \tau_{yx}}{\partial y}dz\right)-\tau_{zb} \tag{2.45}$$

According to Liebnitz's rule, the third term could be written as:

$$\int_{z_0}^{z_s}\frac{\partial \tau_{yx}}{\partial y}dz=\frac{d}{dy}\int_{z_0}^{z_s}\tau_{yx}dz+\tau_{yx}(z_0)\frac{\partial z_0}{\partial y}-\tau_{yx}(z_s)\frac{\partial z_s}{\partial y} \tag{2.46}$$

The term $\frac{\partial z_s}{\partial y}$ is zero since water surface is assumed as horizontal over the lateral direction. By introducing the depth-averaged lateral shear stress $\bar{\tau}_{yx}$,

$$\bar{\tau}_{yx} = \frac{1}{H}\int_{z_0}^{z_s} \tau_{yx}\ dz \tag{2.47}$$

where z_s = water surface level (constant) and z_0 = bed level (*-y/s*) on the side slope, equation (2.45) becomes:

$$\frac{\partial H(\rho UV)_d}{\partial y} = \rho g S_o H - \frac{\tau_{yb}}{s} + \frac{\partial H\bar{\tau}_{yx}}{\partial y} - \tau_{zb} \tag{2.48}$$

where τ_{yb} and τ_{zb} are the shear stresses at bed. The values of these stresses can be expressed in terms of bed shear stress τ_b. The shear force balance on Figure 2.12 can be written as:

$$\tau_{yb}\ dxdz + \tau_{zb}\ dxdy = \tau_b\ \sqrt{dz^2 + dy^2}\ dx \tag{2.49}$$

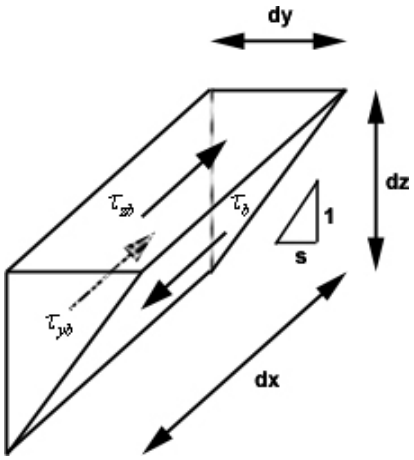

Figure 2.12 Side slope shear stresses.

Since *dz*/*dy* = 1/*s*, dividing (2.49) with *dxdy* yields:

$$\frac{\tau_{yb}}{s}+\tau_{zb}=\sqrt{1+\frac{1}{s^2}}\ \tau_b \tag{2.50}$$

Substituting (2.46) to (2.44) yields:

$$\frac{\partial H(\rho UV)_d}{\partial y}=\rho g S_o H+\frac{\partial H\bar{\tau}_{yx}}{\partial y}-\sqrt{1+\frac{1}{s^2}}\ \tau_b \tag{2.51}$$

For flat bed region, *s* is infinity, thus equation(2.47) becomes:

$$\frac{\partial H(\rho UV)_d}{\partial y}=\rho g S_o H+\frac{\partial H\bar{\tau}_{yx}}{\partial y}-\tau_b \tag{2.52}$$

Equations (2.47) and (2.48) can be solved analytically by assuming a quadratic friction law, based on the Darcy-Weisbach friction factor (*f*), the Boussinesq eddy viscosity (ε_{yx}) and a dimensionless eddy viscosity model:

$$\bar{\tau}_{yx}=\rho\varepsilon_{yx}\frac{\partial U_d}{\partial y} \tag{2.53}$$

$$f=\frac{8\tau_b}{\rho U_d^{\ 2}} \tag{2.54}$$

$$\varepsilon_{yx}=\lambda H U_*=\lambda\ H\ U_d\sqrt{\frac{f}{8}} \tag{2.55}$$

Therefore (2.52) can be expressed as (Shiono & Knight, 1988):

$$\frac{\partial H(\rho UV)_d}{\partial y}=\rho g S_o H+\frac{\partial}{\partial y}\left(\rho\lambda H^2\sqrt{\frac{f}{8}}U_d\frac{\partial U_d}{\partial y}\right)-\rho\frac{f}{8}U_d^{\ 2}\sqrt{1+\frac{1}{s^2}} \tag{2.56}$$

In other words, equation (2.52) relates the secondary flow term to the weight component plus Reynolds stress acting on vertical and horizontal planes. In an earlier paper, Shiono & Knight (1988)

assumed that the secondary flow term is zero. Using this approach, the predicted lateral distribution of depth-averaged velocity was in good agreement with the experimental data (e.g. an example shown in Figure 2.13), but the prediction of boundary shear stress was not as good as the prediction of the depth-averaged velocity. The additional of the secondary flow term was found to make a significant improvement in boundary shear stress prediction, (Knight *et al.*, 1994). Furthermore, Shiono and Knight (1991) demonstrated that, for the particular cases considered, the shear stress term due to secondary flow decreases approximately linearly either side of a maximum value that occurs at the edge of the floodplain and the main channel. The secondary flow term, $\partial H(\rho UV)_d / \partial y$, may be expressed as a single parameter, Γ (Shiono and Knight, 1991). Using this expression, (2.56) becomes a second order linear differential equation which can be solved analytically.

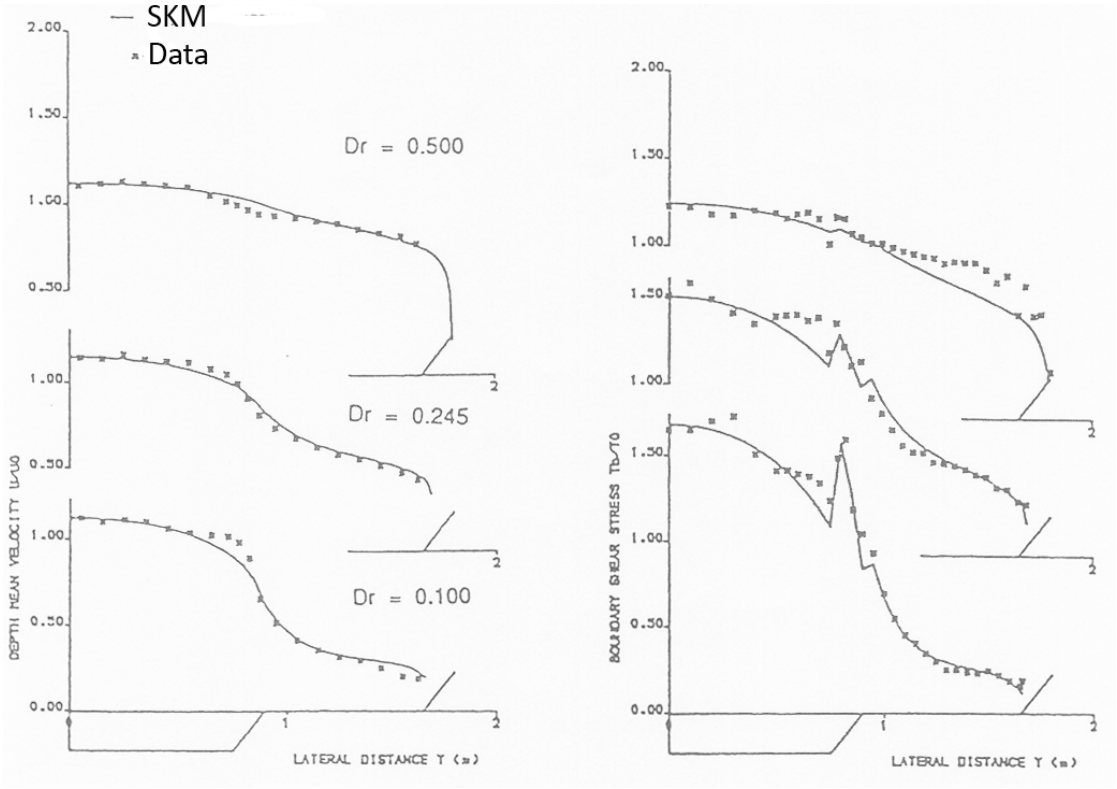

Figure 2.13 Transverse variation of U_d and τ_b in a two stage channel at various depth ratio values (Shino and Knight, 1991).

Equation (2.56) can be solved, provided the appropriate boundary conditions are specified. The approach used in the SKM is by subdividing the channel cross section into various subareas (panels) with either constant depth domains or sloping side slope domains, then solving the boundary conditions between adjacent panels and between the edge panels and their boundary, assuming no-

slip condition. Three calibration parameters, *f*, λ and Γ, are required for each panel. An example of the subdivision of a cross section is shown in Figure 2.14.

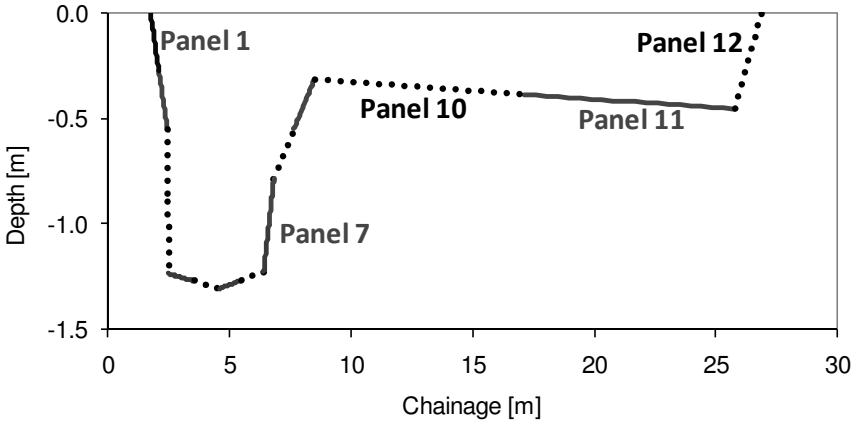

Figure 2.14 Subdivision of CS 4 of the River Blackwater.

The depth-averaged velocity (U_d) for a constant depth panel is given by:

$$U_d^{(n)} = \left[A_{n1} e^{\gamma_n y} + A_{n2} e^{-\gamma_n y} + k_n \right]^{1/2} \tag{2.57}$$

For linear side slope panel, U_d can be expressed as:

$$U_d^{(n)} = \left[A_{n1} \xi_n^{\alpha_n} + A_{n2} \xi_n^{-(\alpha_n+1)} + \omega_n \xi_n + \eta_n \right]^{1/2} \tag{2.58}$$

where

$$k = \frac{8gS_0H(1-\beta)}{f}\ ; \quad \gamma = \sqrt{\frac{2}{\lambda}}\left(\frac{f}{8}\right)^{1/4}\frac{1}{H}\ ; \quad \beta = \frac{\Gamma}{\rho g H S_0}$$

$$\alpha = -\frac{1}{2} + \frac{1}{2}\sqrt{1 + \frac{s(1+s^2)^{1/2}(8f)^{1/2}}{\lambda}}\ ; \quad \omega = \frac{gS_0}{\frac{(1+s^2)^{1/2}}{s}\frac{f}{8} - \frac{\lambda}{s^2}\left(\frac{f}{8}\right)^{1/2}}$$

$$\eta = -\frac{\Gamma}{\frac{(1+s^2)^{1/2}}{s}\frac{\rho f}{8}}\ ; \quad \xi = \text{Local depth} = H - \left(\frac{y-b}{s}\right); \quad \mu = \lambda\sqrt{\frac{f}{8}}$$

The side slope, *s,* is the horizontal length divided by vertical length. A positive sign of sloping side is used for panels whose slope angle is in between 0-90 or 180-270 degrees (clockwise). The number of boundary conditions required for solving equation (2.58) is twice of the number of the panels, since

there are two unknown constants in each equation. The boundary conditions in SKM, according to Shiono and Knight (1988) are:

Continuity of depth averaged velocity:

$$(U_d)_i = (U_d)_{i+1} \tag{2.59}$$

Continuity of the lateral gradient of depth averaged velocity:

$$\left(\frac{\partial U_d}{\partial y}\right)_i = \left(\frac{\partial U_d}{\partial y}\right)_{i+1} \tag{2.60}$$

Continuity of the unit force:

$$(H\bar{\tau}_{yx})_i = (H\bar{\tau}_{yx})_{i+1} \tag{2.61}$$

In order to obtain realistic mean velocity distribution, by smoothing the spikes caused by the abrupt changes in the local friction and dimensionless eddy viscosity, Omran (2005) suggested a modification to (2.60):

$$\left(\mu\frac{\partial U_d}{\partial y}\right)_i = \left(\mu\frac{\partial U_d}{\partial y}\right)_{i+1} \tag{2.62}$$

where,

$$\mu = \lambda\sqrt{\frac{f}{8}} \tag{2.63}$$

In addition, since no slip condition holds on the edges of the channel, the depth averaged velocity at the channel edges is zero. The boundary condition equations of SKM in this research are solved using a matrix approach.

2.4.3.2 A short review of previous work on SKM

One of the main concerns of numerical models users is to be able to use the "correct" values of calibration parameters in their models. However, this is not an easy task since the calibration parameters generally vary with discharge, depth and channel geometry. Furthermore, it is quite often that a set of parameters tends to work for a specific case only. Finding the relationship between calibration parameters values and the aforementioned factors above will make the modelling task easier.

The SKM has been shown to be efficient in predicting the distributions of depth averaged velocity, boundary shear stress and discharge in laboratory flumes (e.g. Shiono and Knight, 1988; 1990; 1991; Chlebek, 2009; Sharifi, 2009; Tang and Knight, 2009) and natural rivers (e.g. Knight *et al*., 1989; Abril and Knight, 2003; Sharifi, 2009). Some guidance on estimating the calibration parameters, f, λ and Γ, has also been established from this previous work. Based on the modelling of overbank flow in the River Severn at Montford Bridge (Knight *et al.*, 1989), which was schematised as a trapezoidal compound channel, two equations were developed to estimate the variation of f over the depth on the floodplains, i.e.:

$$f = 0.0183 D_r^{-0.5} \quad \text{(for left hand floodplain)} \tag{2.64}$$

$$f = 0.0721 D_r^{-0.5} \quad \text{(for right hand floodplain)} \tag{2.65}$$

These equations cause the friction factors to rise significantly at low relative depths.

Knight and Abril (1996) and Abril and Knight (2004) calibrated the SKM based on compound channel data and provided the following guidelines for determining the secondary flow term:

$$\Gamma = 0.05 H \rho g S_0 \quad \text{(for inbank flow)} \tag{2.66}$$

$$\Gamma = 0.15\, h \rho g S_0 \quad \text{(for the main channel during overbank flow)} \tag{2.67}$$

$$\Gamma = -0.25 h \rho g S_0 \quad \text{(for the floodplain during overbank flow)} \tag{2.68}$$

They also reported that the value of λ is not sensitive to the modelling result and adopting a constant value of λ for the whole channel (0.13). Assuming a constant value of λ for the whole channel does not technically represent of the actual physics, since it is known to be a function of geometry and friction (Knight and Abril, 1996). On the other hand, obtaining the lateral variation of λ for the whole channel through measurement is not straightforward.

Knight *et al*. (2007) proposed a means of defining the appropriate number of panels in SKM based on the number and distribution of secondary flow cells in trapezoidal channels. Using this method, Knight *et al*. (2007) were able to predict the velocity and boundary shear stress in simple trapezoidal channels reasonably accurately. However, in order to apply the method appropriately, the distribution of the secondary cells has to be known. Furthermore, this method is difficult to apply if secondary flow cells are on top of each other (e.g. as shown in Figure 2.2).

Chlebek (2009) applied the SKM to the inbank flow in simple straight trapezoidal and rectangular channels with homogeneous and heterogeneous roughness. The simulation results indicate that the SKM is able to accurately determine the discharge as well as the percentage shear force on the wall, typically within 2%. It was also reported that the contribution of the secondary flow term on the model is on average around 5%. Whether such a value is considered as significant, or not, is debatable.

More recently, Sharifi (2009) performed a detailed analysis of model calibrations using a multi-objective evolutionary algorithm and revealed that on occasion, there are a number of sets of model parameters that will allow successful predictions. This is often known as the equifinality problem (Beven, 2001). It was also reported that the values of the friction factor were found to be less dependent on the panel structure, while the depth-averaged lumped values of λ and Γ were highly affected by the panel structure (Sharifi, 2009). He argued that this might be due to the fact that these lumped parameters lose some degree of physical interpretation when averaged over time and depth and hence become dependent on the size and position of the panels.

Rameshwaran and Shiono (2007) proposed an additional term in the SKM in order to take into account the effect of vegetation on the model. The drag force due to vegetation is modelled as an additional momentum sink term in the Navier-Stokes equation. Tang and Knight (2009) have used a similar approach for modelling the flow in a partially vegetated compound channel. Both,

Rameshwaran and Shiono (2007) and Tang and Knight (2009), have reported good agreement between simulation and experimental data.

While the work reported in this section shows that SKM can predict the depth averaged velocity and boundary shear stress distributions reasonably accurately, many authors do not report on the quantitative values of the accuracy, apart from Knight, *et al*. (2010). This is unfortunate, since comparing the modelling accuracy from such work could provide a better understanding of the relationship between calibration parameters and the accuracy of the modelling.

2.5 Previous works on ADCP velocity measurement in rivers

ADCP was firstly produced in the mid 1970's (Rowe and Young, 1979), as an adaptation of a speed log, an instrument used to measures the speed of ships. In addition to measuring the water velocity, the ADCP is also capable of measuring the water depth and hence the ability to measure the cross sectional profile of the channel bed. Thus, by traversing an ADCP across the channel the discharge can be obtained. An ADCP was used to measure the discharge of the Mississippi River with encouraging results in 1982 (Christensen and Herrick, 1982). However, the technology at that time was not able to process the velocity data on a real-time basis. The first generation of ADCP that was able to produce water velocity measurements with sufficient quality for use by oceanographers used a narrow-bandwidth, single-pulse, autocorrelation methods that computed the first moment of the Doppler frequency spectrum. In 1985, the U.S. Geological Survey (USGS) purchased a narrowband ADCP and successfully developed a discharge measurement system using it (Simpson and Oltmann, 1993). However, the ADCP's minimum depth limitations of 3.4m restricted its use in small and shallow rivers. In 1991, significant improvement in ADCP technology was made with the introduction of Broadband ADCP. With typically 100 times as much bandwidth, broadband ADCPs reduced variance nearly 100 times when compared with narrowband ADCPs. The broadband ADCP could then be optimised for measurement in shallow water, due to the reason above. Morlock (1996) evaluated the broadband-ADCP for discharge measurement at 12 stream-gauging locations and concluded that the broadband ADCP system can be used to accurately measure discharges at sites similar to those measured by Morlock (1996). Muste *et al.* (2004a) state that given the efficiency and speed of the measurements, quantifying the mean velocities in rivers using an ADCP collected from moving vessels is very attractive. Simpson (2001) suggested that an ADCP may be the only feasible, accurate method for measuring discharge in tidally affected rivers and estuaries, as well as in rivers

or canals with unsteady flow. The ADCP also has proven useful in many upland rivers with depths too deep for wading.

Despite having great potential for studying the flow in rivers, ADCP measurements is currently lacking any standard procedures for measurements on a full range of rivers and flow conditions (Muste *et al.*, 2004a; Szupiany *et al.*, 2007). Shields *et al.* [2003] also reported that the lack of custom software for data analysis is one of the main difficulties in studying river reaches using ADCPs. Recently, a Commission for Hydrology (CHy) of the World Meteorological Organization (WMO) identified the need to develop a proposal and to implement a project to assess the performance of flow measurement instruments and techniques in response to the dramatic changes in hydrometric instrumentation and the need to compute associated discharge measurement uncertainties.

Discharge in rivers is frequently obtained by traversing an ADCP from one riverbank to the other river bank (termed moving vessel measurements) or from fixed ADCPs often embedded into the side of a river bank (side scanning ADCP). The accuracy of the ADCP in predicting velocity and discharge has been benchmarked against standard stream gauging techniques, e.g. current meter, ADV, towing basin, and most results show agreement within 5% (Shih *et al.*, 2000; Oberg 2002; Mueller 2003; Oberg & Mueller 2007; Gunawan *et al.,* 2008; 2009). Due to its capability in providing a velocity time series quickly, the use of ADCP has expanded beyond simple discharge measurements.

Turbulence intensity, large scale turbulence and secondary currents have all been investigated in both field and laboratory scale using ADCPs (Lemmin & Rolland, 1997; Barua & Rahman, 1998; Muste *et al.*, 2004a; 2004b; Dinehart & Burau, 2005a; Nystrom *et al.*, 2007; Stone and Hotchkiss, 2007; Szupiany *et al.*, 2007). ADCPs have also been used for measuring bed shear stress (Rennie *et al.*, 2007; Rennie & Church, 2007; Sime *et al.*, 2007), dispersion coefficient (Carr & Rehmann, 2007), sediment transports (Holmes & Garcia 2002; Dinehart & Burau, 2005b; Wagner, 2004; Merckelbach, 2006; Klein, 2003) and tidal flux (Turnipseed, 2002).

The lateral distribution of depth-averaged velocity along a cross section is often required for the calibration of hydrodynamic models, such as the Conveyance Estimation System and Afflux Estimation System {CES-AES} (CES, 2010; Knight *et al*., 2010; McGahey *et al*., 2008), SKM (Shiono & Knight, 1991). However, ADCP data may not be used for that purpose in a straightforward manner,

as there are fluctuations in its velocity data due to turbulence and instrument error. For instance, Muste *et al.* (2004a) reported multiple velocity fluctuations as large as 45% on ADCP instantaneous velocity data. Thus, despite the simplicity of obtaining instant velocity data via moving vessel measurements, a certain degree of averaging to reduce the velocity fluctuation is required in order to use the data. This issue is examined in detail in section 4.7.1, and the working principles of ADCP are described in section 4.1.1.

One method often used to reduce the velocity fluctuations is to average, with respect to over a reasonably long period of time (e.g. 3 to 15 minutes), the velocity data measured at a fixed location in the river (fixed-vessel measurement). However, this method is often impractical if velocity data across a cross-section is to be obtained, especially for wide rivers, and unreliable if the discharge changes quickly. Considering the limitations above, two alternative methods have been recently used to reduce the velocity fluctuations in the ADCP transverse data: (1) applying regression to ADCP transverse data (Muste *et al.,* 2004a), (2) averaging several ADCP transects together (Dinehart & Burau, 2005; Szupiany *et al.*, 2007; Le Coz *et al.*, 2007). However, the latter is not without its own difficulties, e.g. every ADCP transverse has the potential to be different, and as such, a decision has to be made as to whether any such differences are significant or not.

Six regression methods were applied by Muste *et al.* (2004a) for the first approach: (A) 3-point interpolation, (B) 5-point interpolation, (C) 2nd order polynomial regression, (D) Log-law regression, (E) Power-law regression, (F) Spatial non weighted averaging. These methods were applied to velocity profiles collected within an ensemble, with the exception on method (F), which combined information from three adjacent velocity profiles. Muste *et al.* (2004a) reported the results as follows. Methods A and B do not smooth the data very much. Method C shows good smoothing; however, the regression lines are drastically affected if large scattering at the top and bottom of the profiles exists. Methods D and E illustrate beneficial effects on the data, with respect to smoothing and the regressed profiles agree with typical open-channel velocity distributions (Figure 2.15). Method F biased the smoothed velocity profile to lower values due to velocity magnitude differences in neighbouring sections. Although not mentioned explicitly, Muste *et al.* (2004a) seem to use the velocity data obtained from a 600 kHz ADCP with 3Hz sampling frequency for testing the regressions. They concluded that the best smoothing of the data scattering was obtained with one-seventh power law. Based on his experiments, Muste *et al.* (2004a) also concluded: '*...there is a high probability of equally sampling 'negative' and 'positive' fluctuations around the mean velocity profile (large-scale*

turbulence) at successive transect locations. Differences between depth-averaged velocity profiles and the true ones due to the large-scale fluctuations cancel out each other for the successive ensembles taken along a transect. Similarly, but not at the same extent, the effect of the small-scale turbulence is cancelled out within a velocity profile. A similar conclusion was drawn by Gonzalez-Castro et al. (2002) when comparing discharges estimated from fixed ADCP and transect measurements'. This might justify why ADCP discharge measurement is generally stable for repeated measurements, despite the large fluctuation on its velocity data.

The Muste *et al.* (2004a) approach, however, might be less suitable for investigating the flow structures in a river. As it employs regressions on each one (or three for method F) velocity profiles (over-depth), there is a possibility to have discontinuity in the lateral velocity profile. Furthermore, using the power and log regression will result in profile which is possibly too smooth compared to reality and will always result in the maximum velocity being located at the water surface (Figure 2.15), which is clearly not the case when velocity dip phenomenon exists.

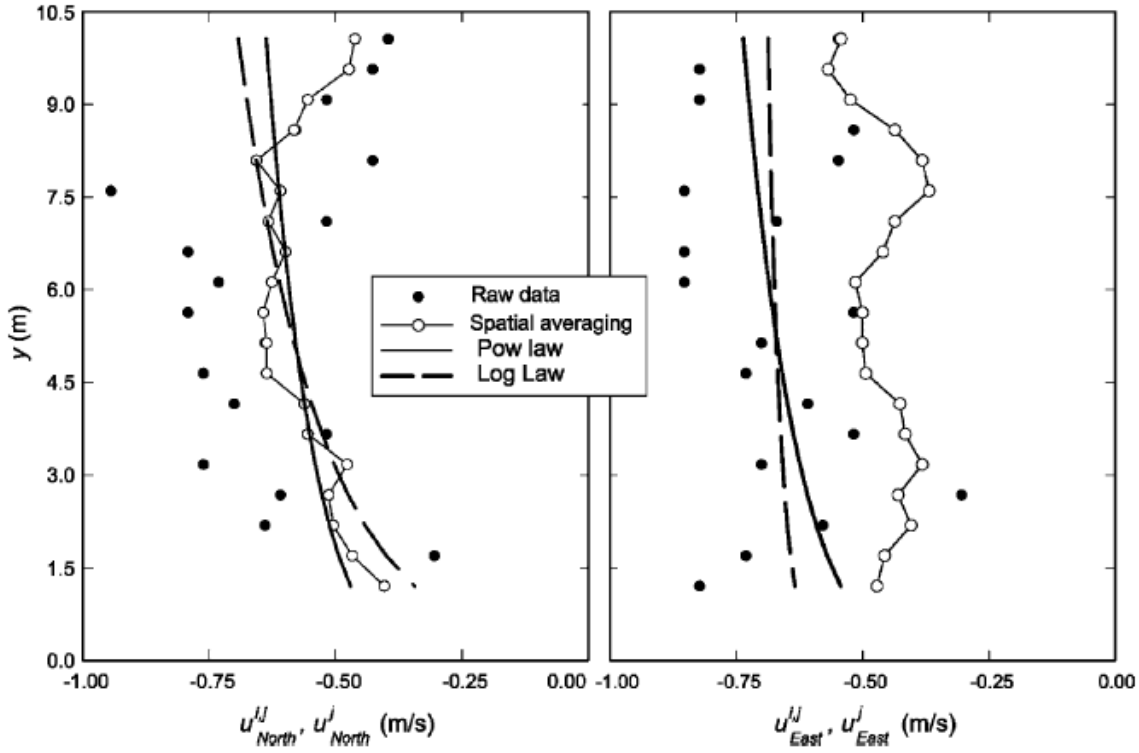

Figure 2.15 Spatial averaging, logarithmic, and power-law regressions applied to conditioned ADCP measurements for north and east velocity components (Muste *et al.,* 2004a).

The second method, averaging several ADCP transects together, has been adopted by a small number of researchers, each with their own unique approach, as outlined below.

Dinehart and Burau (2005) investigated the secondary flow pattern on a large river bend using data obtained from an ADCP (RDI Workhorse 1200kHz). The measurements were undertaken at various cross sections, with typical river width and depth of 130-220m and 7-15m respectively. In order to average the transect data, they first projected the velocity data of each transect along a straight line. This was done because measuring along a straight line is hardly possible due to the effect of pilot steering, lateral shear, and river turbulence that can push the boat (that carries the ADCP) off a linear path. It was reported that the deviations of the boat were usually less than 10% of the total width of the section. Dinehart and Burau (2005) averaged the velocity data from each ADCP transect by interpolating them into a 2-D grid representing the cross section of the corresponding measurement. The value at each nodes of the grid was calculated using an inverse distance weighting method (six samples points were selected by an equipartite arrangement). Each set of the interpolation grids was averaged together to obtain the final velocity grid. The result, as shown in Figure 2.16, appears to provide improvement from single transects. It was shown that the lateral velocity could be as large as 30% of the mean streamwise velocity in the section. In addition, Dinehart and Burau (2005) also mentioned that a few days of surveys required several weeks of processing and analysis. The work of Dinehart and Burau (2005) therefore highlights that the amount of work required to transform the ADCP data into a more useful form should not be underestimated.

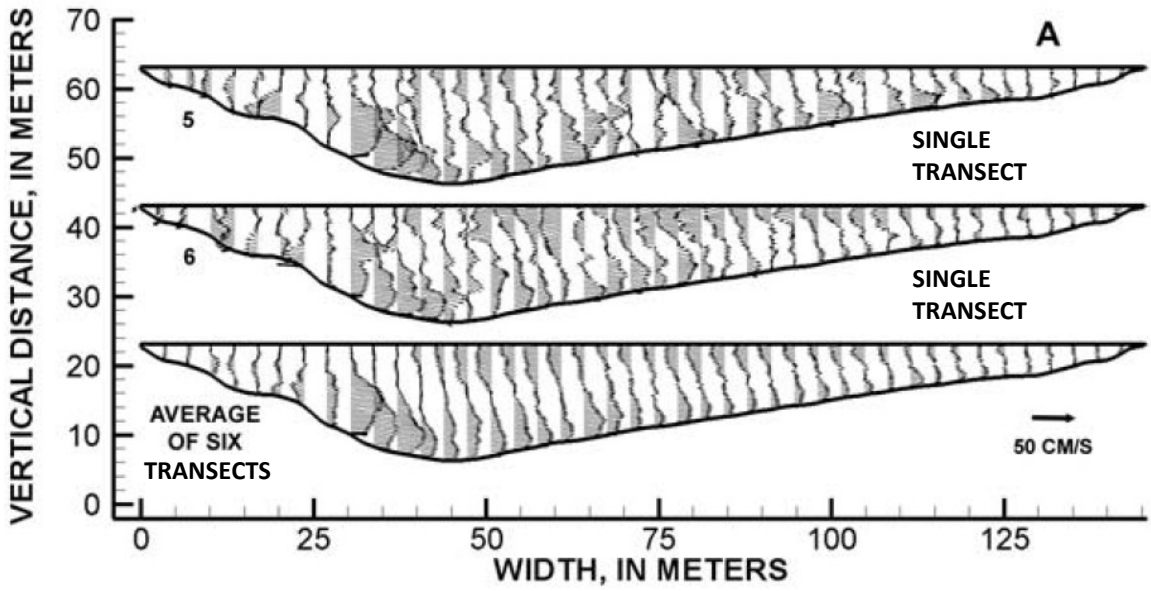

Figure 2.16 Lateral and vertical velocity distribution in a river bend (Dinehart and Burau, 2005).

Szupiany *et al.* (2007) used a Sontek aDP (acoustic Doppler Profiler) in order to measure the three-dimensional velocity in River Parana, Argentina, at several cross sections of 600-2400m widths and 5-12m depths. The aDP has the same working principles as ADCP, but different in name due to manufacturer preference. The velocity data on the aDP used by Szupiany *et al.* (2007) can be configured to output data every 5 to 30s. Two values of 5 and 10s which correspond to a length of 7.5 to 15m (a boat speed of $1.5ms^{-1}$) were chosen for the measurements. In order to average velocity data from a set of transects, Szupiany *et al.* (2007) employed a representative straight cross section for all transects data, and then averaged the velocity data on each transect to each 20m length of the representative section. Unfortunately, the averaging method adopted was not outlined in the report. It was stated that averaging ten transects will reduce the downstream-velocity fluctuation up to an average differences of $0.03 – 0.05ms^{-1}$, when compared to velocity profiles obtained from fixed-vessel measurements. Furthermore, the finer detail of the existence of secondary flow cells can be obtained by averaging five transects (Figure 2.17). While a general pattern of the secondary flow cells can be derived from the lateral velocity direction shown in Figure 2.17, it is difficult to see how the magnitudes of lateral velocity vary spatially. A clearer picture of this, plus a similar figure for the vertical velocity, might provide better prediction of secondary flow cells distribution, which could possibly be different to that described by Szupiany *et al.* (2007). Furthermore, it may be less appealing to use the aDP such as the one used by Szupiany *et al.* (2007) for investigating the spatial variation of velocity in small rivers, due to its 0.2Hz data output frequency.

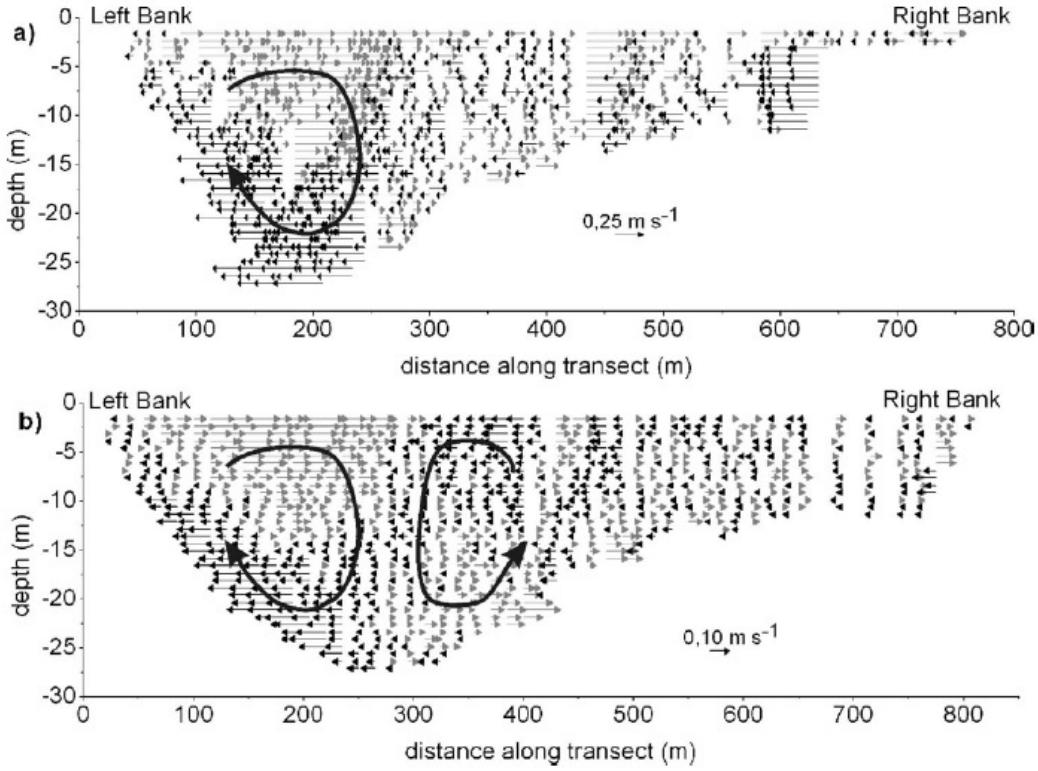

Figure 2.17 Lateral velocity distribution at a measured cross section: (a) obtained with one aDp transect; (b) averaged over five transects (Szupiany *et al.*, 2007).

Le Coz *et al.* (2007) used a similar approach to that of Dinehart and Burau (2005) in order to average ADCP transect data obtained from a 100m wide river at various discharge values. Instead of using six samples points for each interpolation points, Le Coz *et al.* (2007) used a variety of number of sampling points (*N*), i.e. 1, 2, 4, 8, 12, 16 and 32. The location from which the sampling points for each interpolation point can be taken is limited to a rectangular area of 0.8m height and 2m width within the corresponding interpolation point. The interpolation was not conducted if the number of available sampling points is less than *N*. For *N* = 1- 4, the velocity profiles over the depth appear to be similar the raw instantaneous ADCP profiles, and appear quite distorted. The averaged profiles for *N* = 16 – 32 have an agreement of typically within 5% against each other.

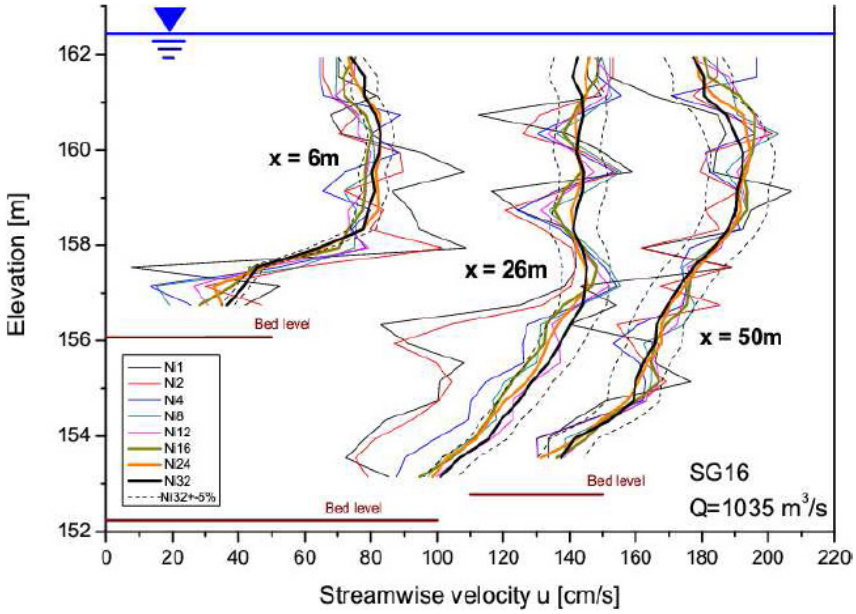

Figure 2.18 The result of interpolation using various number of sampling points at three different locations (Le Coz *et al.*, 2007).

There are similarities between the approaches used by Dinehart & Burau (2005), Szupiany *et al.* (2007), Le Coz *et al.* (2007) mentioned above, such as:

1. All methods were applied for wide rivers (≥100m width)
2. All methods require cross section straightening
3. Typical mean velocity of the sections is ≥ 0.95ms^{-1} (data not available for Le Coz *et al.*, 2007).
4. The difference in discharge values before and after averaging were generally not reported, except for Le Coz *et al.*, 2007, who reported that the differences were always within 3%.

Whether or not these approaches are applicable for a wider range of river size and flow conditions requires further investigation. An alternative approach is presented in chapter 4.

In conclusion, reliable data is crucial for flow studies in rivers and the development of numerical models for predicting stage-discharge relationship. However, there is typically never enough data for adequate calibration at suitable spatial or temporal scales (Knight, 2008). ADCP has a great potential for obtaining the whole velocity profiles in a cross section within a relatively short time. The accuracy and reliability of such data should be tested and improved.

3 EXPERIMENTAL SITE AND PREVIOUS RESEARCH ON THE RIVER BLACKWATER

3.1 Introduction

The River Blackwater is located approximately 20 kilometres southeast of Reading. The river rises from Rowhill Copse, south of Aldershot, and flows in a northerly direction to its confluence with the River Loddon at Swallowfield. Due to the construction of a major trunk road in 1993-1994, a 3 kilometre reach of the river near Farnborough was relocated. The relocation of the reach enabled the then National Rivers Authority (NRA) to undertake a programme of multidisciplinary-research into the design of an environmentally acceptable channel. This work involved examining the hydraulic performance of the new channel, the ecological colonization of the channel and floodplain, the geomorphology and stability of the channel, the effect on fish and the biological diversity of life in the relocated reach (Lambert, 1993). There often exists conflict where the most efficient hydraulic solution may not necessarily be the most environmentally acceptable solution. In order to ensure the richness of wildlife and the aesthetics of the landscape, the relocated reach was redesigned as a doubly meandering two-stage channel as opposed to a traditionally engineered straight channel.

A hydraulic performance study of 520m of the relocated reach (Figures 3.1 and 3.2) was undertaken using 1:5 and 1:25 scale models. The first model was built at the SERC-Flood Channel Facility at HR Wallingford while the latter was built at the University of Bristol. Stage-discharge relationships and flow structures in both models were studied in order to provide an insight into the hydraulic performance of the reach. Research on the full scale river was limited to only investigating the stage-discharge relationships and the seasonal variation of roughness coefficients over a number of years (Sellin and van Beesten, 2002; 2004). The current research has now added to this previous body of data by providing detailed velocity, slope and roughness data at various cross sections in the full scale river.

Figure 3.1 Plan view of the study site.

Figure 3.2 An upstream view from the foot bridge in June 2007(a) and March 2007(b).

3.2 Cross sections of particular interest

The current research adopted a naming convention of the cross sections as shown in Figure 3.3. In order to study the flow structure at different types of cross section, measurements of velocity and depth were undertaken in the full scale river at four cross sections, comprising two straight sections (1 & 2), a cross-over section (3) and a meandering section (4). However, due to difficult access as well as safety reasons, only a few sets of data were obtained from cross sections 1 and 3. Throughout this thesis, all cross sections will be viewed from upstream to downstream, i.e. the right floodplain will always refer to the right floodplain when looking downstream.

Measurements were made at cross section 1 for a number of reasons: (i) the rectangular cross sectional shape enabled data to be collected across a large proportion of the cross section, since the immeasurable zone near the walls of the channel was limited (see Section 4.1.4); (ii) the cross section was located under a bridge, which, due to the lack of natural light, limited the growth of vegetation and enabled easier data collection; (iii) the cross section was located at a short distance downstream from an electromagnetic gauging station operated by the Environment Agency (EA); and (iv) the width of the channel at this location was sufficiently large to ensure that the flow remained inbank

even when the flow downstream was overbank. This was an important requirement since in most cases the ADCP could not measure on the floodplains due to its minimum depth restriction (see Section 4.1.4).

Measurements on the 1:5 scale physical model were undertaken at cross sections 2b, 3 and 4 (Lambert, 1993; Lambert and Sellin, 1996; Naish and Sellin, 1996; Sellin *et al*., 2001). In this research, the stage data of the full scale river used for analysis were obtained from five pressure transducers installed at cross sections 1b, 1c, 2b, 4b and at a section 50m downstream of transducer 4b (Sellin and van Beesten, 2002; 2004). Unfortunately, these transducers were not in working order during the course of the current project. Hence, stage boards were installed at various locations throughout the reach (see Chapter 4) and monitored when required. Sellin and van Beesten used the electromagnetic gauge located 100m upstream of cross section (CS) 1 in order to provide discharge data. The same gauge was used in the current research to verify discharge measured by ADCP but on a number of occasions the data obtained from the electromagnetic gauge was found not to be reliable.

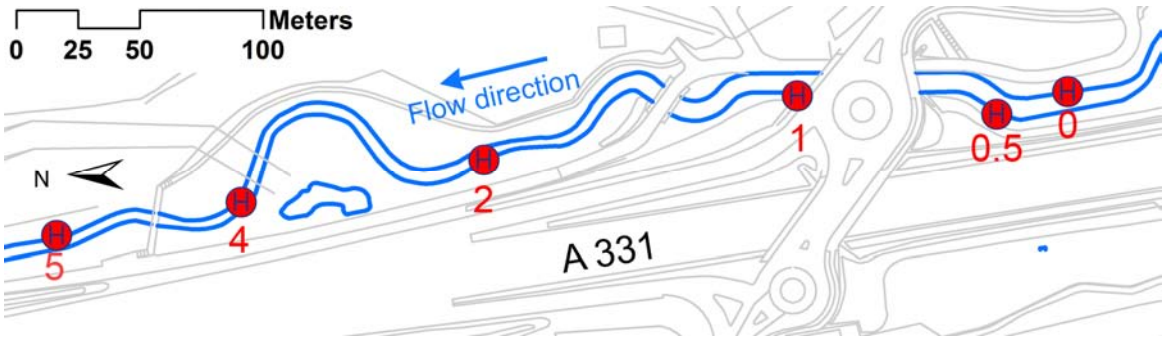

Figure 3.3 Naming convention of the cross sections with particular interest.

3.3 Channel characteristics and geometry

The first few kilometres of the River Blackwater are relatively steep with the river descending from an elevation of 125m AOD to 75m AOD by Weybourne Road (Clarke *et al*., 2007), approximately two kilometres downstream the source of the river (i.e. an approximate bed slope of 0.025). The total catchment area of the river is 356km^2 and consists mainly of Bracklesham Beds Sandstone, overlain by patches of Barton Sands. The catchment area at the research site is approximately 35km^2 and the hydrological response is considered as "flashy" since 40% of the upstream reach is dominated by an urban area. The relocated reach of the River Blackwater was designed for one-in-a-hundred year flood design capacity of 4.3m^{3}s^{-1} whilst the bankfull capacity of the main channel was 1.5m^{3}s^{-1}. The

reach was redesigned as a trapezoidal channel with a base width of 4.25m, top width of 5.75m and depth of 0.75m. The sinuosities of the meandering inner channel and the flood channel were 1.18 and 1.05 respectively. The valley gradient within the reach was 1/1020 while the gradient of the main channel thalweg varied from 1/1170 to 1/1020. Between 1998 and 2001, 46 flood events, at or above bankfull for over 24 hours, were recorded. The average and maximum durations of these were 25 hours and 155 hours, suggesting a high probability of a suitable flood event during the current project (EPSRC, EP/E002250/1).

A survey was conducted in March 2007 to obtain bathymetry and ground elevations in order to check any changes from the original survey and also to be used in the building of a numerical model of the river geometry (see Chapter 5). In total, 9236 levels were measured at 0.5 to 1m intervals. Figures 3.4 - 3.6 illustrate the profiles of cross sections 2, 3 and 4, obtained from the 2007 survey. Changes of river geometry were observed: the current floodplains slope away from the main channel, i.e. opposite to that of the original design. The most important change of geometry appears to have been caused by deposition of sediment on the floodplain, typically in the region adjacent to the main channel. This was confirmed by comparing the changes of profiles at cross sections 1b, 1c, 2b and 4b, surveyed in three different years: 1995, 1997 and 2007 (Figures 3.7 – 3.10). The locations of the 2007 profiles were approximately the same locations as the 1995 and 1997 data reported by Sellin and van Beesten (2004). Although there might be slight shift in locations of the profiles being compared between the two dates Figures 3. 7 – 3.10 clearly show that the floodplain elevations close to the main channel have risen, in some cases by 200mm. This may help to explain why less flood events occurred during the course of the current project than previously anticipated. Recent records show that only six events, at or above bankfull capacity for over 24 hours, were recorded during 34 months between 2006 and 2008. The number of these events is significantly lower than what was observed between 1998 and 2001. The average and maximum durations of these were 35.3 hours and 38.25 hours respectively.

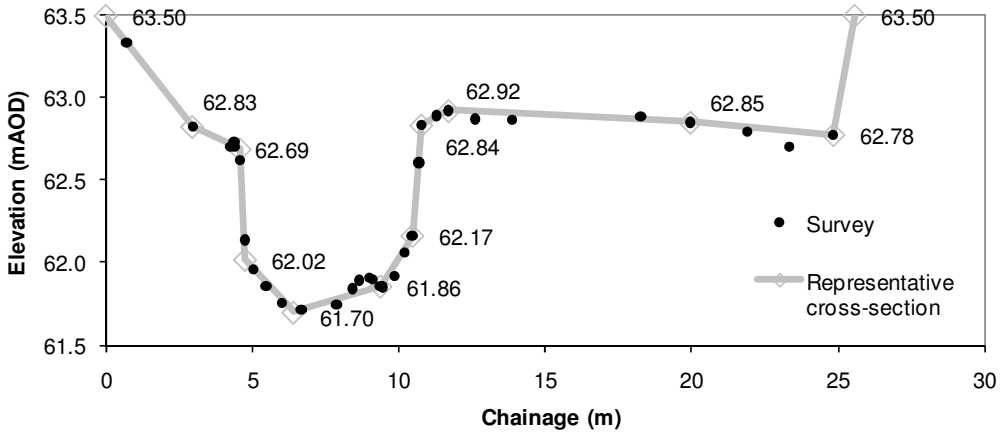

Figure 3.4 Profile of CS 2 (2007).

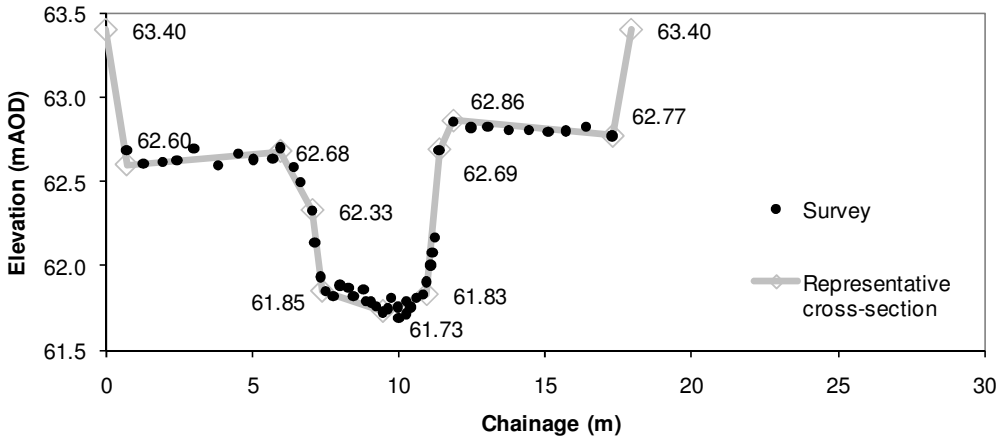

Figure 3.5 Profile of CS 3 (2007).

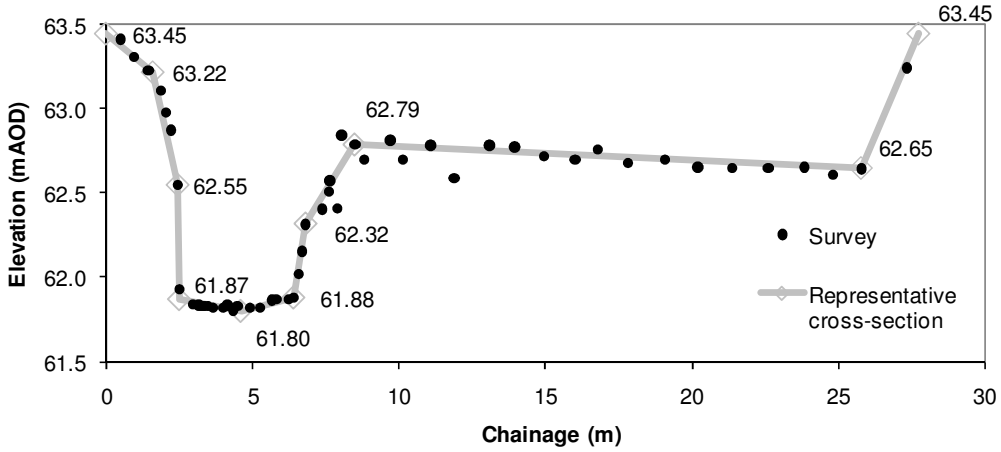

Figure 3.6 Profile of CS 4 (2007).

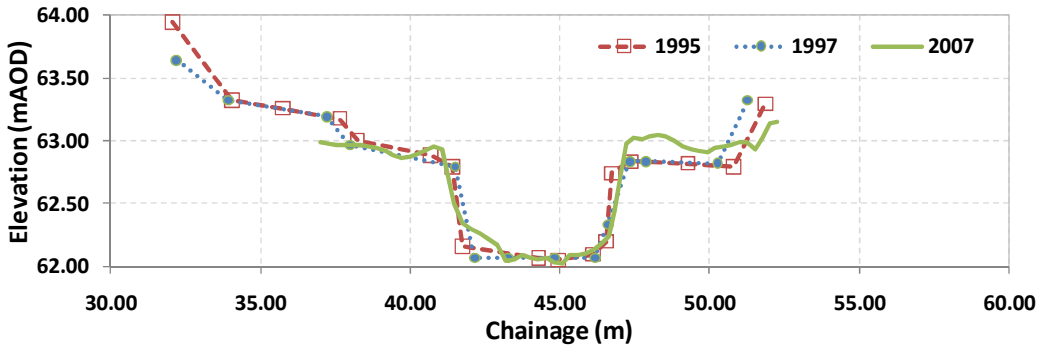

Figure 3.7 Changes of profile at CS 1b.

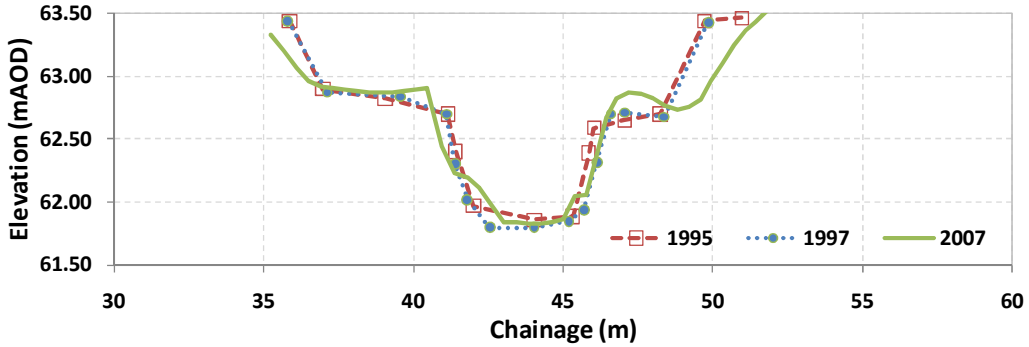

Figure 3.8 Changes of profile at CS 1c.

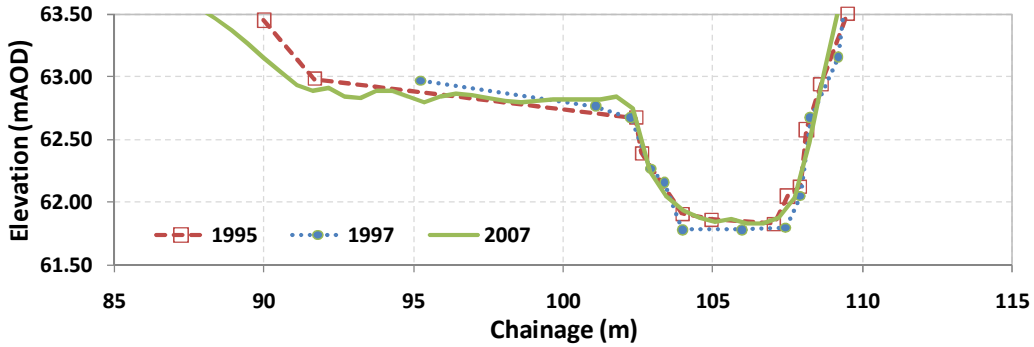

Figure 3.9 Changes of profile at CS 2b.

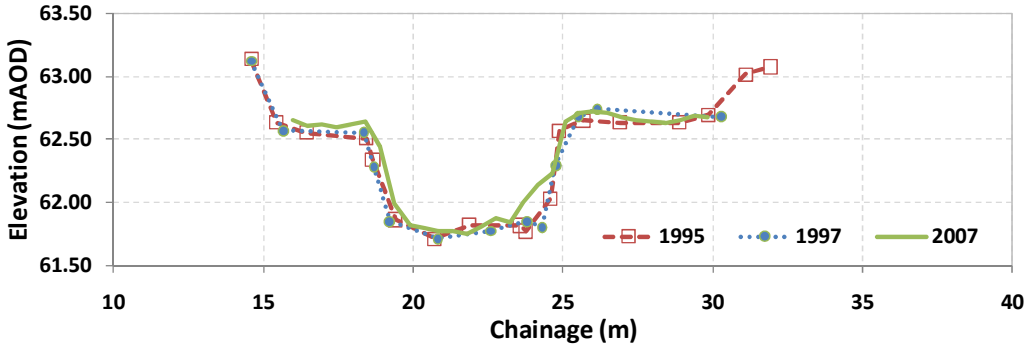

Figure 3.10 Changes of profile at CS 4b.

The variation of hydraulic parameters with water level at cross sections 2, 3 and 4 are presented in Figures 3.11 - 3.13. Cross sectional area (*A*), wetted perimeter (*P*) and hydraulic radius (*R*) of the corresponding sections were computed for every 50mm level increment, and also including the levels of the points used to generate the representative cross sections (Figures 3.4 – 3.6) for representing the changes of those parameters more precisely. The water levels during an overbank and an inbank event, on 10/2/2009 and 16/1/2008 respectively, are also plotted in the Figures. Since the floodplain slopes away from the main channel, some regions on the floodplain were often inundated when the interfaces between floodplain and main channel were still relatively dry. However, the water in the floodplain during such condition was stagnant.

At CS 2, the right floodplain was still dry or filled with stagnant water from downstream the cross section (Figure 3.14) when water level at CS 2 was in between 62.78m AOD and 62.92m AOD (see Figure 3.4). The same condition applies to CS 4 when the water level was in between 62.65m AOD and 62.79m AOD (see Figures 3.15 and 3.6). It is also interesting to see that the right floodplain at cross sections 2 and 4 in Figures 3.14 and 3.15 was still dry although the discharges during those measurements, at 2.13m^3s^{-1} and 1.81m^3s^{-1}, exceeded both the bankfull design capacity (1.5m^3s^{-1}) and the range of bankfull discharge measured in the river reported by Sellin, *et al*. (2001) (0.37m^3s^{-1} to 1.35m^3s^{-1}).

As the floodplain at CS 2 was still dry or filled with stagnant water at H = 62.92m AOD, the parameter *P* is calculated without including the floodplain region for H < 62.92m AOD. This approach is also adopted for the calculation of *P* for CS 4. As a result of using this approach, sharp arithmetic discontinuities on the parameters *P* and *R* near or at bankfull condition occurred. This discontinuity appears only once for cross sections 2 and 4 since only one floodplain side is sloping away from the main channel in both cross sections. However, the discontinuity appears twice at CS 3 since both floodplain sides in the corresponding cross section are sloping away from the main channel. Such discontinuity was also reported by Knight *et al.* (1989; 2008) and Knight (2005) on a study of River Severn at Montford Bridge. They reported that the decrease of hydraulic radius just above bankfull level (Figure 3.16) resulted in a sharp decrease in the Manning's *n* parameter. This is in contrast to what one would intuitively think, since Manning's *n* would be expected to increase due to the bankside vegetation.

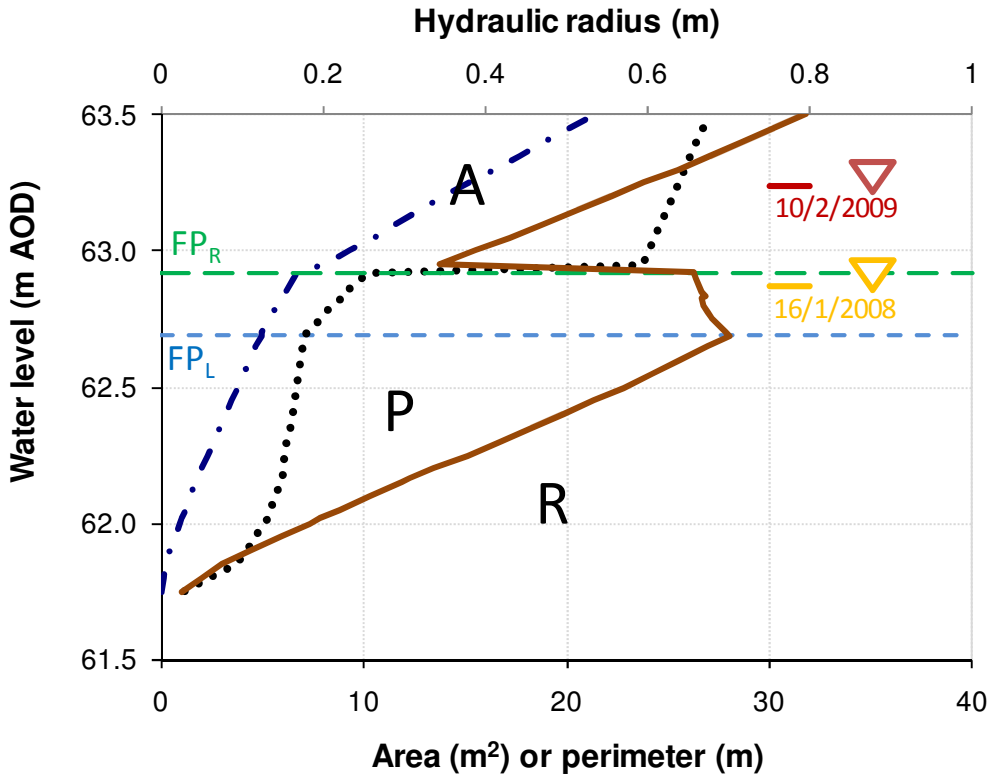

Figure 3.11 Relationship of *A, P, R* and water level at CS 2.

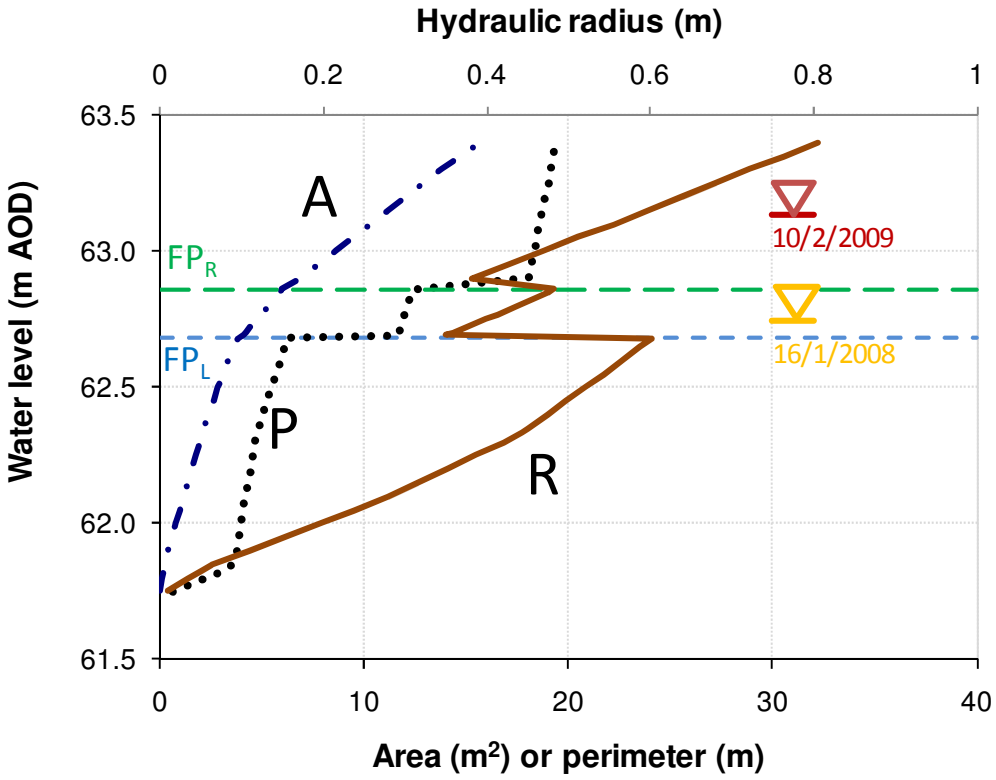

Figure 3.12 Relationship of *A, P, R* and water level at CS 3.

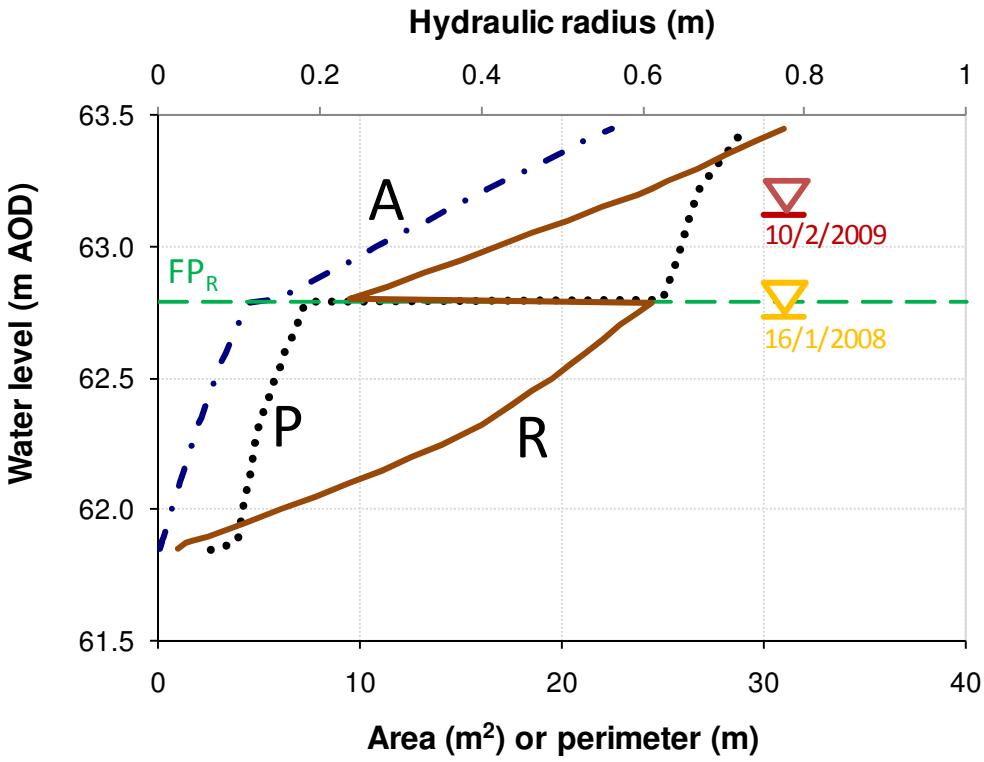

Figure 3.13 Relationship of *A, P, R* and water level at CS 4.

Figure 3.14 Flood-plain condition at CS 2 at bankfull condition with Q = 2.13m^{3}s^{-1} (16 January 2008).

Figure 3.15 Flood-plain condition at CS 4 at bankfull condition with Q = 1.81m^{3}s^{-1} (16 January 2008).

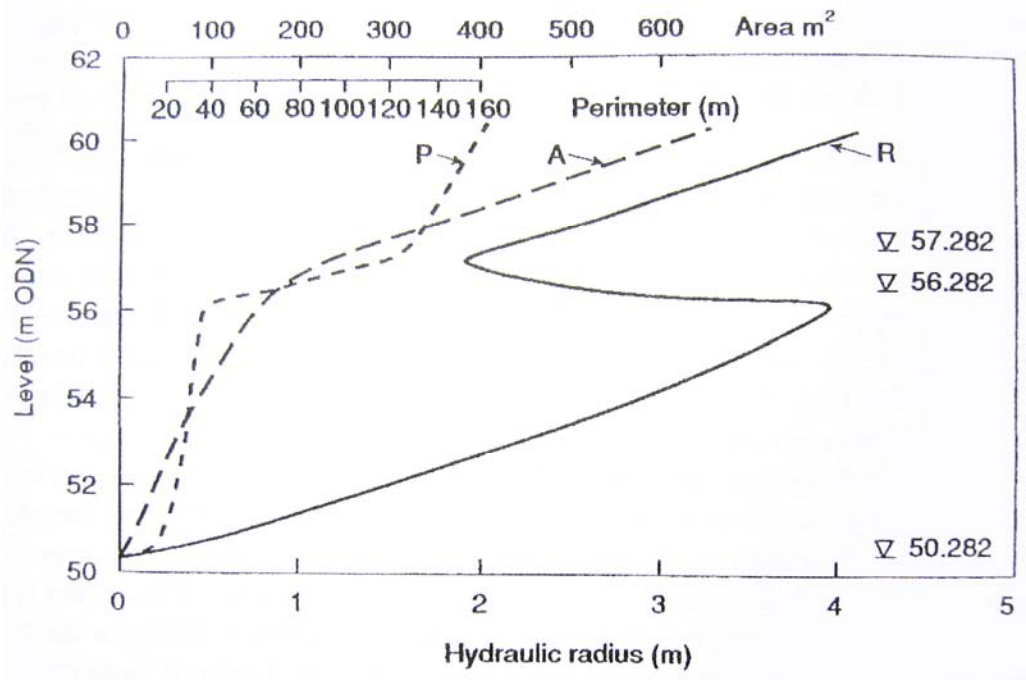

Figure 3.16 Variation of hydraulic parameters with level, River Severn at Montford Bridge (after Knight *et al*., 1989).

Figure 3.17 shows the comparison between the survey data obtained in 2007 and that in 2002. The comparison was made only on the floodplain since the bathymetry data was not available for the 2002 survey. The 2002 survey covered a larger region than the 2007 survey but has a lower measurement density (Figure 3.17a). In total, 1932 and 9236 levels were collected in 2002 and 2007 respectively. Figure 3.17b shows the comparison of the main channel edge from the 2007 survey and the measurement boundary near the main channel from the 2002 survey. It is not certain whether the boundary of the 2002 precisely reflected the edge of the main channel. However, the edge of the main channel edge appears to have moved slightly between 2002 & 2007, particularly at CS 3 (the crossover).

The difference in floodplain elevations obtained from the 2007 and 2002 surveys was assessed by initially constructing a raster-type Digital Terrain Model (DTM) from the survey data using ArcGIS 9.2. The elevation information for each cell in the DTM was interpolated from the survey data using a simple Inverse Distance Weighting method. Figure 3.17c was obtained by subtracting the 2007 DTM from the 2002 DTM. The Figure shows that the floodplain elevations stayed relatively constant between 2002 and 2007. It shows that the elevation changes in more than 90% of the area being compared are less than 0.1m. High changes in the boundary of the comparison area can be neglected as they are caused by the unavailability of the 2002 bathymetry data and 2007 data near the edge of the comparison area.

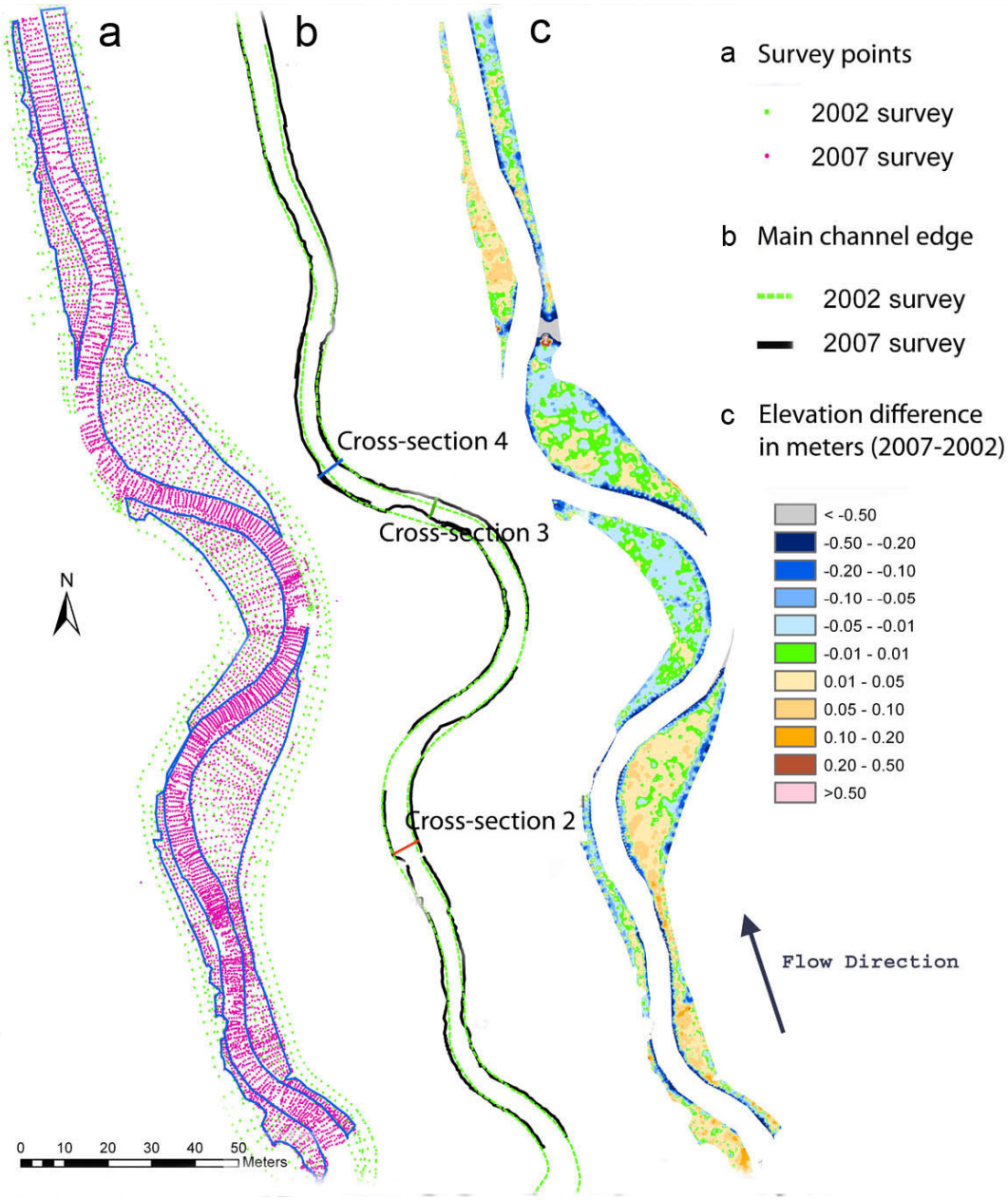

Figure 3.17 Comparison of 2007 and 2002 surveys: (a) measurement locations, (b) main channel edge and (c) floodplain elevations difference.

The elevation contour of the study reach from 2007 survey is presented in four separate sections in Figure 3.18. The contours were computed from a Triangular Irregular Network (TIN), delineated from the survey data. The left and right outer boundaries of the contour are virtually the right and left floodplain banks that will not be overtopped during most overbank flow. Water levels during recent flood events that exceeded the hundred-year flood design capacity were between 63.1 and 63.2m AOD, which is typically still 0.5m below the top of the floodplain banks.

It can be seen that sediment deposition occurred typically on the inner meanders and crossovers (green regions adjacent to the main channel banks). In such locations, the maximum velocity is generally shifted towards the opposite bank where sediment transport occurred and caused scour/erosion. The resulting bed scour caused deeper regions to occur next to areas of the deposition, e.g. Figures 3.18b and c.

Figure 3.18 illustrates that the majority of the floodplains today tend to slope away from the main channel (Figures 3.18a, b, c and d). This highlights the existence of complex flow structures responsible for sediment transport. Furthermore, overbank flow also plays an important role in the sedimentation-erosion characteristics previously being mentioned, especially at the crossover section. In the CS 3, both banks of the main channel have moved towards the downstream of the valley (Figure 3.17b). During overbank flow, high boundary shear stresses appear in the outer bank due to the complex interaction between the flow in the flood plain and main channel. Such phenomenon was previously mentioned by other researchers, e.g. Ervine *et al.* (1993; 2000) and Morvan *et al.* (2002). Overall, the sedimentation and erosion tends to increase the sinuosity of the meanders.

Figure 3.18 shows that the maximum depositions generally occur on the upstream side of the meander tongue. This suggests that velocities are weakened after water was expulsed from the main channel to the floodplain. This behaviour is an opposite of what was observed by Bathurst *et al.*, (2002) (who undertook measurements in a laboratory flume), where the maximum deposition occurred on the downstream side of the meander tongue.

Figure 3.19 illustrates contours of slope for the research site. The regions with high slope correspond to the river and floodplain banks (blue colours). Some narrowing in the main channel can be clearly seen, e.g. upstream CS 2 and downstream CS 3. Furthermore, the Figure also shows that in areas where sediment has been deposited, the slopes vary, indicating that deposition does not occur at a uniform rate along the channel, e.g. the sedimentation on the right bank just upstream CS 2 in Figure 3.19a, is separated from the main channel and floodplain high slopes. Other regions have a more gradual slope that results in the height of the deposited area being the same level as the surrounding floodplain, e.g. Figure 3.19b near bottom at the right bank indicated by yellow/red region.

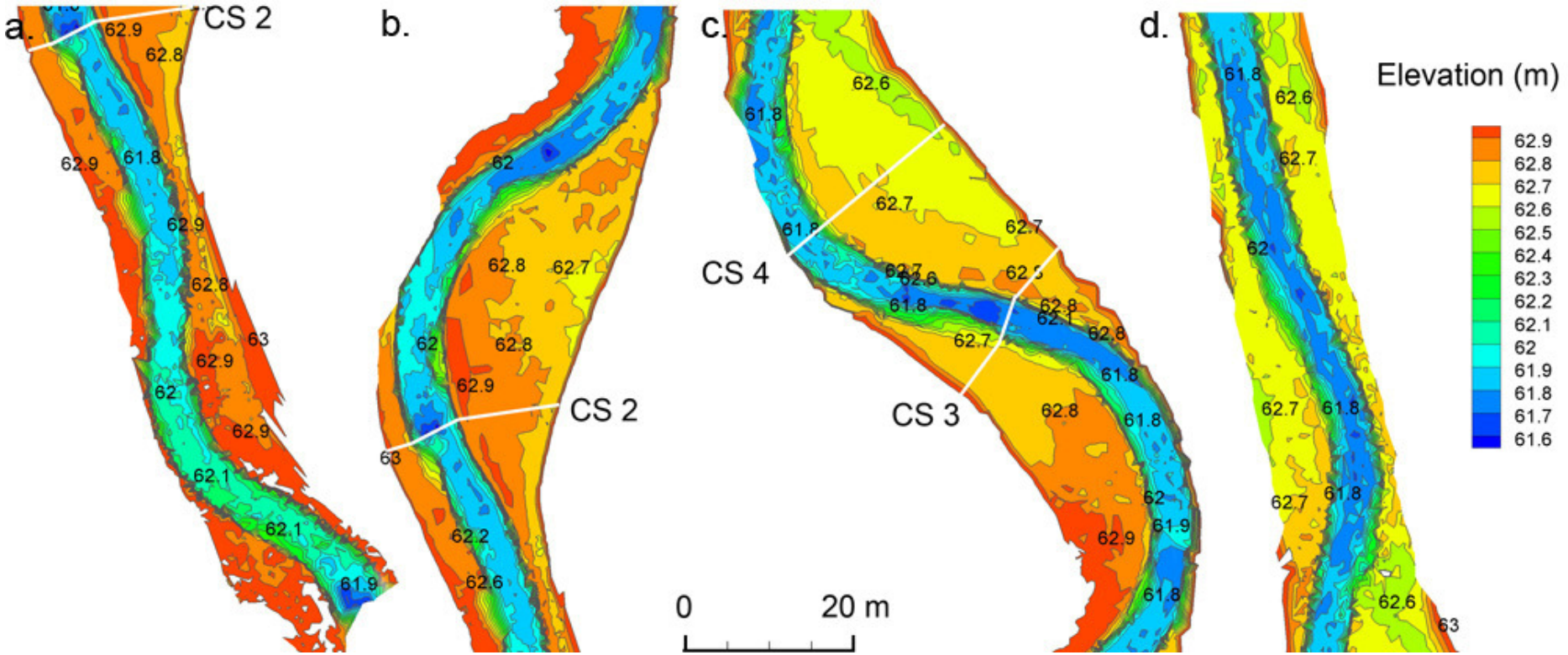

Figure 3.18 Floodplain and main channel elevation contours for the research site (2007 data).

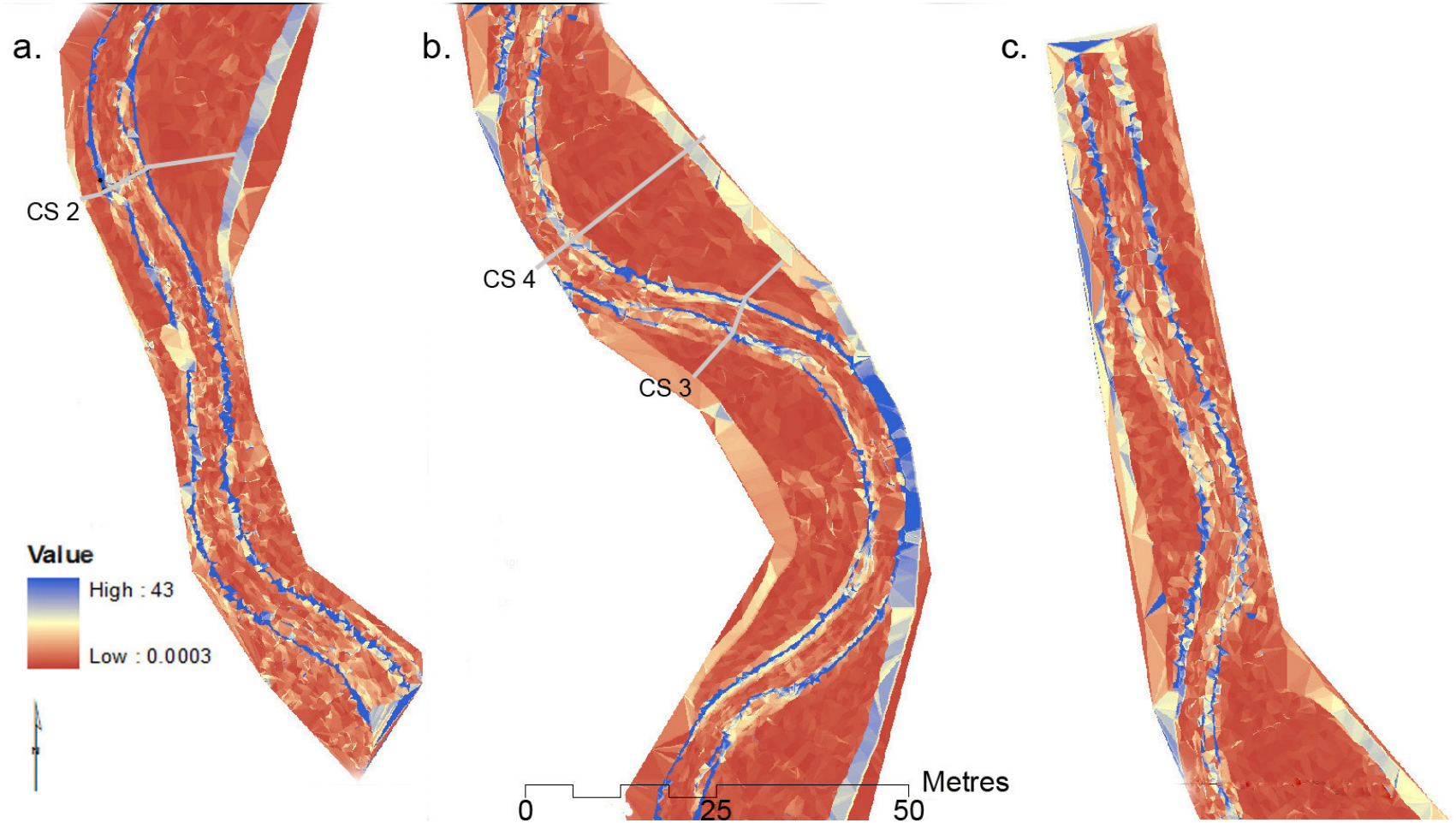

Figure 3.19 Slope contours for the research site (2007 data).

3.4 Previous research on the River Blackwater

This section discusses in detail the previous research that has been carried out on the River Blackwater. In particular, the work of Lambert (1993), Lambert and Sellin (1996), Naish and Sellin (1996), Sellin *et al.* (2001) and Sellin and van Beesten (2002; 2004) are examined.

3.4.1 Full-scale experiments

Previous analysis of the stage-discharge relationships, roughness coefficients and the effect of seasonal variations on the study reach are each examined in the following subsections.

3.4.1.1 Instrumentation and methodology

As stated previously, an Environment Agency Sarasota electromagnetic gauging station, installed 100m upstream of CS 1, has been used to monitor the discharge in the river Blackwater. The accuracy in 2002 was found to be ±15% at low flows and ±1.5% at high flows (Sellin and van Beesten, 2004). Pressure transducers installed in the locations outlined in section 1b, 1c, 2b, 4b and at a section 50m downstream of transducer 4b (Sellin and van Beesten, 2002; 2004) were used to record the water level along the reach. The accuracy of these transducers was estimated to be of the order of ±3mm. Sellin and van Beesten (2004) used only readings from the pressure transducers located at stations 2, 3 and 4 to compute the depth of flow, since those located at stations 1 and 5 were either in close proximity to a sharp bend or influenced by a five-arch culvert under a railway embankment further downstream, respectively. The water level readings were converted to a height above UK Ordnance Datum for analysis. Data from the electromagnetic gauging station and pressure transducers were recorded by an on-site data logger every 15 minutes. Figure 3.20 shows the variations of water surface profiles measured by the pressure transducers at various times between 1999 and 2003. An analysis of these data indicates that the water surface slope ranges from 3×10^{-4} to 10^{-3} between stations 2 and 4.

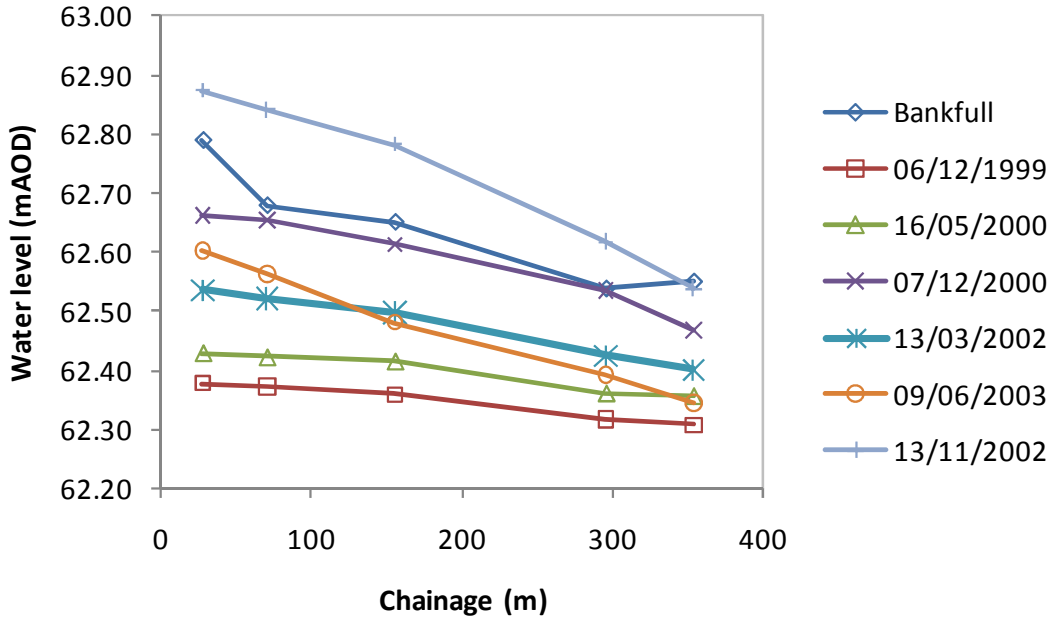

Figure 3.20 Water surface profiles at five pressure transducers at various times (after Sellin and van Beesten, 2004).

Sellin and van Beesten (2004) used a representative CS (Figure 3.21) to simplify the river geometry and to aid their analysis. The average floodplain width of the representative CS was calculated from the total floodplain area within the reach divided by the flood channel length. This value was then arbitrarily divided equally between the two banks. A floodplain slope of $^{1}/_{30}$ towards the main channel was adopted as an approximation to the actual conditions.

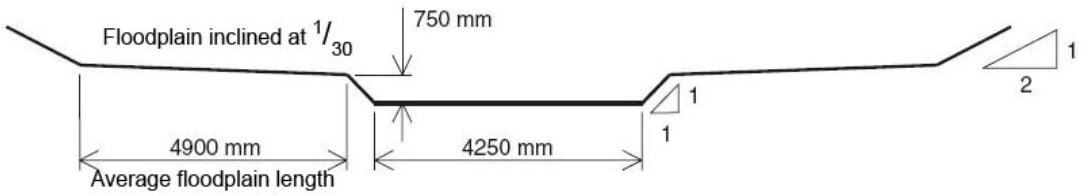

Figure 3.21 Representative CS used by Sellin and van Beesten (2004) for flow data analysis.

The data obtained from the electromagnetic gauging station and pressure transducers were interrogated before being used in the analysis. This enabled data corresponding to specific unsteady events (e.g. the passage of a flood wave) to be removed in order to ensure that values of *n* corresponded to steady flow conditions. Hence, Sellin *et al.* (2001) used only discharge data that had a difference of $0.05 m^3 s^{-1}$ between three consecutive readings (45 minutes) and computed the

mean depth of flow through the study reach by averaging the readings at the pressure transducers located within the reach (Sellin *et al,.* 2001).

3.4.1.2 Main findings

Previous research suggested that no unique stage-discharge relationship existed for the study reach for all seasons (Figure 3.22). Figure 3.22 shows that at a depth of 0.6m the discharge varies from 0.1 - 0.7m^3s^{-1}, while at a depth of 0.85m the discharge varies from 0.55 to 1.9m^3s^{-1}. This high variation in discharge is related to the changes which occur to the vegetation, both within the main river channel and on the floodplains, throughout the year. Figure 3.22 shows that higher stage-discharge relationships were measured during summer months, when the vegetation in the main channel was significant, while lower stage-discharge relationships were measured during winter months. If the summer and winter data are treated separately, then the variations in discharge decrease to the order of 0.25m^3s^{-1} and 0.5m^3s^{-1} in both summer and winter data for depths of 0.6m and 0.85m respectively. Figure 3.23 shows the variation of Manning's *n* with depth corresponding to the data shown in Figure 3.22. It can be observed that the summer data generally implies higher values of *n,* and the rate of increase of *n* with respect to depth is more significant than the winter data. Furthermore, the behaviour of *n* for depths greater than approximately 0.85m is particularly interesting. Sellin *et al.* (2001) stated that the aquatic and floodplain vegetation growth resulted in larger values of the roughness coefficient. Compared with bankfull conditions the lumped *n* values for the channel decrease initially when the flow goes overbank due to the single-channel method used in the data analysis (Sellin and van Beesten, 2004).

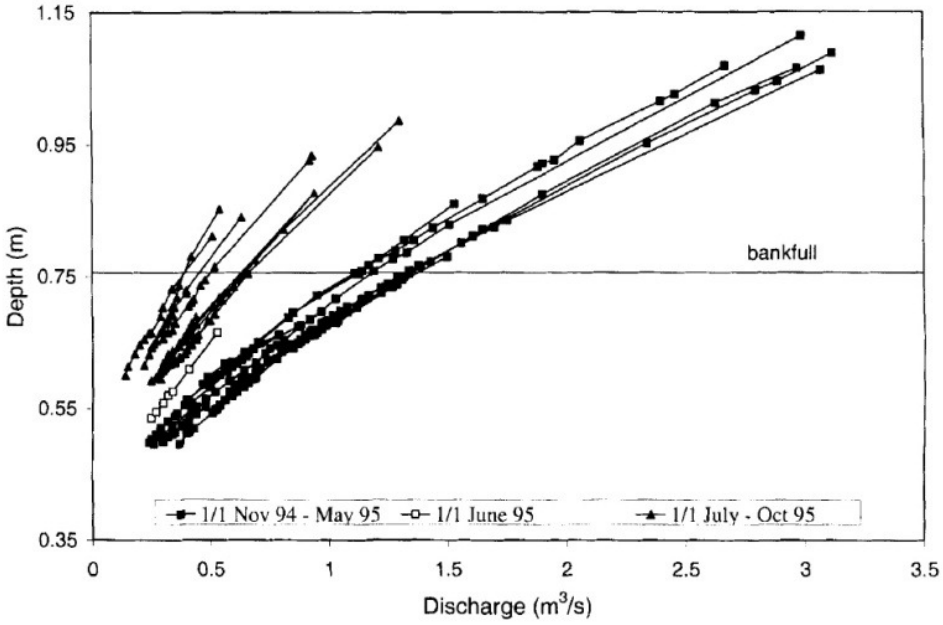

Figure 3.22 Stage-discharge relationship for prototype study reach 1994-1995 (Sellin *et al.,* 2001).

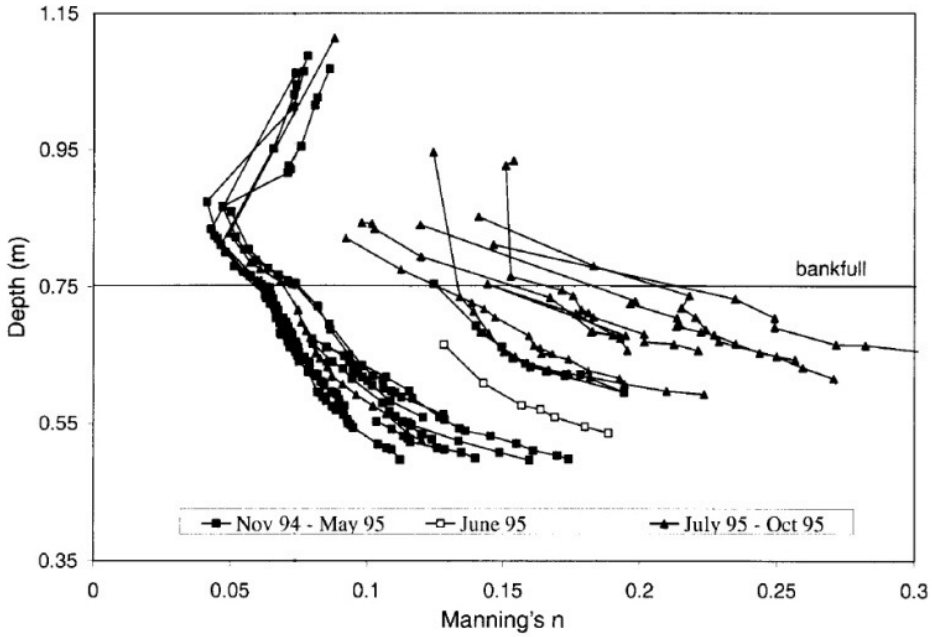

Figure 3.23 Variation of Manning's roughness coefficient for prototype study reach 1994-1995 (Sellin *et al.*, 2001).

Sellin and van Beesten (2004) reported that the stage-discharge relationship often had the form of a hysteresis-type curve, with greater discharge capacity on the recession limb than the rising limb, as illustrated in Figure 3.24. This was attributed to a reduction in channel resistance, caused by flattening of the live vegetation and removal of dead material and detritus. The corresponding increase in conveyance capacity was clearly seen during one event with two successive hydrograph peaks, as shown in Figure 3.25. The stage-discharge relationship of the corresponding event

illustrated in Figure 3.26 shows a complicated relationship, with a tendency that conveyance capacity of the river increases on the second peak. The relationship of water depth and Manning's *n* also appears to be complex, but in general *n* values decreased on the second peak (Figure 3.27).

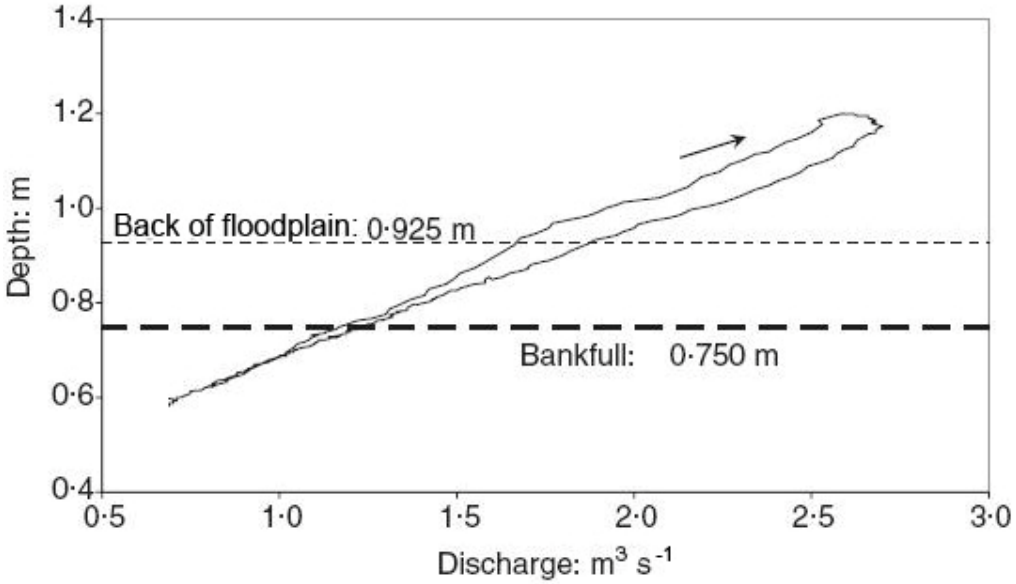

Figure 3.24 Stage-discharge relationship for storm of 16-19 January 1999 (after Sellin and van Beesten, 2004).

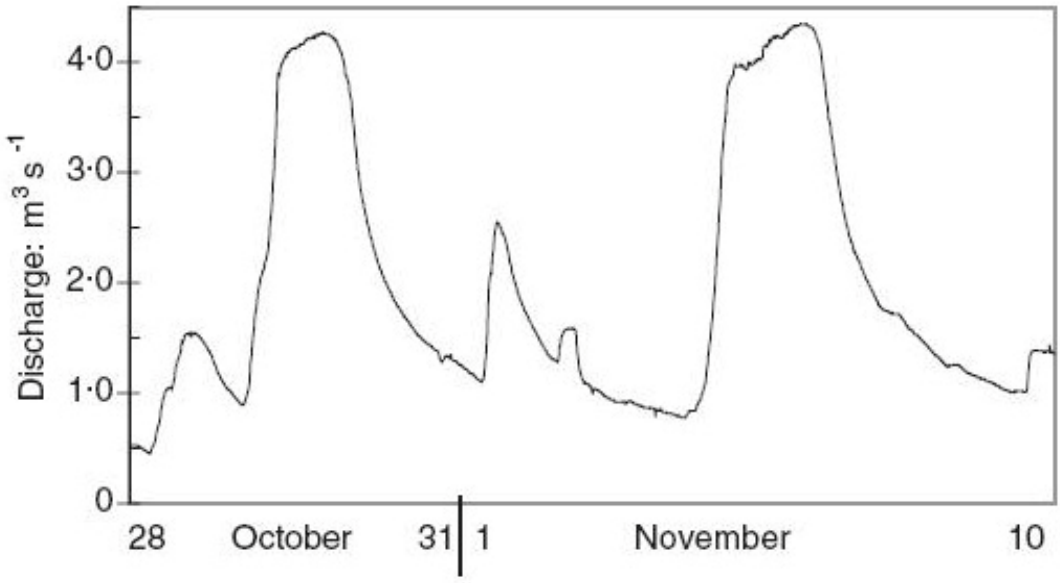

Figure 3.25 Discharge hydrograph with two successive storm peaks (after Sellin and van Beesten, 2004).

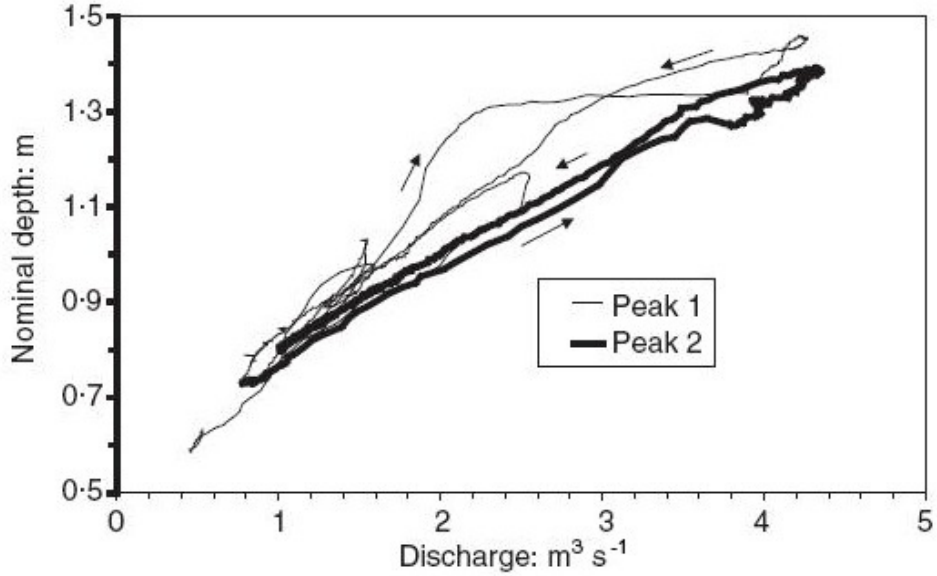

Figure 3.26 Stage-discharge relationship of the event in Figure 3.25 (Sellin and van Beesten, 2004).

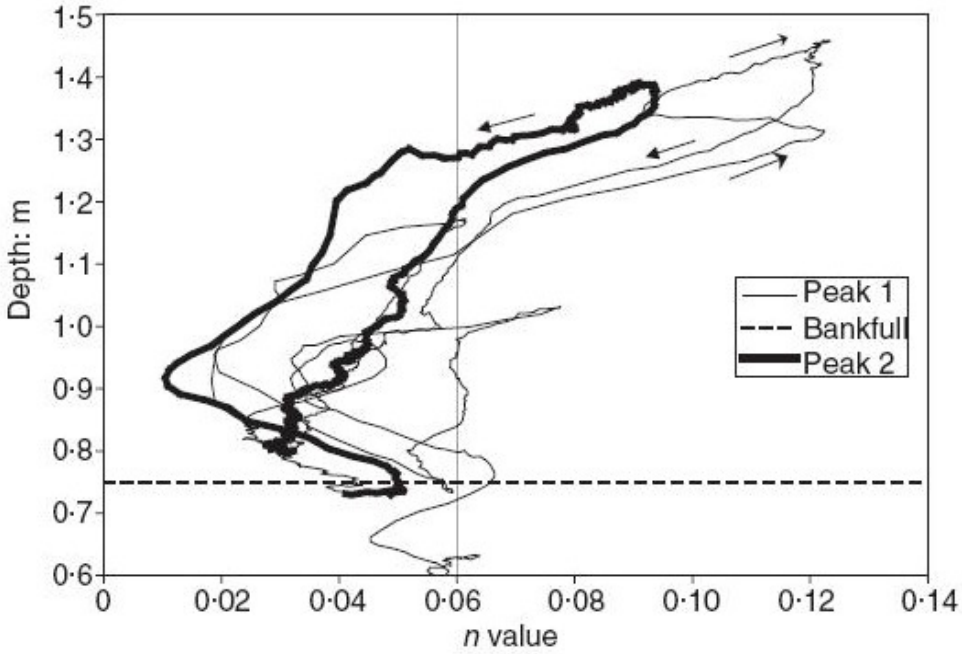

Figure 3.27 Depth-Manning's *n* relationship Figure 3.25 (Sellin and van Beesten, 2004).

Furthermore, Sellin and van Beesten (2004) reported that the effect of rising and falling river level is difficult to quantify, although Figure 3.28 shows that the discharge during the summer months of June to September tends to be greater for a falling river level. Manning's *n* during the summer period from May to September ranges from 0.05 – 0.25 at bankfull flows, while the values of the same parameter during winter months are generally 3 – 5 times lower than the summer months.

The increase of the resistance coefficient is attributed to the existence of emergent vegetation in the main channel during summer months that has a significant effect on blocking the flow. As consequence of this behaviour, the conveyance capacity of the river increases rapidly in the months of October-November, e.g. bankfull conveyance increases from $0.6m^3s^{-1}$ in the summer, when the reed beds are fully developed, to $1.4m^3s^{-1}$ in the winter. Figure 3.29 shows the variations of *n* values during the months of September-November, in which *n* values decrease rapidly from 0.15 in September, to 0.09 in October, and finally to 0.06 in November. Regular management of the vegetation (i.e. cutting) in the river does not affect the values shown in Figure 3.29 (1999), since the cutting in that year was delayed to January 2000. Additionally, *n* values increase strongly at high overbank flow for most years but remain constant during the winter period after the floodplain vegetation has been cut and cleared (Figure 3.30).

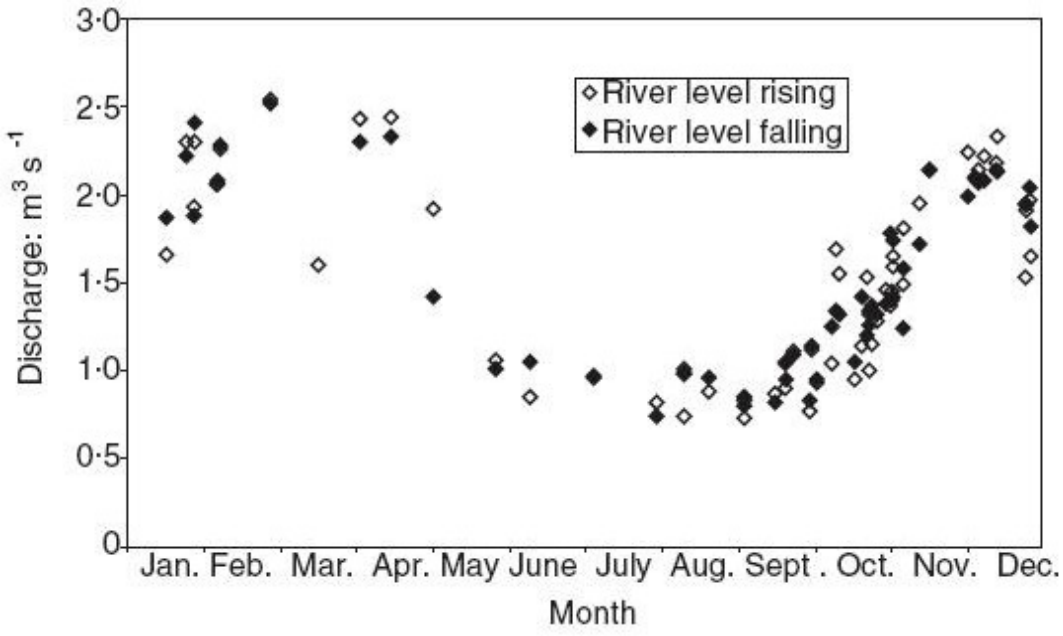

Figure 3.28 Inner channel conveyance at bankfull during falling river level (Sellin and van Beesten, 2004).

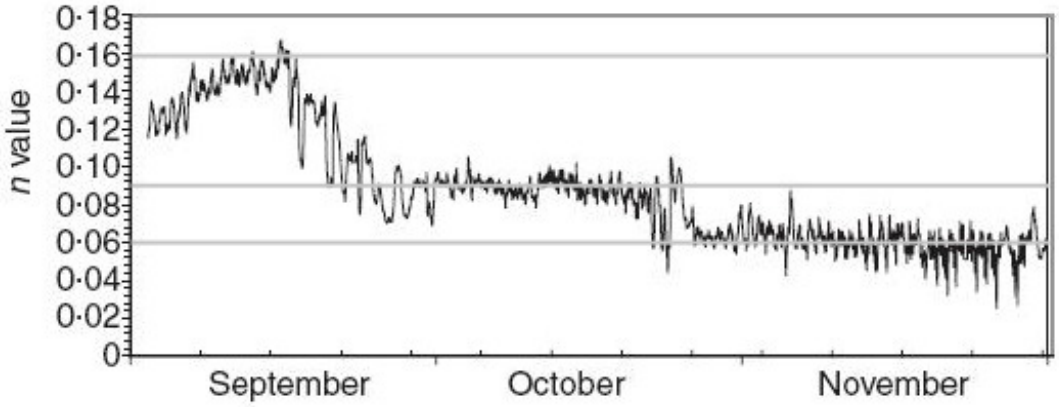

Figure 3.29 Inner channel conveyance at bankfull during falling river level (Sellin and van Beesten, 2004).

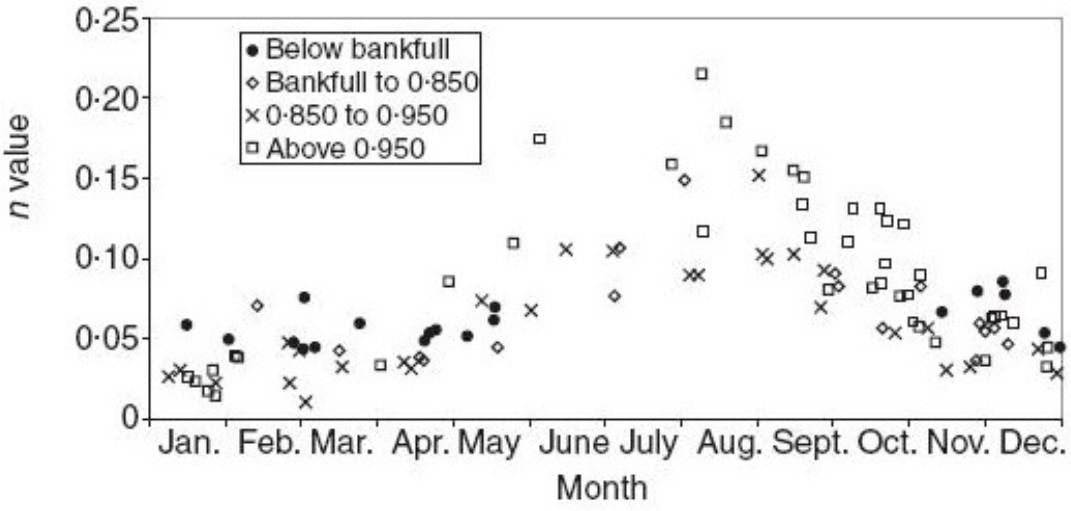

Figure 3.30 Variations of *n* values over the years at various water depth (after Sellin and van Beesten 2004).

3.4.2 Small-scale physical model

This section discusses the previous research undertaken to assess the hydraulic performance of the River Blackwater using the 1:5 scale model built in the UK Flood Channel Facility. The results from a smaller scale study on the River Blackwater (1:25 scale model) are also discussed.

3.4.2.1 Experimental setup

The 1:5 scale model of the river Blackwater model was constructed in the 10m wide and 56m long UK Flood Channel Facility at HR Wallingford, using mortar as the surface material (Lambert and Sellin, 1996). Three pumps with a maximum discharge of $0.25m^3s^{-1}$ supplied water to the flume. Water

levels were controlled by a set of downstream tailgates and measured at eight different locations along the model by digital pointer gauges set in externally mounted stilling wells. Velocity measurements were taken at cross sections 2b, 3 and 4 (Figures 3.31 – 3.33). Flow direction and magnitude along the specified cross sections were measured using a balanced vane mounted on a rotary potentiometer and a miniature propeller current meter. The propeller was rotated at each measuring point into the flow direction as recorded by the vane. Lambert and Sellin (1996) reported that the model and prototype main channel and flood channel sinuosities were 1.18 and 1.06 respectively. The flood channel sinuosity is slightly different from the value of 1.05 reported in Naish and Sellin (1996) and Sellin *et al.* (2001). The model main channel was trapezoidal throughout, with a constant bankfull depth of 0.15m and a side slope of 1.0. Various configurations of the model were established by varying the roughness condition on the floodplain from a smooth condition to a rough one using 8mm and 13mm gravels. The main channel was roughened with 8mm gravel on its bed and left smooth on its sidewalls. The floodplain slope was varied from horizontal and $^{1}/_{30}$ inclination towards the main channel. The presence of the gravel caused slight changes in cross sectional geometry but this was taken into account by an extensive survey of the gravel surface.

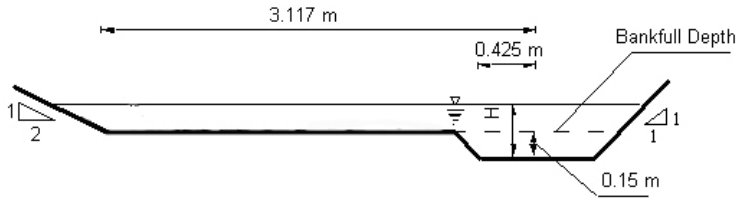

Figure 3.31 Geometry of CS 2B (Lambert and Sellin, 1996).

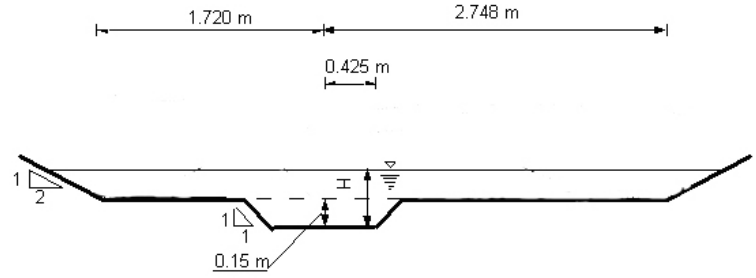

Figure 3.32 Geometry of CS 3 (Lambert and Sellin, 1996).

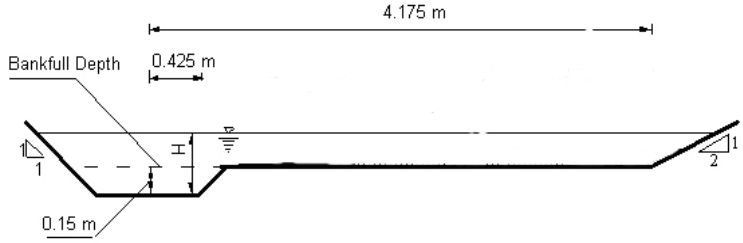

Figure 3.33 Geometry of CS 4 (Lambert and Sellin, 1996).

A small 1:25 scale model was constructed at the University of Bristol, and three different roughness applied to the main channel and floodplain surfaces using 0.4mm sand (D_{50}), 1.4mm sand (D_{50}) and 10mm gravel (D_{50}). Water levels were controlled by a downstream tailgate and were measured at the same eight positions as in the 1:5 model, using the same methodology. In later stages in the investigation, the model was modified to a 2:1 vertical-scale exaggeration to bring the scaled discharge values closer to those in the 1:5 scale model.

3.4.2.2 Main findings

Based on the investigation using the 1:5 model, Lambert and Sellin (1996) concluded that the three-dimensional flow structure and velocity distribution in the model was complex. It was observed that the magnitude of the averaged velocity in the main channel decreased with rising water level (Figures 3.34-3.37). This is contrary to the assumption implicit in the Divided Channel Method (DCM) (c.f. Section 2.4.2). Using such a traditional method in this condition will result in an undersized channel. In Figures 3.34 – 3.37, the floodplain conditions 1 and 2 refer to horizontal and $^{1}/_{30}$ floodplain slopes respectively. In both cases 13mm gravel (D_{50}) was used on the floodplain.

The introduction of a floodplain crossfall slope tends to reduce the flow interaction between the main channel and the floodplain which, in return, reduces the rate at which the depth-averaged velocity decreases with rising water depth in the main channel. Figure 3.38 shows that the stage-discharge relationships computed using the Single and Divided Channel Methods (SCM & DCM) (c.f. Section 2.4.2) are inadequate in representing the experimental results, although the SCM values agree to a certain degree with the experimental results at high overbank flow.

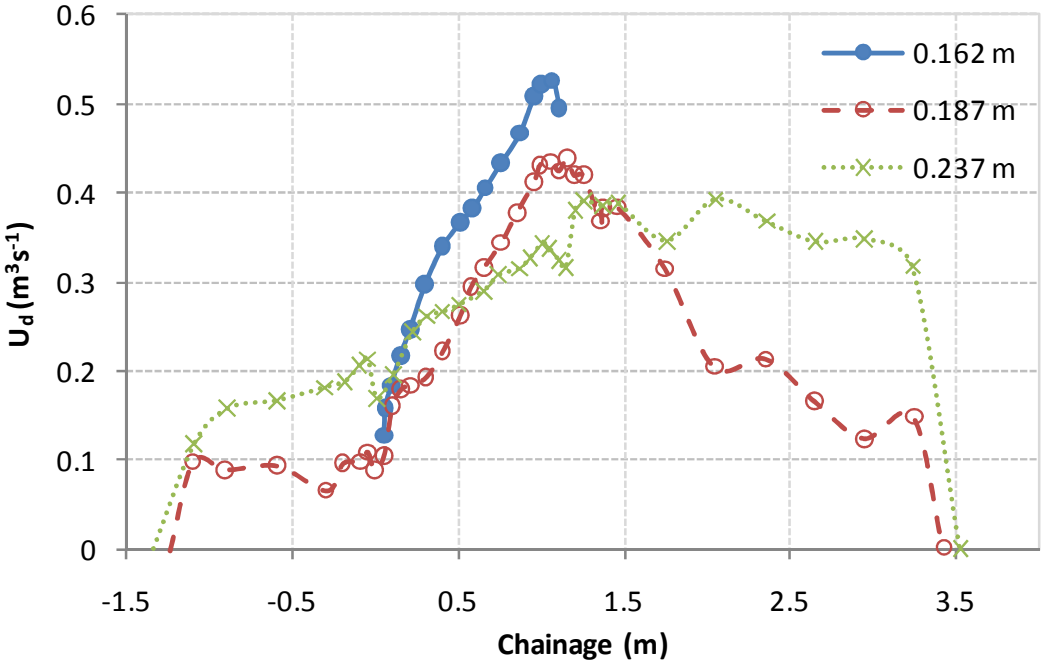

Figure 3.34 Variation of depth-averaged velocity across the channel at CS 3 for floodplain condition 1 (adapted from Lambert and Sellin, 1996).

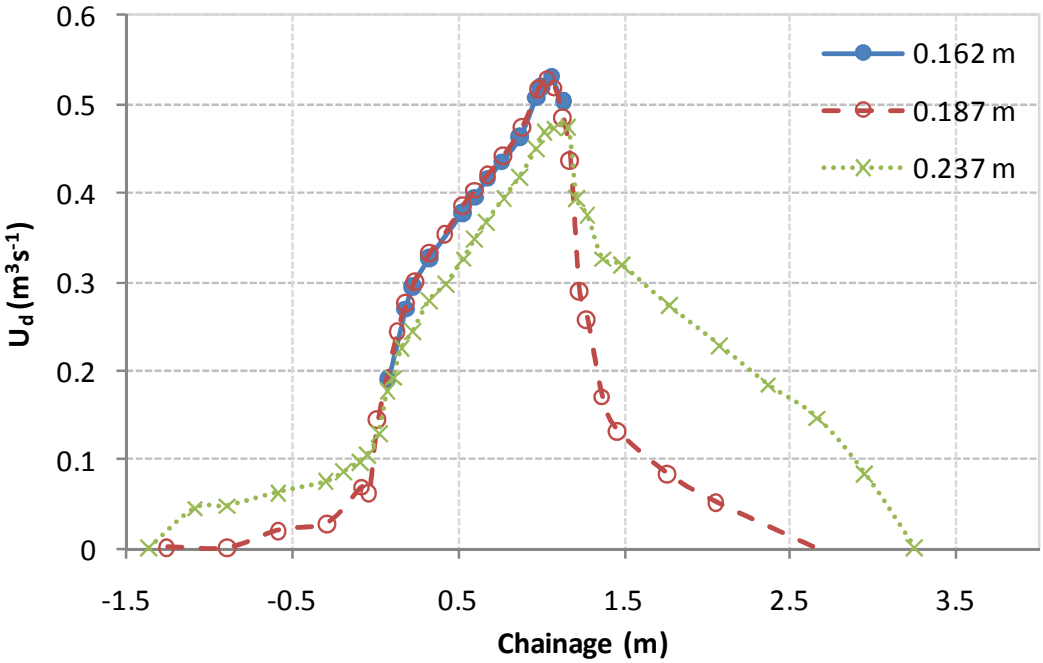

Figure 3.35 Variation of depth-averaged velocity across the channel at CS 3 for floodplain condition 2 (adapted from Lambert and Sellin, 1996).

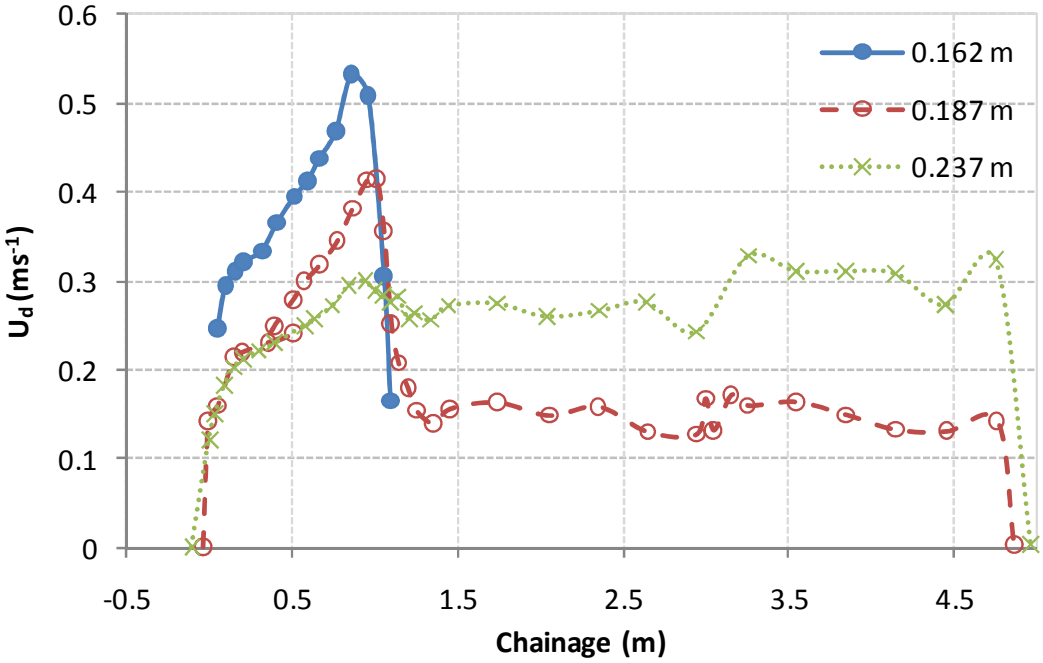

Figure 3.36 Variation of depth-averaged velocity across the channel at CS 4 for floodplain condition 1 (adapted from Lambert and Sellin, 1996).

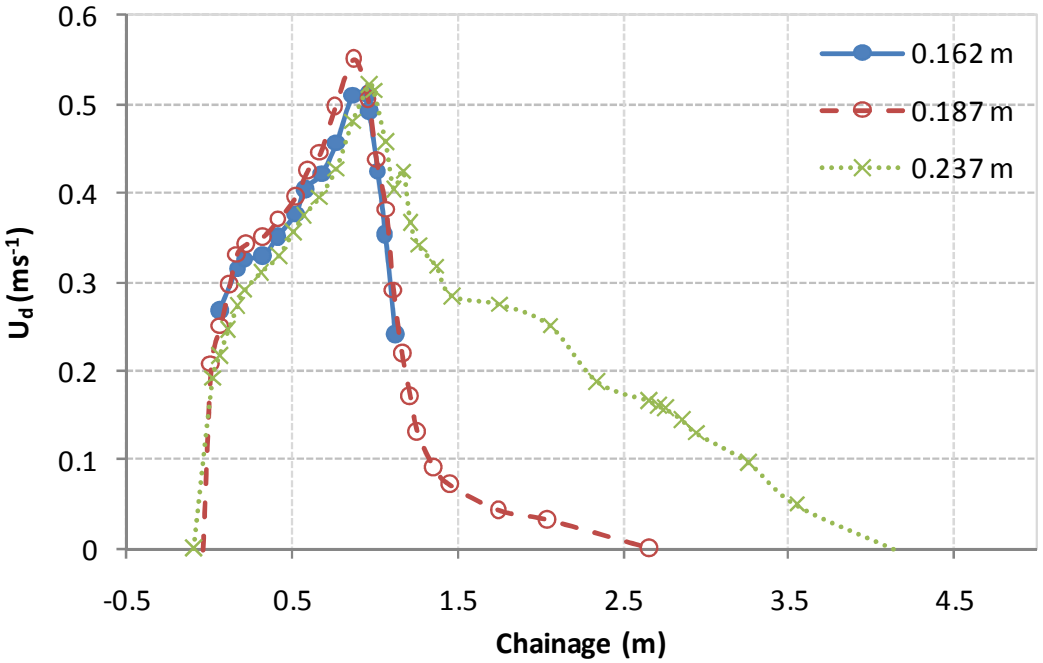

Figure 3.37 Variation of depth-averaged velocity across the channel at CS 4 for floodplain condition 2 (adapted from Lambert and Sellin, 1996).

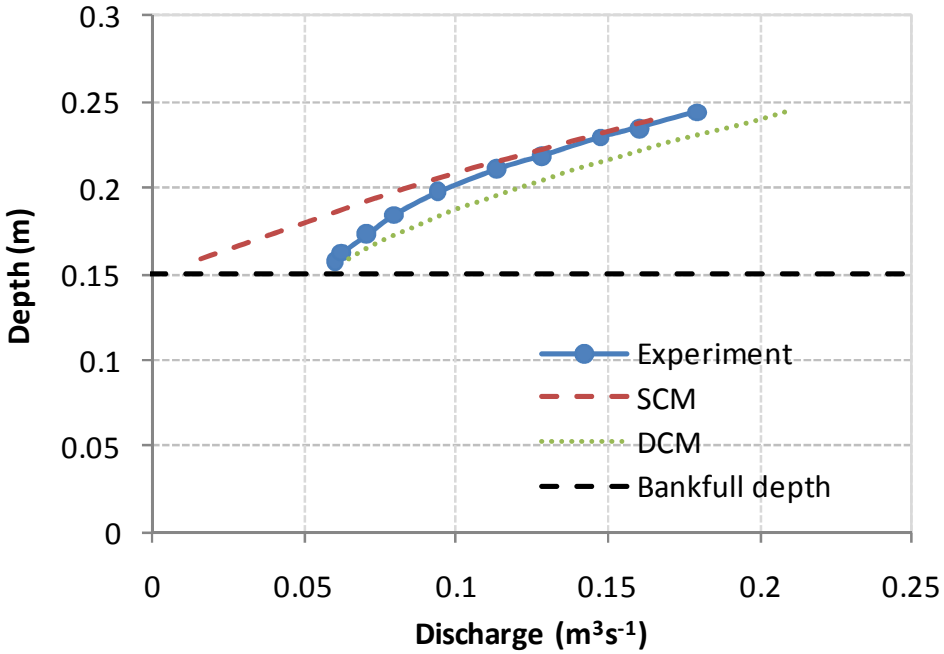

Figure 3.38 Comparison of depth-discharge relationship for floodplain condition 2 between the experimental results and computations using SCM and DCM (adapted from Lambert and Sellin, 1996).

Figures 3.39 and 3.40 show the contours (isovels) of streamwise velocity and the profiles of transverse velocity at cross sections 2b and 3 for floodplain condition 1, corresponding to inbank and overbank flows respectively. For all cross sections being examined, the magnitude of the depth-averaged streamwise velocity increased with flow depth for inbank flow conditions but then decreased when the flow went overbank (Lambert, 1993).

For CS 2b, it was observed that the maximum velocity moved from the outer meander to the inner meander (right to left when facing downstream) for all floodplain roughness conditions. The velocity distribution for inbank flow at CS 3 was similar to that observed in CS 2b, in the sense that the maximum velocity was located on the right. However, this was not the case for overbank flow (Figure 3.40), where the maximum velocity in CS 2b moved to the left while that of CS 3 moved to the right floodplain. The velocity distribution in CS 3 for the overbank flow condition appears to be greatly affected by the strong lateral flow coming from the upstream floodplain (left floodplain). This tends to force the higher-velocity region in the main channel to the downstream floodplain, producing high velocities on the right hand side of the main channel and large boundary shear stresses on the right main channel bank. For the horizontal floodplain condition (Figure 3.40), the magnitude of the maximum velocity decreases up to 25% from CS 3 and 4 at overbank condition.

This indicates that the most energy contained in the higher velocity flow had rapidly dissipated due to the momentum interaction in the vicinity of CS 3 (cross-over). The rotational direction of the main channel secondary flow cells was found to be unaffected by overbank flow. However, an additional secondary cell circulation was detected at CS 4 for the overbank flow condition, due to plunging of the flow from the floodplain into the main channel.

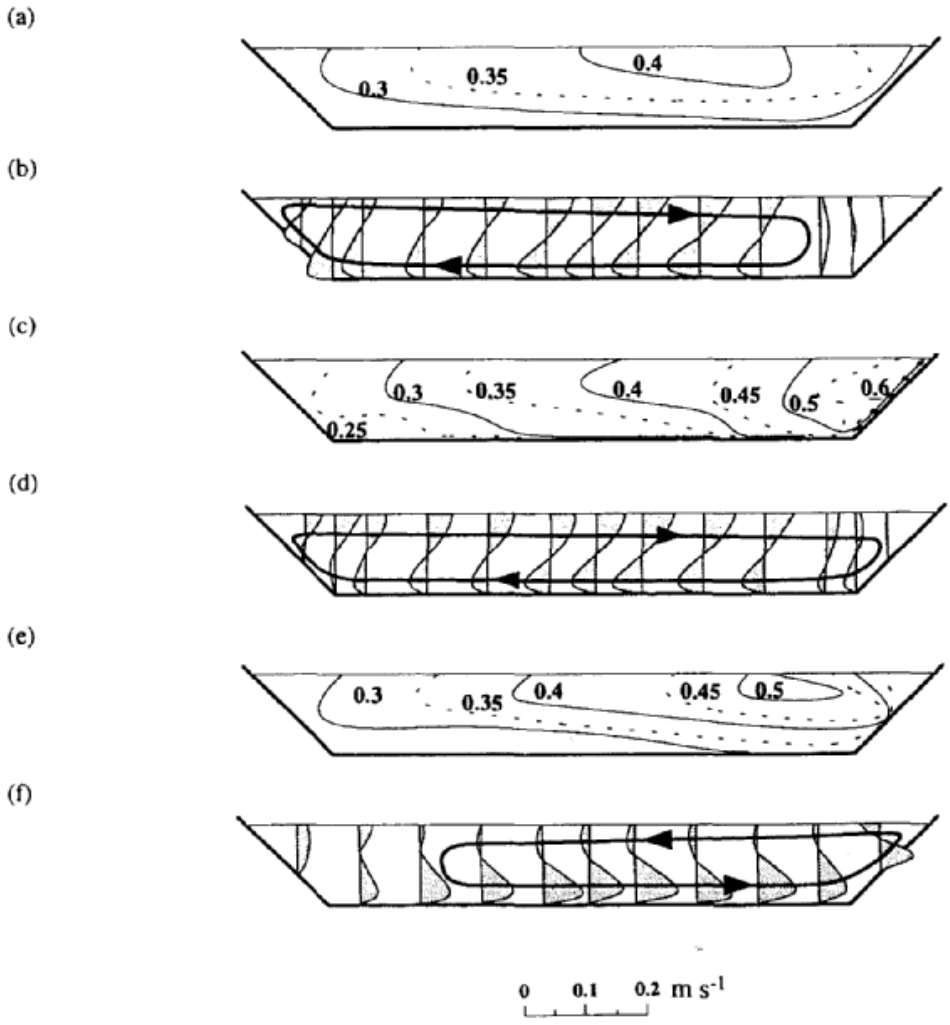

Figure 3.39 Contours of streamwise velocities and transverse velocity profiles for sections 2b (a,b), 3 (c,d) and 4 (e,f) at inbank condition (H = 0.132m) for floodplain condition 1 (Naish and Sellin, 1996).

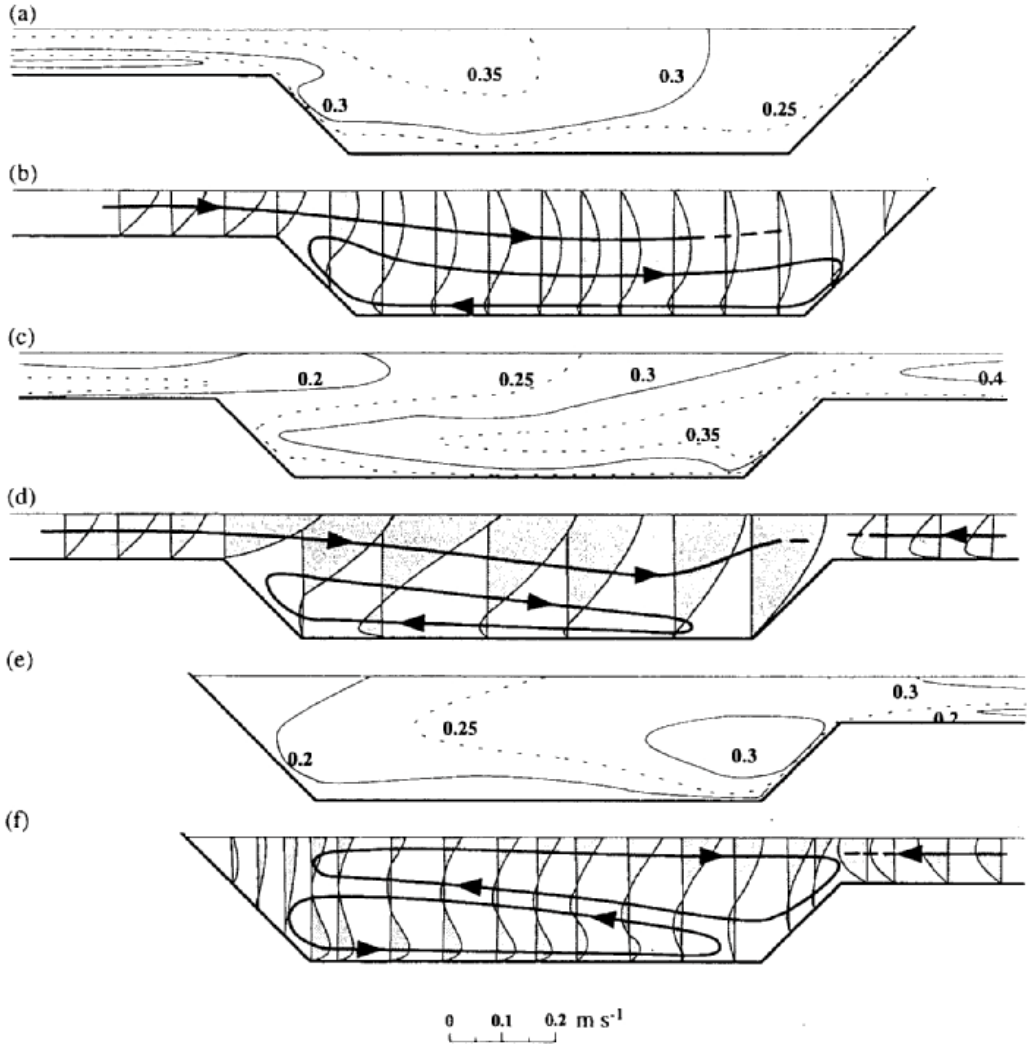

Figure 3.40 Contour of streamwise velocities and transverse velocity profiles for sections 2b (a,b), 3 (c,d) and 4 (e,f) at overbank condition (H = 0.237m) for floodplain condition 1 (Naish and Sellin, 1996).

Dye injection was used to investigate the flow structure in both the 1:5 and 1:25 scale models. This revealed some localised floodplain flow travelling upstream, or trapped in stationary vortices, possibly triggered by flow separation at the floodplain bend (Naish and Sellin, 1996). The introduction of a lateral crossfall for the floodplain appeared to increase the size and strength of these vortices.

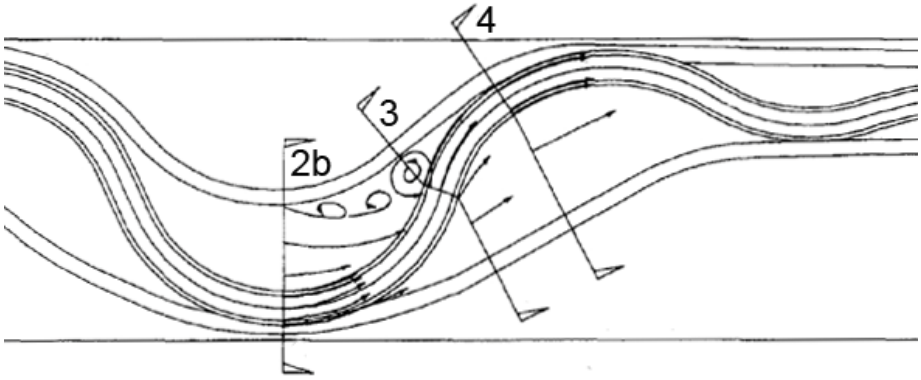

Figure 3.41 Flow patterns detected on the 1:5 model with horizontal floodplain slope and water depth of 0.2m (Naish and Sellin, 1996).

A comparison of the full-scale river and the physical models was undertaken to determine any scale effects which might be present in the models. Difficulties regarding the scaling of the bed roughness were a particular issue. It was discovered that the relationship for surface roughening elements in different scale models was not linear (Figure 3.42). The comparison revealed that the full-scale river roughness was higher during most of the year than that used in the models based on undistorted scales and Froudian scaling. This resulted in larger discharges in the models when all data was suitably scaled. For example, it can be shown that the 1:5 model conveyed an equivalent of 300% of the full-scale river discharge at the same flow depth. It was later found that a two-time vertical exaggeration was required for the 1:25 model so that the stage-discharge curve of the 1:25 model coincided with that of the full-scale river.

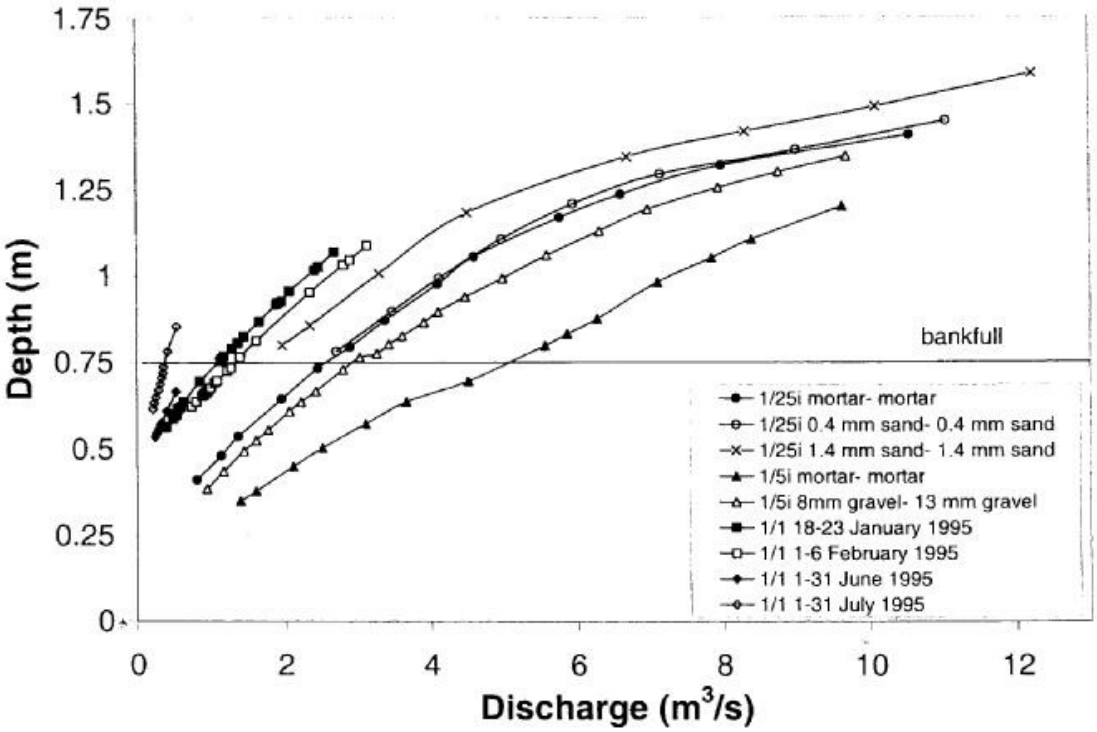

Figure 3.42 Selected stage-discharge data or river and models: model data for inclined floodplain only (Sellin *et al.,* 2001)

3.5 Closing remarks

The aim of this chapter has been to analyse changes of topography on the reach being studied and highlight the main findings of the previous work undertaken on the small-scale physical model and the prototype of the river Blackwater. Comparison of topography surveys conducted in the study reach at various times (2007, 2002, 1995 and 1993) shows that the river geometry has changed since 1993 (Figures 3.7 – 3.10, 3.17). The floodplain of the current time tends to slope away from the main channel (Figures 3.4 – 3.6, 3.18), as opposed to the original design with $^{1}/_{30}$ floodplain cross-fall. This was caused by the sedimentation deposition near the main channel, which in some cases has raised the floodplain elevation by 200mm. As a direct result from these changes, the bankfull discharge in the river has increased significantly. Sellin *et al.* (2001) reported that the bankfull discharge in of the study reach varies from $0.37m^3s^{-1}$ and to $1.35m^3s^{-1}$. However, recent discharge measurement (2008) shows that overbank flow condition had not been reached at a discharge of $2.13m^3s^{-1}$ (Figure 3.14). This could explain why less flood events occurred during the course of the current project than previously anticipated. Only six events, at or above bankfull design capacity, for over than 24 hours, were recorded between 2006 and 2008 while 46 of the same events were recorded during 1998 and 2001.

The sharp discontinuity on the wetted perimeter and hydraulic radius values around the bankfull level (Figures 3.11 - 3.13) decreases the value of Manning's *n*.

Analysis of the roughness coefficient values performed at the full-scale river shows that aquatic, emergent and floodplain vegetations have a dominant role on the conveyance capacity in the river over the year. Lower conveyance capacity was observed for summer months due to the larger extent of vegetation in the reach during those periods (Figures 3.22 and 3.28). This phenomena was also reflected on the values of Manning's *n* roughness coefficients, which were observed to be up to ten times higher value of Manning's *n* was observed in the summer months as opposed to in the winter months (Figures 3.29 and 3.30). Due to the Single Channel Method used for the analysis, the lumped *n* values decreased for low overbank flow condition (a relative depth less than 0.2) and then increased for higher values of relative depth.

With a low overbank flow condition, the streamwise velocity in the 1:5 physical model decreased below those recorded at the bankfull condition (Figures 3.34 and 3.36). This is contrary to the implicit assumption of the commonly used approach to compute discharge, i.e. the Divided Channel Method which, if used, will result in seriously undersized channel. The streamwise velocity magnitude increased in the main channel and decreased the floodplain with the introduction of floodplain cross-fall toward the main channel (Figures 3.35 and 3.37). Furthermore, it was also found that although the water depth in the main channel did not affect the direction of the rotation of the main channel secondary flow cells, an additional secondary flow cell might occur due to the interaction with the flow in the floodplain (Figures 3.39 and 3.40).

Flow visualisation experiments on the models reveal the generation of stationary planform vortices in certain locations associated with a shrinking floodplain area. The size and the strength of such vortices decrease with the increase in flow depth (Figure 3.41). Particular difficulty in building a comparable physical model to the full-scale river lies in the scaling of the bed roughness. The non-linear relationship for surface roughening elements in different scale models resulted larger discharges in the models (Figure 3.42).

4 CHAPTER 4 - INSTRUMENTATION AND METHODOLOGY

This chapter is divided into two main parts. The first part begins with a brief explanation of the working principles of an ADCP, followed by the description of the different types of ADCP, other data collection techniques used in this research and finishes with a discussion on the instrumentation and methodology actually adopted by the author in applying the ADCP techniques, particularly to small rivers (Sections 4.1 – 4.6). The second part of the chapter is devoted to the analysis of the characteristics of ADCP velocity data and discharge measurement (Sections 4.7 and 4.8).

4.1 ADCP working principles

This section discusses the principles and limitations of an ADCP in measuring velocity and estimating discharge in a river. ADCPs can be mounted on a boat or fixed on a platform in the bottom of the river (upward looking), near surface (downward looking) or on the side of the river (side scanning). This project used boat-mounted ADCPs, such as the one shown in Figure 4.1. The ADCP principles in measuring velocity and estimating discharge are discussed below.

Figure 4.1 RDI ADCPs: StreamPro (left) and Rio Grande (right).

4.1.1 Doppler principle

The ADCP works on the principle of Doppler shift, i.e. by comparing the difference in frequency between the emitted and received sound pulses it is possible to obtain the speed of the water at a variety of levels or 'bins' within a column of water. In using this technique, it is implicitly assumed

that particles in the water, which cause the sound pulses to be reflected, move at the same velocity as the water, and that the water is homogeneous over a vertical. The Doppler principle can be best described using the water-wave analogy illustrated in Figure 4.2. In Figure 4.2a, a stationary observer is watching a series of wave passing at a rate of one wave per second. When the observer moves towards the source of the wave at four waves per second, he/she notices the passage of five waves during every second. However, the frequency at which the waves are emitted has not altered (i.e. 1Hz). The difference in the perceived and transmitted frequency is called the Doppler Shift. The Doppler Shift can be expressed mathematically as:

$$\frac{F_D}{V_{SO}} = \frac{F_S}{C} \tag{4.1}$$

where:

F_D = Doppler Shift frequency (Hz)

F_S = frequency of sound source when everything is still (Hz)

V_{SO} = relative velocity between sound source and observer (ms^{-1})

C = speed of sound (ms^{-1})

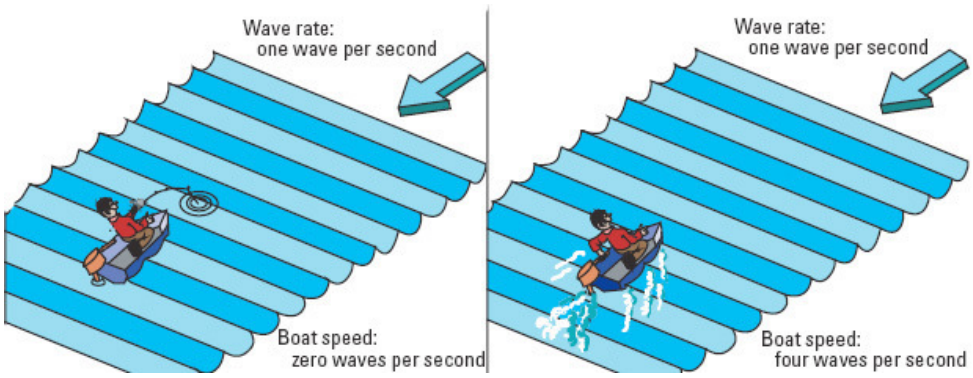

(a) stationary observer (b) moving observer

Figure 4.2 The Doppler principle and a water-wave analogy (Simpson, 2001).

ADCP transducers emit sound waves with a known frequency and velocity through water (Figure 4.3). Some of the emitted sound is reflected back to the ADCP by particles in the water. The frequency of the returning sound or echoes are measured by the transducers enabling the Doppler shifted frequency F_D to be obtained. Hence, since F_S and C are known, V can be computed. However, the reflected echoes involve two Doppler Shifts. The first Doppler Shift is perceived by the particle when

sound waves move toward the moving particle and the second Doppler Shift is perceived by the transducers when sound waves are reflected back to the transducers by the particle (Figure 4.4). Hence, equation (4.1) is modified as:

$$\frac{F_D}{V_{SO}} = \frac{2 \cdot F_S}{C} \tag{4.2}$$

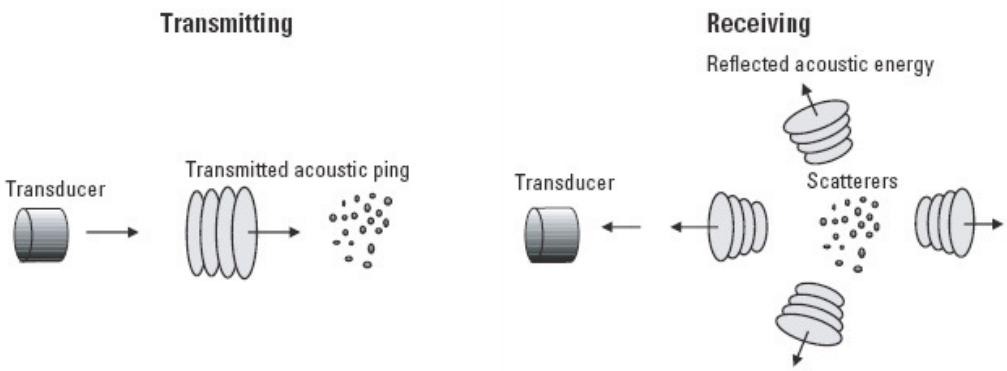

Figure 4.3 Sound wave transmission and reflection by particles (Simpson, 2001).

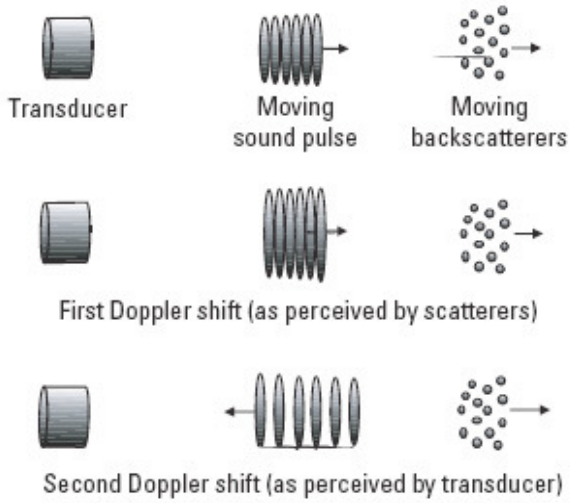

Figure 4.4 Reflected pulse shows two Doppler Shifts (Simpson, 2001).

4.1.2 Coordinate system

The Doppler Shift can be measured only if the particle in the water moves closer to or further away from the transducers (radial motion). In the case of the particle moving in angular motion, a Doppler Shift does not exist since the distance between transducers and the particle is constant. When the particles are not moving parallel to the beams (Figure 4.5), the Doppler Shift formula is modified as:

$$\frac{F_D}{V_{SO}} = \frac{2 \cdot F_S \cdot \cos(\alpha)}{C} \tag{4.3}$$

where α is the angle between the velocity vector and the transducer beam.

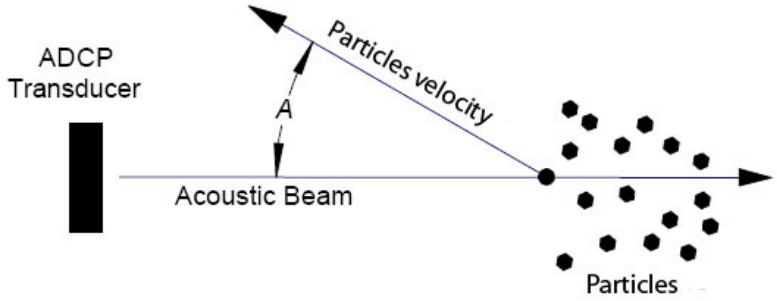

Figure 4.5 Transformation of velocity component into beam coordinate system (after RDI, 1996).

The ADCP used in the current project, uses multiple beams to sense different velocity components. At least three beams are required to construct all of the velocity components in a three-dimensional coordinate system. In an ADCP with four transducers, each pair of beams measures one horizontal velocity component and one vertical velocity component (2D). Thus, two horizontal velocity components and two vertical velocity components are obtained (Figure 4.6). Assuming that the four ADCP transducers in Figure 4.6 are pointing to the North, South, East and West directions, the velocity component along the East-West axis can be obtained only if both East and West beam velocity components are known (Figure 4.7). The same condition similarly applies to the velocity components along the North-South axis. The three dimensional velocity is the resultant of the velocity components in the North-South axis and the East-West axis. In four transducers ADCPs, the surplus in the vertical velocity component is used to calculate an error velocity, the difference between the two vertical velocity components, which indicates the homogeneity of the velocity in a horizontal layer.

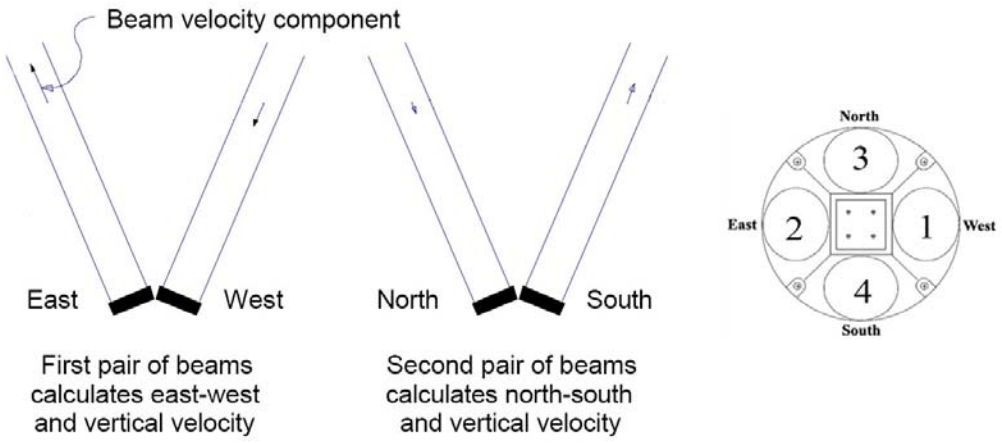

Figure 4.6 Beam velocity components (RDI, 1996).

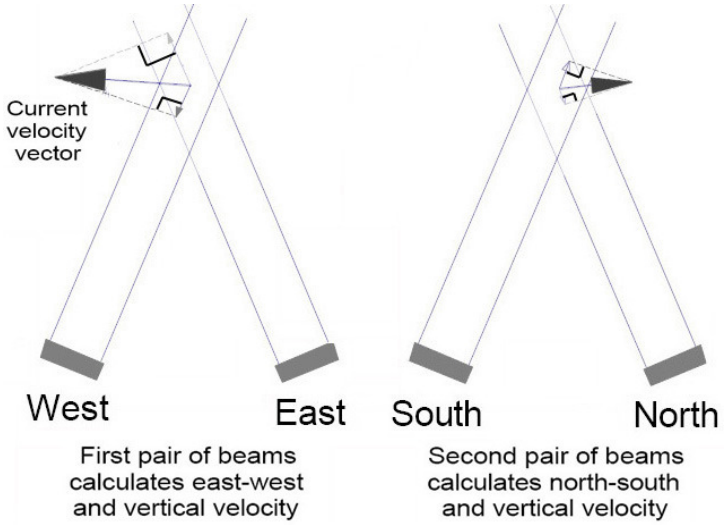

Figure 4.7 Velocity magnitude and direction in the E-W and N-S axis (RDI, 1996).

4.1.3 Bottom tracking

Bottom-tracking pings are used to measure the bottom depth and ADCP boat velocity relative to the river bed. The bottom-tracking pings have a lower frequency (longer pulse) than the water velocity profiling pings in order to properly identify the bottom. The concept of the bottom depth and boat velocity measurements is similar to the one for the water profiling. Here, the particles are replaced by the river bottom. The boat velocity is also measured using the Doppler Shift concept, but this time the boat is moving while the river bottom is standing still. Knowing the boat velocity and movement time, the boat path can be computed. As the water velocity relative to the ADCP and the velocity of the ADCP relative to river bottom are known, the water velocity relative to the bottom can be calculated.

4.1.4 Discharge approximation

Since boat path and bottom depth data can be obtained from each ping, traversing the ADCP across the channel yields the cross sectional area and water velocity. Thus, the discharge can be obtained. Although the ADCP measures three components of velocity, the horizontal components are not necessarily in the lateral and streamwise direction, since there is no guarantee that the operator(s) have positioned the ADCP perpendicular to the main flow direction. However, if the operator is only interested in the discharge measurement then this is not an issue since, unlike the velocity, the discharge is frame invariant. The formulation of discharge computation using the manufacturer's software, WinRiver 2, is described in this sub section. The general equation to calculate discharge through an arbitrary surface *s*, is:

$$Q_T = \int_s \overline{V_f} \cdot \overline{n}\ ds \tag{4.4}$$

The area s is defined by the vertical surface beneath path along which the boat travels. Note that the dot product of mean water velocity vector ($\overline{V_f}$) and its unit vector normal ($\overline{n}$) to *ds* will be equal to zero when the boat is moving parallel to the direction of the flow and will equal to the mean water velocity vector if the boat is moving normal to the direction of the flow, since:

$$ds = \left|\overline{V_b}\right| dz\ dt \tag{4.5}$$

and

$$\overline{V_f} \cdot \overline{n} = \left|\overline{V_f}\right| \cdot \sin\theta \tag{4.6}$$

hence

$$\begin{aligned} \int_s \overline{V_f} \cdot \overline{n}\ ds &= \int_0^T \int_0^d \left|\overline{V_f}\right| \left|\overline{V_b}\right| \sin\theta\ dz\ dt \\ &= \int_0^T \int_0^d (\overline{V_f} \times \overline{V_b})\ k\ dz\ dt \end{aligned} \tag{4.7}$$

where

θ = angle between water velocity and boat velocity (^{o})

k = unit vector in the vertical direction (-)

The discharge calculation above is only for the region of the cross section where ADCP data are available. Some parts of a cross section that cannot be measured by the ADCP are (see also Figure 4.8):

(a) The top of the cross section, due to the blanking distance and transducer depth.

(b) The bottom of the cross section, due to side lobe interference.

(c) The edges of the cross section, mostly because it is out of the range of the ADCP (i.e. too shallow).

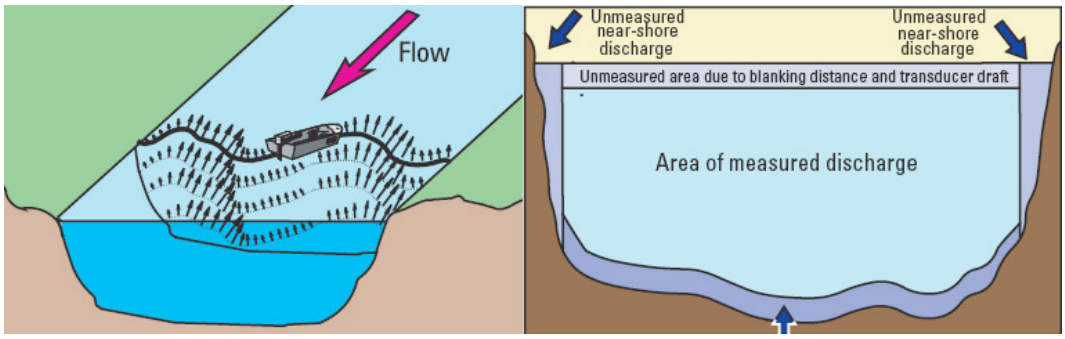

Figure 4.8 Cross-product vectors during a cross section transverse (left), unmeasured area (right) (Simpson, 2001).

To obtain the total discharge of the cross section the discharge in the unmeasured region should be estimated. WinRiver 2 has two options to estimate the velocity profiles in the unmeasured regions near surface and bottom: power and constant methods (RDI, 2008). The power method extrapolates the velocity in the unmeasured region using a $^1/_6$ power law according to the formula:

$$\frac{u}{u_*} = 9.5\left(\frac{z}{z_0}\right)^{\frac{1}{6}} \tag{4.8}$$

where

z = distance to the channel bed (m)

u = velocity at distance z from bed (ms^{-1})

u_* = shear velocity (ms^{-1})

z_0 = bottom roughness height (m)

According to the WinRiver 2 help file (RDI, 2008), the constant method uses the ensemble averaged velocity data in the first bin for the unmeasured region near surface and corresponding data in the

last bin for the unmeasured region near bottom (Figure 4.9). However, the accuracy of the help file is questionable since when the constant method is chosen, the velocity of the last bin is extrapolated linearly to zero at the river bed. The discharges in these regions are then computed by integrating each extrapolated velocity profiles over the depth and then integrating over the path of the boat.

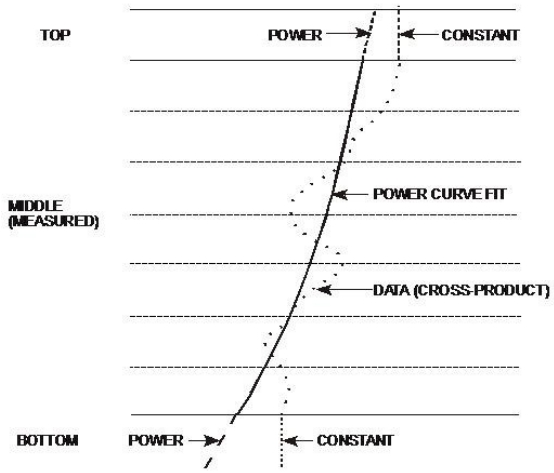

Figure 4.9 Velocity profile extrapolation in WinRiver 2 (RDI, 2008).

Discharges near the river banks are estimated using the simple formula:

$$Q_{shore} = C_{shore}\, V_m\, L\, d_m \tag{4.9}$$

where:

C_{shore} = Edge shape coefficient (0.3535 - for triangular, 0.91 - for rectangular shape)

V_m = Mean water velocity in the first or the last bin (ms^{-1})

L = Distance from the shore to the first or the last segment specified by the user (m)

d_m = Depth of the first or the last bin (m)

The estimated discharge is a cross product of the mean water velocity in the first/last bin, the distance from shore to the first/last bin (specified by user), the depth of the first/last segment to a coefficient which has a value of 0.3535 for a triangular shape of edge and 0.91 for a rectangular shape of edge. The total discharge of the cross section is the integral of the discharges in the measured and unmeasured regions.

4.1.5 Limitations

A condition that needs consideration when performing ADCP measurements is that the channel might be transporting a significant amount of sediment. This condition, commonly referred as a "moving-bed" in ADCP terminology, will bias the measured streamwise velocity towards lower values if the ADCP bottom-tracking is used as a reference in calculating the water velocity. Readers interested in this issue are referred to Mueller (2002), Simpson (2001) and Mueller *et al*. (2007). In addition, the author's experience has shown that the presence of vegetation can significantly inhibit the ability of the ADCP to give reliable measurements. This is perhaps not too surprising if one considers the principle of operation, i.e. vegetation near the channel bed has the propensity to disrupt the bottom tracking and also to cause anomalous velocity measurements to occur. Readers interested in further details of ADCP measurement techniques are directed to Gordon (1989), RDI (1996, 2008) and Simpson (2001).

4.2 ADCPs StreamPro & Rio Grande

Two different ADCPs were used in this research, the StreamPro and Rio Grande, both manufactured by RD Instruments. Due to its smaller size and blanking distance, the StreamPro was considered to be more suitable than the Rio Grande for measurements in small rivers, such as the River Blackwater. Furthermore, the StreamPro can be hosted in a small boat, due to its small transducer sizes, while the Rio Grande requires a larger boat due to the size of its transducers (Figure 4.10). Hence, when circumstances allow (i.e. the edge region is deep enough for ADCP measurements), the StreamPro can obtain more data near the edge region than Rio Grande since its boat size is narrower than the Rio Grande's. In addition, the smaller transducer size of the StreamPro yields a shorter blanking distance (~0.16m), compared to the Rio Grande (~0.40m). Consequently, the StreamPro can collect more data near the surface than the Rio Grande (Figure 4.11). Despite this, the Rio Grande's system is more advanced than StreamPro's. Some of these advances are the ability to perform single-ping measurement, integrated heading sensor on the system and more choices of water profiling modes. The next two paragraphs discuss brief details relating to both of these instruments.

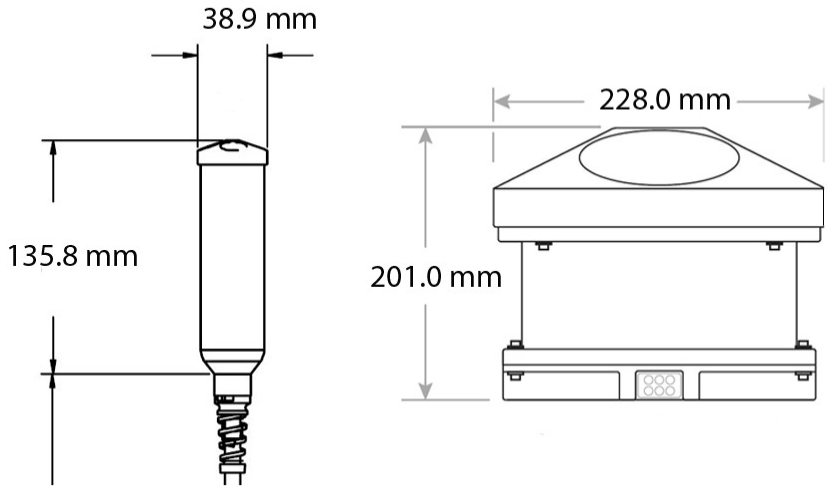

Figure 4.10 Transducers dimensions: StreamPro (left) and Rio Grande (right).

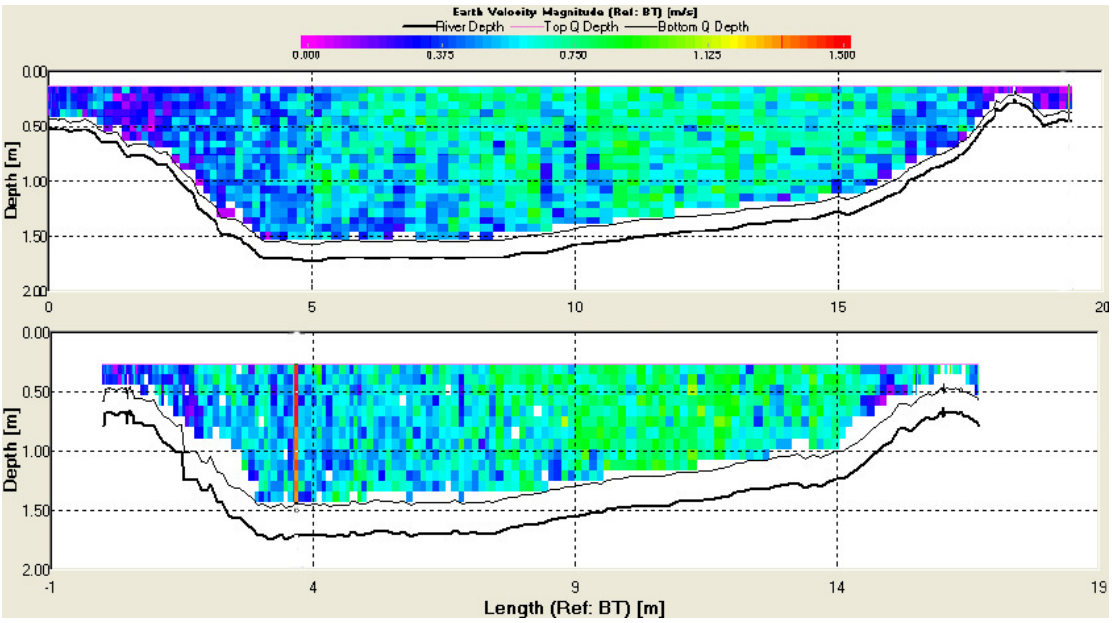

Figure 4.11 Blanking distance comparison: (top) StreamPro, (bottom) Rio Grande.

The velocity in a cross section is measured by an ADCP by sub-dividing the cross section into small rectangular elements over the depth and width (bins). The bin size of an ADCP is user configurable, but is restricted to only 20 bins over one vertical for the StreamPro ADCP. Bins located below the measured region will simply be marked by the processing software (WinRiver 2) as missing data. The StreamPro is capable of measuring water velocity up to $2ms^{-1}$ on standard boat and up to 2m depth in normal circumstances. According to the manufacturer's specification, the StreamPro has a velocity profiling accuracy of ±1% ±0.2cms^{-1}. It measures 48 Doppler shifts per second and computes the

average Doppler shift for every 6 samples. However, it can only output the velocity data once every second. The StreamPro has four 3.5cm-diameter transducers aligned in a janus configuration, i.e. tilted 20 degrees from vertical. It can be operated using WinRiver 2 software from a PC using Bluetooth technology. A common way of deploying the StreamPro in practice is simply by pulling it across the river by means of a ropeway (Figure 4.12).

Figure 4.12 ADCP measurements by means of ropeway.

The Rio Grande ADCP is designed to measure real-time current profiles from temporary or permanent mountings in a vessel. The Rio Grande model used in this research was the 1200kHz model, with a maximum profiling range of 21m depth. The transducer configuration in the Rio Grande was similar to that of the StreamPro, but with larger diameter. According to the manufacturer's specification, the Rio Grande has a velocity profiling accuracy of ±0.25%±0.25cms^{-1}. The number of bins on the Rio Grande can be set to 128, with a minimum bin size of 0.05m. Unlike the StreamPro, the Rio Grande can perform single ping measurement, typically at 2Hz. It is commonly operated using a PC via a wired or wireless connection.

Different water profiling modes are available for operating the StreamPro and Rio Grande ADCPs in different environmental conditions, e.g. fives modes are available for the Rio Grande (RDI, 2008). Mode 11 is used if the flow and depth are less than 1ms^{-1} and 4m. Mode 12 is recommended if the flow is too fast or too turbulent for mode 11. If both modes 11 and 12 are not suitable, then mode 1 will work in all but the most extreme situations. Modes 5 and 8 are included for backward compatibility and for users who are familiar and satisfied with their performance with older systems. General descriptions and the recommended setup for these various modes are given in Table 4.1. Only two water profiling modes are available for StreamPro: mode 12 and mode 13. StreamPro's

mode 12 is similar to the mode 1 for Rio Grande, and mode 13 is designed for measurements at low water velocity, i.e. less than 0.25ms^{-1} (Murphy, 2009; Mueller and Wagner, 2009). All StreamPro measurements in this project were undertaken using mode 12 since the typical velocity magnitudes in 30% to 70% of the measured region are higher than 0.25ms^{-1} (during inbank flow).

	Mode 1	Mode 12	Mode 11
Typical application	Fast water of all depths. Rough and dynamic situations. Good in streams too fast or deep for modes 5, 8 & 11 or where Mode 12 has problems.	Fast water of all depths. Good in streams too fast or deep for modes 5, 8 &11. Good for deep, slow water.	Slow, shallow streams with velocities < 1.0 ms^{-1} (depth dependant) with low shear and/or turbulence.
Minimum recommended cell size (meters)	**0.50*** 0.25	**0.25*** 0.10	**0.10** 0.05
Recommended Cell Size (meters)	**0.50** 0.25	**0.25** 0.10	**0.25** 0.05
Single ping standard deviation (cm/s) (using rec. cell size)	**13.62** 13.64	**6.24** 6.95	**0.74** 1.34
First range cell (meters)	**0.97** 0.51	**0.73** 0.26	**0.49** 0.09
Minimum profiling range (meters) Bottom Mode 5	**1.7** 1.0	**1.7** 1.0	**1.6** 0.9
Minimum profiling range (meters) Bottom Mode 7	**NA** 0.7	**NA** 0.5	**NA** 0.3
Maximum profiling range (meters)	**73.1** 19.55	**68.29** 15.82	**<8.0** <4.0
Maximum relative velocity (m/s)	10 m/sec	10 m/sec	1m/sec (Depth Dependant)

* 600kHz values are in **bold** font, and 1200kHz values are in regular font.

Table 4.1 Typical Rio Grande's water profiling modes (RDI 2008)

4.3 Other techniques for data collection

For completeness, this section briefly describes other data collection techniques used on the River Blackwater during the course of the project. In addition to ADCP measurements, the water velocity was also recorded by other parties (Centre for Ecology and Hydrology & Loughborough University) using an Acoustic Doppler Velocimeter (ADV) and large scale particle image velocimetry (LS-PIV). A brief description on both techniques is presented below, with a comparison of velocity distributions measured using the three different methods presented in Chapter 5. In addition to velocity

measurements, bathymetry surveys, staff gauges and discharge measurements via an electromagnetic gauge were undertaken and are discussed below.

4.3.1 Large-Scale Particle Image Velocimetry

LS-PIV measurements were undertaken using a high resolution camcorder (Sony DCR-TRV22 High8 Handycam and JVC Everio GZ-MG275). After a number of trial runs it was discovered that biodegradable packing chips represented a suitable seeding material for the LS-PIV. During measurements, the biodegradable packing chips were released in to the river using a simple system of containers attached to a pole (Figure 4.13). This container system ensured that a large area of the river could be seeded at one time. The movement of the material on the water surface was recorded by the video camera, and converted subsequently to 2D surface velocity vectors using an algorithm developed by Fujita et al. (1998). Permanent dGPS markers (Figure 4.13) were established on the edge of the floodplain banks in the scanned area, so that the inclined video image could be ortho-corrected to an appropriate horizontal datum.

Figure 4.13 Clockwise from top left: seeding for PIV, benchmarks for PIV, video camera attached on a hydraulic pole, video camera recording.

4.3.2 Acoustic Doppler Velocimeter

An acoustic Doppler Velocimeter (ADV) was used for benchmarking the velocity data obtained from the ADCP and also for measuring the flow on the floodplain during floods. The ADV in question was a 10MHz velocimeter with capability of obtaining 3D point velocity data at 25Hz (Nortek 10MHz velocimeter). The ADV was housed in a T-shaped aluminium beam (Figure 4.14) enabling the ADV to be positioned accurately. The sampling time corresponding to the ADV measurements was of the order of five minutes.

4.3.3 Ground survey

The ground level and bathymetry of the research site were surveyed using two motorised total stations at the beginning of the project (March 2007). Both data are essential for building the digital elevation model required for numerical models. Several benchmarks, established using a differential GPS (dGPS), were used as references for the total stations. In total, 9236 levels were measured at 0.5m to 1m intervals. A comparison with a previous survey (2002) was made to monitor changes in the ground elevation (Figure 3.17a, see also Section 3.3). ArcGIS 9.2 was used to build and compare the Digital elevation models of the data from both surveys. Further details relating to these issues were discussed in Chapter 3.

4.3.4 Staff gauges

The water surface slope, required for hydraulic roughness coefficient calculations, was measured using several permanent staff gauges installed along the research reach. The positions of the staff gauges are indicated on Figure 4.15. The height Above Ordnance Datum (AOD) of these gauges was surveyed using a level.

4.3.5 Electromagnetic gauging station

A Sarasota-electromagnetic gauging station, operated by the Environment Agency, was used to monitor the discharge in the research site. The electromagnetic gauge was installed in a short length of channel with a simple trapezoidal section upstream of cross section (CS) 1 (Sellin and van Beesten 2002). An on-site data logger recorded data from the instrument at 15 minute intervals. Sellin and van Beesten (2004) reported that the corresponding gauging station could measure discharge to 15%

accuracy at low flows and 1.5% accuracy at high flows. This particular gauging station works on the principle that the motion of water 'cuts' through a magnetic field generated by a large coil buried beneath the riverbed. An electromagnetic force and corresponding change in voltage is induced as a result of the water movement as is measured by signal probes at each side of the channel. This change in voltage is directly proportional to the average velocity of flow in the cross section. Readers interested in more details on this issue are directed to Boiten (2000), Herschy (1985) and Tavoularis (2005).

Figure 4.14 Clockwise from top left: total station survey, ADV measurement, staff gauge installation, a staff gauge.

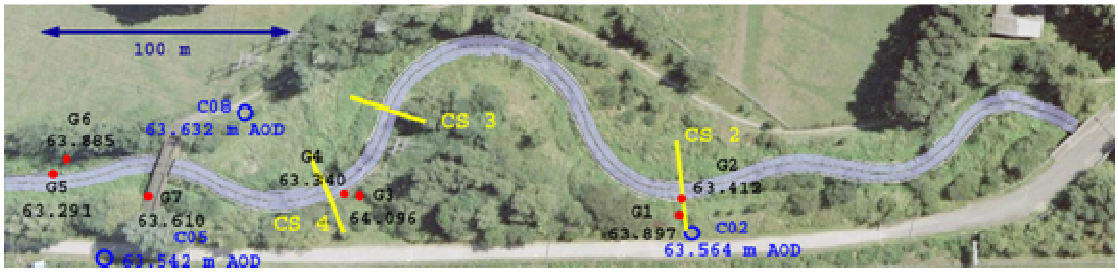

Figure 4.15 Staff gauges locations (red dots) and dGPS benchmarks (blue circles).

4.4 Application of the StreamPro ADCP to small rivers – physical modifications

The velocity data that are outlined subsequently were obtained from two types of measurements, namely transverse and stationary. The data relating to transverse measurements or transects were obtained by slowly traversing the ADCP across the river while the stationary measurements relate to data recorded by the ADCP when it was held stationary at a particular position in the river for an extended period of time. In order to enable reliable and repeatable measurements to be taken it was important to ensure that the ADCP was either located at the same position in the river or traversed the same path, since unlike the discharge, the velocity is frame variant. The accuracy of ADCP positioning becomes more crucial when working at a smaller scale, i.e. in small rivers. To minimise errors associated with the positioning of the ADCP, a simple winch and pulley system was devised which was fixed to the banks of the river. In order to orientate the velocity data, the heading (i.e. the local position) of the ADCP transducers was required. To provide such information, the ADCP boat was modified to include a digital compass. Both modifications are discussed below (see also Gunawan *et al.,* 2008; 2009).

The winch and pulley system is illustrated schematically in Figure 4.16. A requirement of this system was that it had to be portable since it would be needed at different locations in the channel at different times. Therefore, in order to ensure that the system could be erected at the same location, the entire reach of the river outlined below was surveyed and temporary benchmarks installed. Hence, on any given day it was possible to consistently locate the pulley and winch system at the same location. However, in practice ground conditions often changed resulting in a slight offset in the location of the vertical posts between different experimental campaigns. The magnitude of the offset was estimated to be of the order of 20mm and thus considered to be negligible for most practical purposes.

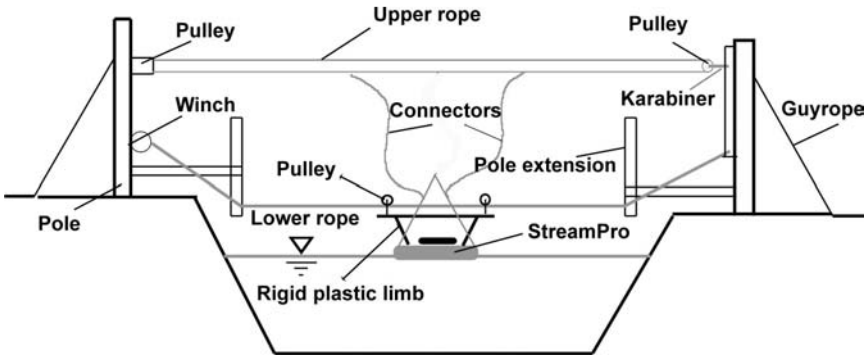

(a) Schematic view of the system.

(b) The system as used.

Figure 4.16 The winch and pulley system.

For each of the transect measurements, the ADCP (attached to a small boat) was pulled slowly across the river. Initially, a remote control system was used in order to drive the boat across the river, but it quickly became apparent that the drag on the boat was too strong for the system adopted. Although a stronger motor could have been used, this was considered to be an inappropriate refinement for the purposes of the current work.

The simple winch and pulley system proved to be very effective in ensuring that the same cross section was measured during each transect. For example, Figure 4.17a illustrates the local position recorded by the ADCP's bottom tracking system for a number of different transects. The legend number in Figure 4.17 simply refers to the different transects of the same cross section, and for each transect the location of the boat is assumed to start from (0, 0). As the boat traverses from the left

bank to the right bank, negative values of local Eastings and Northings were recorded, while the reverse was true when the boat travelled from the right bank to left bank.

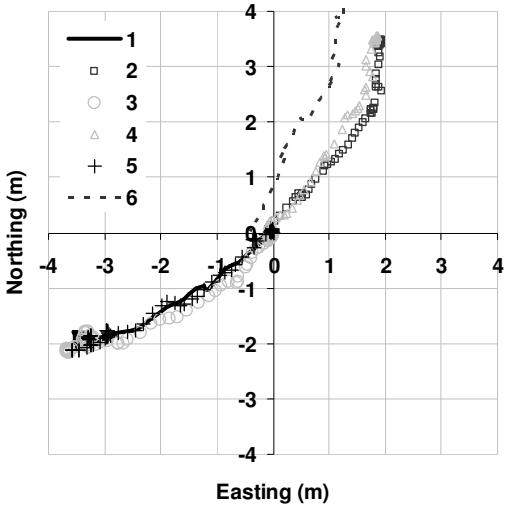

(a) Local positioning obtained without using the winch and pulley system.

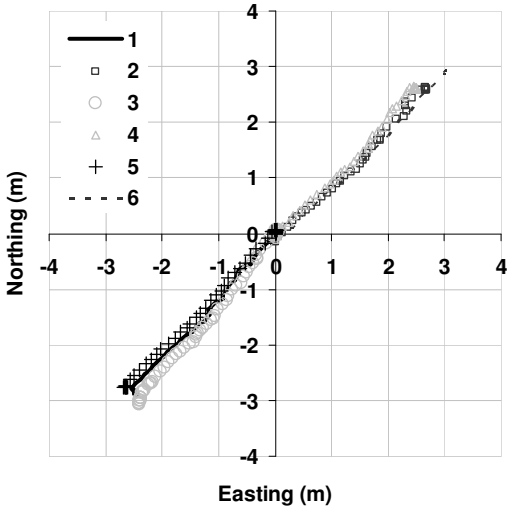

(b) Local positioning using the winch and pulley system.

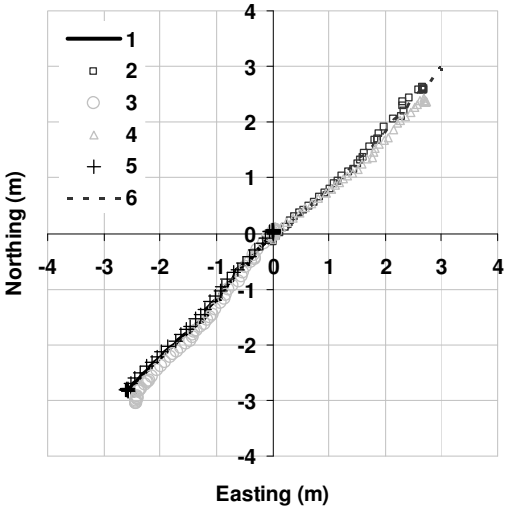

(c) Local positioning using the winch and pulley system corrected using compass alignment.

Figure 4.17 The effect of the winch and pulley system.

The pulley and winch system ensured that the ADCP followed the same track during each transect (Figure 4.17b). However, in order to orientate the velocity data, the heading (i.e. the local position) of the boat was required. To provide such information, the ADCP boat illustrated in Figure 4.18 was modified to include a digital compass (PNI Sensor Corporation TCM 3 Tilt- Compensated Heading Module). The results of this orientation are illustrated in Figure 4.17c. The inclusion of the compass

represented a significant improvement to the standard StreamPro ADCP. Although it was not possible within the scope of the current project to devise new software capable of ensuing that the compass software and the StreamPro software communicated with one another in real time, this proved not to be critical; both software programmes time stamp the data and it was thus possible to align the data after each experiment. While it is acknowledged that such an approach is not ideal (e.g. the compass outputs data every 1.4 second while ADCP outputs every 1 second), for the purposes of the current analysis and the measurement times scales involved, this was considered reasonable. In order to avoid the complication of wires extending between the ADCP and compass and the PC, communication was achieved through the installation of two serial Bluetooth adapters (Sena-Parani SD-100). The Bluetooth adapters were capable of transmitting data within 100m and were powered through a 9Volt PP3 battery which was installed in a water proof box housed on the ADCP boat (Figure 4.18).

Three main issues concerning the compass application are as follows:

(a) Coordinate system orientation

The StreamPro records velocity data in the local ADCP co-ordinate system. In this system the 0^{o} reference is the bearing of the transducer beam 3 at the time the ADCP starts to ping. In order to orientate the co-ordinate system of each transect, the bearing of beam 3 should be recorded each time the ADCP starts pinging.

(b) Compass housing

The TCM 3 was accommodated in a black electronic housing which was placed in a white waterproof electronic housing. The double-layer protection was adapted to provide more security to the relatively expensive TCM 3. The TCM 3 was fitted in the black housing using brass screws due to their non-magnetic properties. The Bluetooth adapter and batteries were accommodated in a separate waterproof white electronic housing connected with the TCM 3 housing via waterproof cable connections. Separate housings were required to ensure that any electromagnetic signature from the batteries did not contaminate the compass data. All holes made for cable insertion were sealed using silicone sealant to prevent water entering the holes. The batteries housing was fixed on top of the ADCP housing using adhesive sealant (Sikaflex). The compass housing was fixed on the left front of the ADCP boat at the beginning, but later on moved to the rear part of the boat to improve the balance of the boat (Figure 4.18). A plan view photo taken from the ADCP was processed in an

image editor to check the accuracy of the compass bearing alignment to the symmetrical axis of the boat. Based on the lines indicating bearing deviations of 1 and 5 degree from the boat symmetrical axis (Figure 4.18), it is thought unlikely that the inaccuracy of the compass bearing position was more than 2 – 3 degrees (constant offset).

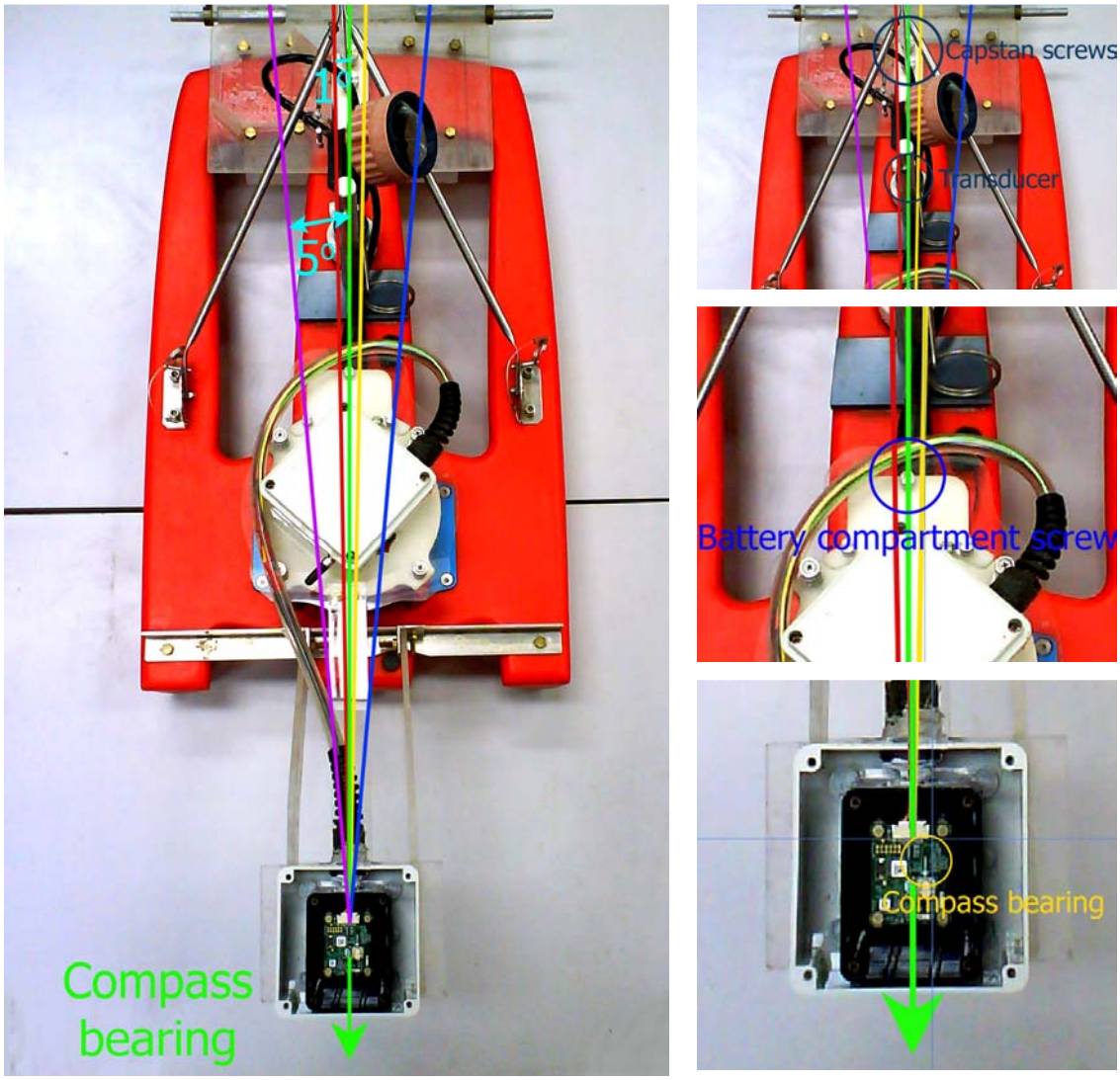

Figure 4.18 Compass bearing direction.

(c) Hard and soft iron calibration

The TCM3 compass has a feature to calibrate distortion due to hard and soft iron effects. Hard iron distortions are caused by permanent magnets and magnetized steel or iron objects within close proximity to the sensors. This type of distortion will remain constant and in a fixed location relative to the sensors for all heading orientations. Hard-iron distortions will add a constant magnitude field component along each axis of sensor output and can be easily compensated for by using a simple

subtraction method. Soft-iron distortions are the result of interactions between the earth's magnetic field and any magnetically "soft" material within close proximity to the sensors. In technical terms, soft materials have a high permeability. The permeability of a given material is a measure of how well it serves as a path for magnetic lines of force, relative to air, which has an assigned permeability of one (PNI Corp, 2008).

The hard and soft iron distortion compensation uses magnetic sensors to magnetically map the system environment in the 3D space. The algorithms then take this 3D shape (typically an ellipse) and resolve it back to a centred sphere (PNI Corp, 2008). The calibration requires the compass and its housing (including the ADCP) to be placed at several different heading and tilt positions when obtaining calibration parameters. The positions should be well distributed well in 3D space. Users can choose between 12 and 50 calibration points, with a higher number providing a chance to obtain better coverage. Coverage in *x*, *y* and *z* direction and standard deviations of magnetic field generated by static hard and soft iron material in the device recorded during calibration process were used to determine the quality of the calibration. The goal of the calibration was to obtain more than 85% coverage for *x* and *y* direction and less than 0.2μT for the standard deviation of magnetic field. The standard deviation score represents how well the distortion was able to be described and compensated for. Poor calibration result will likely be experienced if sources of distortion to be calibrated out moves relatively to the module, or if calibration is performed in a magnetically noisy environment (PNI Corp, 2008). A new calibration has to be performed whenever the compass position relative to its housing is changed.

Combining the digital compass and the winch and pulley system with a survey of the reach in question ensured that the exact position of the ADCP could be determined. It is perhaps worth noting that a further modification was also made to the boat to enable the ADCP to be tracked continuously by a total station. However, the development of this system is still within its early stages and as such details are not presented below. At one stage, digital GPS was considered; however, the costs involved and the additional problems created (e.g. the tree coverage near the reach is likely to cause a significant deterioration in the quality of the GPS data) ruled out such a development. The winch and pulley system evolved during the project (Figure 4.19): starting with a simple 1-loop rope cableway without a compass in January 2007, followed by a guiding rope and remote controlled deployment in June 2007. The limb extension was introduced in January 2007,

and finally the compass housing was moved to the rear part of the boat to provide more stability (May 2008).

Figure 4.19 Evolution of StreamPro deployment system during the course of the project.

4.5 Measurement methodology.

As previously discussed in section 4.4, two types of measurements, namely transverse and stationary, were used for data collection. The methodologies of both types are now discussed in detail.

4.5.1 Transverse measurements

The user's manual for the supplied software (RD Instrument, 2008) suggests that differences in discharge (ΔQ) between a minimum of four transects should be less than 5% of the mean of all the samples. Other approaches have also been suggested. For example, the United States Geological Survey (USGS) suggests that if the measurements of four transects differ by more than 5%, then a

total of 8 transects should be made and the average discharge obtained from all of the measured transects (Mueller and Wagner, 2009). While this approach is possibly less time consuming it does have the possibility of including measurements that contain significant errors, whereas the first approach can be considered in effect to have an automatic filter since transects containing erroneous measurements are disregarded and the experiments repeated until four transects agree to within 5%. The approach adopted by the UK Environment Agency is the same to that adopted by the USGS (Environment Agency, 2008a, 2008b).

Reported ADCP and measurement protocols have generally been restricted to large rivers, where the scale of the river helps to ensure that measurement errors are relatively small. However, as indicated previously, these same errors can become relatively large when the scale of the river decreases. In the current work, a different approach to those outlined was employed which is particularly suited to small rivers. In this approach at least six transects were undertaken, from which the mean discharge was calculated. The methodology for computing cross sectional discharge is outlined in Figure 4.20.

At first, a visual observation is undertaken to exclude transects within the criteria outlined below from the discharge computation:

(a) Transects having more than 10% (from the total length of the section) deviation to the straight route. The deviation is computed perpendicular to the straight route.
(b) Transects with overshooting length exceeding 10% of the length of the cross section (Figure 4.21).
(c) Transects with more than 10% missing data.

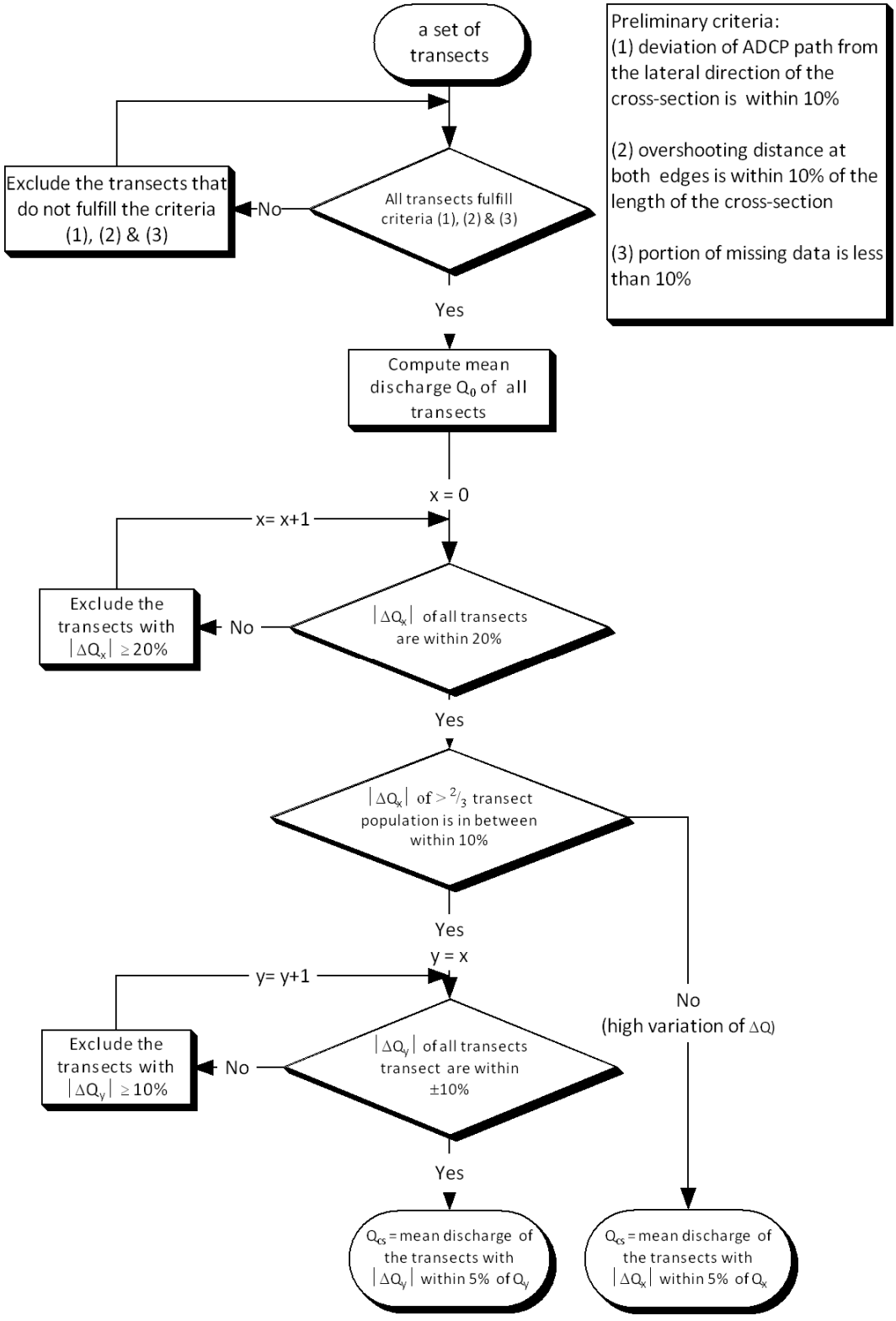

Figure 4.20 Methodology of obtaining cross section discharge from a set of ADCP transects for the current research.

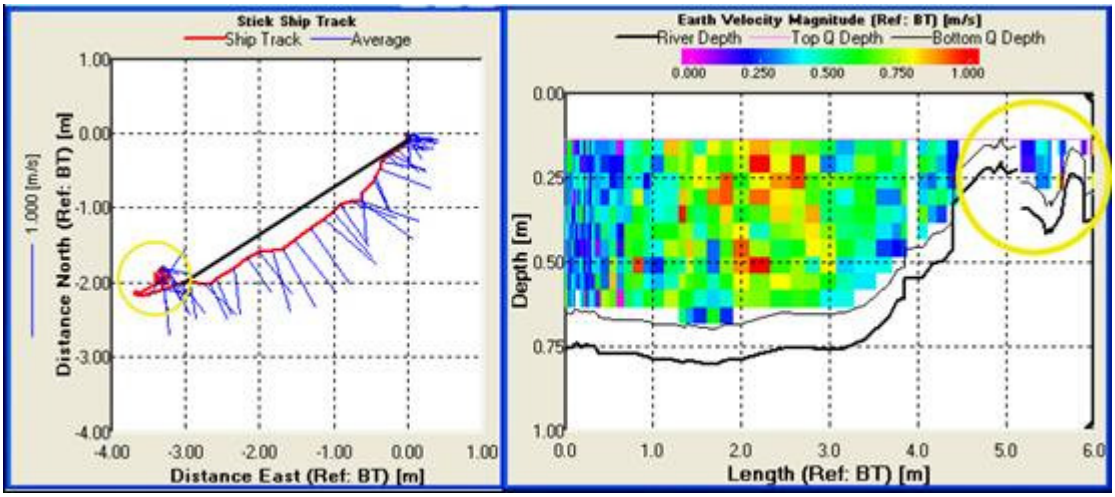

Figure 4.21 Path deviation from lateral direction (left) and overshooting on edge (right).

As illustrated in Figure 4.20, after the initial criteria are fulfilled, any transects which have an experimental error greater than ±20% are removed and a new discharge is calculated from the remaining subset of transects (Q_x). If less than two thirds of the measurements have an absolute ΔQ_x less than 10%, then the discharge of the transect (Q_{CS}) is computed from the mean of the transects whose variation is within 5% of Q_x. However, if less than one third of the measurements had ΔQ_x of greater than 10% then those corresponding transects were removed and a new mean discharge was calculated (Q_y). The acceptable transects were taken to be those whose discharge was within ±5% of the revised mean value and the cross section discharge was the mean discharge of the corresponding transects. Although this approach seems longwinded it can be easily executed using WinRiver 2. In addition, this approach has the benefit of removing erroneous or outlying velocity data, which experience has shown can occur frequently in small rivers. Furthermore, a decision on whether additional transects are required can be done instantly since the discharge difference is computed in real-time in WinRiver 2.

A practical example how the results from this approach can be different from RDI and USGS approaches is now presented. Figure 4.22 shows the histogram of discharge difference from 6 transverse measurements at CS 4 (21/11/2007). All transects fulfil the 3 criteria for being included for discharge calculation. Table 4.2 shows the magnitude of discharge difference from all transects. The USGS approach will require 4 more transverse measurements to be undertaken since the transect with ΔQ = -22.66% is within the first four transects. Similarly, the RDI approach will require more transects, until the differences in discharge between a minimum of four transects are less than 5% of the mean of all the samples. Using the approach adopted by the author, the transect

Blackwater033 would be excluded from the computation of the mean discharge since it has more than 20% discharge difference (Table 4.3). The second filter is not required since the discharge differences in the transects are already within 10% of the mean discharge. The cross section discharge is then computed from the mean of transects with discharge differences less than 5% from the mean discharge (Table 4.4).

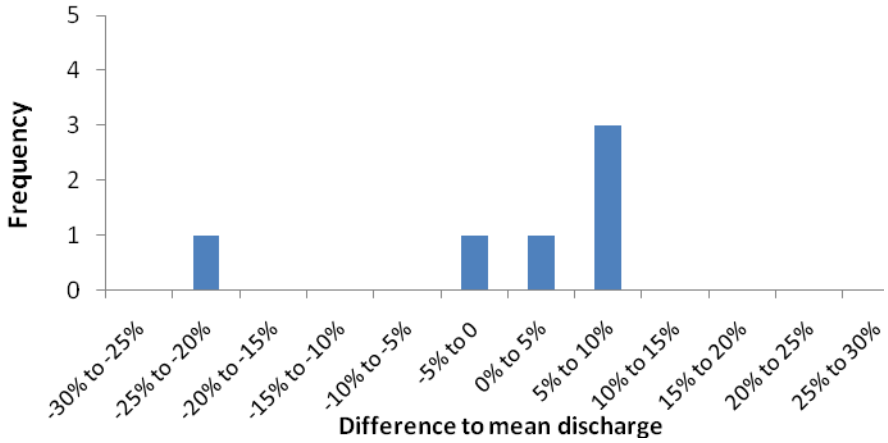

Figure 4.22 Discharge difference histogram from 20/11/2007 measurement at CS 4 (Q=1.039ms^{-1}).

Discharge Summary - TRDI

Transect	Start Bank	# Ens.	Start Time	Total Q m³/s	Delta Q %
Blackwater033	Right	79	09:51:04	0.755	-22.66
Blackwater034	Left	62	09:53:30	1.002	2.65
Blackwater035	Right	72	09:55:25	1.054	7.97
Blackwater036	Left	70	09:57:01	1.042	6.74
Blackwater037	Right	61	10:03:16	0.945	-3.19
Blackwater038	Left	70	10:05:48	1.059	8.49
Average		69		0.976	-0.00
Std Dev.		7		0.116	11.93
Std./| Avg.|		0.10		0.12	0.00

Table 4.2 Mean discharge and discharge difference from all samples (CS 4 - 20/11/2007).

Discharge Summary - TRDI

Transect	Start Bank	# Ens.	Start Time	Total Q m³/s	Delta Q %
Blackwater034	Left	62	09:53:30	1.002	-1.80
Blackwater035	Right	72	09:55:25	1.054	3.29
Blackwater036	Left	70	09:57:01	1.042	2.12
Blackwater037	Right	61	10:03:16	0.945	-7.39
Blackwater038	Left	70	10:05:48	1.059	3.78
Average		67		1.020	0.00
Std Dev.		5		0.048	4.68
Std./| Avg.|		0.07		0.05	0.00

Table 4.3 Mean discharge and discharge difference after removal of transect with ΔQ>20% (CS 4 - 20/11/2007).

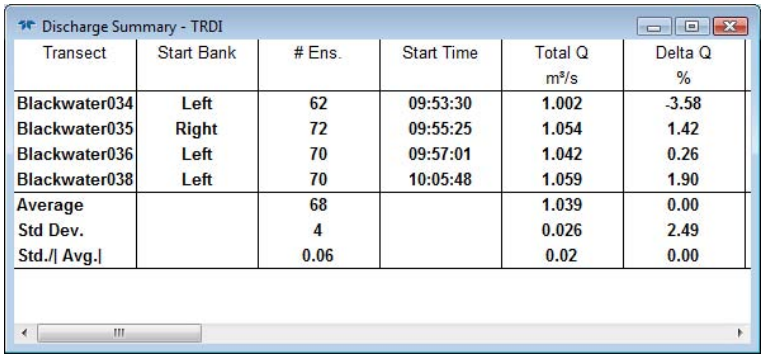

Transect	Start Bank	# Ens.	Start Time	Total Q m³/s	Delta Q %
Blackwater034	Left	62	09:53:30	1.002	-3.58
Blackwater035	Right	72	09:55:25	1.054	1.42
Blackwater036	Left	70	09:57:01	1.042	0.26
Blackwater038	Left	70	10:05:48	1.059	1.90
Average		68		1.039	0.00
Std Dev.		4		0.026	2.49
Std./| Avg.|		0.06		0.02	0.00

Table 4.4 Mean discharge and discharge difference from transects with ΔQ<5% (CS 4 - 20/11/2007).

The coefficient of variation of the discharge (defined as the ratio of standard deviation divided by mean) from a set of transects (before filtering processes) is in the region of 3% – 13 %. For practical purposes, a ten percent threshold is adopted instead of 13%. Occasionally, some transects might lie within the 10% to 20% discharge difference range. These are often experienced during low flow conditions (and therefore also a low mean velocity), when the discharge in the river Blackwater is less than $\pm 0.5 m^3 s^{-1}$. In such conditions the standard deviation of transect discharges are higher than that of at higher discharge magnitude and, as consequence, more samples (and therefore also time) will be required to ensure a sufficient number of transects agree within 5% of the mean discharge. The author's approach in computing transect discharge in such a case is first to verify whether more than $^1/_3$ population of the samples (after exclusion of the transects with ΔQ > 20%) has ΔQ values between 10% and 20%. When this is the case, the variation of ΔQ is considered as high. Thus, the end ΔQ would be computed relative to Q_x (that includes ΔQ < 20%) instead of Q_y (that includes ΔQ < 10%, refer to Figure 4.20). This would, consequently, reduce the time required for the measurement.

This higher variability in cross sectional discharge at low main channel velocity has also been highlighted in a recent USGS report (USGS, 2009), stating that StreamPro discharge measurements for individual transects have much greater variability when the mean channel velocity is less than $0.24 ms^{-1}$: Discharge measurements made when mean velocities were less than $0.24 ms^{-1}$ had an average coefficient of variation for individual transect discharges of 12%, whereas measurements with mean velocities greater than 0.24 ms^{-1} had an average coefficient of variation of 2.5%. Despite this larger variation, the measured discharges (the mean discharge for all transects) do not seem to be biased, provided that enough transects (potentially more than eight) are included in the mean discharge (USGS, 2009).

The absolute difference between discharges computed using the author's and RDI's approaches range from 0 - 4.7%. However, this comparison is only for transect discharges that fulfil the

requirements of both approaches. In some cases, especially at low flow conditions, more measurements had to be taken if RDI's approach requirement was to be fulfilled. Typical absolute differences of discharge computed using the author's and USGS's approaches ranged from 0.3 - 11.1%. The high differences are found at low discharge, where USGS's approach uses only 8 transects for computing discharge while variation of transect discharge is high.

4.5.2 Stationary measurements

An alternative way of ensuring that the correct averaging procedure is used is to fix the ADCP at several specific locations in a cross section and sample for an extended period of time. The benefit of this approach is that it provides detailed information relating to the velocity distribution and turbulence parameters at a particular point in the river. Figure 4.23 illustrates the variation of the mean streamwise velocity for averaging periods of 1 second, 180 seconds and 300 seconds. It is evident that the instantaneous data (1 second average) differs significantly from the 180 and 300 second averaged data. Figure 4.24 illustrates the variation of the depth average mean streamwise velocity and corresponding standard deviation with respect to the averaging period. In Figure 4.24 it can be seen that after approximately 150 seconds the mean standard deviation tends to a constant value of 0.18ms^{-1}. This gives an indication that the velocity data can be considered statistically stationary after this time. However, this approach is time consuming and does not yield information relating to the discharge. A comparison between the stationary approach and the transect method is given later in Chapter 5.

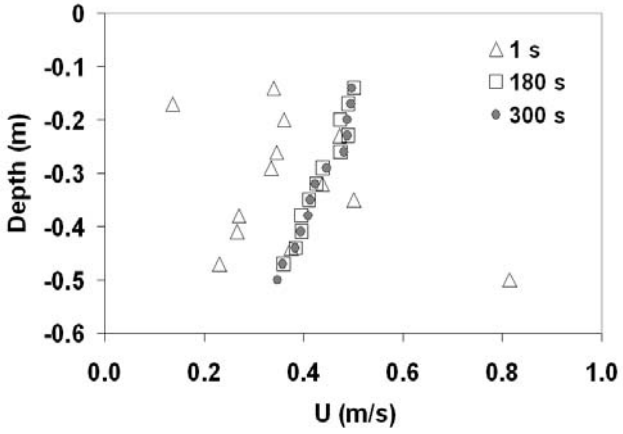

Figure 4.23 Variation of velocity distribution with respect to averaging time.

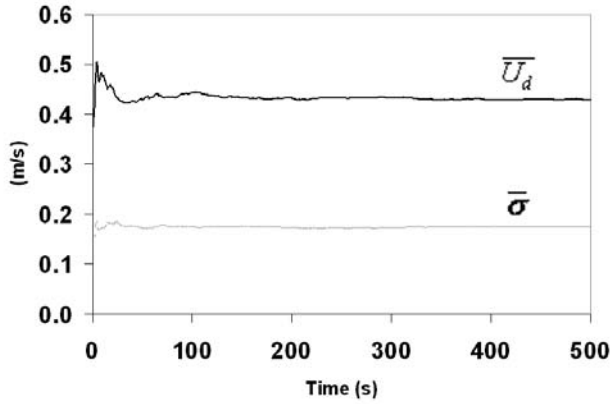

Figure 4.24 Variation of depth average streamwise velocity and standard deviation with respect averaging period.

A typical measurement campaign in a single cross section containing ten transverse measurements and four stationary measurements in the River Blackwater requires approximately 60 minutes to be completed. The time breakdown of such measurements is illustrated in Table 4.5.

ADCP & cableway setup	20 minutes
10 transverse measurements	15 minutes
Four-5 minutes stationary measurements	25 minutes
Total time required in a single cross section	60 minutes

Table 4.5 Breakdown of time in a single cross section measurement

4.6 Data analysis issues

This section is concerned with the ADCP data post-processing. It begins with the processing of the heading data recorded by the TCM 3, followed by an explanation of the author's methodology for performing transects averaging and closes with a brief example of the application of the transects averaging methodology, using data from the River Blackwater.

4.6.1 Heading data processing

The TCM 3 records the measurement time of the heading data using a unit called a "tick" (1/60s). Since the starting time of the measurement is recorded internally by the compass, the heading data could be synchronized with the ADCP clock to obtain the heading of transducer no.3 when pinging was initiated. The heading data output could be chosen as Magnetic or True heading. When True

heading is chosen, the local declination value in the measurement location should initially be inputted in the measurement software. The author's approach was to select Magnetic heading as output, then incorporating the local declination value for computing the True heading. The Magnetic Declination values for the research site (51°17'50.51"N, 0°44'20.64"W) were obtained from the National Oceanic and Atmospheric Administration (NOAA) geomagnetic model (NOAA, 2009). The True heading is then used for computing the required offset for velocity projection (Figure 4.25).

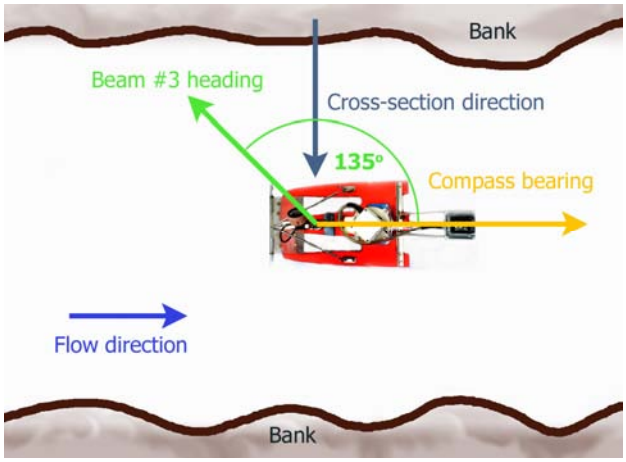

Figure 4.25 Computation of transducer 3 bearing.

4.6.2 Transects averaging

The author found that in the current arrangement, relatively little post processing was required to obtain the discharge measurement. However, this is not always the case. For example Muste *et al.* (2004a) suggested that a power law regression should be fitted to the velocity measurements, from which the depth averaged velocity could be estimated. Average values of depth-averaged velocity can then be computed between consecutive profiles from which the discharge can then be obtained. Using this approach, Muste *et al.* (2004a) extracted velocity profiles and showed that some followed a reasonably well defined power law.

The author has chosen not to follow the approach of Muste *et al.* (2004a) since he did not wish to predict or impose the trend of the velocity distribution prior to the analysis, nor impose such a distribution on the final data. The approach adopted in the current work was to create an interpolation domain in the form of a structured mesh. At each mesh point the data were interpolated using a simple inverse distance weighting method (IDW) (Amtec Engineering Inc., 2003) which has both an averaging and smoothing effect on the data. The IDW simply applies different

weights to the measured data depending on their distance from an assumed interpolation point, i.e. the further away from such a point the less weight is given to the data. Two main parameters to be considered on the smoothing process are the number of data considered for IDW interpolation at each interpolation point (*N*) and the minimum distance (*D*). The parameter *N* is intended to ensure that sufficient data are considered for each interpolation point. Generally, as *N* is increased more data are used to calculate the velocity at each interpolation point and the velocity distribution is smoothed. Beyond a certain value of *N*, further increase in this parameter will have little noticeable effect on the trend of velocity distribution (Le Coz, 2007). The second parameter *D* also effects the smoothing of the velocity and is introduced in order to reduce the peaking and/or plateauing of the interpolated data when the source data are near to the interpolated point. The parameter *D* reduces the weighting factor of source points located within the radius of *D* by applying the value of *D* instead of their actual distance to the interpolation point (Figure 4.26). The effect of changing these two parameters is illustrated in Section 4.6.3.

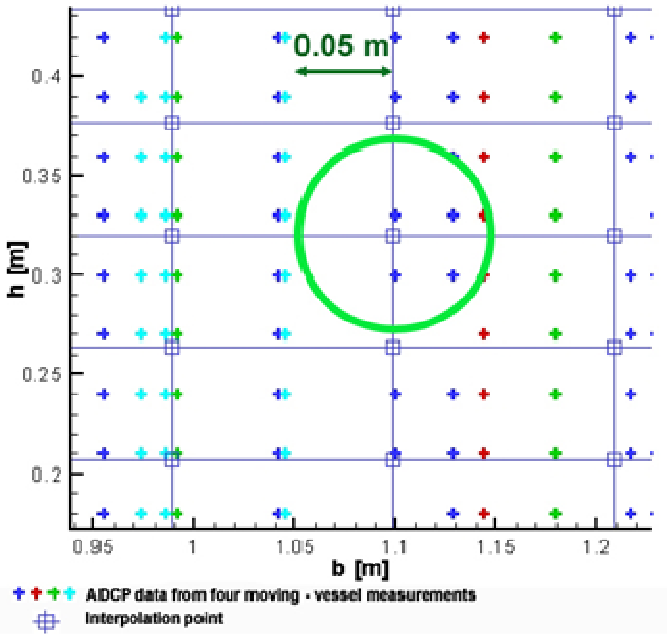

Figure 4.26 Minimum distance for the IDW interpolation.

The methodology for averaging the transects is shown in Figure 4.27 and explained in detail as follows. Firstly, the bottom profile and velocity data were extracted from each transect (step 2 & 3). At this stage, the bottom profiles of the transects might be not in the same horizontal position referenced with each other. Thus, the bottom profiles should first be brought to the same reference by shifting the horizontal position of the transects. This will also bring the velocity data to the same

reference. At the same time, a structured-rectangular mesh with a similar dimension to that of the transects was created (4). The next step was to compute the deepest bin from all transects and average them using the IDW interpolation (5). The weighting parameter of each source point for the IDW interpolation was computed using the formula:

$$w_i = \frac{1}{d_i^{\,E}} \tag{4.10}$$

where:

w_i = weighting parameter point i to the interpolation point (m^{-2})

d_i = distance of point i to the interpolation point (m)

E = exponent, 2 is used in this research (m)

Then the velocity data from all transects were also interpolated to the rectangular mesh using the same method (6). The adjustment of parameter *N* and *D* takes place in this step (6). There are two sets of data at this stage: a deepest bin line and a rectangular mesh containing the IDW-interpolated velocity data. The next step is to remove the area below the deepest bin from the rectangular mesh (7). This will create a mesh that represents the ADCP-measured region in the cross section (8) (Figure 4.28). The discharge from this mesh is then computed and compared to the initial discharge. Since the bin size of the mesh is uniform, the discharge is computed by adding together all the bin velocities, then multiplying it by the bin size and the number of bins in the mesh.

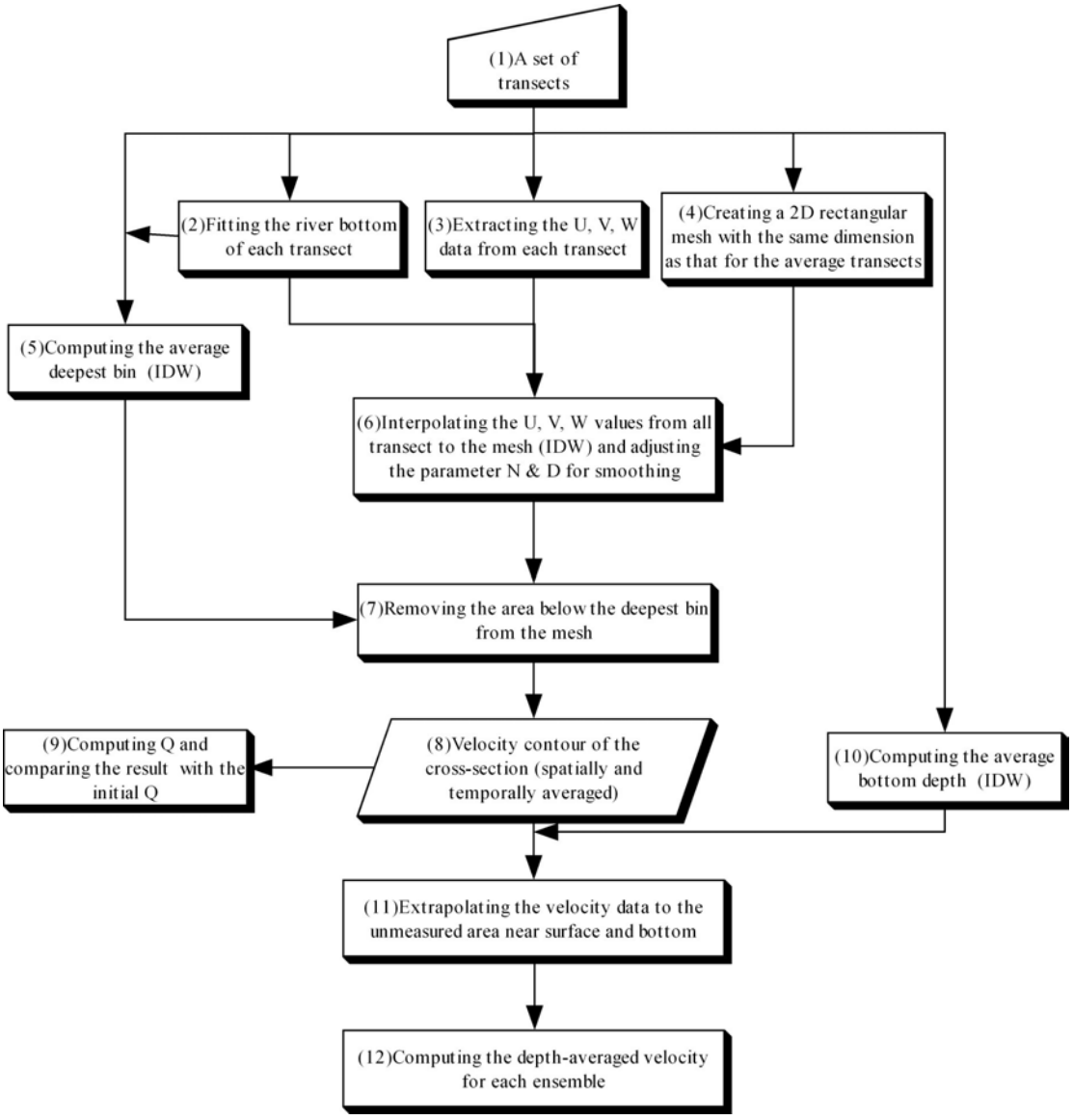

Figure 4.27 Methodology of transect velocity averaging for the current research.

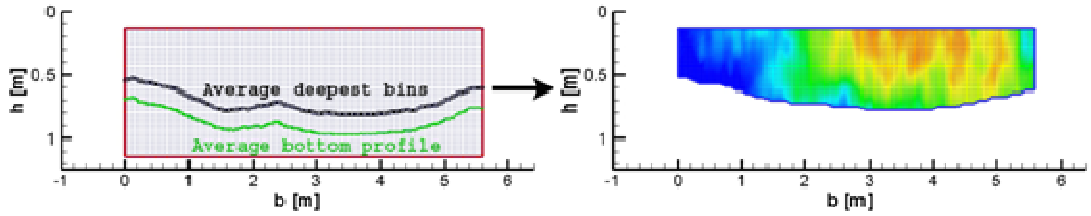

Figure 4.28 Interpolation domain mesh (left), the domain after interpolation & removal of area below deepest bins (right).

The calibration of numerical models in this research was undertaken by comparing the lateral distribution of depth-averaged velocity between transects from the river and in various models. In order to obtain the depth-averaged velocity, a set of transect data was averaged using transect

averaging methodology and the depth-averaged velocity distribution obtained by integrating the transect averaging result over the depth. Extrapolation of the velocity profiles was required for the unmeasured area near the water surface and bottom of the river. The methods for extrapolation used were constant value for the area near the water surface and linear interpolation to zero for the area near the bottom. While the distance from the first bin and the water surface was already fixed, the distance between the deepest bins and the local river bottom still needed to be determined for each ensemble. A Visual Basic program was created to automate the extrapolation and depth-averaging process. A further two Visual Basic programs were also written to speed up the processes. These programs perform input/output conversion from spreadsheet and Tecplot (and vice versa), remove the area below the average deepest bins from the mesh and calculate the discharge on the mesh.

4.6.3 An example using data from the River Blackwater

This section illustrates how the above techniques and equipment have been applied to CS 2 of the River Blackwater. Figure 4.29a indicates a view of CS 2 on 16th January 2008. At 08:00 the discharge reading from the electromagnetic gauging station suggested that the flow was 2.50m^{3}s^{-1} and subsequent readings and visual observation indicated that the stage fell throughout the day (Figure 4.29b). Two sets of transects measurements were undertaken using the ADCP at 11:27 and 11:43 and indicated discharge values of 2.30 and 2.13m^{3}s^{-1} respectively. Interpolating the corresponding discharge values from the electromagnetic gauging station data yields values of 2.18 and 2.16m^{3}s^{-1} for 11:27 and 11:43 respectively. Hence the ADCP values and the gauging stations differ by 5.5% and -1.0% respectively, which for the purposes of the current work is considered acceptable.

The data collected at 11:43 is now used to demonstrate the effect of the post processing techniques outlined above. Figure 4.30 gives a visual interpretation of the three different size meshes that were used in the current investigation. For the example outlined below, the value of parameter *N* is set to 64. Table 4.6 illustrates the results of using these different mesh sizes with a constant value of *D* = 0. In Table 4.6, the first column refers to the mesh size adopted, the second column refers to the interpolated discharge using the IDW technique, while the final column illustrates the percentage error between the calculated and the measured discharge, i.e. 2.13m^{3}s^{-1}. It is interesting to note that as the mesh size increases the error between the interpolated discharge and the measured discharge decreases from 2.9% to -1.0%, suggesting that in this case a mesh size between 100 x 13 and 200 x 26

would be appropriate in order to minimise the error. It is perhaps worth noting that altering the mesh size may also alter the cross sectional area since the resolution at the channel bed is changed. However, for the mesh size investigated here, such changes will have a minimal impact on the value of *Q*.

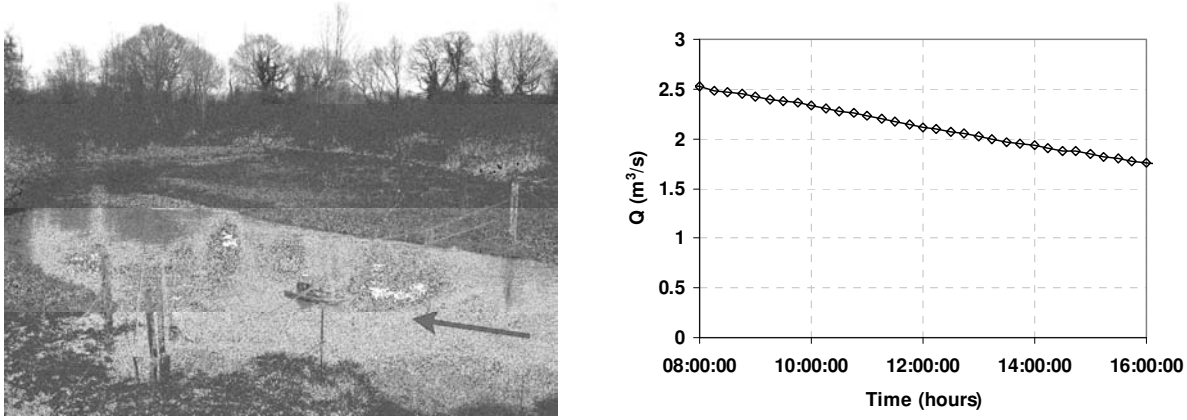

(a) View of cross section with ADCP deployed. (b) Hydrograph corresponding to measuring period.

Figure 4.29 A view of CS2 on the corresponding hydrograph for the 16th January 2008.

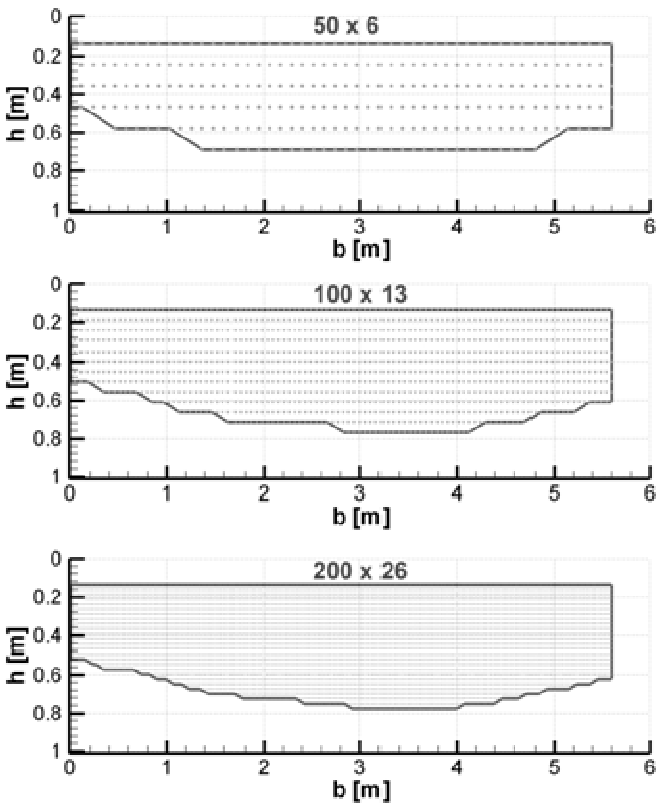

Figure 4.30 Examples of three possible interpolation meshes.

Mesh Size	Interpolated Q (m^3s^{-1})	Error (%)
50 x 6	2.19	2.9
100 x 13	2.14	0.7
200 x 26	2.11	-1.0

Table 4.6 A comparison between the discharges computed using the WinRiver 2 and interpolation data (in all cases D = 0).

Figures 4.31 - 4.33 illustrate the effect of increasing the mesh size on the streamwise, lateral and vertical velocity components respectively. In all cases it can be observed that increasing the mesh size not only increases the resolution of the velocity data, but results in a less smooth distribution. However, as indicated above, it is important to consider the minimum distance, D, which will yield appropriate results in addition to the mesh size. Figure 4.34 illustrates the results of increasing the minimum distance on a fine mesh. Figure 4.34 indicates that as D is increased the local peaks in the velocity distribution are smoothed and a more uniform distribution is obtained. This smoothing has a small effect on the calculated discharge with values of $2.04m^3s^{-1}$ obtained for $0 \leq D \leq 0.05$ and $2.03m^3s^{-1}$ for $0.1 \leq D \leq 0.8$. As a result of the trade off between velocity detail and discharge value a mesh size of 200 x 26 with a D value of 0.05 was adopted for the current work. Experience has shown that these values enable the velocities to be smoothed while still retaining the important flow features. However, it is acknowledged that for different sized rivers, different values may be required.

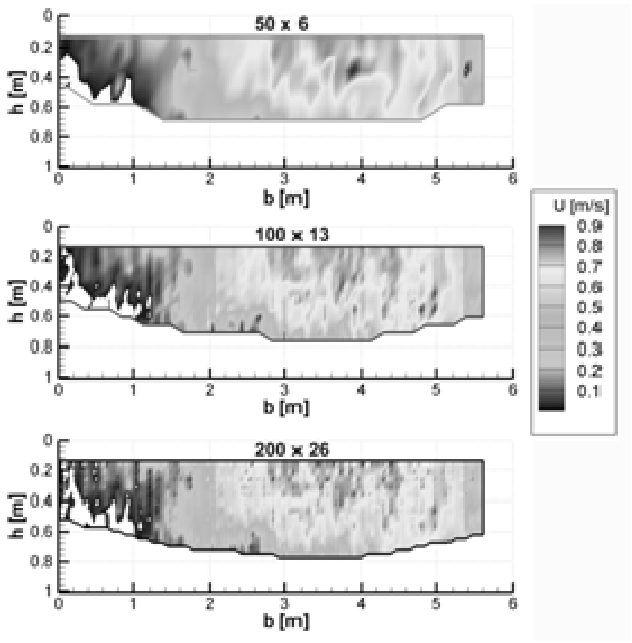

Figure 4.31 Effect of increasing the mesh size on the streamwise velocity distribution.

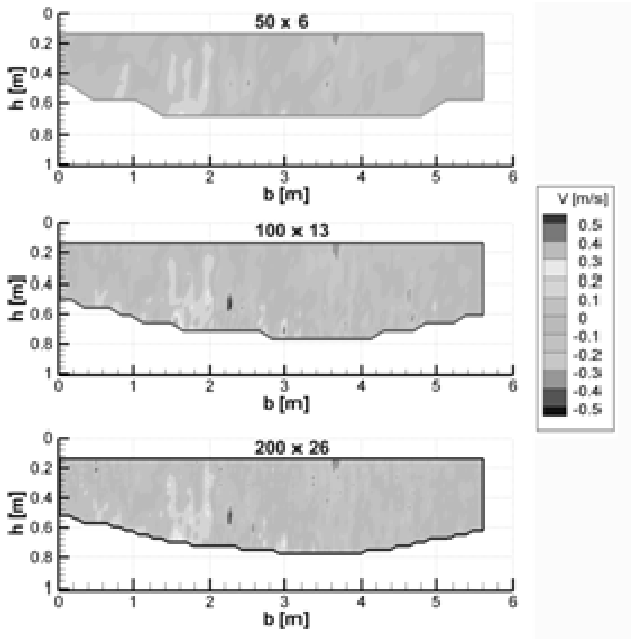

Figure 4.32 Effect of increasing the mesh size on the lateral velocity distribution.

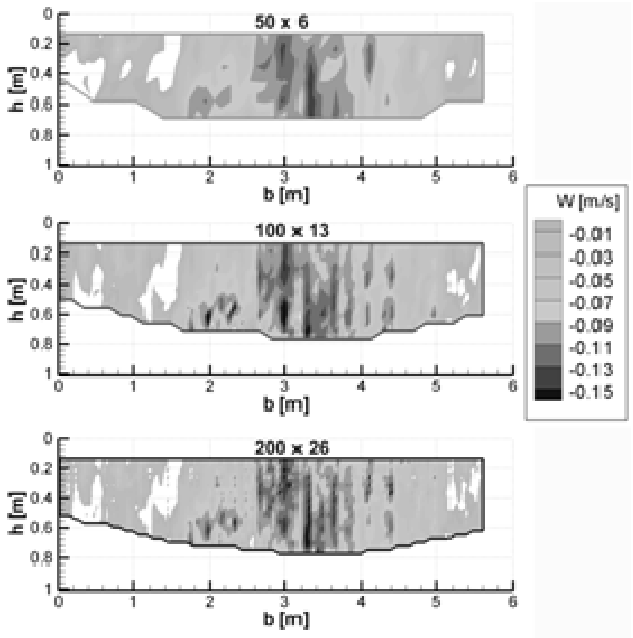

Figure 4.33 Effect of increasing the mesh size on the vertical velocity distribution.

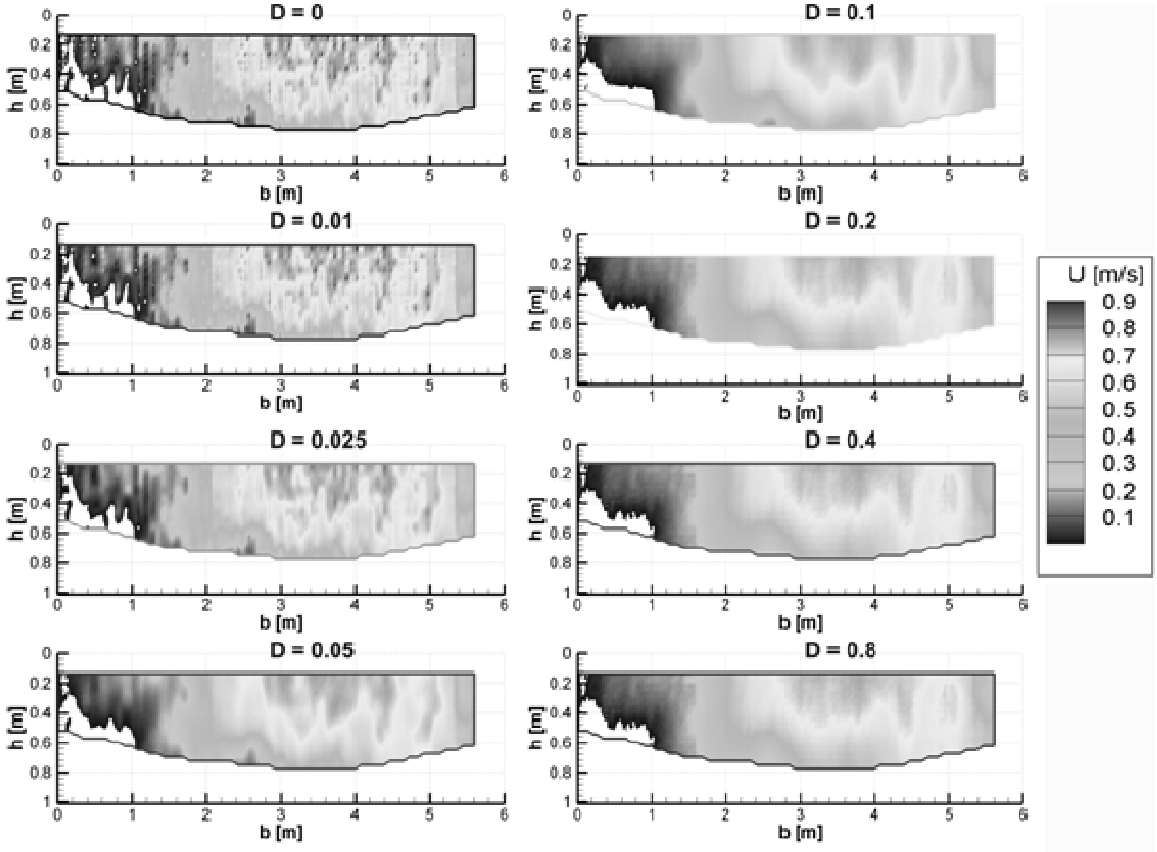

Figure 4.34 Effect of varying D on the streamwise velocity for a mesh size of 200 x 26.

Figure 4.35a indicates the distribution of depth averaged velocity for an interpolation mesh size of 200 x 26 with a minimum distance of 0.05m. Also shown in Figure 4.35a are five data points which were obtained from a series of stationary measurements extending over a period of five minutes. The results of Figure 4.35a are encouraging, and illustrate consistency between the data obtained from the stationary measurements and those obtained from the measurement protocol outlined above, combined with the IDW post processing technique; the sum of the squares of the difference between the stationary and transect data is 0.002. The distribution of bottom profiles in Figure 4.35b shows a good agreement between bottom level obtained from transverse and stationary measurements.

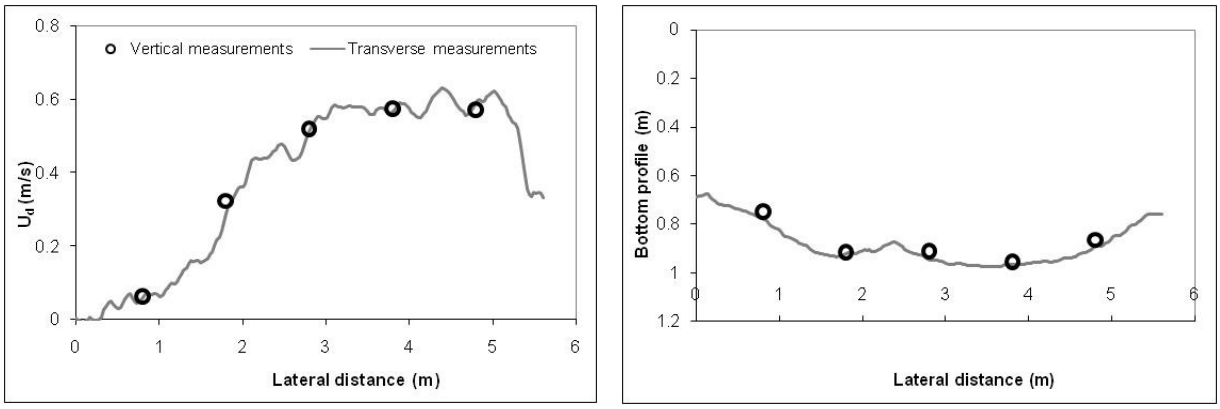

(a) Distribution of streamwise velocity (b) Distribution of bottom profile

Figure 4.35 The distribution of depth averaged streamwise velocity and bottom profiles for CS2 on the River Blackwater. Data obtained on the 16th January 2008.

4.7 Characteristics of the ADCP velocity data

The convergence of the ADCP velocity data obtained from stationary measurements in the River Blackwater was investigated. This is important as it shows whether the stationary measurements had sufficient accuracy to verify the ADCP velocity data obtained from the transverse measurements. The relationship between velocities and the corresponding standard deviations are analysed and velocity profiles obtained from ADCP measurements are compared to those obtained using an ADV.

4.7.1 Temporal averaging requirement to obtain statistically stable velocity data

There are two types of intrinsic errors in ADCP velocity data, i.e. random error/velocity fluctuation (see also section 4.8.1) and bias. Temporal averaging can reduce the effect of random errors present in instantaneous velocity data (Gordon 1989, Simpson 2003). Figure 4.24 indicates how temporal averaging can result in a more uniform velocity profile.

Time averaged velocity profiles obtained from stationary measurement have often been used to verify the velocity profiles obtained from transverse measurement (Muste *et al.*, 2004b; Szupiany *et al.*, 2007). However, as previously indicated, stationary measurements are time consuming. The averaging time to obtain stable streamwise velocity profiles depends on many variables, e.g. flow characteristics of the river, ADCP setting and the intrinsic factor of the instrument itself. A small summary of the suggested averaging time for various rivers, ADCP models and setting is presented in Table 4.7 to give a better overview on its magnitude.

In practice, often only a small number of stationary measurements can be undertaken (along a traverse) before the discharges changes. Hence, knowledge of the minimum averaging time is beneficial, since it enables more measurements to be undertaken while still giving adequate accuracy on the velocity profile. A variety of minimum averaging time has been reported. Stone & Hotchkiss (2007) reported that velocity profile becomes stable after 250s averaging (Table 4.7), after observing the convergence rate of velocity statistics (mean and standard deviation). Szupiany *et al.* (2007) reported stability velocity profiles at 420 to 600s averaging by observing the convergence rate of mean velocity in various bins (Figure 4.36). Furthermore, Barua & Rahman (1998) reported that turbulence intensity stabilises to a nearly constant value of about 300s averaging, or more (Figure 4.37). The effect of the non-stationarity due to large scale turbulence during an ADCP stationary measurement has been documented in several reports, e.g. Szupiany *et al.* (2007) shows the effect of large scale turbulence on velocity profiles recorded for 10 minutes in a large river (Figure 4.38).

Unfortunately, this type of averaging cannot address the issue of bias. ADCP single-ping random error can range from a few mms^{-1} to as much as $0.5ms^{-1}$ while bias is typically less than $0.01ms^{-1}$ (RDI, 1996).

Source	Stone & Hotchkiss (2007)	Szupiany *et al* (2007)	Barua & Rahman (1998)
Suggested averaging time	100 - 250s	420 - 600s	900s
River width	12.8 -15.4m	600 – 2,500m	~ 11,000m
River depth	0.75 – 1.1m	5 – 12m	8.3 - 10m
ADCP model	1200kHz RDI Rio Grande ADCP	1000kHz Sontek aDp	RDI Broadband ADCP
Sampling frequency	~1 pings/s	12 pings/s	~0.5 ping/s
Bin size	5cm	50 - 75cm	50cm
Max. boat movement	-	5m	3m

Table 4.7 Suggested averaging time by various researchers.

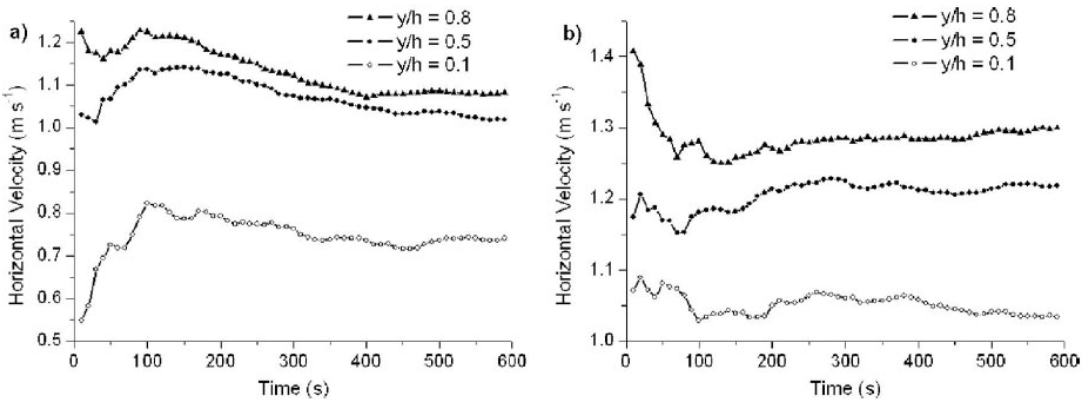

Figure 4.36 Cumulative mean velocities with respect to averaging time at two different locations (Szupiany *et al*., 2007).

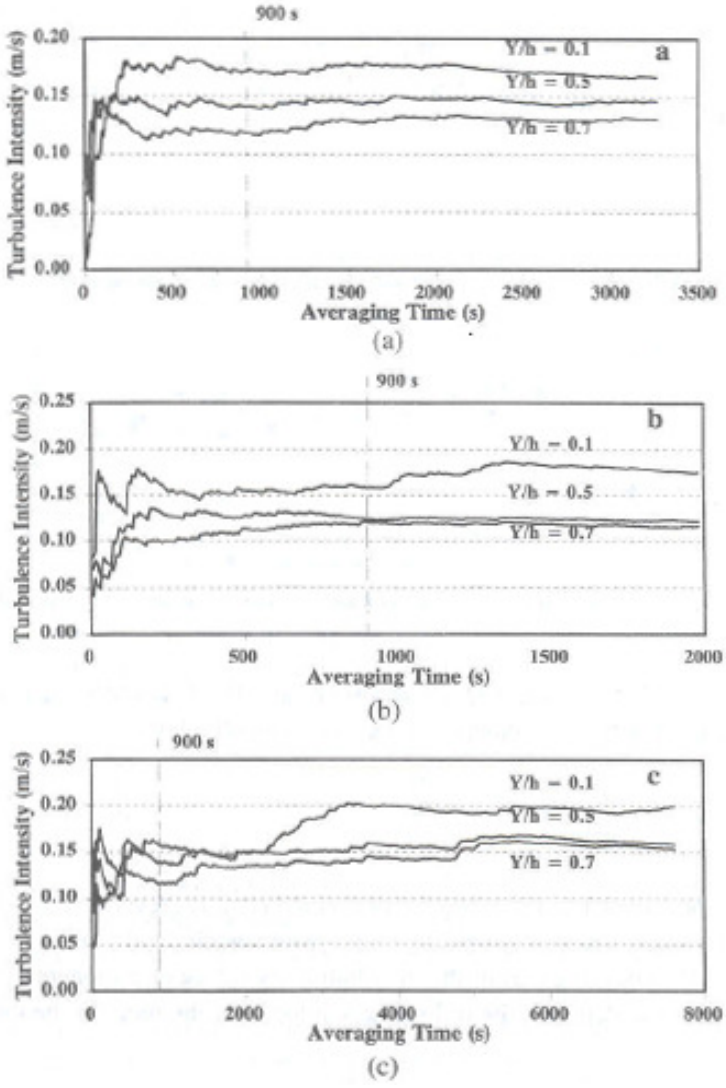

Figure 4.37 Turbulence intensity at various depth as a function of averaging time for different stations (Barua & Rahman, 1998).

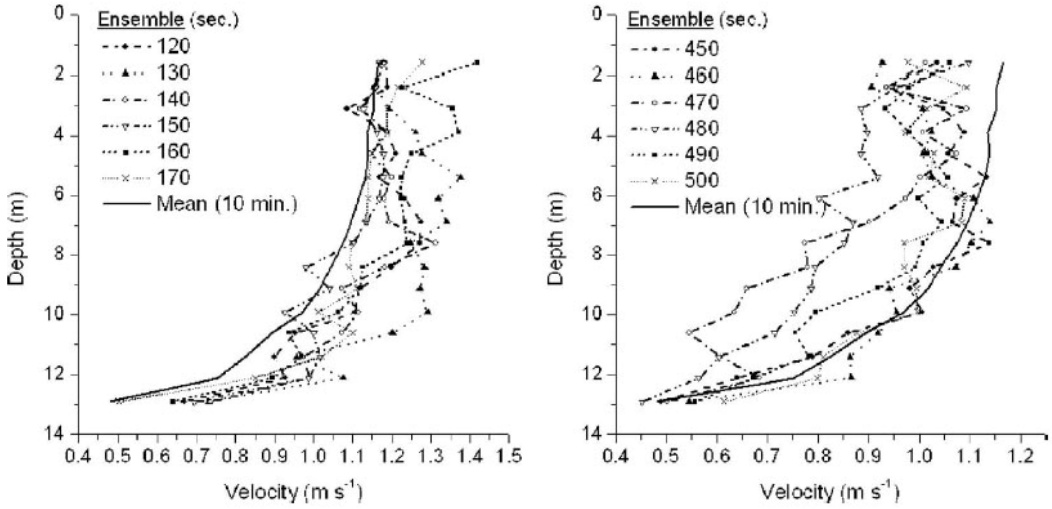

Figure 4.38 Effect of large-scale turbulence flow on velocity profiles for different stations (Szupiany *et al.*, 2007).

4.7.2 Dataset description

The datasets analysed in sections 4.7.3 - 4.7.8 are obtained from four stationary measurement campaigns during inbank, bankfull and overbank conditions (18/8/2008, 16/1/2008 and 10/2/2009 respectively) at cross sections 2 and 4. The discharge values from the four campaigns ranged from 0.283 to 4.473m^3s^{-1}. The typical cross sections profiles and stationary measurement locations are illustrated in Figure 4.39, and the conditions of the site during the measurements are shown in Figures 4.40 – 4.42.

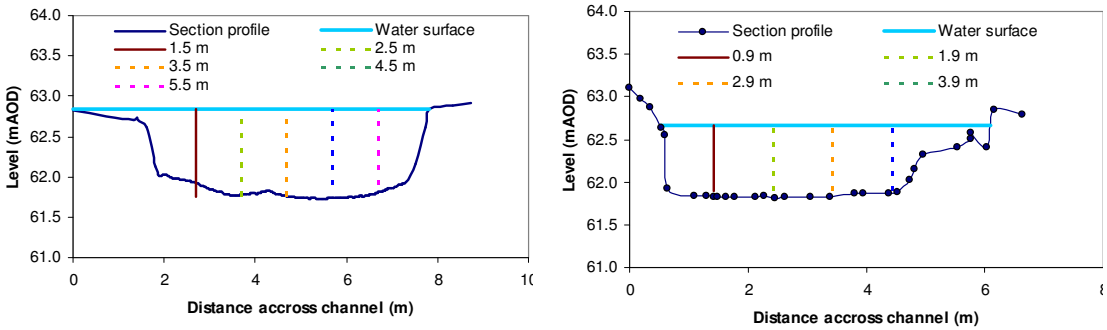

CS 2 CS 4

Figure 4.39 Stationary measurement locations during the 16/1/2008 measurements.

Figure 4.40 View of CS 2 at various dates.

Figure 4.41 View of CS 4 at various dates.

Figure 4.42 View of CS 1 during 10/2/2009 measurements.

4.7.3 Statistical stability of the streamwise velocity at various depths

Figures 4.43 and 4.44 illustrate the variation of the averaged streamwise velocity and the corresponding standard deviation for different averaging periods for the CS 2 inbank case. Similar figures for other cases are presented in Appendix I. The standard deviations of streamwise velocity were computed based on the following equation:

$$\sigma = \sqrt{\frac{\sum (x_i - \bar{x})^2}{(n-1)}} \tag{4.11}$$

where :

- σ = the standard deviation of n population
- x_i = velocity at i ensemble
- $\bar{x}$ = mean velocity from n population
- n = number of samples

Only data in bins 3 to 5 bins for each stationary measurement are presented in order to ease interpretation. In general, the average streamwise velocity with respect to averaging time (will be referred as U in throughout this chapter) for various depths becomes stable (i.e. does not appear to exhibit changes with respect to average time) within 300 seconds or less. There are bins in which U does not seem to become stable and converge to a constant value, which indicates a degree of non-stationarity of the flow at that particular bin position (e.g. bin 0.46m at a distance from the left bank

(*DL*) = 2.50m in Figure 4.43). However, the number of data contained in such bins is small and as such does not significantly affect the overall results.

Higher standard deviations of streamwise velocity tend to occur in bins near the channel bed for inbank and bankfull conditions, e.g. Figure 4.44. However, this was not observed during overbank flow, which can be attributed to the larger bin size used during overbank measurements that resulting in a larger averaging area. The magnitude of middle column standard deviation from all measurements was nearly half of that observed by Stone & Hotchkiss (2007) using a Rio Grande ADCP with also 5cm bin size (Table 4.8). This is somewhat surprising, since the Rio Grande ADCP is apparently more advanced than the StreamPro ADCP. The measurements were conducted in a river with similar depth to that of River Blackwater (see Table 4.8). Szupiany *et al.* (2007) reported a standard deviation of 0.067 to 0.139ms^{-1} for measurements in a large river using a Sontek aDp (Table 4.8). However, the bin sizes used for those measurements (50 and 75cm), were far larger than the ones used on the current project.

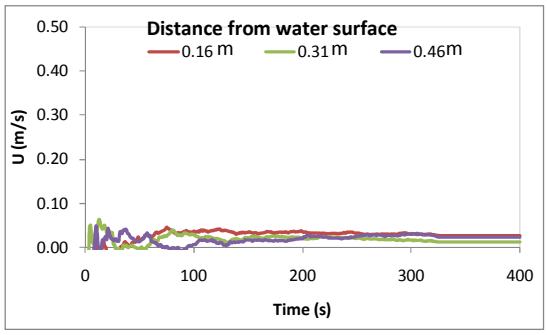

DL = 1.00m (U_d = 0.02ms^{-1})

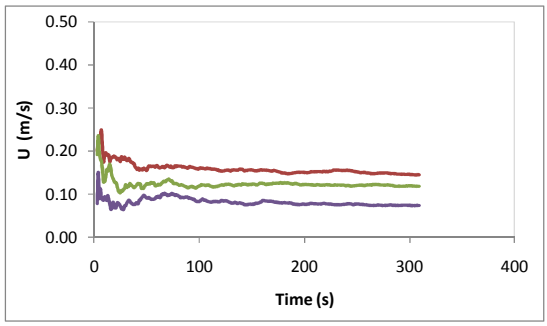

DL = 4.00m(U_d = 0.11ms^{-1})

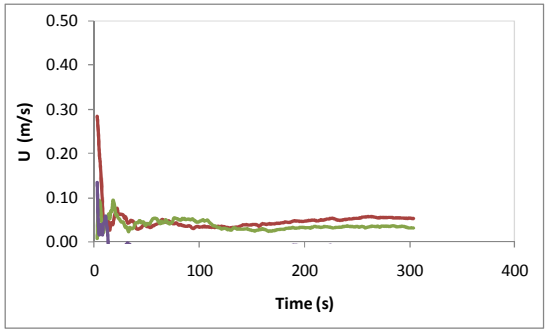

DL = 1.75m (U_d = 0.02ms^{-1})

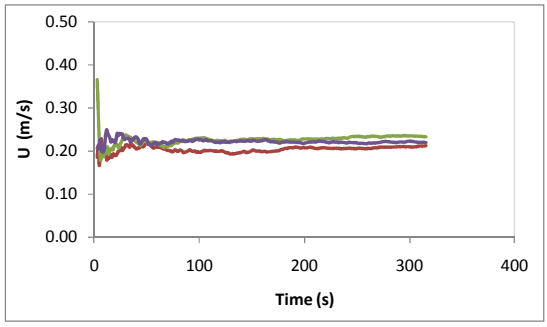

DL = 4.75m (U_d = 0.22ms^{-1})

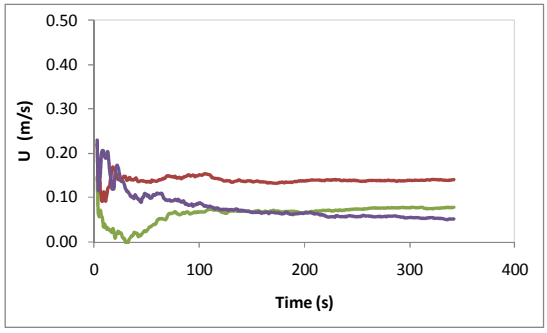

DL = 2.50m (U_d = 0.08ms^{-1})

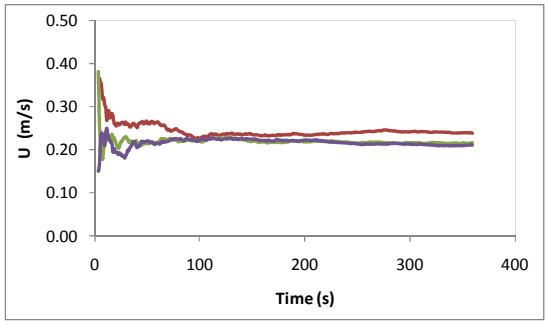

DL = 5.25m (U_d = 0.22ms^{-1})

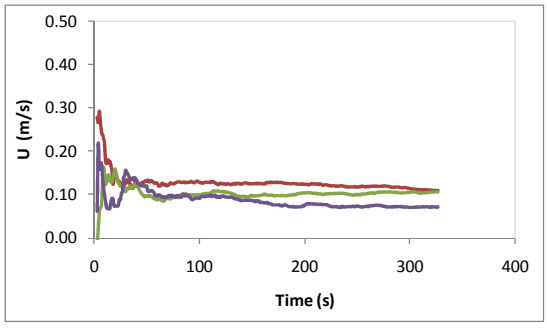

DL = 3.25m (U_d = 0.09ms^{-1})

Figure 4.43 Mean streamwise velocity at various depths with respect to averaging time, measured at various distances from left bank at CS 2 (18/08/2008 - inbank).

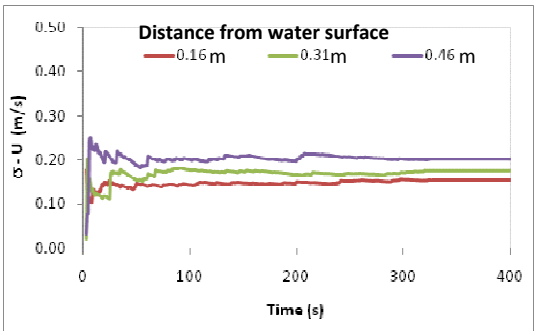

DL = 1.00m (U_d = 0.02ms^{-1})

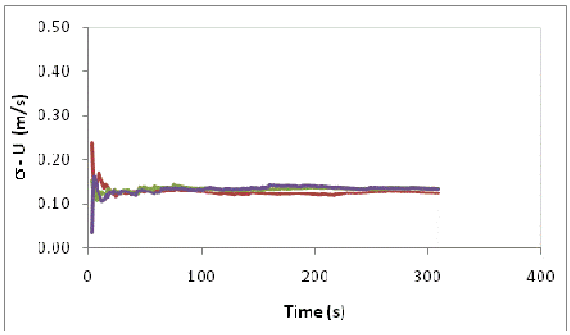

DL = 4.00m (U_d = 0.11ms^{-1})

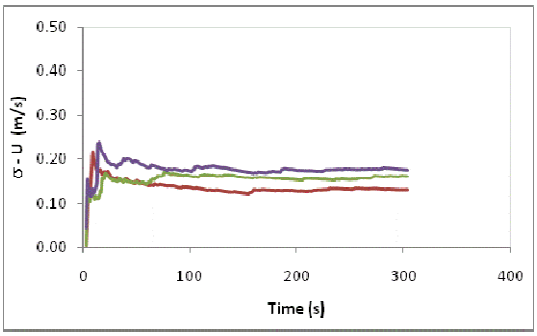

DL = 1.75m (U_d = 0.02ms^{-1})

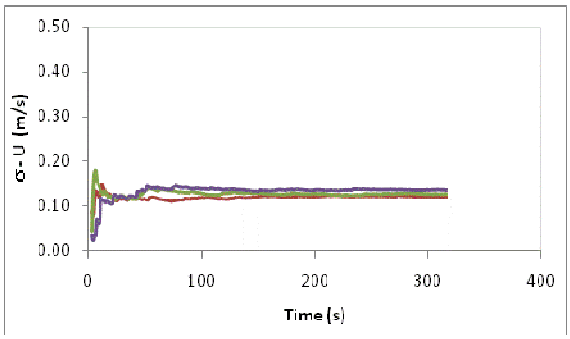

DL = 4.75m (U_d = 0.22ms^{-1})

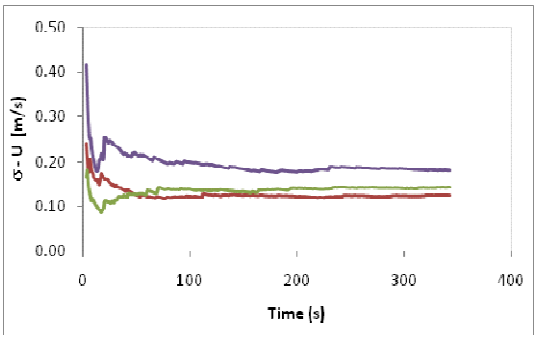

DL = 2.50m (U_d = 0.08ms^{-1})

4

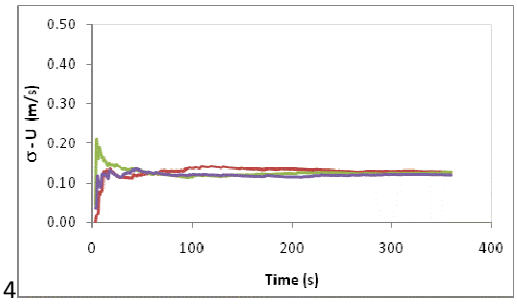

DL = 5.25 m (U_d = 0.22ms^{-1})

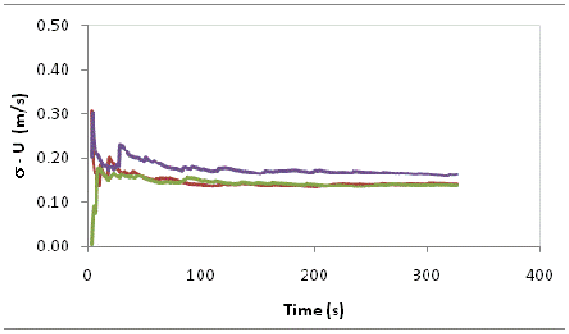

DL = 3.25m (U_d = 0.09ms^{-1})

Figure 4.44 Mean standard deviation of streamwise velocity at various depth with respect to averaging time, measured at various distances from left bank at CS 2 (18/08/2008 - inbank).

Source	Bin size (cm)	σ_{Ud} (ms^{-1})	U_d (ms^{-1})	ADCP model	Avg. time (mins.)
Stone & Hotchkiss (2007)	5cm	0.262 - 0.282	0.671 - 0.841	1200kHz RDI Rio Grande	20.
Szupiany *et al* (2007)	50cm	0.102 - 0.139	0.93 - 1.18	1000kHz Sontek aDp	10
	75cm	0.067 - 0.089	1.01 - 1.20	1000kHz Sontek aDp	10
Marsden (2005)	3cm	0.18	0.30	2400kHz RDI StreamPro	n/a
	5cm	0.14	0.30	2400kHz RDI StreamPro	n/a
	7cm	0.11	0.30	2400kHz RDI StreamPro	n/a
	10cm	0.08	0.30	2400kHz RDI StreamPro	n/a

Table 4.8. Standard deviation of ADCP velocity observed by several researchers.

4.7.4 Statistical stability of depth-averaged velocity in three directions

In general, an averaging time of 300s appears to be adequate to stabilize the depth-averaged velocity all three directions and their corresponding standard deviations at various lateral distances in cross sections 2 and 4 (Figure 4.45 and Appendix II). The standard deviation of horizontal velocities is generally within the range of 0.1 to 0.2ms^{-1} while the standard deviation of vertical velocities is generally 2 to 4 times lower. In some of the cases for inbank and bankfull flows, there is tendency that the standard deviations of U_d, V_d and W_d are higher at lower U_d magnitudes (Figure 4.45, Appendices II-1, II-2 and II-3). However, this tendency is more difficult to identify during overbank flows, e.g. at *DL* = 4.35m in Appendix II-3, the standard deviations of the horizontal velocities are nearly 1.5 times those at other locations in the cross section. Furthermore, the general trend of *U* with respect to time is similar to the trend of its averaged depth-averaged value (Figure 4.45). This is also valid for the other cases in both cross sections (Appendices II-1 to II-5).

The magnitudes of depth-averaged streamwise velocity and the corresponding standard deviation at 300s averaging, $\overline{U_{d\_300}}$ and $\overline{\sigma_{U_{d\_300}}}$ are presented in Tables 4.9 – 4.14. The values of $\overline{\sigma_{U_{d\_300}}} / \overline{U_{d\_300}}$ at 300s averaging range from 12 to 1008%. However, values of this parameter greater than 100% are only found to occur when $\overline{U_{d\_300}}$ is less than or equal to 0.13ms^{-1}. In general, $\overline{\sigma_{U_{d\_300}}}$ tends to decrease at a very small rate with the increase in $\overline{U_{d\_300}}$. As a consequence, $\overline{\sigma_{U_{d\_300}}} / \overline{U_{d\_300}}$ becomes larger at low velocities. The parameter $\overline{\sigma_{U_{d\_300}}} / \overline{U_{d\_300}}$ gradually decreases with $\overline{U_{d\_300}}$ and stays under 22% for $\overline{U_{d\_300}}$ ≥ 0.68 ms^{-1}. For 0.22 < $\overline{U_{d\_300}}$ <0.57 ms^{-1} the value of $\overline{\sigma_{U_{d\_300}}} / \overline{U_{d\_300}}$ varies from 59 to 27%.

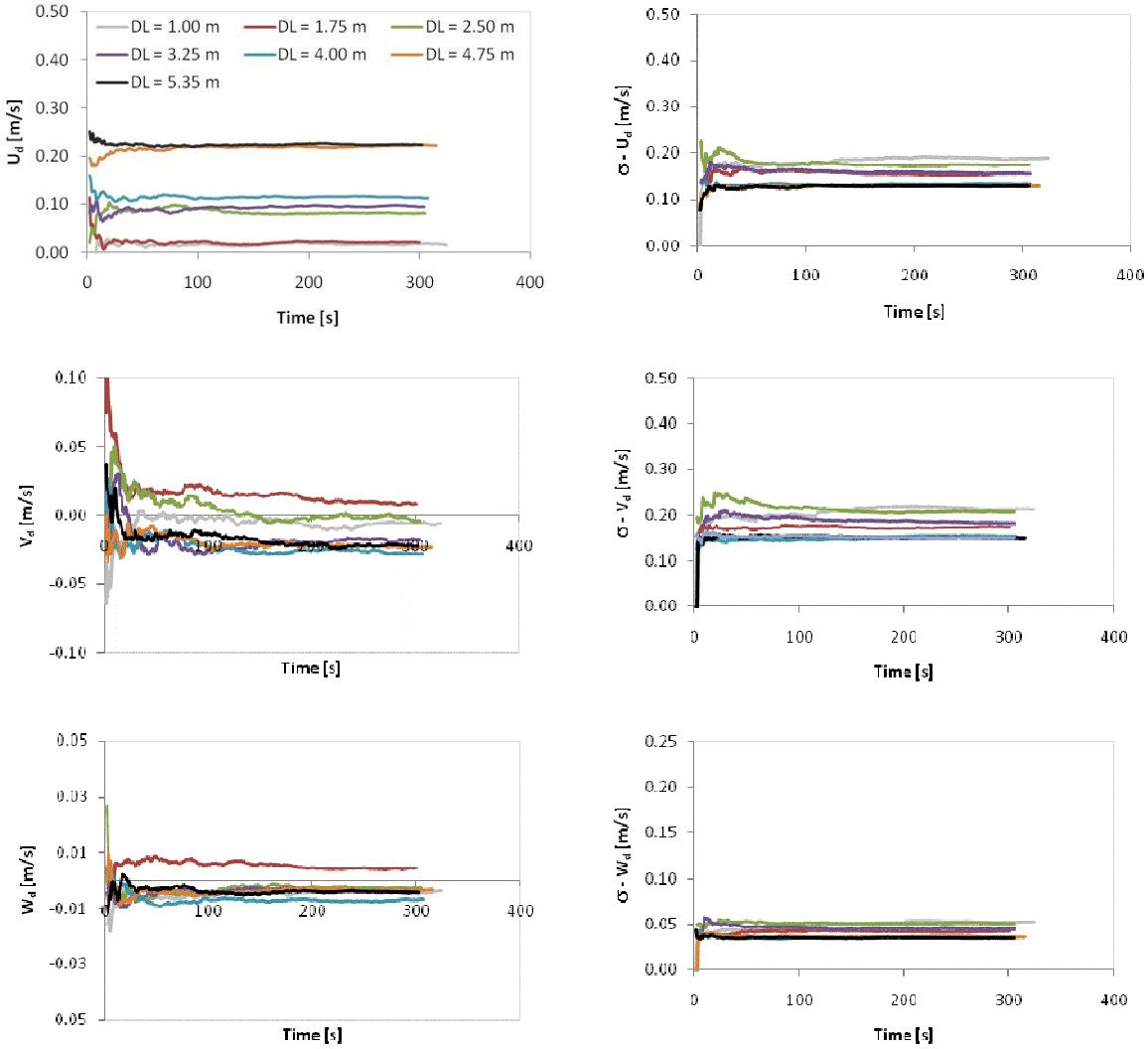

Figure 4.45 Mean U_d, V_d and W_d (left) and their standard deviation (right), with respect to averaging time, measured at various distances from left bank at CS 2 (18/08/2008 - inbank).

DL (m)	U_d (ms^{-1})	σ_{Ud} (ms^{-1})	σ_{Ud}/U_d (%)
1.00 m	0.02	0.19	1008
1.75 m	0.02	0.16	728
2.50 m	0.08	0.17	214
3.25 m	0.09	0.16	166
4.00 m	0.11	0.14	120
4.75 m	0.22	0.13	58
5.35 m	0.22	0.13	58

Table 4.9 Ratio of mean standard deviation and mean velocity after 300s averaging for velocity in streamwise direction for CS 2 data (18/8/2008 - inbank).

DL (m)	U_d (ms^{-1})	σ_{Ud} (ms^{-1})	σ_{Ud}/U_d (%)
1.50 m	0.07	0.16	213
2.50 m	0.38	0.17	44
3.50 m	0.68	0.13	19
4.50 m	0.72	0.13	18
5.50 m	0.69	0.12	18

Table 4.10 Ratio of mean standard deviation and mean velocity after 300s averaging for velocity in streamwise direction for CS 2 data (16/1/2008 - bankfull).

DL (m)	U_d (ms^{-1})	σ_{Ud} (ms^{-1})	σ_{Ud}/U_d (%)
3.35 m	0.18	0.11	61
4.35 m	0.41	0.14	35
5.35 m	0.84	0.10	12
6.35 m	0.95	0.11	11
7.35 m	0.87	0.11	12

Table 4.11 Ratio of mean standard deviation and mean velocity after 300s averaging for velocity in streamwise direction for CS 2 (10/2/2009 - overbank).

DL (m)	U_d (ms^{-1})	σ_{Ud} (ms^{-1})	σ_{Ud}/U_d (%)
1.30 m	0.11	0.14	123
2.05 m	0.13	0.14	109
2.80 m	0.25	0.13	52
3.55 m	0.22	0.13	59
4.30 m	0.04	0.16	363

Table 4.12 Ratio of mean standard deviation and mean velocity after 300s averaging for velocity in streamwise direction for CS 4 data (18/8/2008 - inbank).

DL (m)	U_d (ms^{-1})	σ_{Ud} (ms^{-1})	σ_{Ud}/U_d (%)
0.90 m	0.39	0.17	44
1.90 m	0.73	0.15	21
2.90 m	0.79	0.14	18
3.90 m	0.36	0.15	43

Table 4.13 Ratio of mean standard deviation and mean velocity after 300s averaging for velocity in streamwise direction for CS 4 data (16/1/2008 - bankfull).

DL (m)	U_d (ms^{-1})	σ_{Ud} (ms^{-1})	σ_{Ud}/U_d (%)
1.50 m	0.39	0.14	36
2.25 m	0.57	0.15	27
3.00 m	0.75	0.13	18
3.75 m	0.77	0.14	18
4.50 m	0.52	0.18	35

Table 4.14 Ratio of mean standard deviation and mean velocity after 300s averaging for velocity in streamwise direction for CS 4 (10/2/2009 - overbank).

4.7.5 Convergence level with respect to averaging time

For quantitative measure, the convergence of $\overline{U_d}$ with respect to averaging time was computed using convergence levels of 1, 5, 10 and 20%. The convergence in this thesis is defined as a condition where the difference between $\overline{U_d}$ and $\overline{U_{d\_300}}$ in at least 20 consecutive ensembles are within the convergence level and last until the 300th s. Figures 4.46 and 4.47 show the convergence $\overline{U_d}$ and $\overline{\sigma_{U_{d\_300}}}$ with respect to time for various convergence levels. The data illustrates an exponential type relationship between convergence time and the magnitude of $\overline{U_d}$ (see also Tables 4.9 – 4.14).

The $\overline{U_d}$ in all measurement locations in both sections satisfy the 5% convergence level except for *DL* = 1.00m at section 2 (inbank) where $\overline{U_d}$ is extremely low (0.02ms^{-1}). The maximum $\overline{\sigma_{U_{d\_300}}}/\overline{U_{d\_300}}$ was also observed at the same location (1008%). A convergence level of 1% was achieved by all data with $\overline{U_{d\_300}}$ ≥ 0.68ms^{-1} with less than 150s averaging time. The same convergence level was also achieved by data with 0.22 ≤ $\overline{U_{d\_300}}$ ≤ 0.68ms^{-1} within 300 s averaging time, except at one case at *DL* = 0.90m at section 4 (bankfull). From 12 measurements with $\overline{U_{d\_300}}$ ≤ 0.22ms^{-1}, only 7 converge within the 1% limit. In most cases, the convergence time decreases rapidly from 1 to 5%.

The rapid decrease of convergence time from 1 to 5% level was also observed for $\overline{\sigma_{U_{d\_300}}}$. Only in one case does $\overline{\sigma_{U_{d\_300}}}$ not fulfil the 1% convergence level criterion (*DL* = 7.35m at section 2-overbank), although it does converge in the last 13s of the 300s measurement. The movement of the ADCP boat during the measurement period could possibly be the reason for this; according to the

ADCP bottom track, the boat was displaced by 1.5m during the 366s measurements. It is probable that this movement was caused by high level of turbulence in that area (interface between main channel and floodplain). The movement of the ADCP did not appear to be caused by a "moving bed" condition since ADCP movement was not in an upstream direction (which happens during a moving bed). The ADCP bottom track during the corresponding measurement is shown in Figure 4.48. The fact that there is similarity in characteristics between measurements, i.e. (almost) all $\overline{\sigma_{U_{d\_300}}}$ converge within 300s is not surprising since the magnitude of $\overline{\sigma_{U_{d\_300}}}$ in all measurements are always within a certain range, i.e. 0.11 to 0.19ms^{-1}.

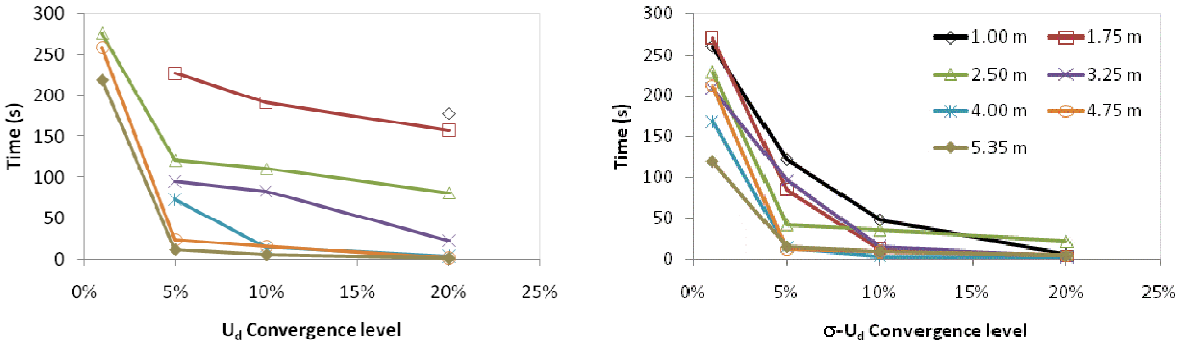

(18/8/2008 - inbank).

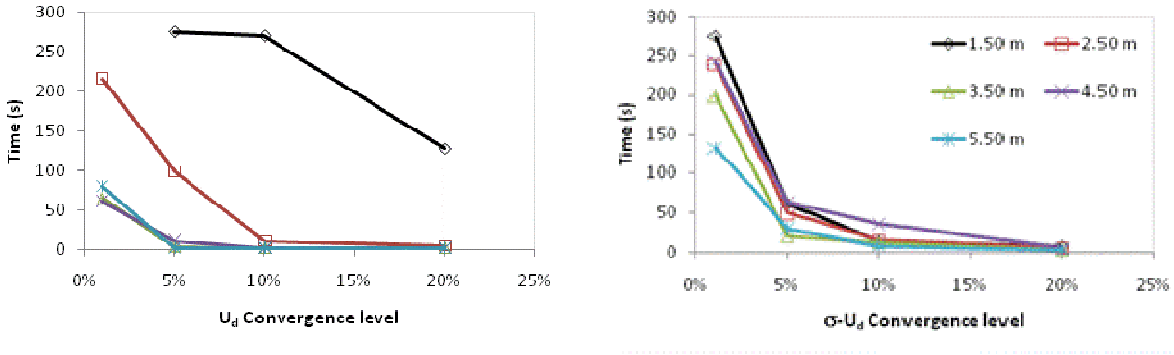

(16/1/2008 - bankfull).

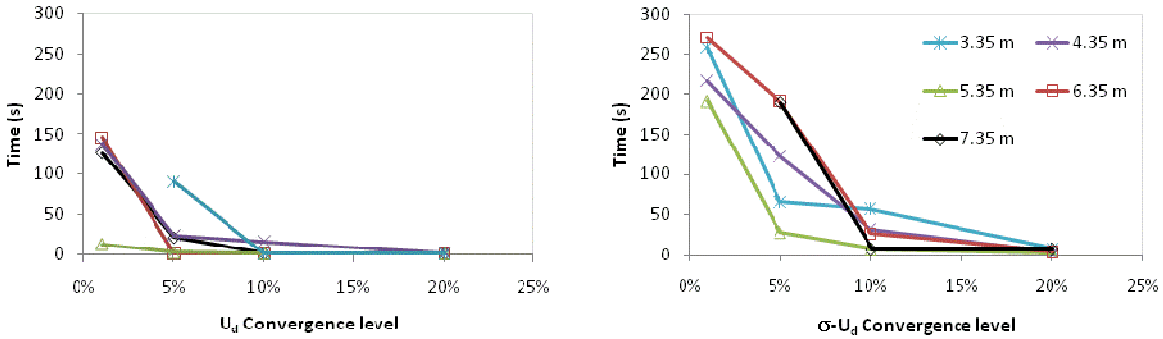

(10/2/2009 - overbank).

Figure 4.46 Convergence time for depth-averaged streamwise velocity (left) and its corresponding standard deviation (right) at various distances from left bank at CS 2.

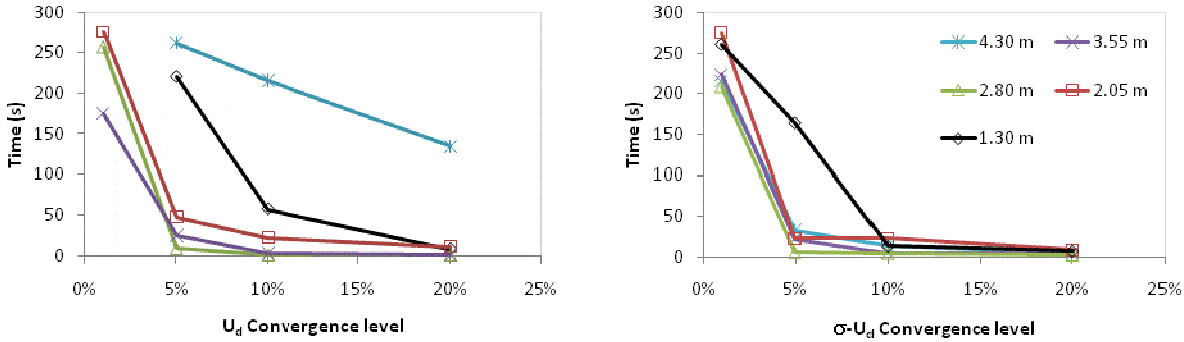

(18/8/2008 - inbank).

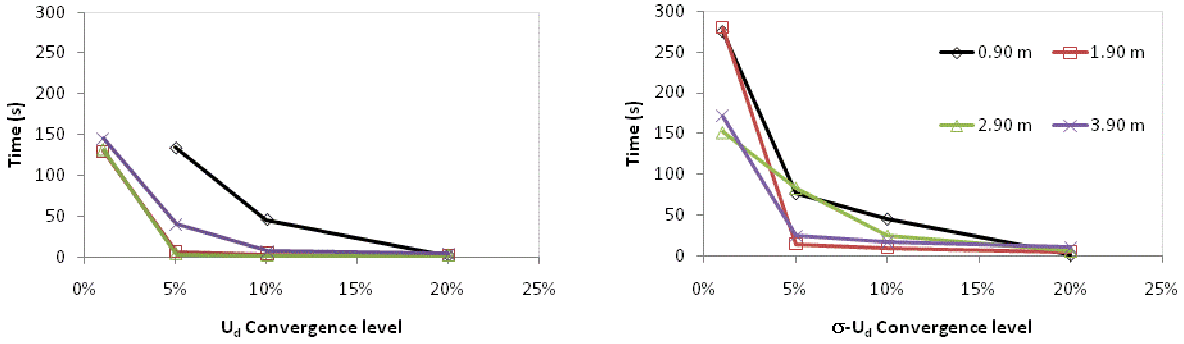

(16/1/2008 - bankfull).

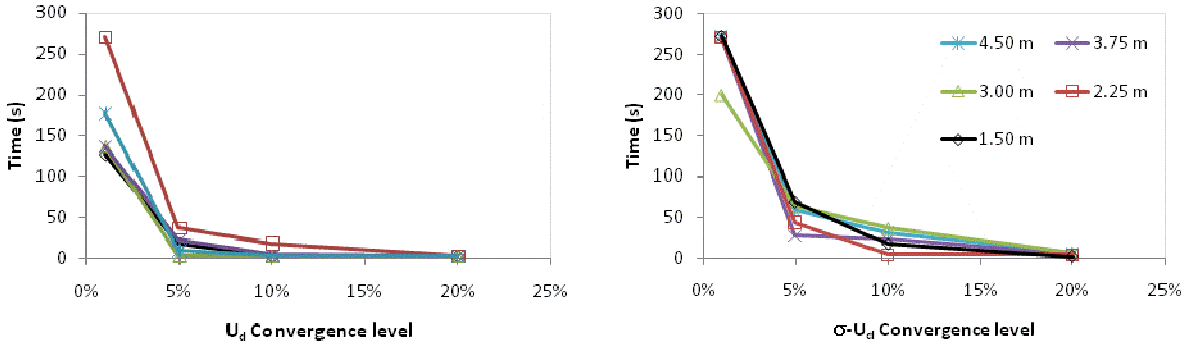

(10/2/2009 - overbank).

Figure 4.47 Convergence time for depth-averaged streamwise velocity (left) and its corresponding standard deviation (right) at various distances from left bank at CS 4.

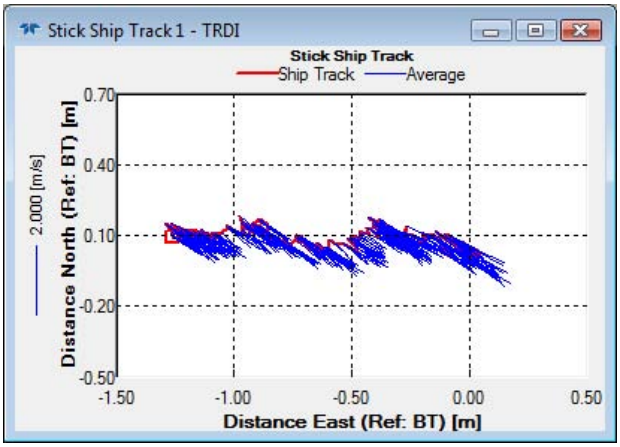

Figure 4.48 ADCP bottom track (red) and velocity direction (blue) at *DL* = 7.35m in CS 2 during overbank condition (10/2/2009).

4.7.6 Relationship of standard deviation and depth-averaged streamwise velocity magnitude

In order to examine the relationship between $\overline{U_{d\_300}}$ and $\overline{\sigma_{U_{d\_300}}}$, Figures 4.49 to 4.50 were constructed. Figure 4.49 shows that $\overline{\sigma_{U_{d\_300}}}$ decreases with increase of $\overline{U_{d\_300}}$. Additional data measured in 13/6/2008 were incorporated to the dataset being analysed. The somewhat higher $\overline{\sigma_{U_{d\_300}}}$ value on the 13/6/2008 measurements compared to that on 18/8/2008 indicates that there is greater variability of $\overline{\sigma_{U_{d\_300}}}$ value at low $\overline{U_{d\_300}}$ values.

Figure 4.50 shows the curve fitting for the data, excluding the overbank data which has a higher bin size. Three approaches were adopted: log fit, power fit and exponential fit. The data were also extrapolated using the three methods in order to illustrate their trend for higher discharge value. However, it is acknowledge that such prediction might not be accurate. All three trendlines indicate high variability to the data set values since their coefficient of determination values (R^2) are less than 0.5. Due to this, two additional lines indicating the trendline value of ± 25% were constructed for each graph. Most of the data points are located within the two additional lines, except for a few points with the exponential regression. The exponential regression predicts that the value of $\overline{\sigma_{U_{d\_300}}}$ is significantly lower than the other regressions for high $\overline{U_{d\_300}}$ values. There are difficulties in verifying this prediction since obtaining data at high water velocities is dangerous. However, the author tried to make comparison with transverse measurements at high *U* values. Data from two

transects, obtained during an flood event in the River Teme, UK, were used to investigate the value of $\overline{\sigma_U}$. A Rio Grande ADCP with a 50cm bin size was used for these measurements. Velocities of around 3ms^{-1} were recorded in some parts of the channel for 200 to 350 consecutive ensembles, along a 13m section of the river. The mean velocities of the various bins in this region range from 1.82 to 1.92ms^{-1}. The computed standard deviation from the corresponding velocity data ranges from 0.30 to 0.40ms^{-1}. The fact that the mean standard deviation is high indicates that the exponential regression might be less accurate than the log/power regression in representing the distribution of $\overline{\sigma_{U_{d\_300}}}$. However, it is noted that the bin size was 10 times larger than the bin size used in the River Blackwater

A logarithmic fit for the trend illustrated at CS 4 (Figure 4.51) indicates an increase of $\overline{\sigma_{U_{d\_300}}}$ with $\overline{U_{d\_300}}$, which contradicts the trend of the similar relationship at CS 2. However, this might be caused by high variability of the available data.

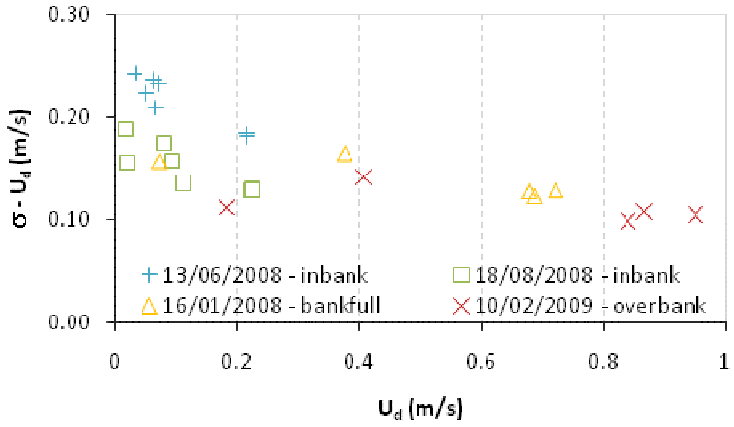

Figure 4.49 Relationship of $\overline{U_{d\_300}}$ and $\overline{\sigma U_{d\_300}}$ at CS 2 with 5cm bin size (10cm for the overbank measurement).

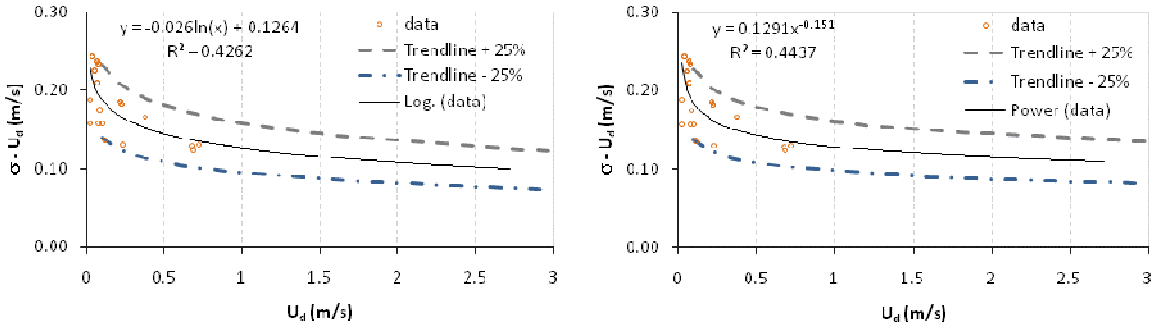

(a) Log fit (b) Power fit

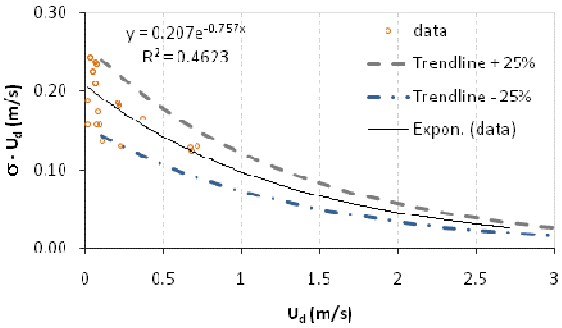

(c) Exponential fit

Figure 4.50 Curve fitting of CS 2 data with 5cm bin size.

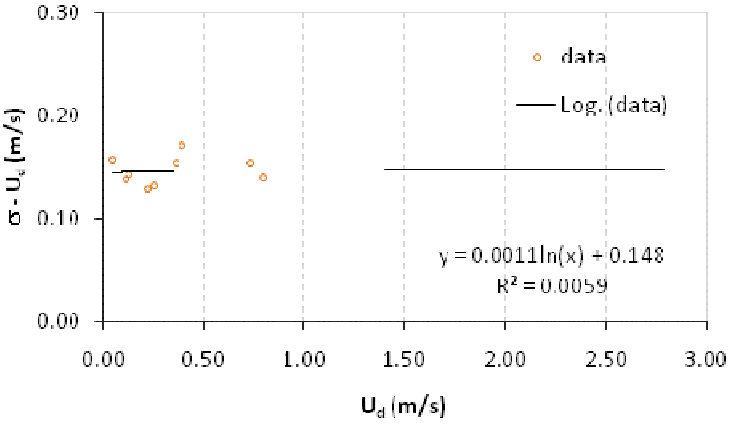

Figure 4.51 Curve fitting of CS 4 data with 5cm bin size (power fit).

4.7.7 Comparison of ADCP and ADV measurements

The velocity profile in a location near the thalweg of CS 4 obtained via the ADCP has been benchmarked with similar data obtained using an ADV. The ADCP measurements were conducted twice, before and after ADV measurements, in order to monitor any changes in discharge. The measurements campaign lasted for 100 minutes. During this time, the velocity data were collected

using ADCP and ADV for 800 and 300s respectively (see Figure 4.52a). The streamwise velocity magnitudes obtained using ADCP that are averaged over 300s have typically less than 2% difference to those averaged over 800s. Furthermore, an analysis of previous measurements indicates that 40s data sampling was required by the ADV to obtain stable mean velocity and standard deviation.

The results of the ADCP data indicated that on this occasion the discharge increased by 13% during the measurement period from 0.775 to 0.873m^3s^{-1}. Hence, an increase in streamwise velocity between the first ADCP transverse, the ADV measurements and the second ADCP transverse can be observed (see Figure 4.52b). Figure 4.52b indicates that the maximum discrepancy in streamwise velocity between the first and second ADCP vertical measurements compared to the ADV measurements were approximately 10 and 7% respectively. The Root Mean Square Error values, relative to streamwise velocity measured by ADV, are 0.037 and 0.023ms^{-1} respectively.

The depth-integrated streamwise velocity measured by the ADCP underestimates the ADV measurement by 6.8% and overestimates by 5.1% for the first and second vertical respectively. These values are similar to those obtained by others in shallow rivers and laboratory experiments (Stone & Hotchkiss, 2007; Nystrom *et. al*., 2007). Similar trends are observed on the lateral (Figure 4.52c) and vertical (Figure 4.52d) velocity measurements although as expected the differences are less pronounced. In Figure 4.52c a positive value of velocity indicates a clockwise rotation of the flow, i.e. at the water surface the maximum velocity is of the order of 0.15ms^{-1} resulting in an anticlockwise rotation. The lateral velocity component can be observed to be a function of depth, whereas the vertical velocity component appears to be depth invariant over the measured range.

Figure 4.53 shows the standard deviation of streamwise velocities at various depths. It is shown that the magnitudes of ADCP's standard deviation are approximately twice of the standard deviation measured by ADV. This indicates that random error and bias have a high contribution to the fluctuation of the streamwise velocity measured by ADCP. Thus, the ADCP is less suitable than the ADV, in terms of accuracy, for measuring turbulence parameters. Furthermore, a smaller bin size increases the standard deviation of streamwise velocity measured by ADCP (Figure 4.53, 3 vs. 5cm bin size). It is also observed that the magnitudes of standard deviation of streamwise velocity measured by ADCP are almost constant over the depth, which indicates that the larger sampling volume for measurements closer to river bed has minimum effect to the standard deviation magnitude.

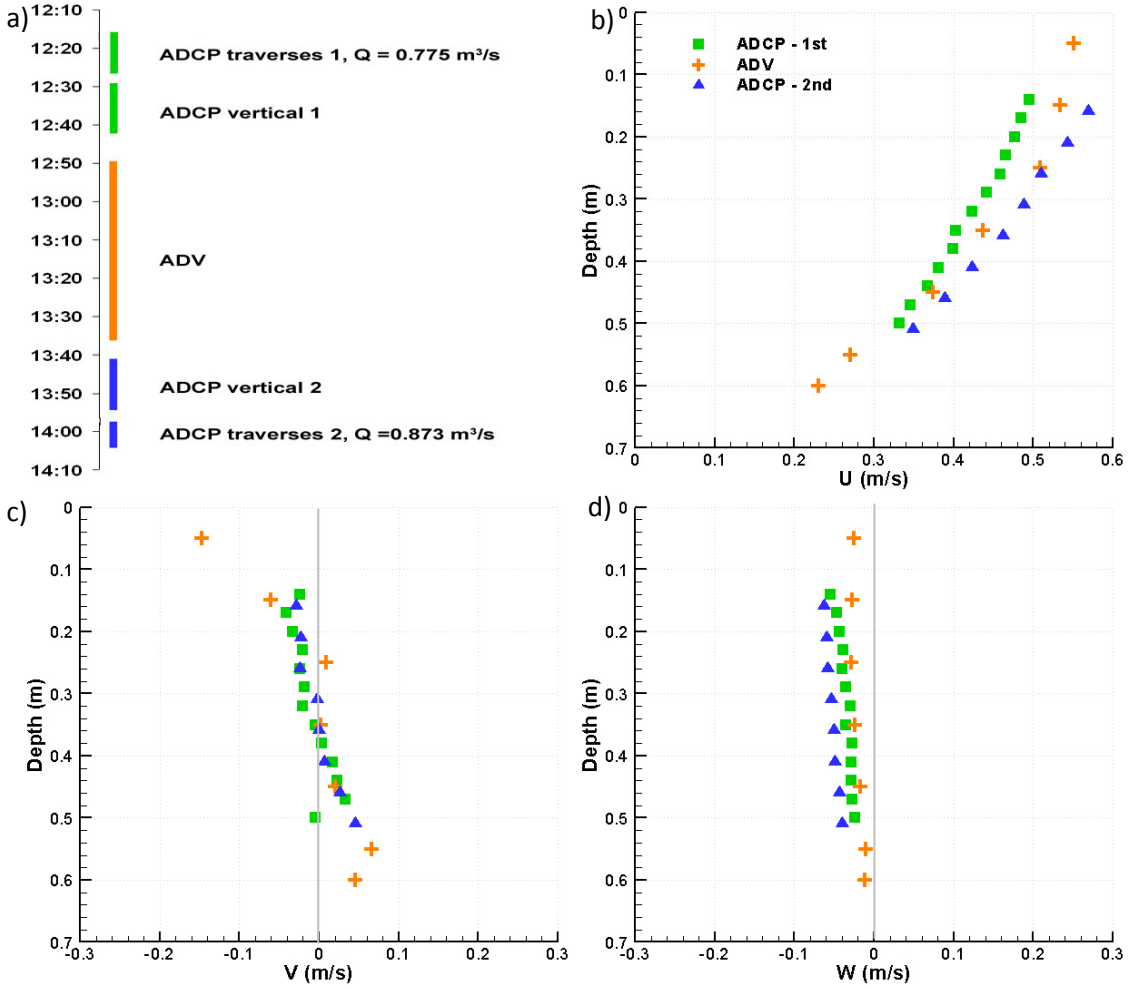

Figure 4.52 Comparison of ADV and ADCP data: (a) time allocation of measurements, (b) streamwise velocity, (c) lateral velocity, (d) vertical velocity. (Data corresponding to measurements made on 7/12/2007).

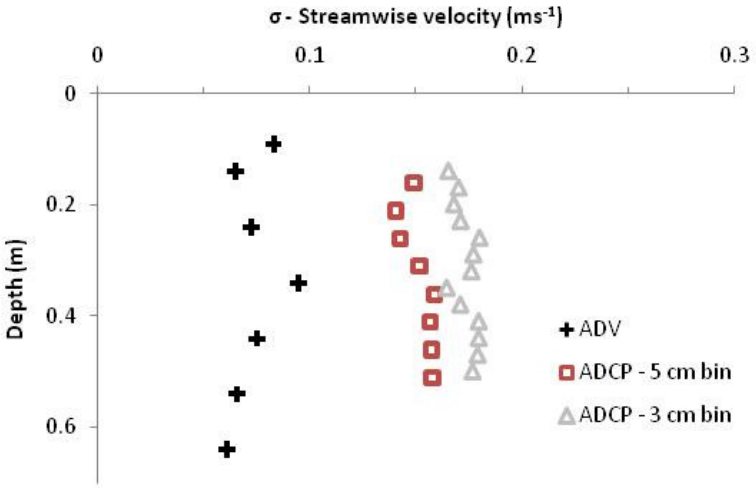

Figure 4.53 Comparison of standard deviation of streamwise velocity magnitudes measured by ADV and ADCP (800 samples averaging).

4.7.8 Conclusions

This section has examined various aspects of the ADCP data characteristics, including stability of velocities with respect to averaging time and magnitude and standard deviation of velocities. The main findings of this section are:

(a) The mean depth-averaged velocities (*U, V, W*), measured at cross sections 2 and 4 for inbank, bankfull and overbank cases, are generally stable within 100 to 300s averaging time (Figure 4.45 and Appendices II-1 to II-5).

(b) Out of 31 stationary measurements undertaken at two cross sections for inbank, bankfull and overbank flow conditions, 30 satisfies the 5% $\overline{U_d}$ convergence level within a 300 s averaging time. This is considered acceptable for the purposes of the current work. The time required to achieve 5% convergence is significantly less than that for 1% convergency (Figures 4.46 and 4.47).

(c) There is a tendency that the mean standard deviation of depth-averaged streamwise velocity decreases with the increase in the magnitude of the mean depth-averaged streamwise velocity (Figure 4.49).

(d) Log and power fit equations assigned to dataset seems to represent the relationship between $\overline{U_{d\_300}}$ and $\overline{\sigma_{U_{d\_300}}}$ more accurately than exponential fit equations (Figure 4.50). However, variations of up to ±25% from the trendline might be expected.

(e) ADCP data have been benchmarked against ADV data, and good agreement in terms of mean velocity and a similar trend of both velocity distributions was observed. The Root Mean Square Error values of two ADCP streamwise velocity profiles relative to that of ADV's are 0.037 and 0.023ms^{-1} respectively (Figures 4.52 and 4.53).

(f) The magnitudes of standard deviation of streamwise velocity measured by ADCP are approximately twice of the standard deviation measured of streamwise velocity measured by ADV. This suggests that ADCP has higher systematic error than ADV (Figures 4.53).

4.8 Characteristics of ADCP discharge measurement

This section investigates the characteristics of ADCP discharge measurement and its accuracy with respect to electromagnetic gauging station measurement.

4.8.1 Possible sources of errors in the ADCP discharge measurements

The error in discharge measurement is defined as the difference between the measured flow and the true value. Similar to the velocity measurements, the true value of the flow is unknown. Hence, an estimate of the limits that bound the possible measurement error is required. Herschy (1995) identifies three sources of errors, namely random, systematic and spurious. Random error is often referred to as experimental errors and the observations deviate from the mean in accordance with the laws of chance such that the distribution usually approaches a normal distribution. Random errors could be reduced by improving the number of samples. Systematic errors (bias) are the instrument errors which is either constant or proportional to the measured velocity, which cannot be reduced by data averaging. However, in most cases, this error is small (typically less than 0.01 ms^{-1} (RDI, 1996)). The spurious errors are human or instrument malfunction, e.g. inaccurate edge distance estimation, overshooting of ADCP path at the edges of measurement, ADCP path that has fluctuated (when comparing velocities from different transects). Since such errors cannot be statistically analysed, they should ideally be discarded. However, these errors are often difficult to quantify and therefore, in common practice, often included in the discharge computation (Everard, 2008). Consequently, the reliability of the ADCP transects data is a subject of debate, e.g. for numerical modelling input (Muste, 2008). The sources of spurious errors in ADCP measurement is further investigated by Gonzalez-Castro & Muste (2007), where they identified 20 elemental sources of error to be considered in their proposed methodology for estimating ADCP discharge measurement uncertainty.

The uncertainty analysis in this section is focused only on random errors since spurious errors have been minimised due to the use of outlined cableway, e.g. the measurement path and transect length for every transects are almost identical.

4.8.2 Sample distribution of transect discharge

The discharge differences from transverse measurement campaigns were processed using WinRiver 2 software and presented as 5% classes histogram in Figures 4.54 and 4.55, for cross sections 2 and 4

respectively. In order to identify a relationship between discharge magnitudes and transect discharge distribution with respect to bin size, data from measurements with 3 and 5cm bins were separated into different tables (Tables 4.15 and 4.16 for CS 2 and Tables 4.17 and 4.18 for CS 4). Tables 4.15 – 4.18 show that most of the discharge differences (ΔQ) are within 20%, many are within 10% and few are within 5%. A tendency that ΔQ values are lower at higher discharge is noticed for CS 2 data with 5 cm bin size (Tables 4.16). However, such tendency is not observed in other cases.

Data from CS 2 (Figure 4.54) show that the variation of ΔQ is higher at low magnitudes of mean velocity. The values of ΔQ vary up to 30 % from the $\overline{Q}$ for $Q_{CS2} \leq 0.417 m^3 s^{-1}$ while they vary within 10% from for $Q_{CS2} \geq 0.829 m^3 s^{-1}$. Unfortunately, the variation in ΔQ for $0.417 m^3 s^{-1} \geq Q_{CS2} \leq 0.829 m^3 s^{-1}$ could not be assessed since data within the corresponding discharge range was not available. High variation of ΔQ for low discharge value is also observed in CS 4 data for $Q_{CS4} \leq 0.401 m^3 s^{-1}$. Furthermore, large variation of measured discharge (> 20%) was occasionally obtained even though the transects are nearly identical. The exact cause of this is difficult to explain.

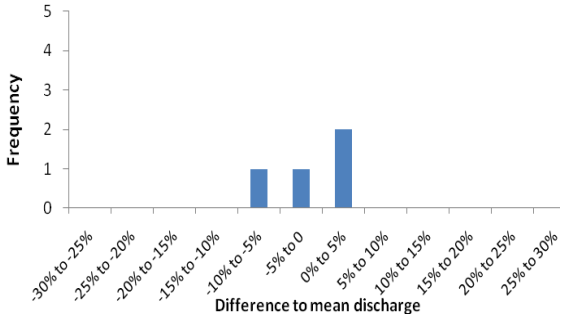

06/03/2007 Q = 3.313m^{3}s^{-1} 7cm bin

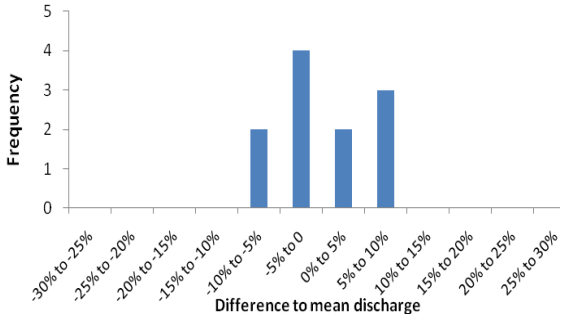

16/01/2008 Q = 2.172m^{3}s^{-1} 5cm bin

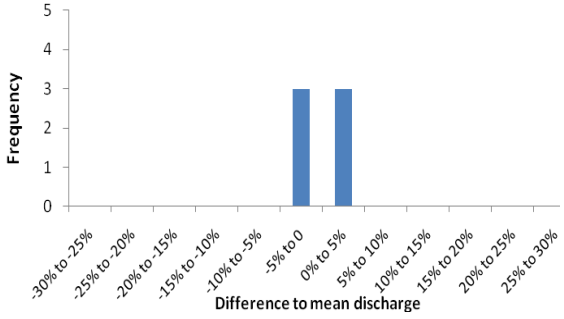

16/01/2008 Q = 1.986m^{3}s^{-1} 5cm bin

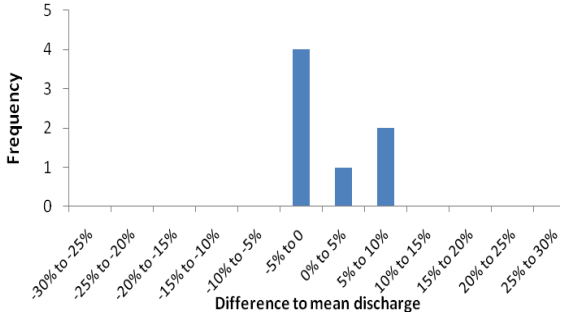

20/11/2007 Q = 1.714m^{3}s^{-1} 5cm bin

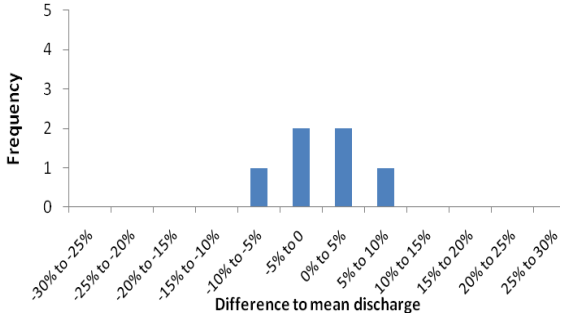

11/03/2008 Q = 0.829m^{3}s^{-1} 5cm bin

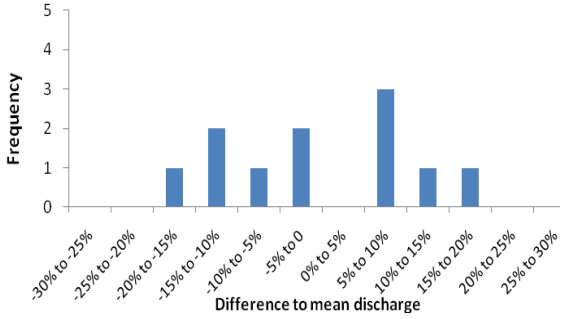

13/06/2008 Q = 0.417m^{3}s^{-1} 3cm bin

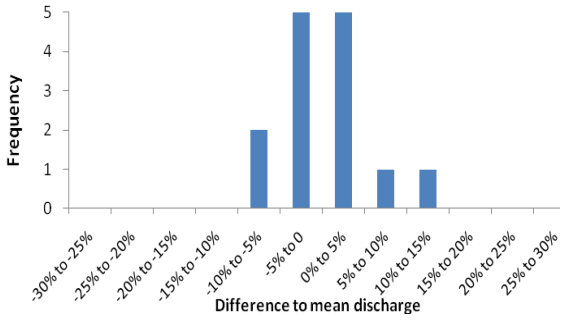

13/06/2008 Q = 0.384m^{3}s^{-1} 3cm bin

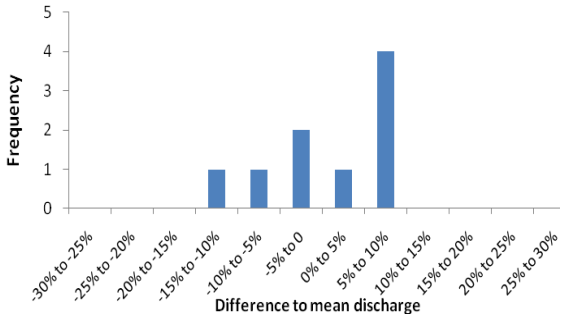

13/06/2008 Q = 0.380m^{3}s^{-1} 3cm bin

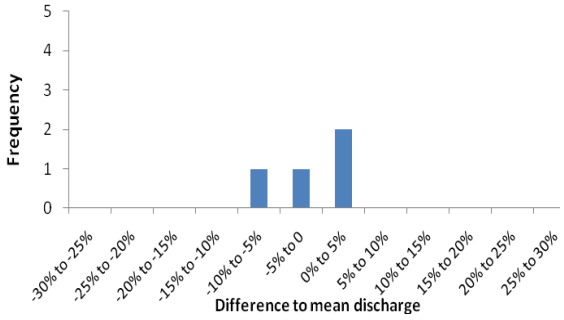

23/06/2007 Q = 0.378m^{3}s^{-1} 3cm bin

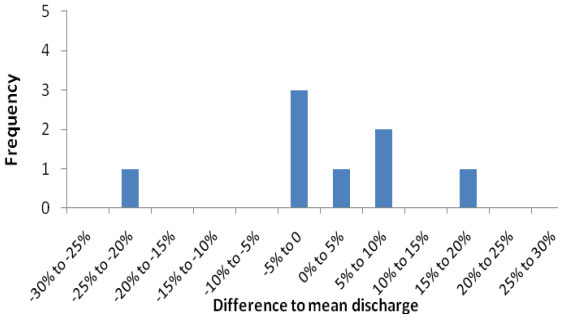

18/08/2008 Q = 0.330m^{3}s^{-1} 3cm bin

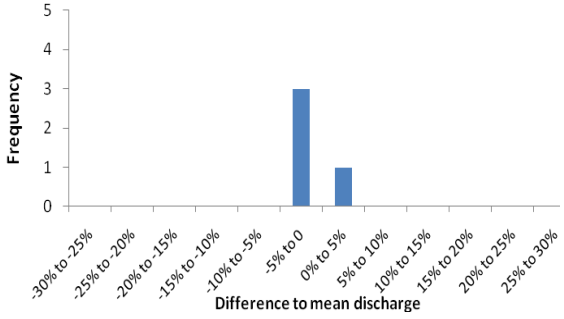

19/08/2008 Q = 0.307m^{3}s^{-1} 10cm bin

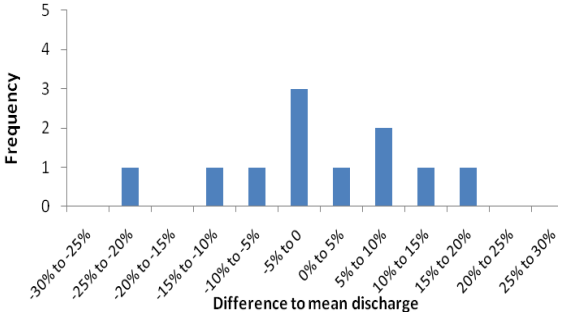

18/08/2008 Q = 0.283m^{3}s^{-1} 3cm bin

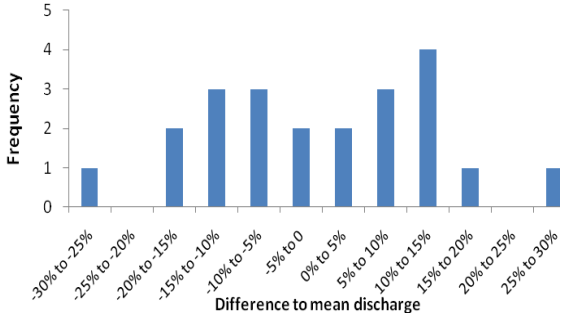

19/08/2008 Q = 0.224m^{3}s^{-1} 10cm bin

Figure 4.54 Discharge difference histogram for CS 2 (January 2007 to August 2008 data).

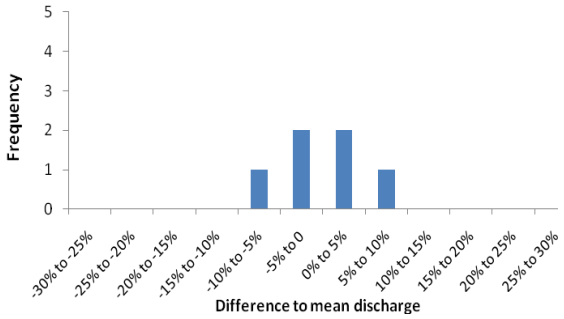

06/03/2007 Q = 3.181m^{3}s^{-1} 7cm bin

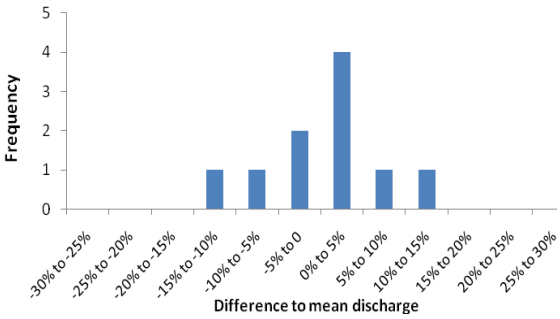

16-17/01/2007 Q = 1.506m^{3}s^{-1} 5cm bin

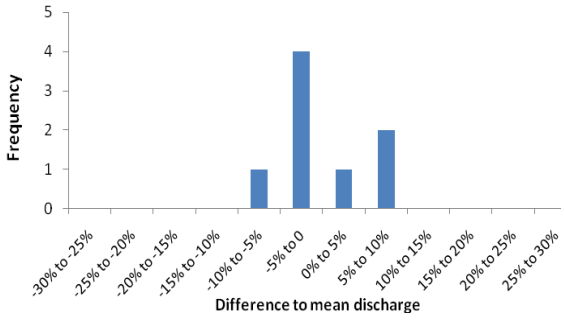

16/01/2008 Q = 1.922m^{3}s^{-1} 5cm bin

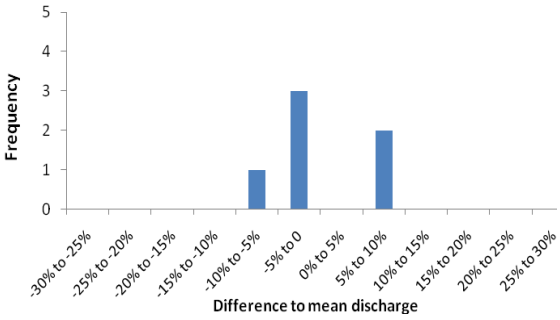

16/01/2008 Q = 1.866m^{3}s^{-1} 5cm bin

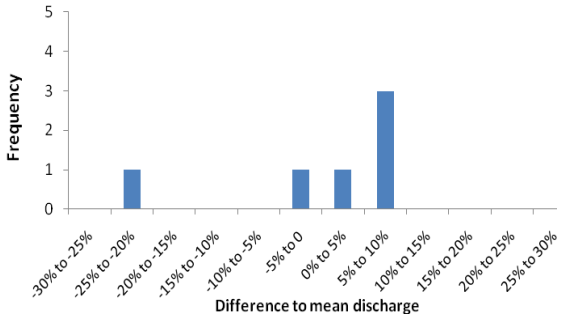

20/11/2007 Q = 1.039m^{3}s^{-1} 3cm bin

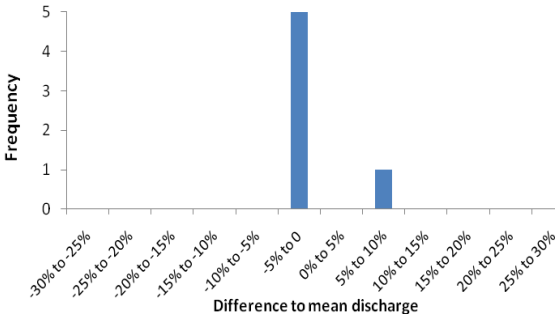

20/11/2007 Q = 1.034m^{3}s^{-1} 3cm bin

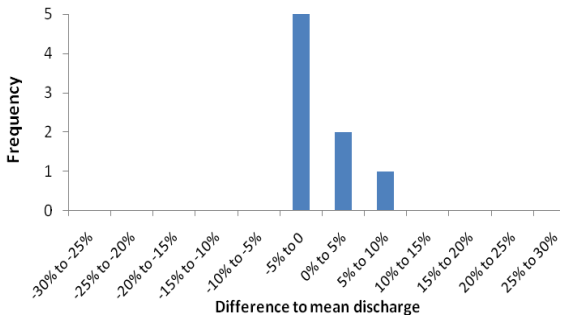

06-07/12/2007 Q = 0.891m^{3}s^{-1} 5cm bin

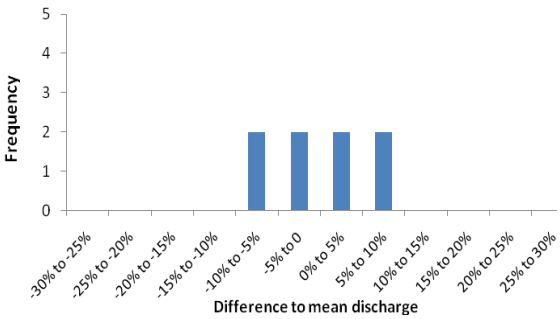

06-07/12/2007 Q = 0.765m^{3}s^{-1} 3cm bin

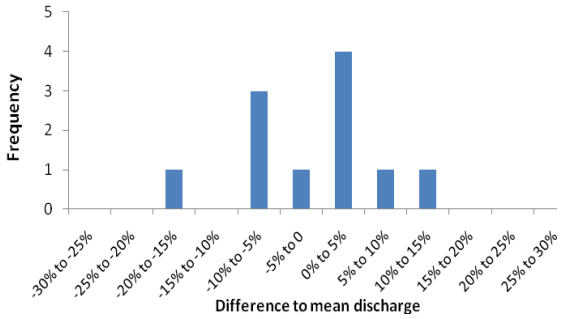

18/08/2008 Q = 0.401m^{3}s^{-1} 5cm bin

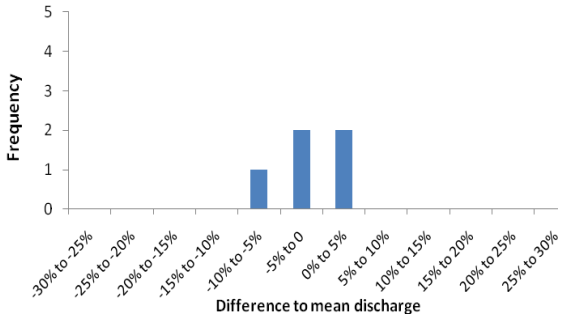

19/08/2008 Q = 0.328m^{3}s^{-1} 3cm bin

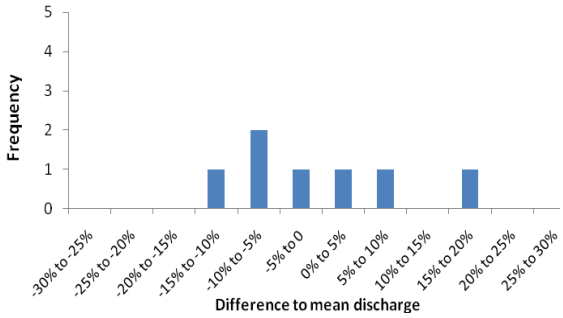

19/08/2008 Q = 0.281m^{3}s^{-1} 3cm bin

Figure 4.55 Discharge difference for CS 4 (January 2007 to August 2008 data).

No	Date	Q	Composition [%]				No. of transect
		[m^{3}s^{-1}]	$\Delta Q \leq \pm 5\%$	$\pm 5\% \leq \Delta Q \leq \pm 10\%$	$\pm 10\% \leq \Delta Q \leq \pm 20\%$	$\Delta Q > \pm 20\%$	
1	13/06/2008	0.417	18	55	100	0	11
2	13/06/2008	0.384	71	93	100	0	14
3	13/06/2008	0.38	33	89	100	0	9
4	23/06/2007	0.378	75	100	100	0	4

Table 4.15 Composition of transect discharge for CS 2 for bin size = 3cm.

No	Date	Q	Composition [%]				No. of transect
		[m^{3}s^{-1}]	$\Delta Q \leq \pm 5\%$	$\pm 5\% \leq \Delta Q \leq \pm 10\%$	$\pm 10\% \leq \Delta Q \leq \pm 20\%$	$\Delta Q > \pm 20\%$	
1	16/01/2008	2.172	55	100	100	0	11
2	16/01/2008	1.968	100	100	100	0	6
3	20/11/2007	1.714	71	100	100	0	7
4	11/03/2008	0.829	67	100	100	0	6
5	18/08/2008	0.33	50	75	88	13	8
6	18/08/2008	0.283	36	64	91	9	11

Table 4.16 Composition of transect discharge for CS 2 for bin size = 5cm.

No	Date	Q	Composition [%]				No. of transect
		[m^3s^{-1}]	$\Delta Q \leq \pm 5\%$	$\pm 5\% \leq \Delta Q \leq \pm 10\%$	$\pm 10\% \leq \Delta Q \leq \pm 20\%$	$\Delta Q > \pm 20\%$	
1	20/11/2007	1.039	33	83	83	17	6
2	21/11/2007	1.034	83	100	100	0	6
3	06/12/2008	0.765	50	100	100	0	8
4	19/08/2008	0.281	29	71	100	0	7

Table 4.17 Composition of transect discharge for CS 4 for bin size = 3cm

No	Date	Q	Composition [%]				No. of transect
		[m^3s^{-1}]	$\Delta Q \leq \pm 5\%$	$\pm 5\% \leq \Delta Q \leq \pm 10\%$	$\pm 10\% \leq \Delta Q \leq \pm 20\%$	$\Delta Q > \pm 20\%$	
1	16/01/2008	1.922	63	100	100	0	8
2	16/01/2008	1.866	50	100	100	0	6
3	17/01/2007	1.491	60	80	100	0	10
4	06/12/2007	0.891	88	100	100	0	8
5	18/08/2008	0.401	45	82	100	0	11
6	19/08/2008	0.328	80	100	100	0	5

Table 4.18 Composition of transect discharge for CS 4 for bin size = 5cm

4.8.3 Accuracy of ADCP discharge measurement

Figure 4.56 and Table 4.19 were constructed to assess the difference of discharge measured by the ADCP and the electromagnetic gauge located upstream CS 1. It should be noted that the electromagnetic gauge (EG) is near the end of its working life and will soon be replaced with a new discharge measurement device. Also, there were periods when the EG was not working properly (Dimmock, 2009), i.e. gauge was out of order for the 10/2/2009 measurements and was therefore not included in the analysis. Unfortunately, the performance of the EG is intermittent and it is difficult to know exactly when the EG was performing correctly. Hence, the reliability of the EG data is somewhat questionable. It appears that the EG was not performing correctly on the 18/8/2008 and the 19/8/2008 as most of the measured discharge is low, and differs from the ADCP data by up to 1550% (see Table 4.19). There is also evidence to suggest that for overbank measurements (6/3/2007) the results from the EG are questionable. Discrepancies of 54 to 66% are observed at overbank measurements (6/3/2007) with EG underestimating the ADCP measurements. The magnitude of EG discharge measured at bankfull (16/1/2008) is similar to that measured by EG during the overbank case in 6/3/2007 while a visual investigation conducted during the

measurements and analysis on ADCP velocity data indicate that such phenomenon was unlikely to happen. However, there are occasions where the differences between the EG and ADCP are within 10% (see Table 4.19 and Figure 4.56).

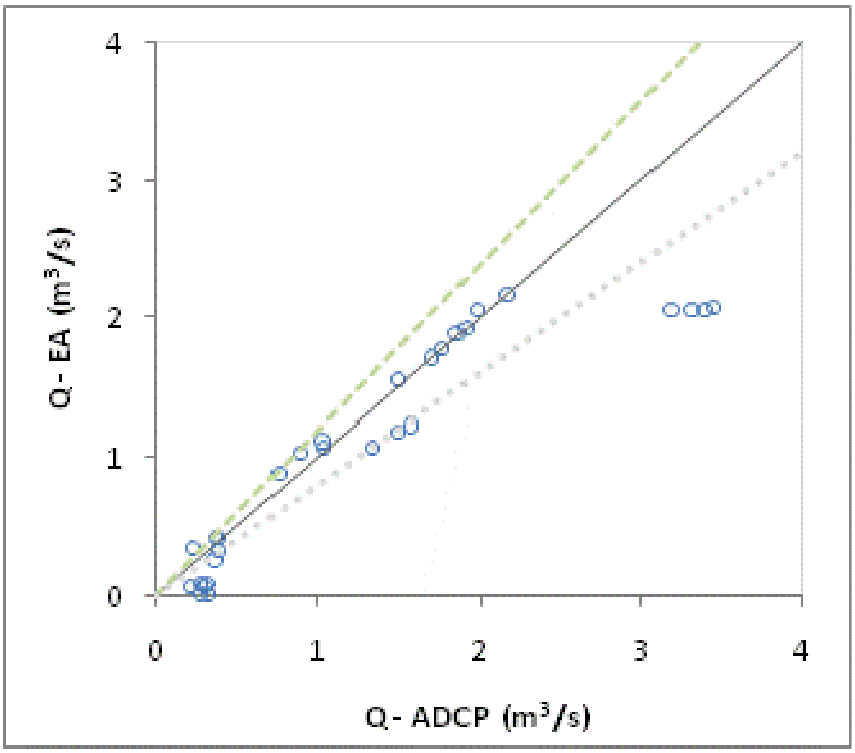

Figure 4.56 Comparison of discharge measured by ADCP and electromagnetic gauge.

Date	Location	Q (m^3s^{-1})	Q-EA	Difference (%)
17/01/2007	1	1.35	1.07	25
	3	1.58	1.23	28
	4	1.51	1.19	27
06/03/2007	2	3.31	2.05	61
	3	3.39	2.06	65
	4	3.18	2.06	54
	1	3.45	2.08	66
13/06/2007	2	0.24	0.35	-32
23/06/2007	2	0.38	0.42	-10
	2	0.40	0.43	-7
20/11/2007	2	1.71	1.71	0
	4	1.51	1.56	-3
21/11/2007	4	1.03	1.12	-8
	4	1.04	1.08	-4
06/12/2007	4	0.77	0.88	-13
	4	0.89	1.04	-15
16/01/2008	2	2.17	2.16	0
	2	1.99	2.05	-3
	3	1.78	1.78	0
	4	1.92	1.92	0
	4	1.87	1.89	-1
18/08/2008	2	0.28	0.02	1315
	2	0.33	0.02	1550
	4	0.37	0.27	39
	4	0.40	0.34	19
19/08/2008	4	0.33	0.09	264
	4	0.28	0.09	212
	2	0.22	0.08	195
	2	0.31	0.07	339

Table 4.19 Comparison of discharge measured by ADCP and electromagnetic gauge.

4.8.4 Conclusions

The distribution of transect discharge and accuracy of ADCP discharge measurement have been investigated in this section. The main findings of this section are:

(a) Variation of discharge difference (ΔQ) increases for mean velocity equal and below 0.42m^3s^{-1} and 0.40m^3s^{-1} for cross sections 2 and 4 respectively. The exact threshold is, however, uncertain since there is a gap of data from the mentioned discharge values to 0.76 and 0.82m^3s^{-1} for cross sections 2 and 4 respectively.

(b) The average difference between electromagnetic gauge and ADCP flow measurements is 10.9% (absolute) for flow rate ≤ 2.17m^3s^{-1} (ADCP), excluding the August 2008 data that was suspected to have error.

(c) An average discharge difference of 1.2% between both instruments is observed for ADCP flow rate between of 1.51 to 2.17 m^3s^{-1}.

(d) The electromagnetic gauge near the research site appears to be less accurate than ADCP in measuring discharge at overbank condition. Similar discharge values were recorded by the EG for a bankfull and an overbank conditions while visual observation on the measurement condition suggests that such phenomenon was unlikely to happen.

5 FLOW STRUCTURES IN THE RIVER BLACKWATER

This chapter is concerned with investigating the structure of the flow during inbank, bankfull and overbank conditions. To that end, the data obtained from the ADCP (transverse and stationary measurements), ADV and LS-PIV are examined. The velocity distribution and secondary flow circulation at cross sections 2 and 4 are compared to those studied on the 1:5 physical model.

5.1 The fieldwork data

This subsection describes the data which are analysed in this Chapter and in Chapter 6. Fourteen measurement campaigns have been undertaken since November 2006 (Table 5.1), with the first four campaigns designated for initial testing of the ADCP, cableway system and compass. The first two columns in Table 5.1 relate, respectively, to the unique reference number of a particular set of experimental data and the date at which that data were obtained. The third column outlines the location at which the data was collected (in terms of cross section number, see Figure 3.3), while the fourth column gives the value of the overall discharge measured at each cross section. The fifth column in the table is the number of transverse measurements where the discharge difference is within 5% of the mean discharge (see also section 4.5.1). The final column in Table 5.1 denotes the number of ADCP stationary measurements which were undertaken at specific cross sections on specific dates (see also section 4.5.1).

It is perhaps worth noting that prior to campaign number 3, the measurements were undertaken with an earlier version of a cableway system that did not straighten the ADCP path, and without a compass. An analysis of the data collected revealed that for datasets 5, 6 and 10 the overall quality was insufficient for detailed analysis. With respect to datasets 5 and 6, an electronic issue with respect to the compass was identified as being the cause for this quality issue, whereas with respect to dataset 10, the existence of excessive vegetation made the results obtained from the ADCP questionable, i.e. 7 transects were undertaken and, on all occasions, the ADCP failed to record data in a large proportion of the channel.

No.	Date	Location (CS)	Discharge in m^3s^{-1}	No. of transverse measurements	No. of stationary measurements
1	*17/01/2007*	*1*	*1.35*	*6*	-
		3	*1.58*	*7*	-
		4	*1.51*	*7*	-
2	*06/03/2007*	*2*	*3.31*	*4*	-
		3	*3.39*	*4*	-
		4	*3.18*	*5*	-
		1	*3.45*	*4*	-
3	*12/06/2007*	*2*	*0.24*	*3*	*5*
4	*23/06/2007*	*2*	*0.38*	*3*	*5*
		2	*0.40*	*3*	-
5	20/11/2007	2	1.71	5	-
		4	1.51	3	-
6	21/11/2007	4	1.03	4	4
		4	1.04	4	-
7	**06/12/2007**	**4**	**0.77**	**4**	**8**
		4	**0.89**	**7**	**-**
8	**16/01/2008**	**2**	**2.17**	**6**	**5**
		2	**1.99**	**4**	**-**
		3	1.78	4	4
		4	**1.92**	**4**	**-**
		4	**1.87**	**3**	**4**
9	11/03/2008	4	0.83	4	-
10	28/05/2008	2	-	-	-
11	**13/06/2008**	**2**	**0.38**	**9**	**15**
		2	**0.38**	**4**	**-**
12	**18/08/2008**	**2**	**0.28**	**4**	**7**
		2	0.33	3	-
		4	**0.37**	**4**	**5**
		4	0.40	5	-
13	19/08/2008	4	0.33	4	8
		4	0.28	3	-
		2	0.22	4	-
		2	0.31	4	-
14	**10/02/2009**	**2**	**4.16**	**5**	**5**
		2	4.40	5	-
		4	**3.57**	**7**	**6**
		4	3.64	5	-
		1	4.47	5	-
			Total	174	81

Italics: test fieldworks

Underlined: without compass/obstructed by vegetations

Bold: used for analysis on velocity distribution

Table 5.1 ADCP measurement campaign in the River Blackwater (2007 – 2009).

Velocity distributions from campaigns 7, 8, 11, 12 and 14 were selected to investigate the flow structures at various conditions, i.e. inbank, bankfull and overbank. The velocity distributions from campaigns 4, 9 and 13 have similar discharge values and time of the measurements (during the years) as for campaigns 7 and 18. Due to this reason they are not included in the comparison. The effect of emergent vegetation downstream and upstream the measurement locations on the flow structures was investigated using the data of campaign 11 and are presented in chapter 6. Although not all of the data illustrated in Table 5.1 was used to analyse the structure of the flow, the discharges obtained in all campaigns were used for constructing the stage-discharge rating curve presented in chapter 6 and for comparison with ADV and PIV data.

Most of the measurements were undertaken at cross sections 2 and 4 as they have easier access than the other cross sections. The hydraulic parameters for the measurements at cross sections 2 and 4 presented in Tables 5.2 and 5.3 were computed based on the main channels of the survey-simplified cross sections from Figures 3.4 and 3.6. Simplified cross sections (i.e. reducing the number of survey nodes by 75%) were used in order to aid comparison with laboratory data and to reduce the computational effort in the numerical modelling. It should be noted that this simplification keeps the major shape of the cross section geometry and is, therefore, considered adequate for this purpose. The hydraulic mean depth parameter, H_m, was calculated by dividing the cross section area by the width of the water surface. For the overbank conditions, the relative depth D_r was defined as the ratio between the mean depth on the floodplain (h_m) to that of the main channel (h_m/H_m).

The hydraulic parameters for the bankfull condition at cross section (CS) 4 are similar to those of Sellin's representative cross section (Sellin and van Beesten, 2002) at the bankfull condition (Table 5.4) as the difference for parameters A, P, R, B_s and H_m used in the current research and previous research (Sellin and van Beesten, 2002) are relatively small, i.e. in the range of 0.2% – 5.3%. The water temperature measured by the ADCP was used as a basis to calculate the kinematic viscosity for the computation of Re. The Re values for cross sections 2 and 4 during the bankfull measurements were 2.59×10^5 and 2.38×10^5 respectively. The flow conditions during all measurements were subcritical, indicated by the Froude Number values of less than 1 (Tables 5.2 and 5.3).

			18/08/2008 Inbank	16/01/2008 Bankfull	10/02/2009 Overbank
water level	H	(mAOD)	62.67	62.85	63.23
discharge	Q	(m^3s^{-1})	0.283	2.172	4.16
water temperature	T	(^oC)	17.50	7.70	4.10
cross-section area	A	(m^2)	4.82	5.92	8.26
wetted perimeter	P	(m)	7.02	7.40	8.15
hydraulic radius	R	(m)	0.69	0.80	1.01
Reynolds number (x 10^5)	Re	(-)	0.531	2.59	4.31
top water surface width	B_S	(m)	6.12	6.20	6.20
hydraulic mean depth	H_m	(m)	0.79	0.96	1.33
Froude number	Fr	(-)	0.03	0.15	0.18
relative depth	h_m/H_m	(-)	-	-	0.39
aspect ratio	B_S/H_m	(-)	7.77	6.49	4.65
mean streamwise velocity	$\overline{U}$	(ms^{-1})	0.08	0.45	0.67

Table 5.2 Experimental conditions during the measurements at CS 2.

			18/08/2008 Inbank	07/12/2007 Inbank	16/01/2008 Bankfull	10/02/2009 Overbank
water level	H	(mAOD)	62.50	62.44	62.66	63.11
discharge	Q	(m^3s^{-1})	0.401	0.765	1.866	3.57
water temperature	T	(^oC)	17.50	11.28	7.70	4.10
cross-section area	A	(m^2)	2.84	2.53	3.71	6.53
wetted perimeter	P	(m)	5.82	5.53	6.65	8.14
hydraulic radius	R	(m)	0.49	0.46	0.56	0.80
Reynolds number (x 10^5)	Re	(-)	0.794	1.29	2.38	3.11
top water surface width	B_S	(m)	5.01	4.79	5.74	6.75
hydraulic mean depth	H_m	(m)	0.57	0.53	0.65	0.97
Froude number	Fr	(-)	0.07	0.16	0.14	0.19
relative depth	h_m/H_m	(-)	-	-	-	0.27
aspect ratio	B_S/H_m	(-)	8.87	9.06	8.89	6.97
mean streamwise velocity	$\overline{U}$	(ms^{-1})	0.17	0.36	0.61	0.61

Table 5.3 Experimental conditions during the measurements at CS 4.

H (m)	A (m^2)	P (m)	R (m)	B_S (m)	H_m (m)
0.6	2.91	5.95	0.49	5.45	0.53
0.75	**3.75**	**6.37**	**0.59**	**5.75**	**0.65**
1	5.19	6.87	0.75	6.25	0.83
1.3	6.91	7.47	0.93	6.85	1.01

Table 5.4 Variation of hydraulic parameter values with respect to main channel depth for the representative cross section used by Sellin and van Beesten (2004).

The bed profile at cross sections 2 and 4 were surveyed in 2007 and 2009 in order to monitor and record any potential changes which may have occurred. On each occasion, two profiles were measured except for CS 2 during the 2007 campaign, where only one set of data was recorded. Unfortunately, the large extent of vegetation and possibly also the sedimentation from a previous flood event hindered finding the location of the wooden pegs that mark the cross section 2. As a result, the exact locations for CS 2 deviated by up to 1m (Figure 5.1). The locations of CS 4 from both surveys are very similar for the main channel. A deviation in measurement locations of up to 0.4m in the floodplain is regarded as acceptable for this purpose, since obtaining deviation less than that value is practically difficult. Figure 5.2 indicates that during the time between the two sets of survey measurements, there appears to have been some movement in the actual cross sections, with the banks moving by approximately 0.4m in some cases. However, it is difficult to conclude whether this was caused by erosion or due to the cross sections geometry being measured at slightly different locations (Figure 5.1). Despite this, there is evidence to suggest that erosion and deposition might have occurred, particularly in CS 4. Figures 5.3a and 5.3b indicate that, for CS 4, erosion has taken place: the permanent wooden stake (red arrow) and control point (white arrow) shown in Figure 5.3, lend credence to this assertion (NB the width of the ADCP boat is 0.44m). It is quite probable that the unstable part of the left bank shown in Figure 5.2a (6/12/2007) was eroded away by the high flow conditions in the river between 6/12/2007 and 16/1/2008 (Figure 5.4). The left bank location between 16/1/2009 and 18/8/2009 appears to be similar, indicating that it was stable during those periods (Figures 5.3b and c). During the high flows associated with the 10/2/2009, the wooden stake was completely submerged, enabling the ADCP to measure closer to the left bank. In normal conditions, the wooden stake restricted the proximity of the boat to the bank.

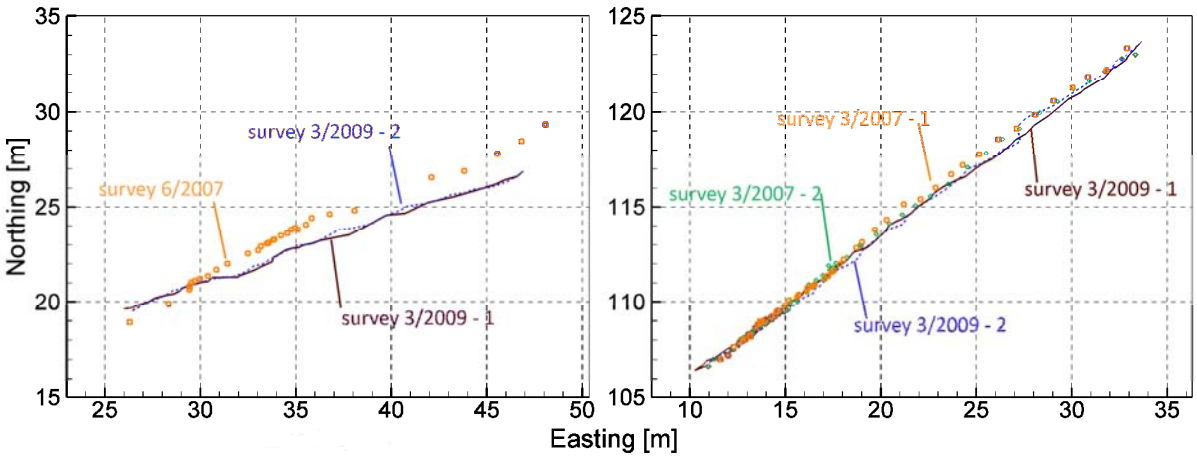

Figure 5.1 Plan view of cross section profiles at cross sections 2 and 4 (2007 and 2009).

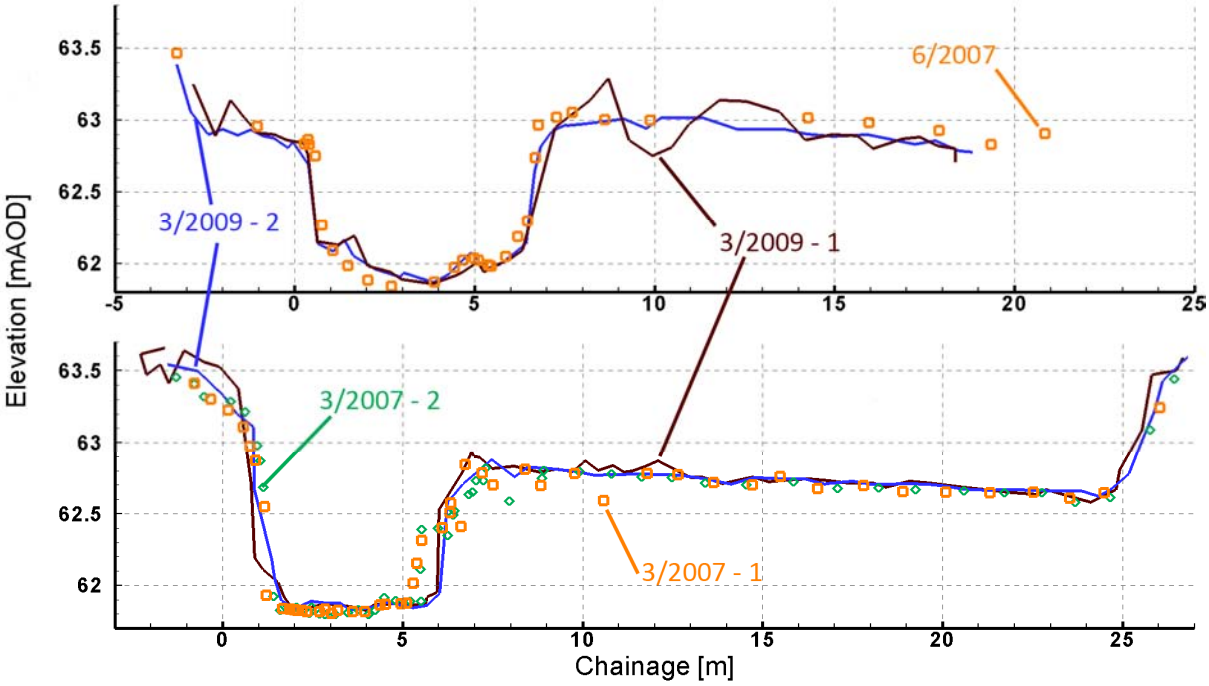

Figure 5.2 Bed profiles at cross sections 2 and 4 (2007 and 2009).

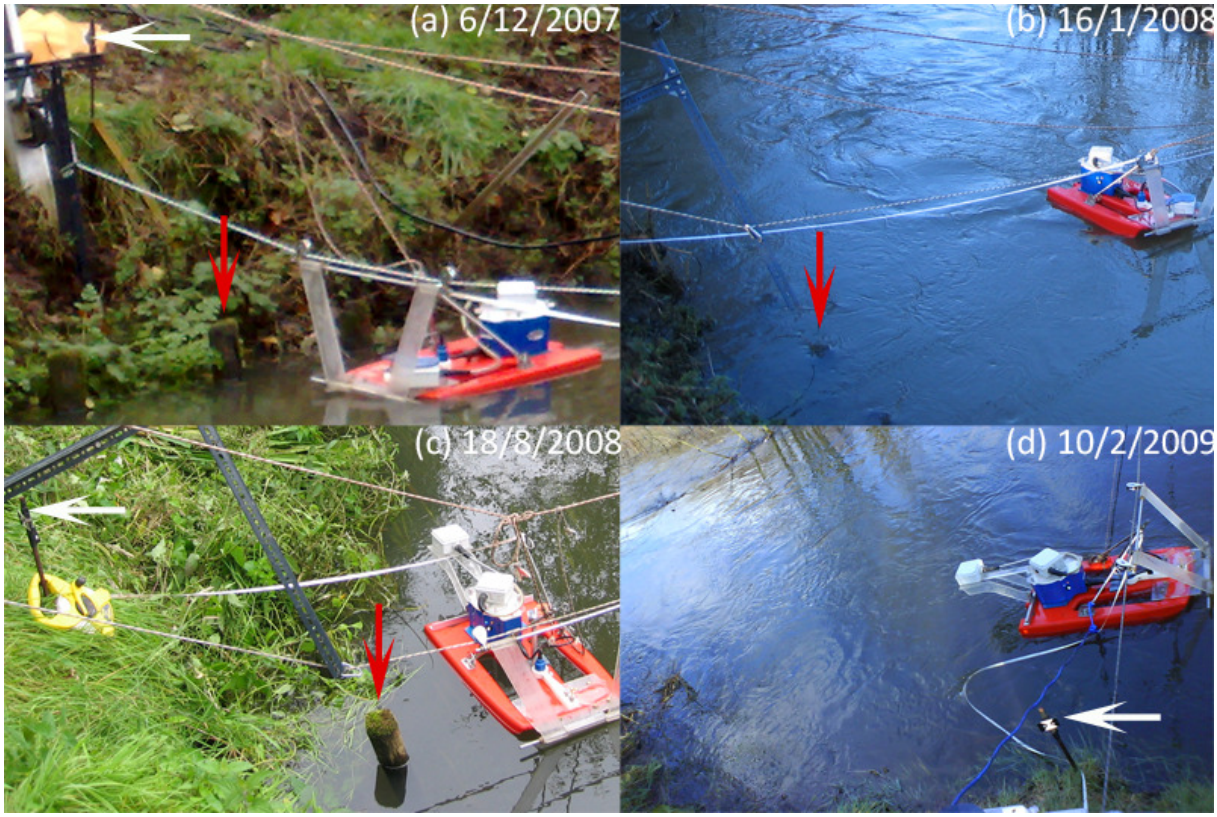

Figure 5.3 Bank erosion at CS 4 (2007 - 2009).

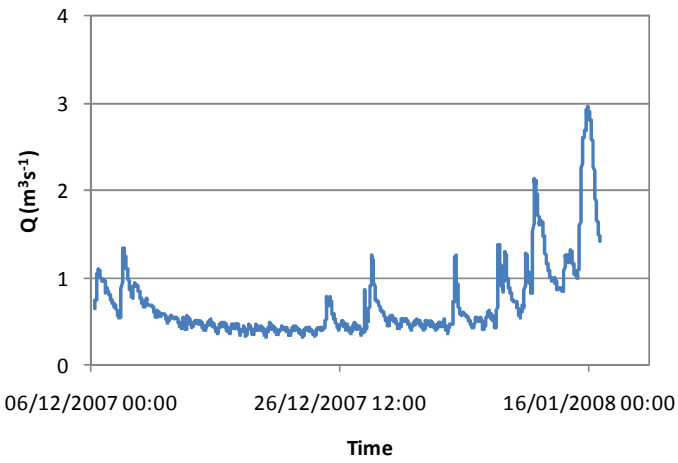

Figure 5.4 Discharge hydrograph between 6/12/2007 and 17/1/2008.

5.2 Spatial distribution of velocities at cross sections 2 and 4

In all cases it was possible to undertake one complete set of transverse measurements in approximately 20 minutes. Subsequently analysis of the discharges (not shown here) indicate that it is not unreasonable to assume that the flow was steady and uniform over this time period.

Furthermore, changes in water depth during this period were always less than 1cm, i.e. within the accuracy of the gauge boards, thus giving strength to the assumption of steady flow conditions.

During each experiment, observation of the stage at each cross section was made at regular intervals (typically, every 10 minutes). The water stage readings were converted into height Above Ordnance Datum (AOD) using offsets values measured using a differential GPS (dGPS) and a total station. The water stage during the ADCP measurements was then interpolated from those readings. The vertical position of the ADCP data (bed and velocities) was converted to mAOD by subtracting the water stage during measurement with the local depth measured by the ADCP.

Before the actual data arising from the experiments is discussed, it is worth noting how these data have been manipulated. The velocity data obtained from ADCP transect averaging (TA) were visualised via a commercial software package, Tecplot 10. For the analysis that follows, the isovels for cross sections 2 and 4 are normalised against $\overline{U}$ (i.e. the total discharge/total area), (see Figure 5.5). Due to the large number of interpolation points in the TA results, it is necessary to blank some of the data to minimise overlapping between the velocity vectors. Since the ADCP measures velocities along its four transducers, projection is required to obtain the velocity data perpendicular and parallel to the cross sections. The former and the latter will be called streamwise and lateral velocity respectively. The cross-sections were defined as the direction perpendicular to the river main channel using visual observation. In order to be able to measure at the same locations in any given time, the edges of the cross-sections were marked. It is acknowledged that the streamwise direction may also be defined in other ways, e.g. the direction where the mean transverse velocity is equal to zero. This approach is likely to alter the cross-section direction for each measurement and cause difficulty in referencing data location when used for numerical modelling. The latter approach was tested for the CS 4 overbank case, which has the highest magnitudes of lateral velocity. In order to obtain mean transverse velocity of zero, the streamwise direction defined using the first approach need to be adjusted by -4.13 degree. The projection result of the latter approach shows little change on the secondary flow pattern. There was also little change in the streamwise velocity data, which is not surprising given that these data would need to be adjusted by *cos* 4.13^{o}, i.e., ~0.997. Hence, the visual approach outlined above to define the direction of streamwise flow was considered to be sufficient for the current purposes.

In order to give a better overview of the spatial position of the data, the bed profiles measured using a total station in 2007 and 2009 are also displayed. In what follows, it is assumed that the CS 2 data for the inbank and bankfull case follows the bed profile measured in 2009 (i.e. 2009-1 in Figure 5.2) as they provide a closer agreement with the ADCP data and that the ADCP data being analysed were measured at times that are closer to the 2009 survey than the 2007 survey. Furthermore, the location of the CS 2 during overbank measurement (10/2/2009) was moved by approximately 4 metres upstream of the actual location of CS 2 due to the difficulty in accessing the floodplain during overbank flow condition. Based on the previous analysis of Figure 5.3, the CS 4 data were assumed to follow the bed profile of the 2009-1 survey, except for the 6/12/2007 data that were assumed to follow the 2007 bed profile.

5.2.1 Spatial velocity distribution at cross section 2

The bed profile measured by the ADCP does not deviate significantly from the profiles measured by the total stations (Figure 5.5). An average RMSE value of 0.08m was achieved for the all cases, excluding the CS 2 overbank case that was measured at a slightly different location from the actual location of CS 2 (c.f. section 5.2). A sudden increase of bed level measured by a total station in 2009, i.e. at y = 5 and 1.6m appears to be a result of local variation in bed topography, as the second profile obtained at the same time does not show the same variation (Figure 5.2). Such local changes are not expected to be recorded by the ADCP since the ADCP is based on an average depth obtained from four transducers.

Figures 5.5a and 5.5b indicate that as the water depth increases from inbank to bankfull, the maximum velocity in CS 2 increases from ~0.2 to ~0.7ms^{-1}. As the flow spills onto the floodplain, the maximum velocity continues to increase but at a slower rate due to the exchange of momentum between the main channel and the flood plain (c.f. Figures 5.5b and c, U_{max} changes from ~ 0.7 to ~0.9ms^{-1}.

To a large extent, the effect that vegetation may have on the ADCP and flow (for the inbank measurement) was minimised at CS 2 by removing any vegetation within 5 metres of the measurement location. It is worth noting that during the summer months, the growth of vegetation was excessive but not uniformly distributed across the channel (c.f. Figure 4.19). Hence, although the vegetation was removed close to CS 2, the vegetation upstream appears to have the effect of diverting the flow towards the right bank as illustrated in Figure 5.5a. This consequently shifts the position of the maximum velocity core to the right. Interestingly, the maximum velocity core for the

inbank case is depressed significantly below the water surface. This is quite different from that corresponding to bankfull and overbank conditions, i.e. the maximum velocity is located at right-centre, closer to the water surface.

The isovels appear to be more compressed between the high velocity core and the river bed for the bankfull case. This was not observed for the overbank condition, suggesting that the high velocity core extends closer to the bed. Furthermore, the magnitude of U_d increases with rising water level (Figure 5.6), which is consistent with the increase of local velocity with water level shown in Figure 5.5.

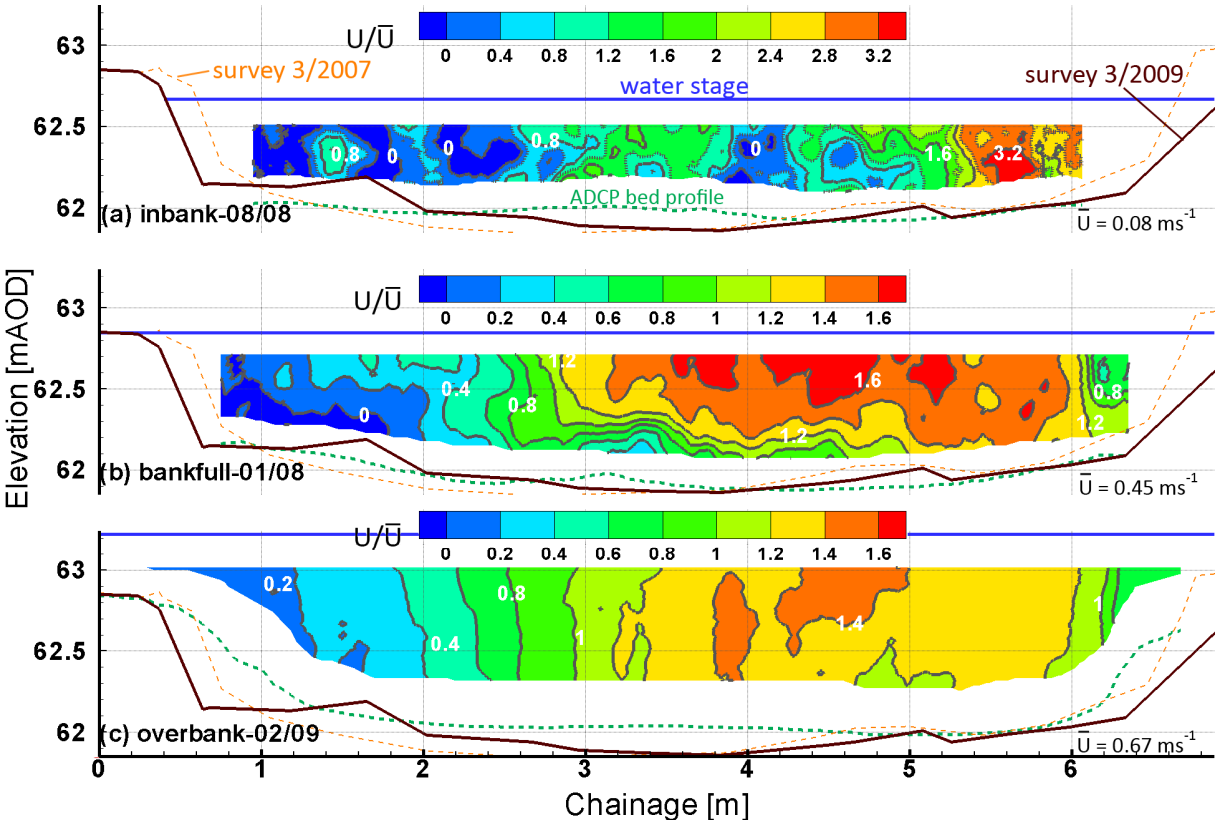

Figure 5.5 Isovels of $U/\bar{U}$ at CS 2.

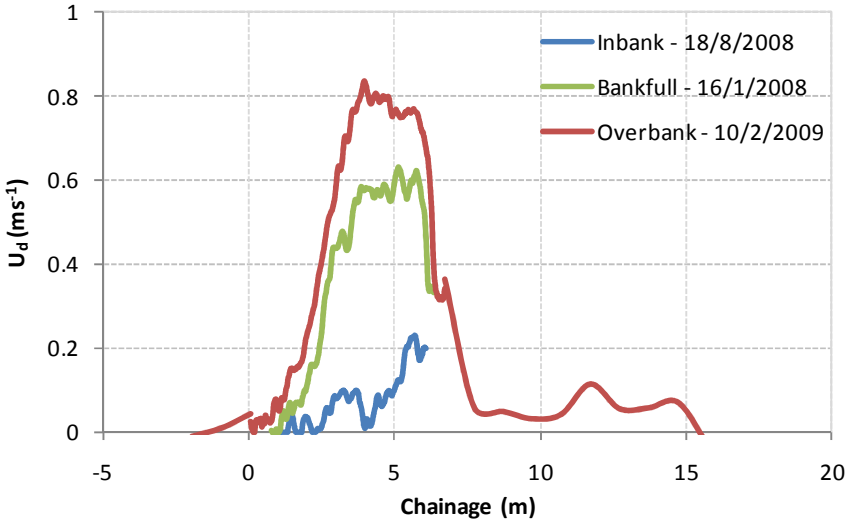

Figure 5.6 Variation of U_d across the channel at CS 2 for various flow conditions.

Figure 5.7 indicates that the magnitude of the maximum lateral velocity remains constant for the bankfull and overbank case. This results in higher $V/\overline{U}$ for the bankfull case. For the inbank case, velocity cores with opposite signs concentrated at y = 3.8 - 5m could be an indication of an anti-clockwise secondary cell (Figure 5.7a). Three similar phenomena could also be observed for the bankfull case (Figure 5.7b).

The average of lateral velocity $\overline{V}$ and $\overline{|V|}$ from Figure 5.7 are presented in Table 5.5 The parameter $\overline{|V|}$ also needs to be considered since the value of $\overline{V}$ depends greatly on the projection angle of the velocity data, e.g. in a straight laboratory flume one would expect to have $\overline{V}$ = 0, but higher value of $\overline{|V|}$. Furthermore, the values of $\overline{V}/U_{max}$ for all cases range from -5.34 to -8.74%, increasing with water depth. On the other hand $\overline{|V|}/U_{max}$ range from 9.55% to 12.57%, at highest for the bankfull condition. The values range of both $\overline{V}/U_{max}$ and $\overline{|V|}/U_{max}$ are higher than what has been observed by Tominaga *et al.* (1989) in a straight laboratory flume that has a value in the region of $0.02U_{max}$. Considering that CS 2 is not perfectly straight and its geometry is far more irregular than a straight laboratory flume, the finding above is not so surprising.

Figure 5.8 indicates that as the water level increases, the values of $W/\overline{U}$ become smaller and less varied. It is likely that the more frequent occurrence of negative vertical velocity is due to the flow around the survey boat, i.e. an experimental bias is introduced. For measurements in a large river

with mean primary velocity in the order of 1ms^{-1}, Dinehart and Burau (2005a) reported that such effects can result in a bias of the vertical velocities by up to -6cms^{-1}.

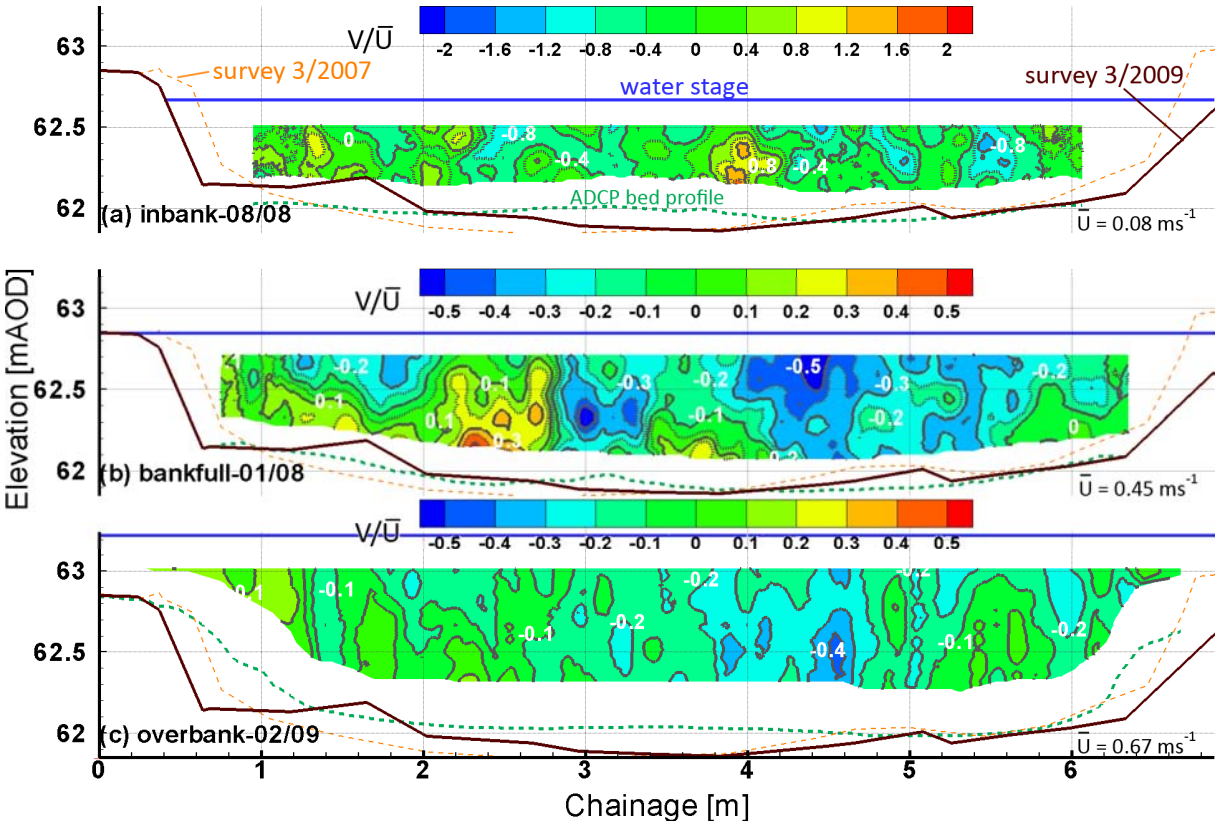

Figure 5.7 Isovels of $V/\overline{U}$ at CS 2.

		18/08/2008 Inbank	16/01/2008 Bankfull	10/02/2009 Overbank
$\overline{U}$	(ms^{-1})	0.08	0.45	0.67
U_{max}	(ms^{-1})	0.29	0.77	1.00
$\overline{V}$	(ms^{-1})	-0.02	-0.07	-0.09
$\overline{\lvert V \rvert}$	(ms^{-1})	0.03	0.10	0.10
V_{max}	(ms^{-1})	0.15	0.24	0.13
V_{min}	(ms^{-1})	-0.11	-0.31	-0.29
$\overline{W}$	(ms^{-1})	0.00	-0.06	-0.04
W_{max}	(ms^{-1})	0.04	0.03	0.03
W_{min}	(ms^{-1})	-0.03	-0.14	-0.11
$\overline{V}/U_{max}$	(%)	-5.24	-8.48	-8.74
$\overline{\lvert V \rvert}/U_{max}$	(%)	11.89	12.57	9.55

Table 5.5 Mean and extreme values of *U*, *V* and *W* for CS 2.

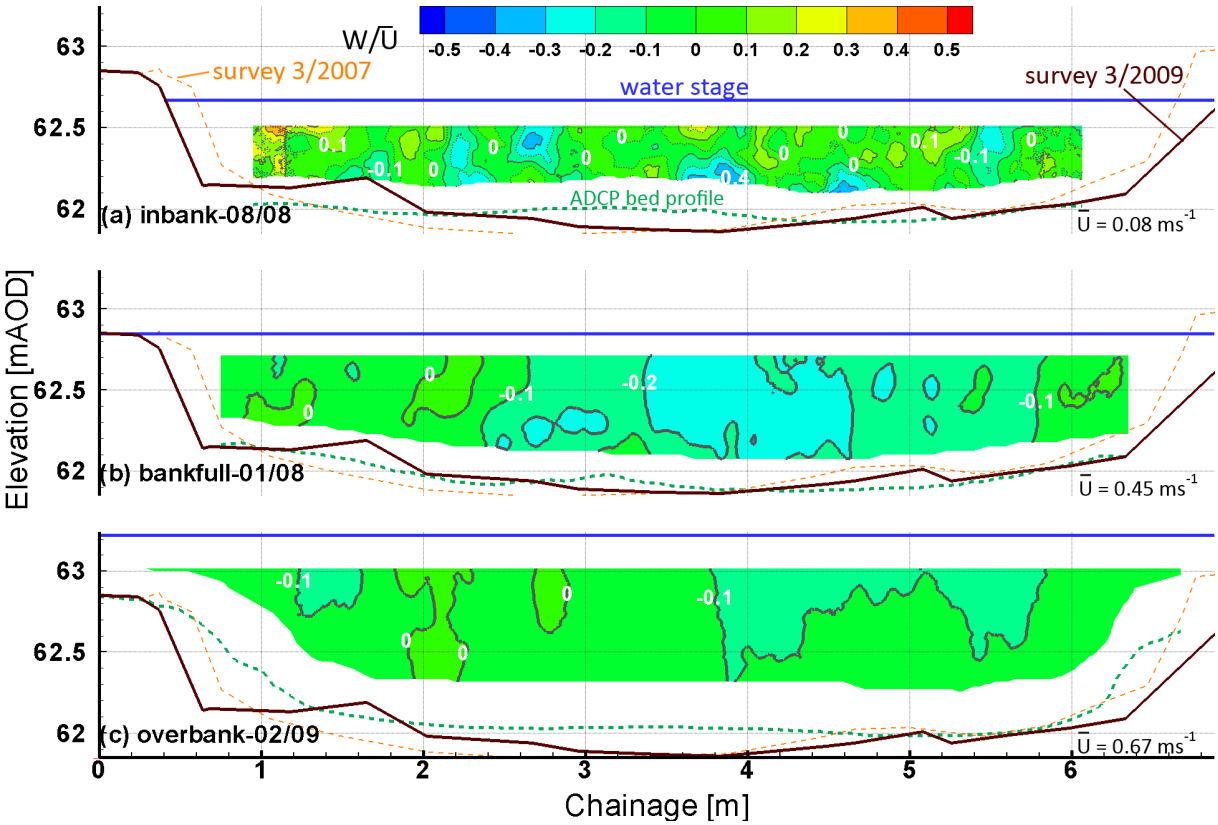

Figure 5.8 Isovels of $W/\overline{U}$ at CS 2.

5.2.2 Secondary circulation pattern at cross section 2

The lateral and vertical velocities have been used to construct secondary flow vectors, the results of which are presented in Figure 5.9. A definitive pattern of secondary flow circulation corresponding to the inbank flow is difficult to discern (Figure 5.9a). This is perhaps not too surprising since the magnitude of velocity vectors is small (< 0.2ms^{-1}) over most of the cross section.

For the bankfull condition (Figure 5.9b), there is evidence to suggest that an anti-clockwise secondary circulation cell exists between *y* = 1.1 and 2.0m. A change of velocity direction over the depth can be observed between *y* = 3.6 and 4.0m. However, it is difficult to infer a secondary cell at this location. The location of the relatively strong lateral velocities between y = 3 and 6m coincide with the location of the high streamwise velocity core (see Figure 5.5b), which perhaps suggests that the velocities in this region are affected by centrifugal force, i.e. Prandtl's secondary flows of the first kind (Perkins, 1970).

For overbank flow (Figure 5.9c) there is evidence to suggest that water is entering the main channel from both floodplains. However, the velocity vectors on the right hand half of the cross section suggest that the flow from the right hand floodplain is more dominant than that from the left. This is perhaps not too surprising given the size and lateral extent of the floodplain at this region (Figure 5.10). Two secondary flow cells appear to exist at y=2.4 and 5.6m.

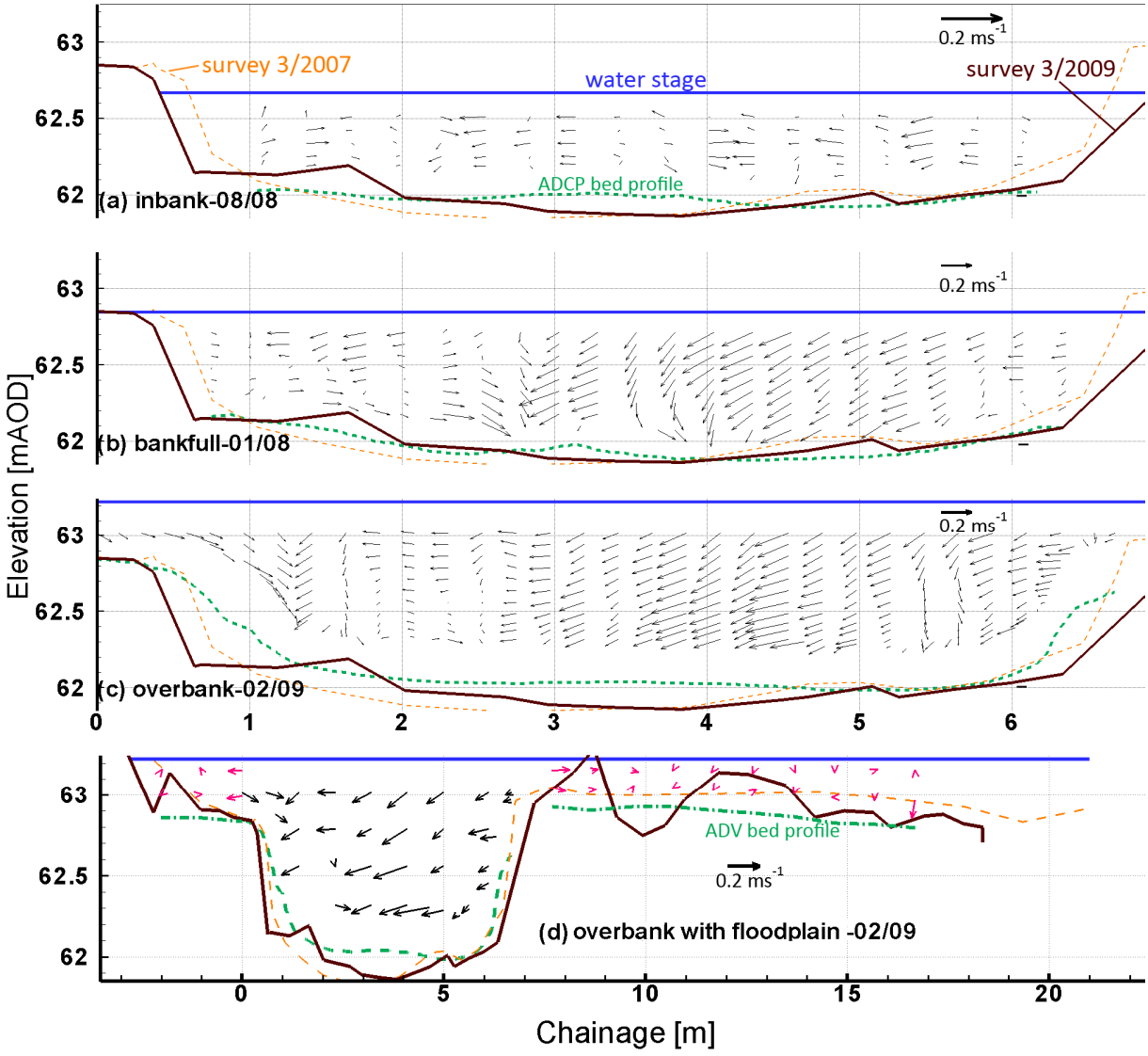

Figure 5.9 Secondary circulation at CS 2.

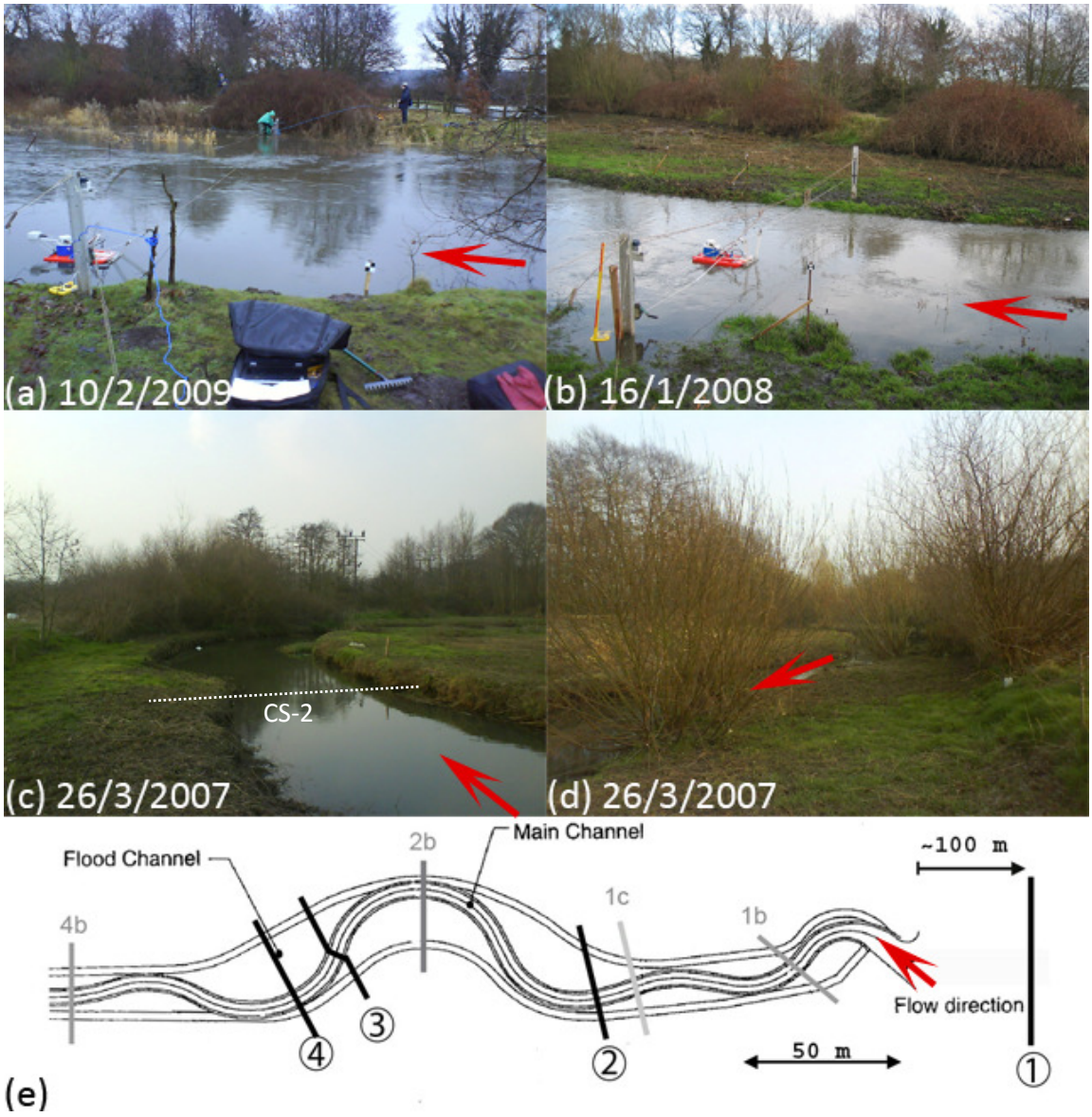

Figure 5.10 Condition of CS 2 at various times.

The magnitude of *U*, *V* and *W* on the floodplain was significantly lower than in the main channel as shown in Figures 5.9d and 5.11. Furthermore, the direction of *V* and *W* at y < -1m and y > 8m, shown in Figure 5.9d, vary greatly. This indicates low interaction between the flow in the floodplain and in the main channel at that particular region. It is postulated that the small values of velocity on the floodplain may be attributed to the high floodplain roughness in this location. For example, Figure 5.10a indicates the presence of large shrubs/bushes which serve to create a low velocity zone immediately upstream. The low, unstable velocities in this zone will further aid in the generation of large scale planform vortices which have a tendency to occur naturally as a result of the floodplain/main channel interaction. It is acknowledged that the apparent different direction of the flow on the right floodplain (Figure 5.9d) to that in the main channel could be caused by an error in

the projection of the velocities obtained by the ADV onto the correct coordinate system. This may arise since the ADV is not equipped with heading sensor/compass enabling exact orientation to be achieved. However, visual observations undertaken during the experiments and the information illustrated in Figure 5.10a would tend to discount this. Figure 5.10b – e also give an indication that the floodplain on the right hand bank increases in size compared to that on the left hand bank, while the main channel remains relatively straight (at this location). This further suggests that the velocities on the right hand floodplain would reduce as a result of the large cross section area. However, it is acknowledged that during periods of high floods this may not necessarily be the case.

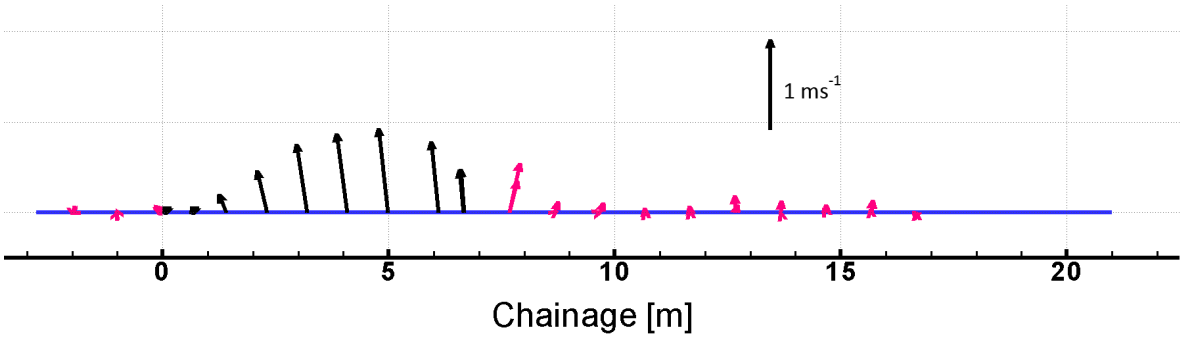

Figure 5.11 Distribution of horizontal velocity for the data located nearest water surface at CS2 for the overbank case 02/09 (planview).

5.2.3 Spatial velocity distribution at cross section 4

Figure 5.12 indicates that the bed profile obtained using the ADCP measurements agrees well with that of the survey data. A noticeable difference was observed near the banks where the bed elevation changes dramatically. In such a location, the bed profiling from the ADCP is less reliable, since the profile is calculated by taking the average of data from four transducers, only one of which is likely to pointing directly at the channel wall. As the flow depth increases, the region of high streamwise velocity can be seen to migrate towards the inner meander (i.e. the right floodplain) (see Figure 5.12).

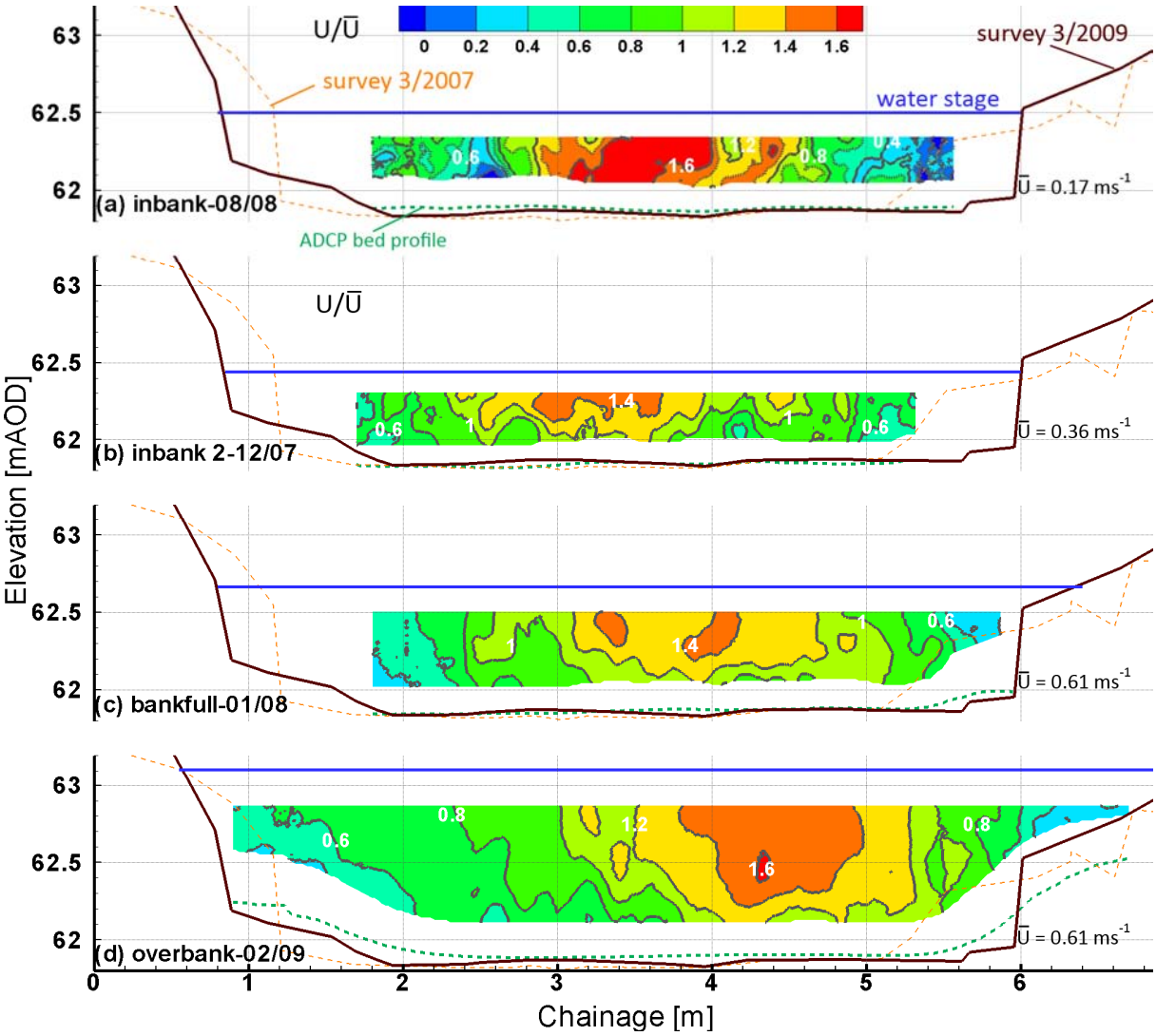

Figure 5.12 Isovels of $U/\overline{U}$ at CS 4.

The overall magnitude of the lateral velocity is observed to increase as the depth of flow increases (Figure 5.13). Two cores of positive sign (region with red colour) lateral velocity occurred on the left and near the centre of the main channel for the overbank case (Figure 5.13). The positive direction of the lateral velocity is defined as the movement from right to left. Both cores are located in the lower part of the channel and both are accompanied by two negative lateral velocity cores located above right from their positions. This suggests the existence of secondary circulations.

The values of $\overline{V}/U_{max}$ range from –0.40% to -7.22% while $\overline{|V|}/U_{max}$ varies in the range of 4.6% to 10.9% (Table 5.6). Interestingly, the largest magnitudes for both parameters are for the inbank condition. The values of both parameters decrease until bankfull then increase again for the overbank condition. The magnitude of $\overline{|V|}/\overline{U}$ is somewhat similar to that observed in CS 2. This is

perhaps surprising but again may arise as a result of flow from the floodplain entering the main channel. In general, the values of $W/\overline{U}$ are becoming smaller and less varied from inbank to overbank condition (Figure 5.14).

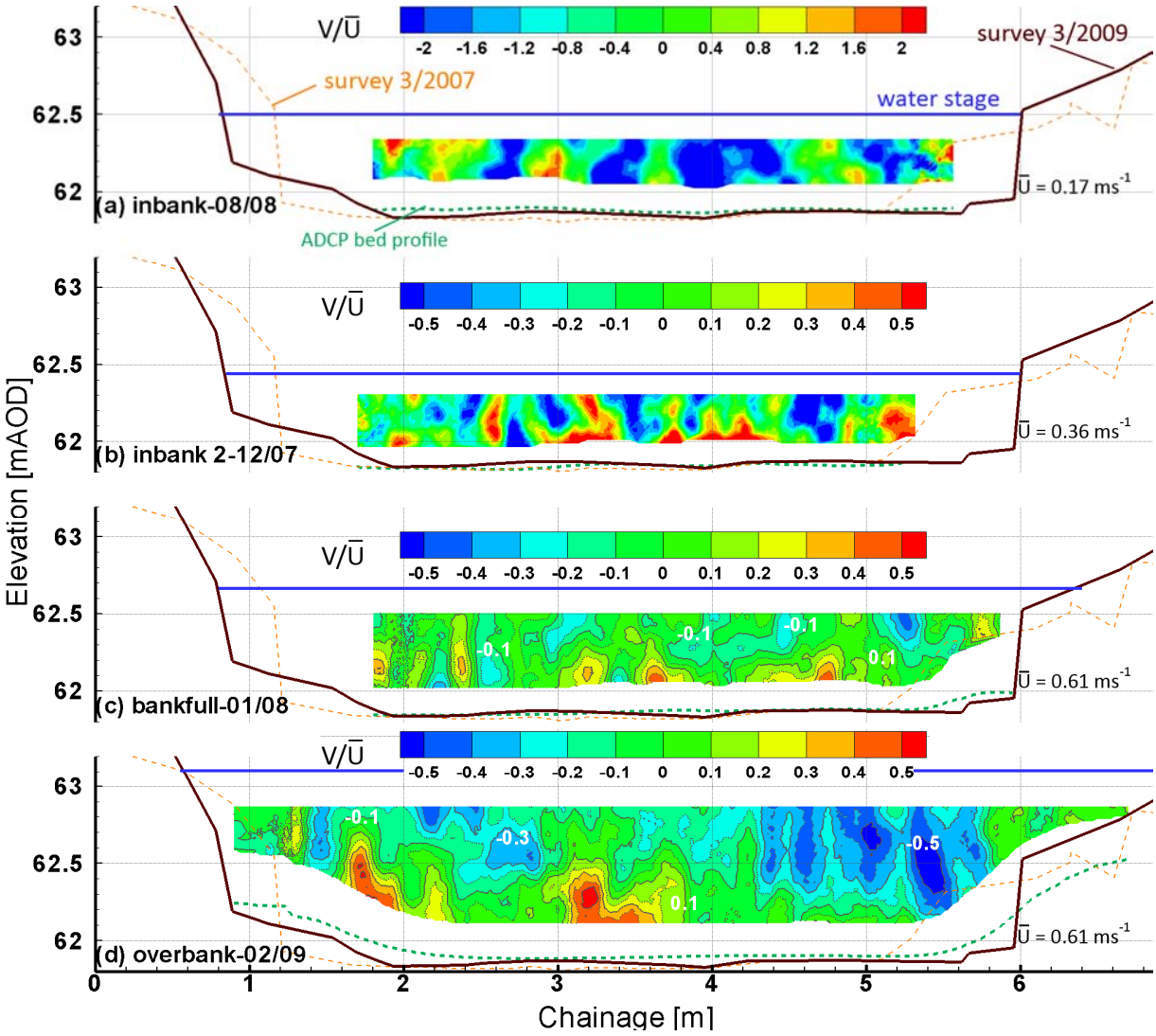

Figure 5.13 Isovels of $V/\overline{U}$ at CS 4

		18/08/2008 Inbank	07/12/2007 Inbank	16/01/2008 Bankfull	10/02/2009 Overbank
$\overline{U}$	(ms^{-1})	0.17	0.36	0.61	0.61
U_{max}	(ms^{-1})	0.35	0.56	0.90	0.98
$\overline{V}$	(ms^{-1})	-0.03	-0.01	0.00	-0.04
$\overline{\lvert V \rvert}$	(ms^{-1})	0.04	0.03	0.04	0.07
V_{max}	(ms^{-1})	0.09	0.12	0.17	0.21
V_{min}	(ms^{-1})	-0.12	-0.12	-0.17	-0.24
$\overline{W}$	(ms^{-1})	0.00	0.03	0.01	-0.03
W_{max}	(ms^{-1})	0.02	0.06	0.08	0.04
W_{min}	(ms^{-1})	-0.04	-0.02	-0.07	-0.10
$\overline{V}/U_{max}$	(%)	-7.22	-1.33	-0.40	-4.45
$\overline{\lvert V \rvert}/U_{max}$	(%)	10.85	6.21	4.61	7.51

Table 5.6 Mean and extreme values of U, V and W for CS 4.

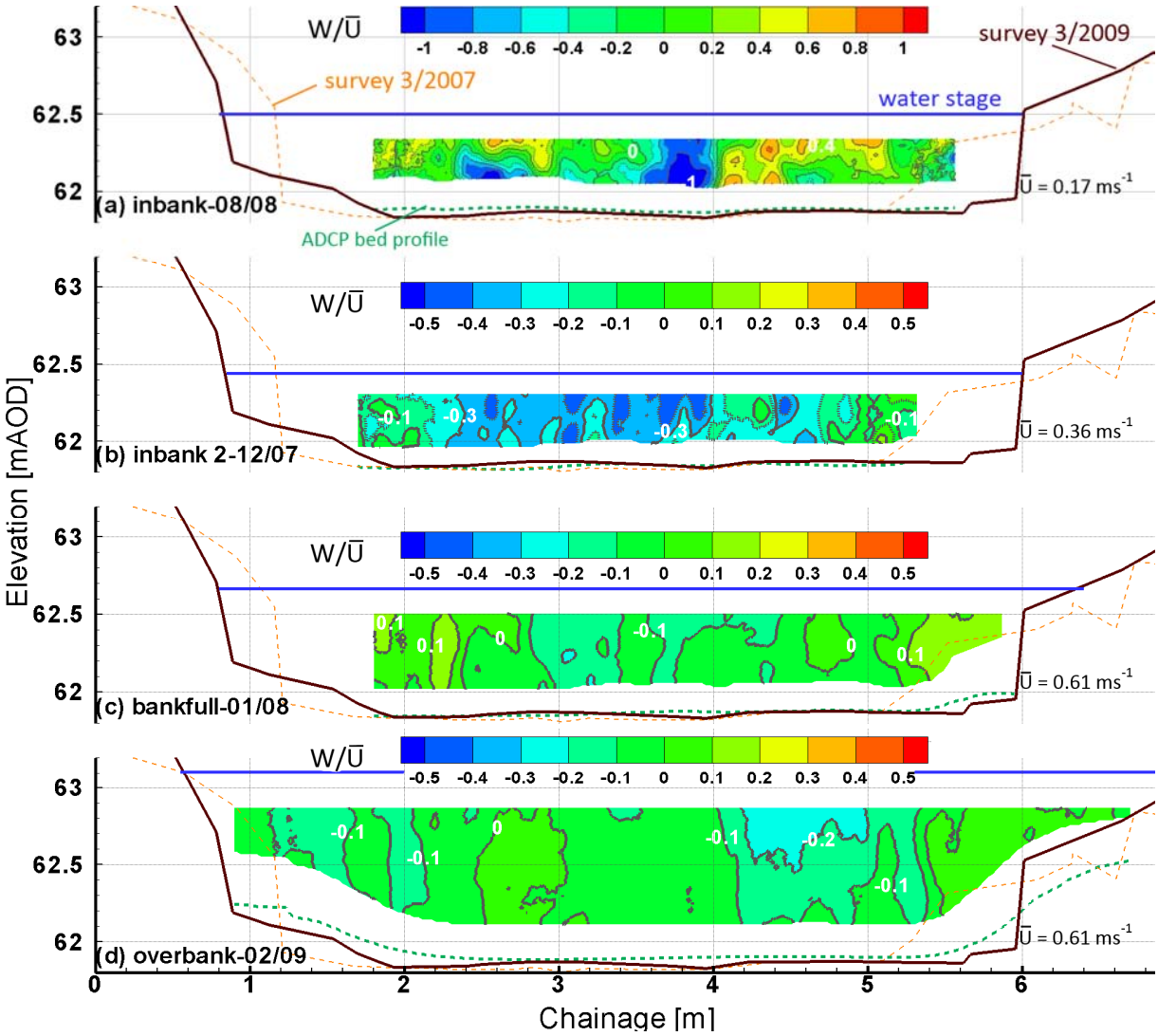

Figure 5.14 Isovels of $W/\bar{U}$ at CS 4.

5.2.4 Secondary circulation pattern at cross section 4

The lateral flow for the inbank case was dominated by a circulation towards the outer meander (Figure 5.15a) that appeared due to the centrifugal force in bend. An indication of a clockwise secondary cell is detected at y = 1.6 – 2m. This pattern is clearer for the second inbank case (Figure 5.15b): an anti-clockwise circulation appears at y = 3 m which possibly extends towards the right bank. Similar circulation patterns but with higher magnitudes appears to exist for the bankfull condition (Figure 5.15c). However, it is acknowledged that an alternative interpretation could be made, i.e. four smaller anti-clockwise cells exist between y = 1.8 – 5.8m.

The strength of the secondary flow in the overbank condition was significantly higher than that in the bankfull condition. The anti-clockwise circulation on the right hand side still exists in the overbank condition (Figure 5.15c). However, an additional anti-clockwise cell, at y = 1.6 – 3m, is apparent. The existence of two cells rotating in the same direction appears to be driven by the centrifugal force on the bend. The magnitude of the lateral velocity appears to be directly related to the magnitude of the streamwise velocity, e.g. the location of the strong lateral flow towards the left bank near the right bank coincides with the location of the maximum streamwise velocity core.

The existence of an anti-clockwise secondary cell near the right bank for the inbank and bankfull case was also confirmed by an ADV measurement (Figure 5.15e). Furthermore, Figures 5.15f and 5.16 shows that the water in half of the floodplain flows toward the main channel while the other half flows away from the main channel, to the lower region near the floodplain edge.

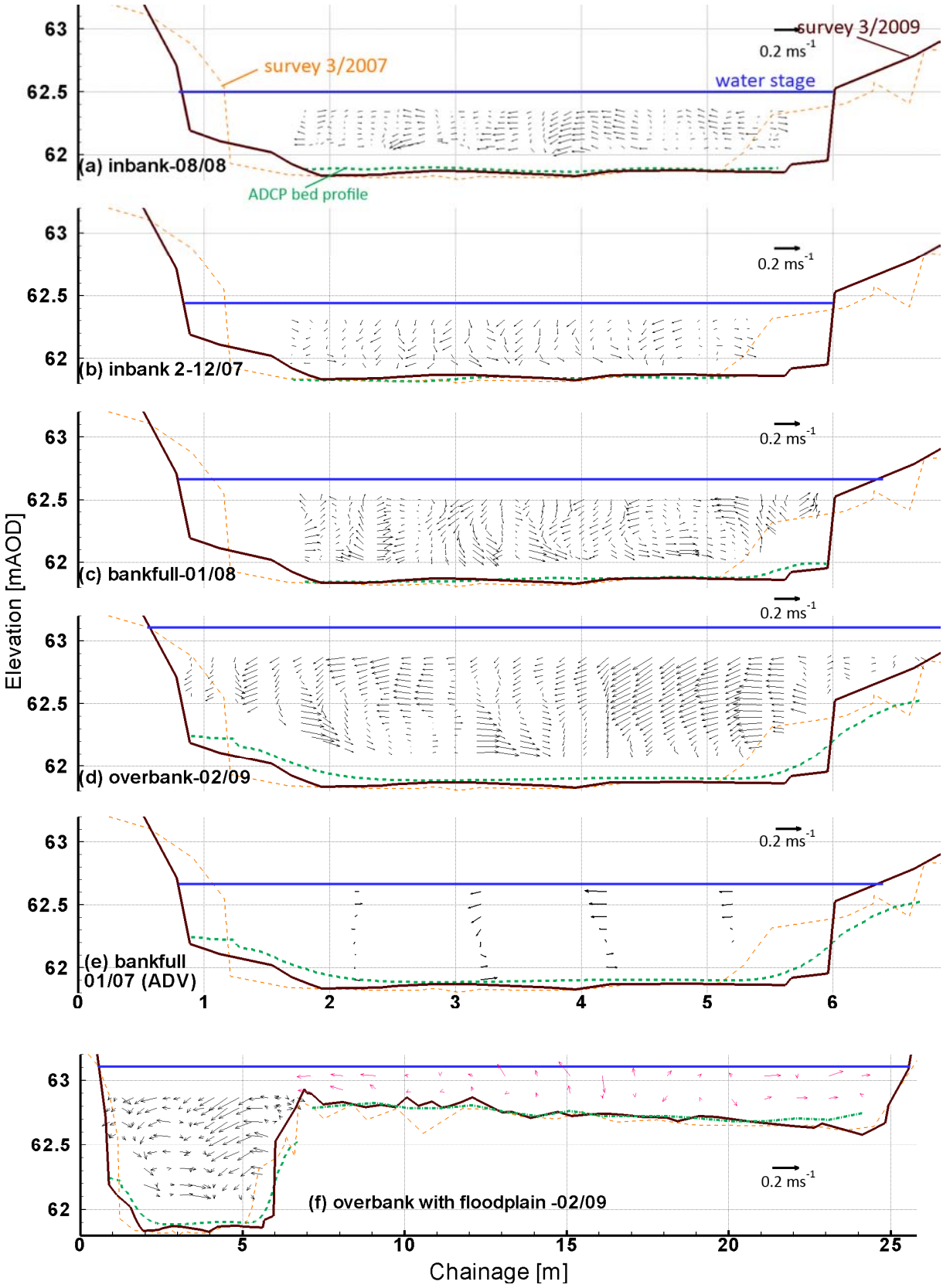

Figure 5.15 Secondary circulation for CS 4.

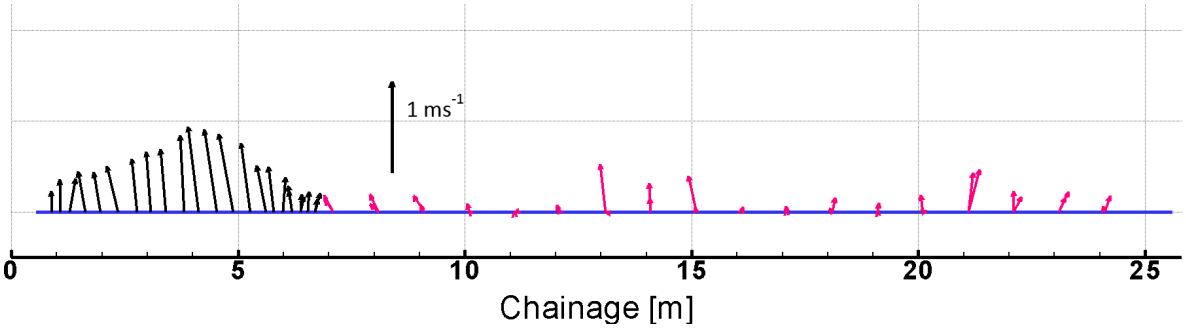

Figure 5.16 Distribution of horizontal velocity for the data located nearest water surface at CS4 for the overbank case 02/09 (planview).

5.2.5 Comparison of the flow in the river and physical model at cross section 4

As the flow depth increases, the region of high streamwise velocity can be seen to migrate towards the inner meander (i.e. the right floodplain) (see Figure 5.12). Such phenomenon was also observed on the 1:5 model with horizontal floodplain as shown in Figures 5.17 a – d_2. In addition, the magnitude of the maximum velocity in the river increases with increasing water depth. This is in contrast to what was observed in the model for the cases with horizontal floodplain. The model results also suggest that an increase of water depth would result in a reduction of the magnitude of U_d in the main channel but an increase on the floodplain (Figure 5.18). Interestingly, this behaviour was not observed at full-scale, i.e. the magnitude of U_d increased both in the main channel and on the floodplain as the water level increased (Figure 5.19).

The model results for an inclined floodplain slope (Figure 5.17 c_3 and d_3) appear to give more realistic results: The magnitude of U_d on the floodplain increases with rising water level but still slightly reduces in the main channel (Figure 5.20). Interestingly, in the current work, the floodplain slopes away from the main channel. This suggests that introduction of slope, regardless of its direction, on the floodplain reduces the flow interaction between the main channel and floodplain. According to Lambert and Sellin (1996) most of the water on the floodplain was flowing towards the main channel in the model. This is not the case at full-scale, with approximately half the water in the floodplain flowing towards the main channel and the other half travelling to the lower part of the floodplain (see Figures 5.15f and 5.16).

According to Figure 5.17, Lambert (1993) suggested two counter rotated secondary cells in all overbank cases. However, the secondary circulation and the number of cells could be easily interpreted differently, i.e. rather than just one single cell, the anti-clockwise cell in Figure 5.17c_3

could also be interpreted as multiple numbers of anti-clockwise cells. While it appears that the indication of secondary cells in the model is very clear, it should be noted that these cells were based on the lateral velocity only. Thus, there is less restriction in interpreting the circulation pattern in the model than in the river, as vertical velocity was also taken into account for interpreting the secondary flow cells in the river.

According to Figure 5.17, the extent of the two secondary cells might be different for each overbank case but generally their position remains the same and the clockwise secondary cell is always located above the anti-clockwise cell. A circulation pattern similar to the anti-clockwise cell recommended by Lambert (1993) can be drawn in the secondary circulation plot at overbank condition in the river (Figure 5.15d). The clockwise cell near the water surface in the model is, however, not apparent in the full-scale river data. This is indicated by the direction of the lateral velocity in the water surface, measured using LS-PIV, showing that most of the water in the surface was flowing towards the left bank (Figure 5.21).

The existence of an anti-clockwise secondary cell on the right side of the main channel for the inbank and bankfull case, confirmed by an ADV measurement (Figure 5.15e), also appeared in the 1:5 physical model, i.e. in Figures 5.17a and b. However, it is also acknowledged that the lateral extent of this secondary cell in the full-scale river is less than in the model for the bankfull case, i.e. while only a single cell is apparent in the model for the bankfull case, multiple cells seems evident in the full scale river for the same condition. More complex geometry and variation of roughness in the river might contribute to this. However, it is also acknowledged that the single secondary cell proposed by Lambert (1993) might be interpreted as multiple numbers of cells.

It is acknowledged that the determination of secondary flow cells in rivers is difficult and often subjective, since several possibilities for the circulation pattern might exist. Interpreting the interaction of the flow in the floodplain and main channel based on the velocity data at one cross section only is difficult, since conditions upstream and downstream of the cross section can affect the flow.

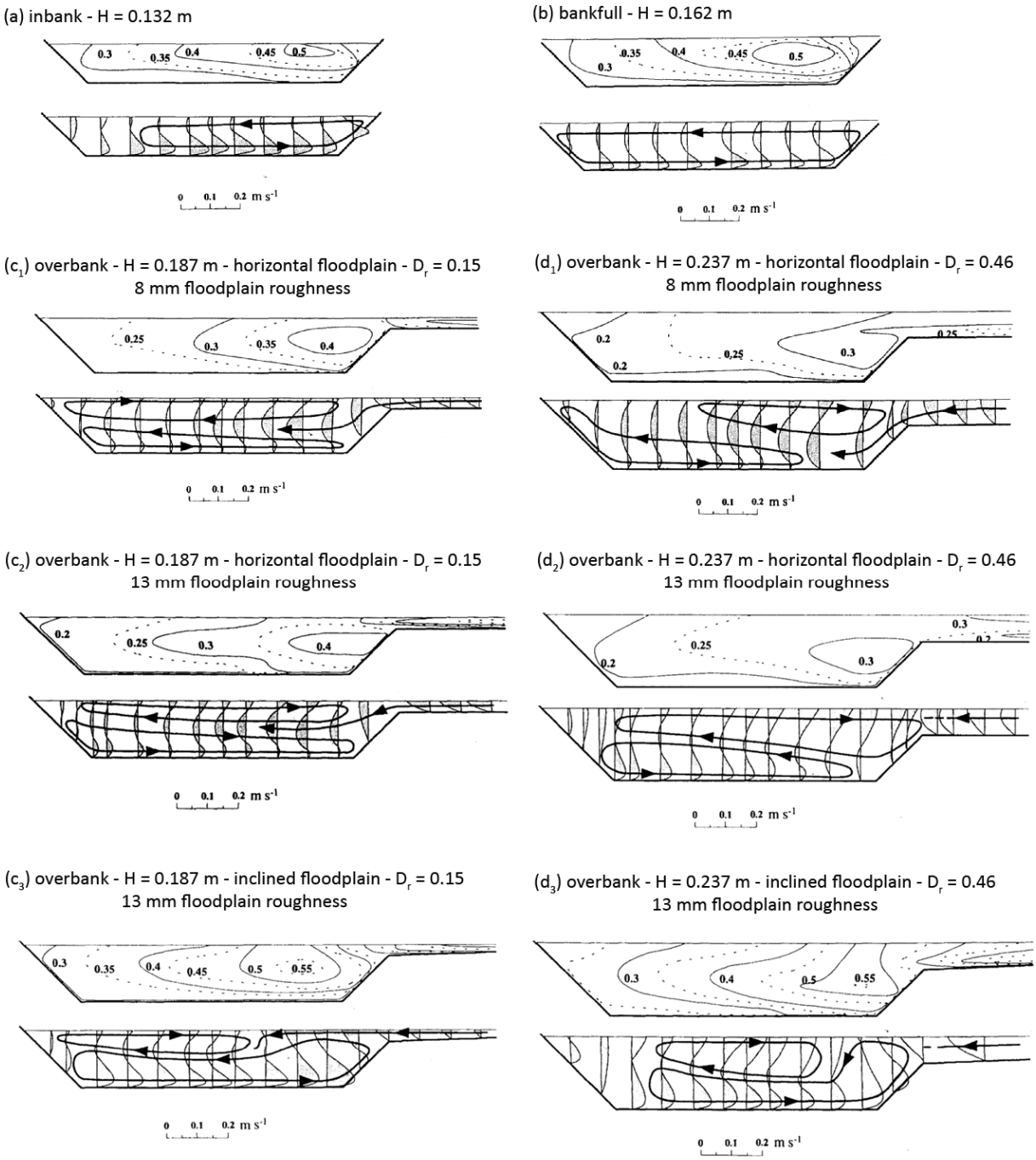

Figure 5.17 Isovel of streamwise velocity and transverse velocity pattern at CS 4 in the 1:5 model (after Lambert, 1993).

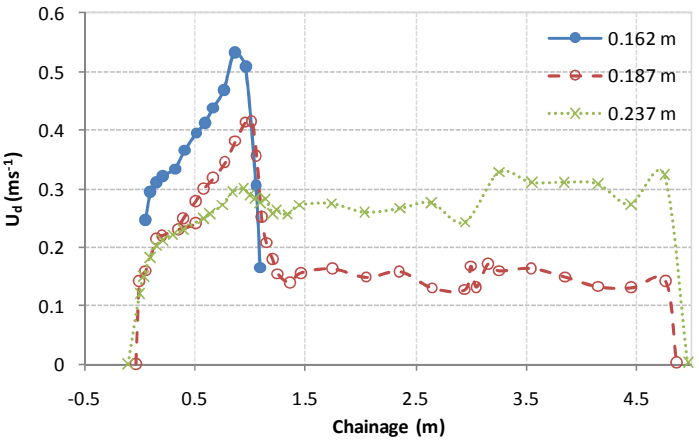

Figure 5.18 Variation of U_d across the channel at CS 4 in the 1:5 model with horizontal floodplain (after Lambert & Sellin, 1996).

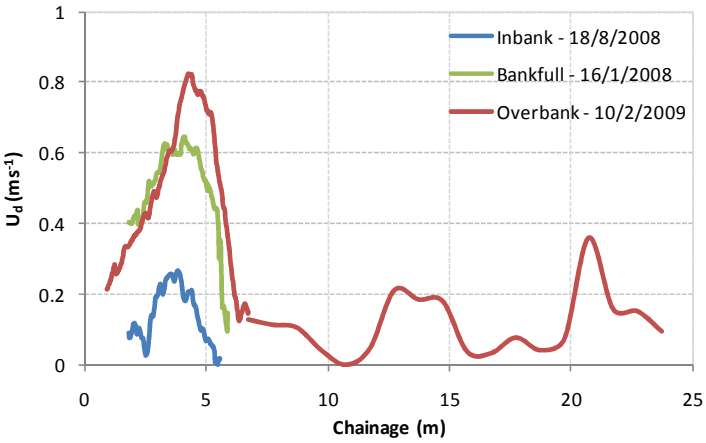

Figure 5.19 Variation of U_d across the channel at CS 4 in the full-scale river.

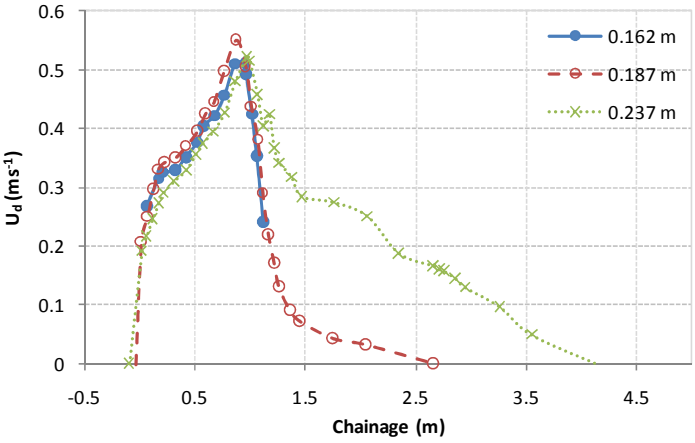

Figure 5.20 Variation of U_d across the channel at CS 4 in the 1:5 model with inclined floodplain (after Lambert & Sellin, 1996).

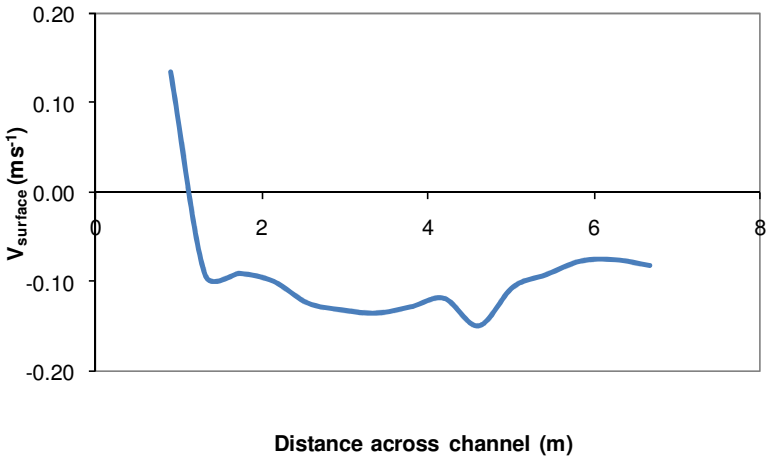

Figure 5.21 Lateral velocity at the water surface during an overbank condition at CS 4 (10/2/2009) obtained from PIV.

5.2.6 Comparison of the velocity data obtained from transect averaging (TA) and stationary measurements (SM)

The isovels of $U_{max}/\overline{U}$ obtained from TA results for CS 2 (Figure 5.5) have a good agreement with similar data obtained from stationary measurements (Figure 5.22), i.e. their magnitudes are similar (quantification of the difference are presented in detail in section 5.3). In general, the secondary circulation patterns obtained from TA agree with the secondary circulation patterns obtained from SM (Figure 5.23). The lateral flow towards the left bank on the right part of the main channel is present in the SM data for all cases. The indication of an anti-clockwise secondary cell on the left part of the channel for the bankfull and overbank case is also present in the SM data. There is an indication of an anti-clockwise secondary cell in the left part of the channel for the inbank case of the SM data between y = 2.2 and 3.2 m. However, this is not shown in the TA data. This may be because the lateral velocity magnitude for the inbank case was low compared to the standard deviation of the horizontal velocity obtained by ADCP (i.e. 0.1 – 0.2ms^{-1}).

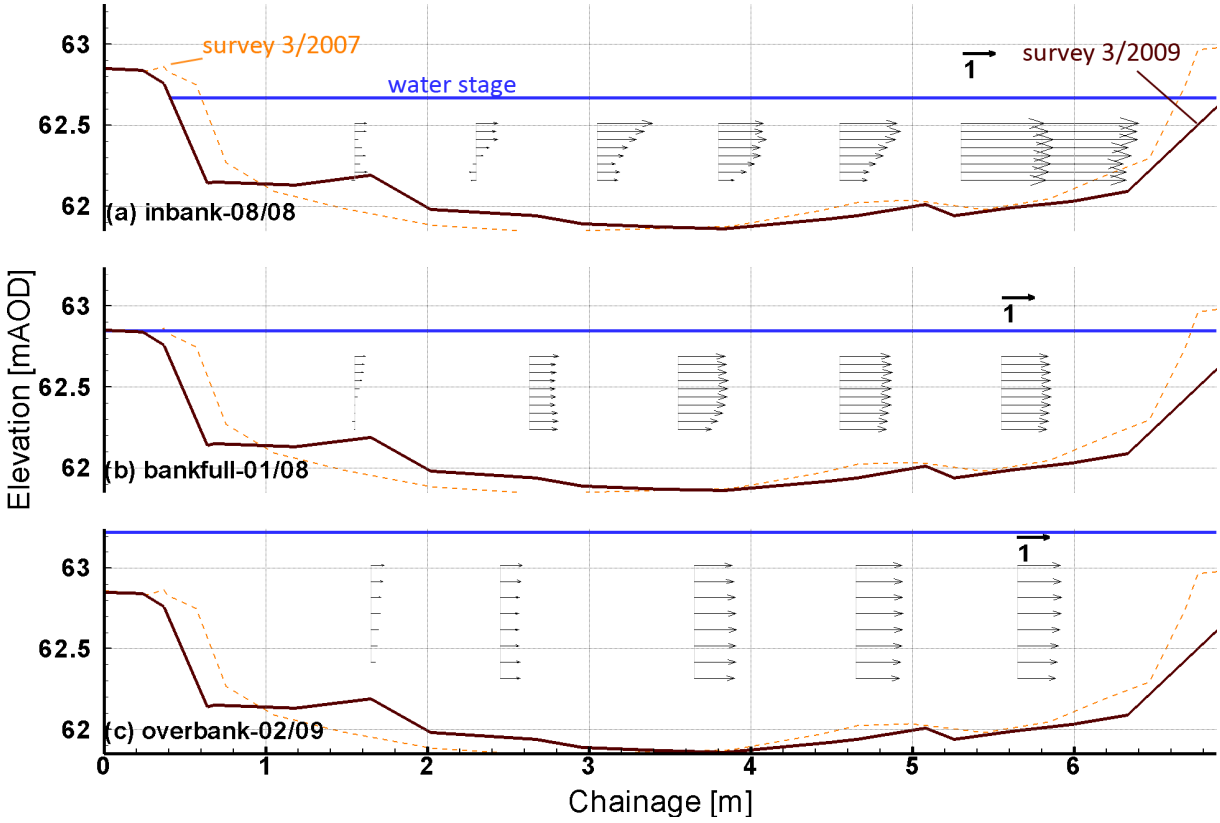

Figure 5.22 Vector plot of $U/\overline{U}$ at CS 2 (stationary measurements).

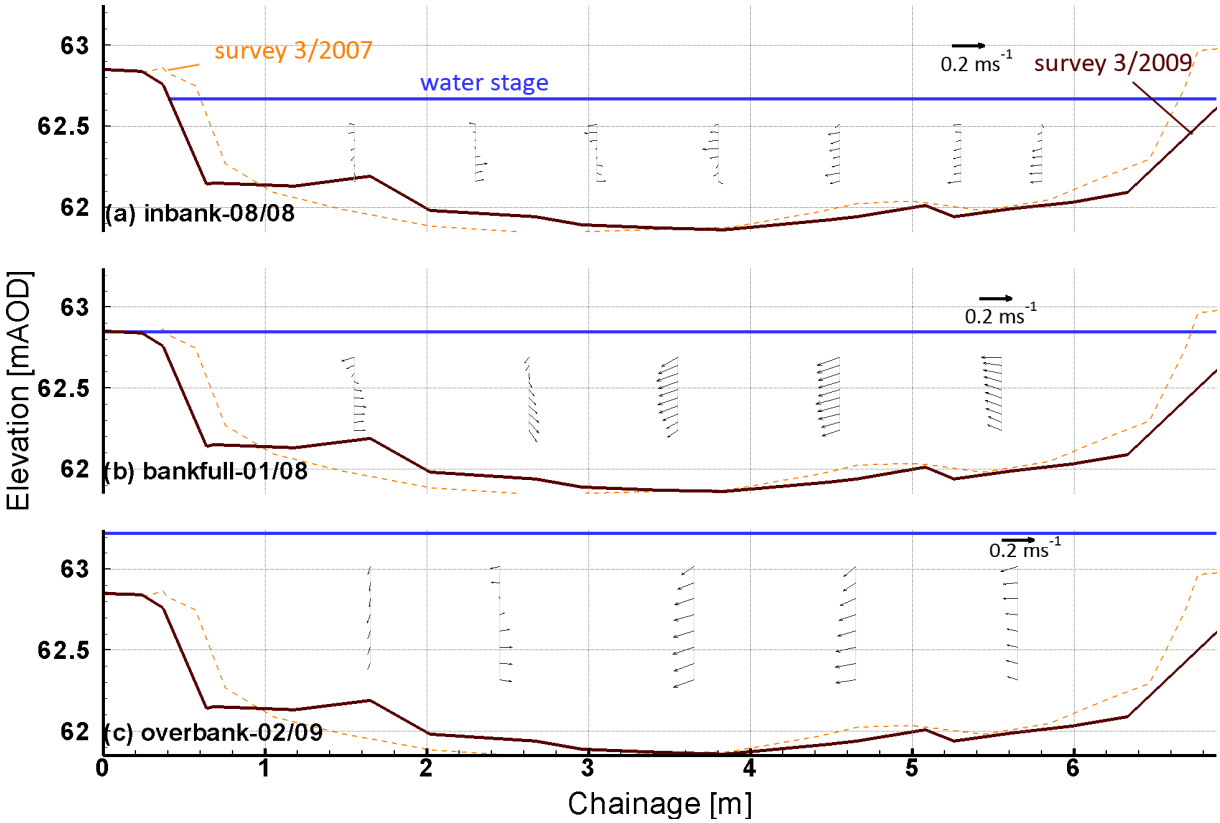

Figure 5.23 Secondary circulation at CS 2 (stationary measurements).

The isovels pattern of $U/\overline{U}$ obtained from TA results (Figure 5.12) are similar to that obtained from SM (Figure 5.24). Comparison of the secondary flow circulation between the data obtained from TA and SM show a reasonable agreement between both methods (Figures 5.15a, c, d and 5.25). Agreement between both methods appears to be better for higher magnitude of *V* and *W* (Figures 5.15a and 5.25a). The magnitude of the velocity vectors obtained from SM for the bankfull case is generally lower than those obtained from TA. The pattern of the circulation at y = 3.2m is similar between both methods. The circulation pattern of the SM data at y = 2.2m is quite similar to that of the TA data at y = 2.1m. Comparison of circulation pattern for the rest of the data is difficult, as the magnitude of *V* and *W* on the stationary data is very low. Good agreement of the circulation pattern is achieved for the overbank data.

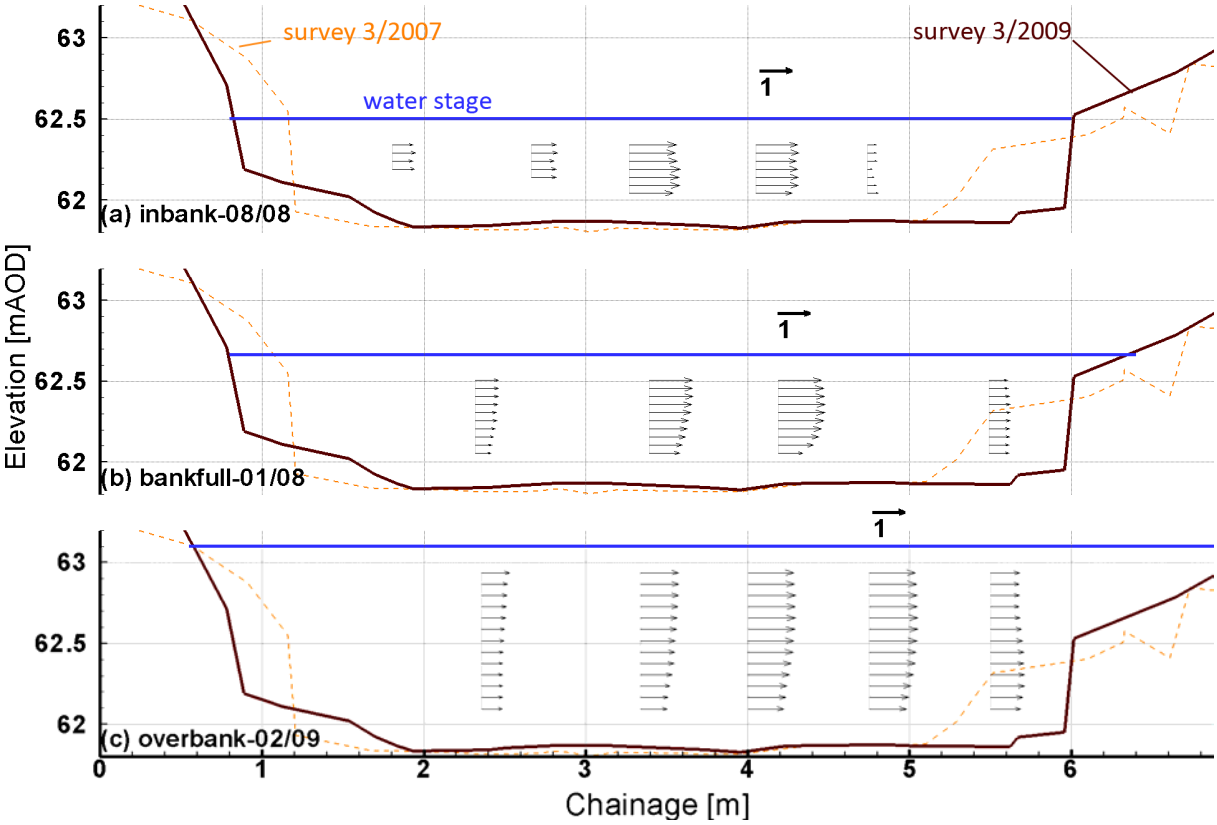

Figure 5.24 Vector plot of $U/\overline{U}$ with respect to depth at CS 4 (stationary measurements).

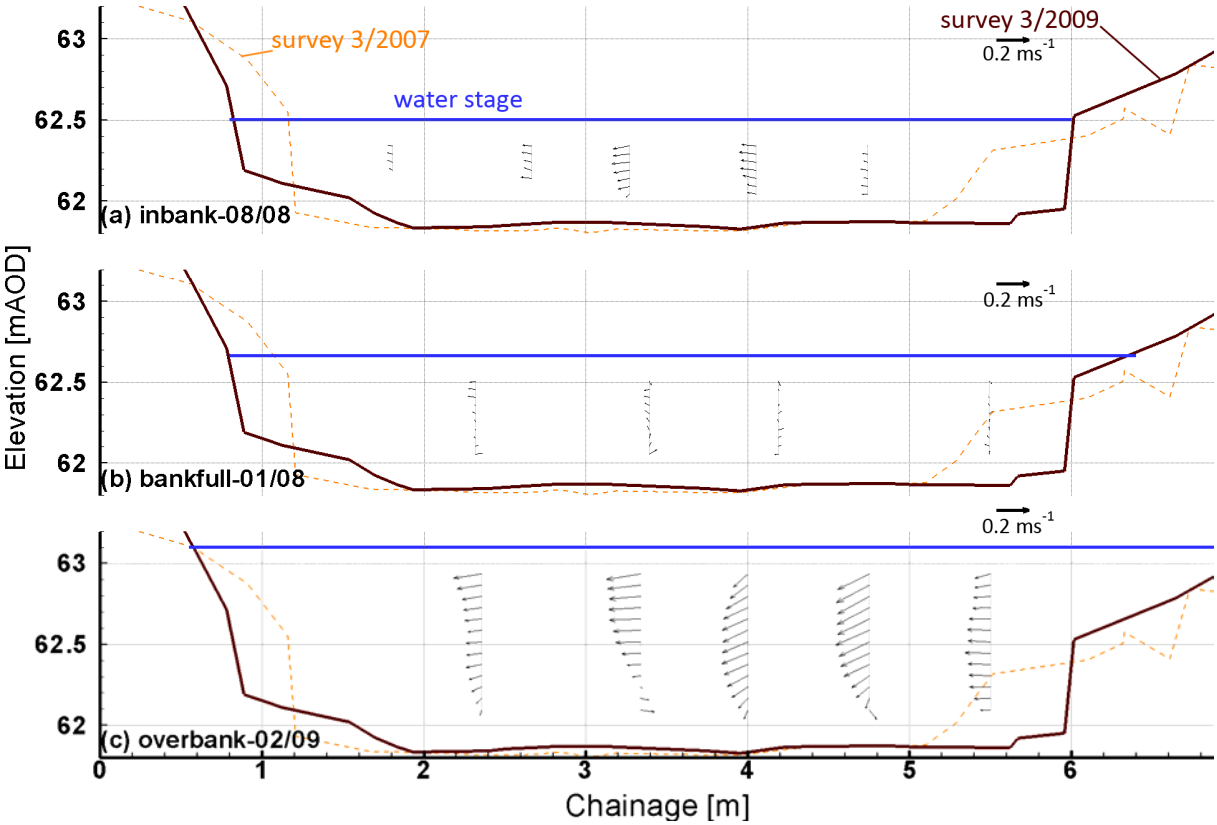

Figure 5.25 Secondary circulation for CS 4 (stationary measurements).

5.3 Lateral distribution of depth-averaged streamwise velocity

The accuracy of the TA method was assessed against the SM method by calculating the Root Mean Square Error (RMSE) between U_d obtained from TA and SM at the locations where SM data are available (Figures 5.26 and 5.27). For one particular case, i.e. the inbank case at CS 2, high differences in U_d, up to 162%, were observed. However, this appeared as the velocity magnitude on the particular case was very low, i.e. less than 0.2ms^{-1}. Thus, this case was excluded in further assessment.

The RMSE value for all the data excluding the CS 2 data for inbank case is 0.18ms^{-1} (Figure 5.28a). The majority of this error is contributed by the SM for CS 4 for inbank flow at y = 2.05m that has a difference of 67%. When this data point is excluded from the analysis, the RMSE value improves to 0.12 ms^{-1}. Furthermore, it should be emphasised that although the ADCP movement during the SM were heavily restricted, a level of uncertainty in the ADCP position during measurements should be expected. This uncertainty is associated with the accuracy of the ADCP bottom track data, human error and possible movement of the ADCP. The aforementioned RMSE value could be easily improved by adjusting the lateral position of the SM. An improvement of the RMSE value to 0.054

ms^{-1} could be achieved by adjusting the lateral position of 11 (out of 24) SM, with an average and a maximum adjustment of 0.12 and 0.20m respectively (Figure 5.28b). The adjusted SM are represented as red triangles in Figures 5.26 – 5.27. Following the adjustment, the depth-averaged streamwise velocity obtained from TA, excluding that for the inbank case of CS 2, overpredict the depth-averaged streamwise velocity obtained from SM by an average of 3.37%.

The difference in discharge after performing TA and depth averaging to the initial discharge using the standard measurement method, i.e. the average discharge of at least four transects that have a difference in discharge of less than 5%, is presented in Table 5.7. Overall, the discharge of the cross section computed after TA process is lower than the initial discharge by an RMSE value of 6.91 %. The majority of the discharges after TA are within 5% of the initial discharge. Higher differences are evident in the overbank case due to the additional difficulties in obtaining data during such conditions. Furthermore, a difference of 6.46% (RMSE) between the initial discharge and the discharge after the depth-averaging process being undertaken was obtained. As shown in Figures 5.6 and 5.19, the magnitude of U_d tended to increase with increasing water depth.

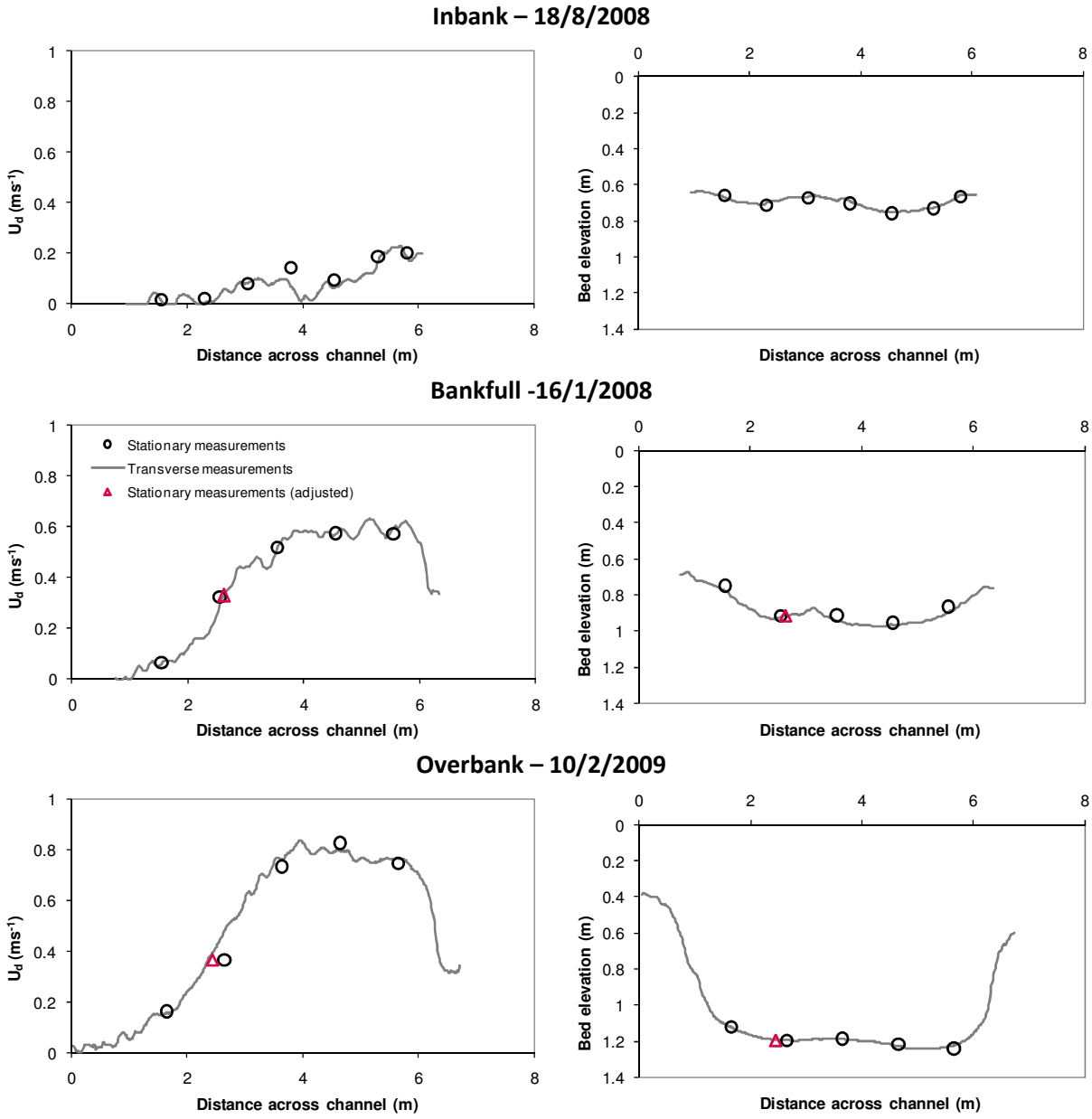

Figure 5.26 Comparison of U_d and bed profiles obtained from ADCP stationary and transverse measurements at CS 2.

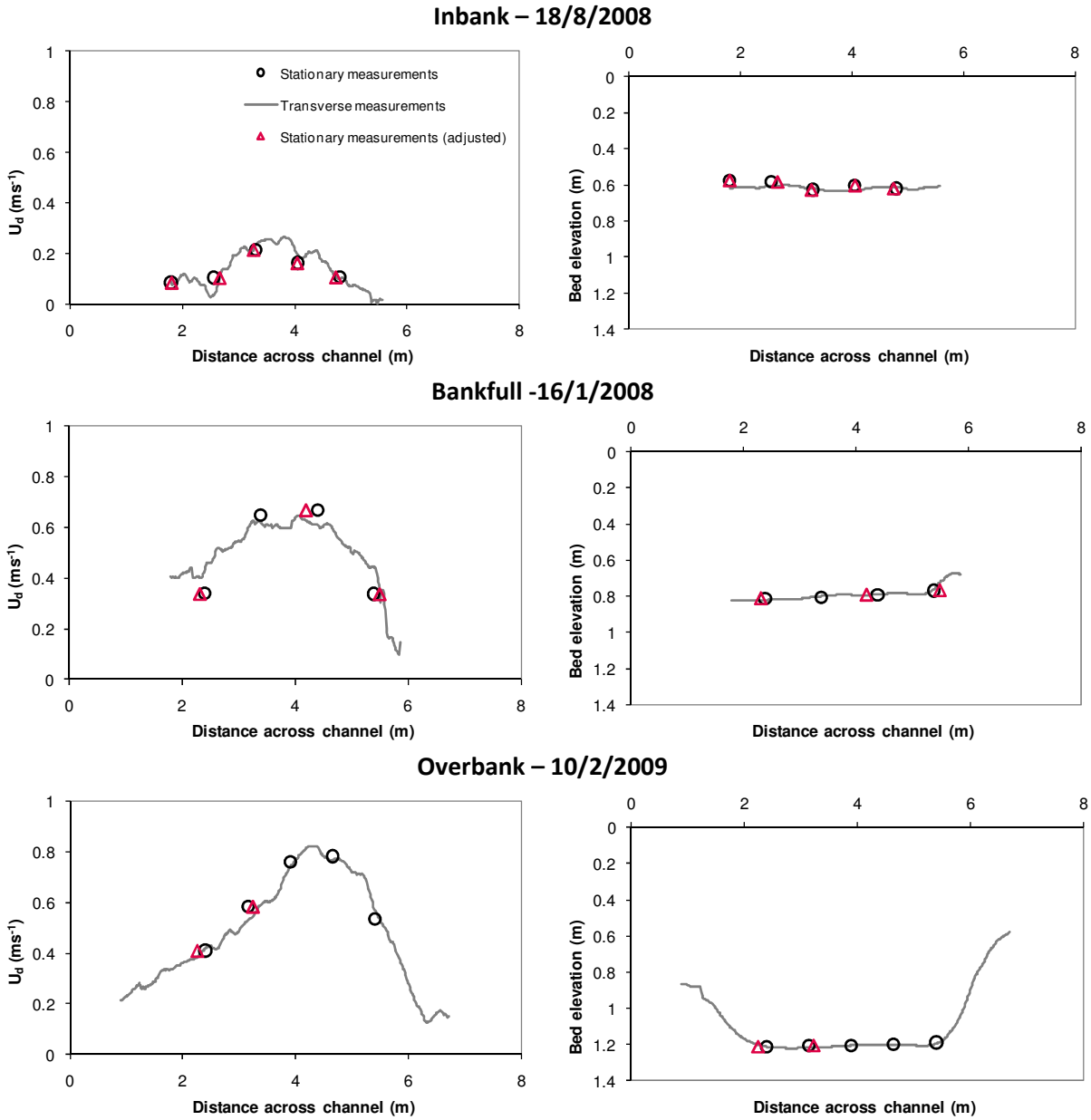

Figure 5.27 Comparison of U_d and bed profiles obtained from ADCP stationary and transverse measurements at CS 4.

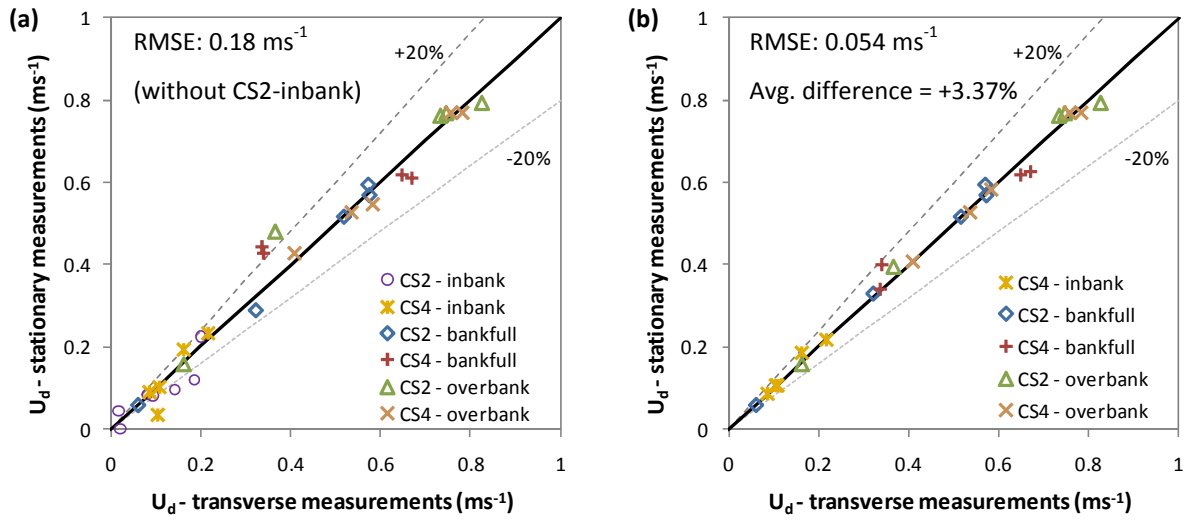

Figure 5.28 Difference of U_d values obtained from ADCP stationary and transverse measurements: (a) before lateral adjustment, (b) after lateral adjustment.

	Initial discharge (m^3s^{-1})	Difference to initial discharge (%)	
		After transects averaging	After depth-averaging
CS2- inbank	0.283	-3.59	2.90
CS2- bankfull	2.172	-2.46	-8.21
CS2- overbank	4.157	-8.90	-10.46
CS4- inbank	0.401	-5.89	-4.73
CS4- inbank 2	0.765	-3.55	-3.54
CS4- bankfull	1.866	-4.65	-4.03
CS4- overbank	3.565	-12.94	-7.48
RMSE		6.91	6.46

Table 5.7 Changes of discharge values after post-processing

5.4 Closing remarks

Several conclusions may be drawn from the study undertaken in this chapter and are outlined below:

1. The high streamwise velocity core at CS 4 moved towards the inner meander with rising water level (Figure 5.12).
2. The magnitudes of the U_{max} and U_d at CS 4 increase with rising water level, which is opposite to what has been observed in the 1:5 physical model for the cases with a horizontal floodplain (Figures 5.12, 5.17, 5.18 and 5.19). This indicates that there is less interaction between the flow in the floodplain and that in the main channel of the river.
3. The trend of the lateral distribution of the depth averaged streamwise velocity for various depths at CS 4 (Figure 5.19) is more similar to the behaviour in the model with an inclined

floodplain (Figure 5.20) rather than the model with a horizontal floodplain (Figure 5.18). This is interesting, considering that the direction of the floodplain slope in the river is opposite to the direction of that in the model. This suggests that introduction of a slope (regardless of its direction) on the floodplain reduces the flow interaction between the main channel and the floodplain.

4. There is a similarity between the secondary flow pattern in the model and river for the inbank and bankfull cases. A clockwise secondary flow cell indicated in the model can also be observed in the river for both inbank and bankfull flow conditions. However, there are also differences, i.e. an additional flow cell near the left bank observed in the river for the bankfull case did not appear in the model (Figures 5.15 and 5.17). Furthermore, the clockwise secondary flow cell indicated in all overbank cases in the model (Figures 5.17c_1 – d_3) did not appear in the river (Figures 5.15).
5. The secondary circulation pattern deduced from the ADCP transect averaging results agrees well with the secondary circulation pattern obtained using ADV (Figures 5.15c and e).
6. There is a reasonably good agreement for the bed profiles, U_d, $U/\overline{U}$ and the direction of the secondary flow for ADCP data obtained using transverse and stationary measurements.
7. Figure 5.7 indicates that the average magnitudes of the lateral velocity at CS 2 (straight section), normalised against the maximum streamwise velocity ($\overline{|V|}/U_{max}$), of the corresponding section were 4.5 – 6.5 times higher than that observed in a straight laboratory flume reported by Tominaga, *et al*. (1989) ($V = 0.02\,U_{max}$).

6 ANALYSIS OF DISCHARGE AND RESISTANCE COEFFICIENTS RELATING TO THE RIVER BLACKWATER

This chapter discusses the water slope, stage-discharge relationship and the resistance coefficients in the study site. The variations of conveyance capacity and resistance coefficient throughout the year due to seasonal variation are also examined. The stage-discharge and resistance data presented in this chapter are used later in the numerical modelling of the river (Chapter 7). In addition, the appropriateness of using LS-PIV data for estimating discharge is also assessed.

6.1 Analysis of water levels and slope data

Water levels in the research site were obtained from six staff-gauges. As some of the staff gauges were installed in 2007, water levels were not obtained during the first seven fieldwork campaigns. The locations of the staff gauges are shown in Figure 6.1. Typically, at least three readings were obtained on each staff gauge during a measurement campaign, typically lasting between 5 and 10 hours. The accuracy of these readings is estimated to be within ±5mm. The readings were then interpolated and extrapolated at 30-minute interval to obtain the water levels over the period of the field work on that day. The ADCP discharge measurements were also interpolated and extrapolated at the same interval, in order to enable the stage-discharge (*H v Q*) relationship to be established.

The water level at one of the staff gauges (cross section 0) was also logged electronically every 15-minutes courtesy of a nearby gauging station run by the Environment Agency - EA (see chapter 3). Unfortunately, the geometry data for this particular cross section was not available. The EA electronically-logged data for this cross section, in contrast to that of the pressure transducers mentioned earlier in chapter 3, appear to be reliable and have been verified with manual readings of the staff-gauge at cross section (CS) 0.

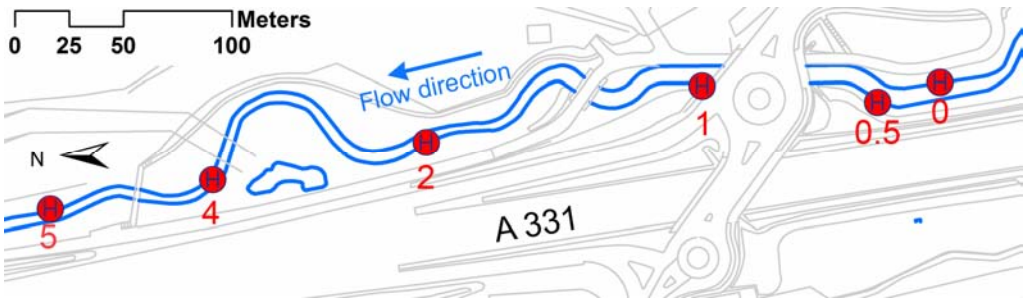

Figure 6.1 Staff gauges locations in the study site.

The ADCP measurements generally undertaken during periods that corresponded to the falling limb of the flood hydrograph with the exception of the data collected on 18/8/2008 (Figure 6.2.). The readings at CS 0 for the 28/5/2008 measurements were excluded from the Figure as there is a suspected error in the recording process, i.e. a high water level difference, of 0.15m, was observed between CS 0 and CS 0.5 for the 28/5/2008 data while the differences for the other datasets were always within 0.04m.

The water levels at every gauging station at the start of each fieldwork campaign shown in Figure 6.2. were plotted against downstream distance in order to show the typical water surface slope (S_W) (Figure 6.3.). The values of the water surface slope (S_W) between station 0 and 5 are between 4×10^{-4} and 1.9×10^{-3}. The slope during the rising limb measurement is on average 1.7 times higher than that during the falling limb measurements. It was noticed that the values of S_W between station 0.5 and 1 in the current research were in the range of 10^{-4} to 4×10^{-4} and significantly lower than in the other sections (Figure 6.3.). It appears that the slope at this section has been set to a certain value as this particular river section is man-made. The river section is made of concrete (and is a straight-rectangular channel) to prevent erosion as it is located directly under a road bridge.

Figure 6.3. indicates that S_W values between station 0 and 5, and that between station 2 and 4 are different. The values of the first are typically 20% to 84% lower than the latter. Occasionally, water level readings were also undertaken at a staff gauge (station 6) located 1100m downstream station 0. The S_W values between station 0 and 6 are similar to those between station 2 and 4. A difference of +1% to -7% was typically obtained for rising water level. Interestingly, the S_W value between station 0 and 6 was 34% lower than that observed at between station 2 and 4 during a rising water level.

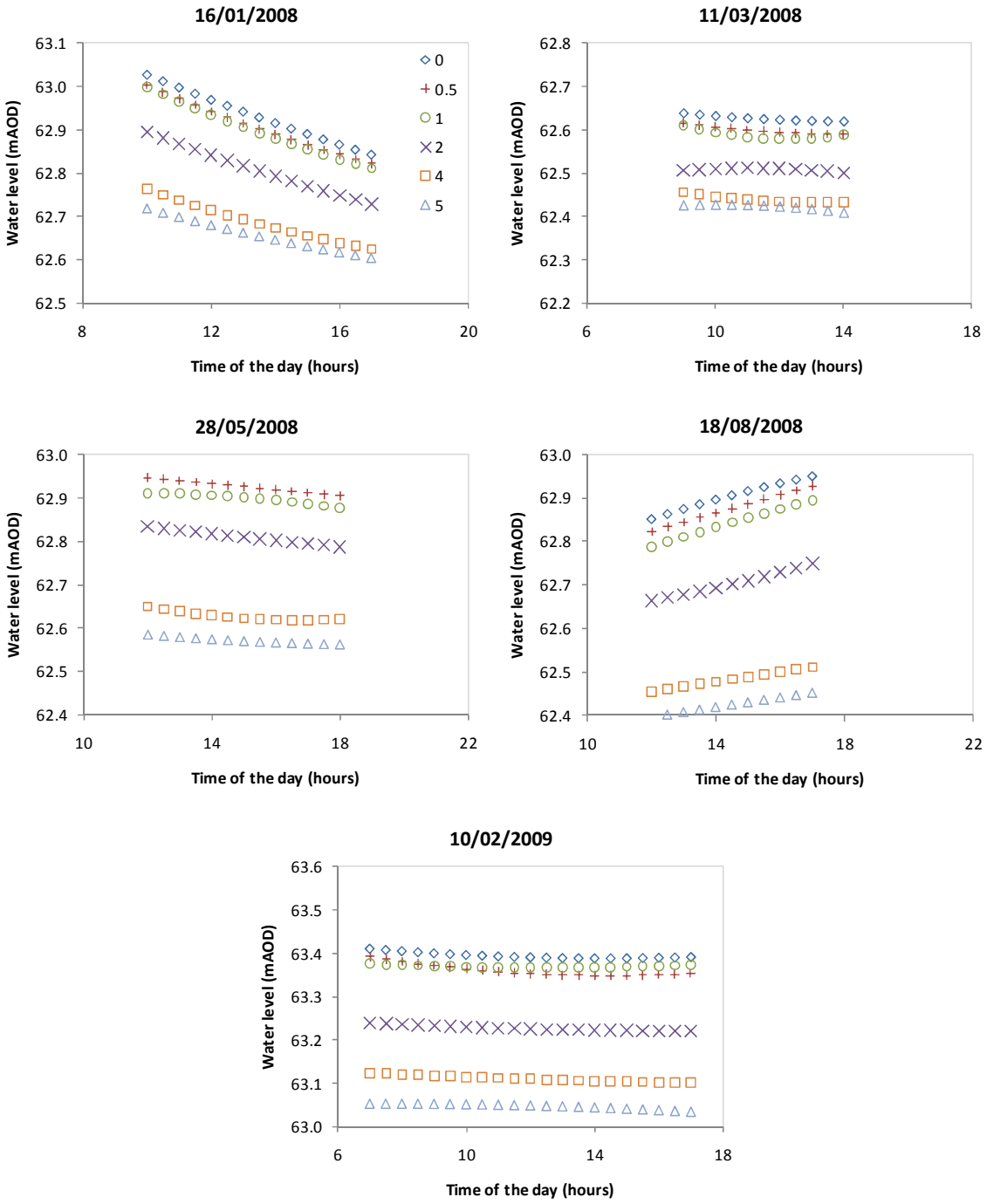

Figure 6.2 Water level elevations during five fieldwork campaigns.

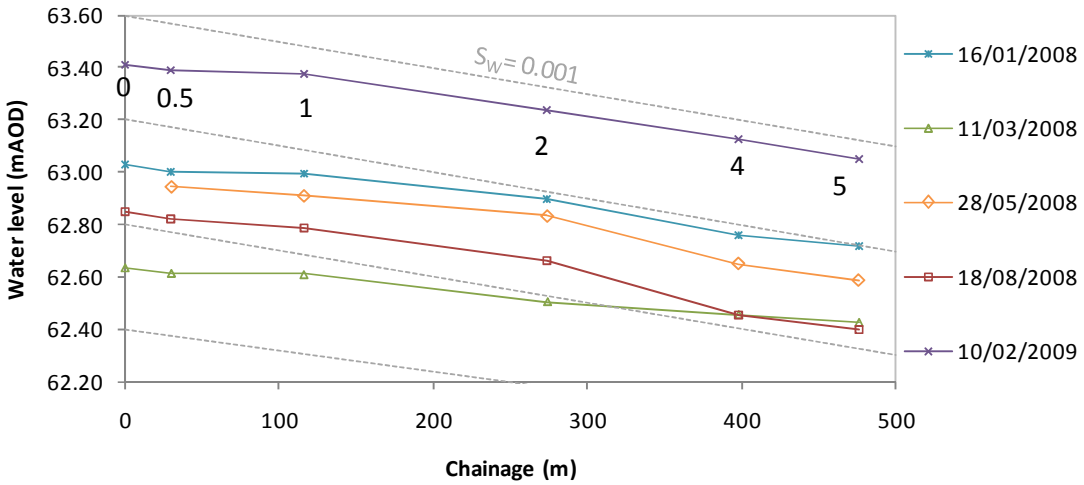

Figure 6.3 Water level elevations at six measurement stations during five fieldwork campaigns.

6.2 Effect of seasonal changes on the discharge capacity

The seasonal changes over the year are known to affect the shape of the stage-discharge (*H* v *Q*) rating curve. Rivers with low water depth and velocity magnitude tend to enable vegetation to grow in the main channel and frequently penetrate the water surface. Figure 6.4. illustrates the different conditions which arose at CS 2 in June 2008. The water depth during the measurement was 0.8m and the height of the weeds above the channel bed was estimated to be 1.5m. Removal of the vegetation located in the middle of the channel resulted in more uniform streamwise velocity distribution across the channel, i.e. the magnitude of velocity was reduced near the banks and increased in the middle of the channel (Figure 6.5.). In addition, it also reduced the perturbation of the flow (due to vegetation) as seen in the clearer secondary flow pattern after the vegetation had been removed (Figure 6.6.), at b ~ 2m.

Figure 6.4 Vegetation extent during an ADCP measurement at CS 2 on 13/6/2008.

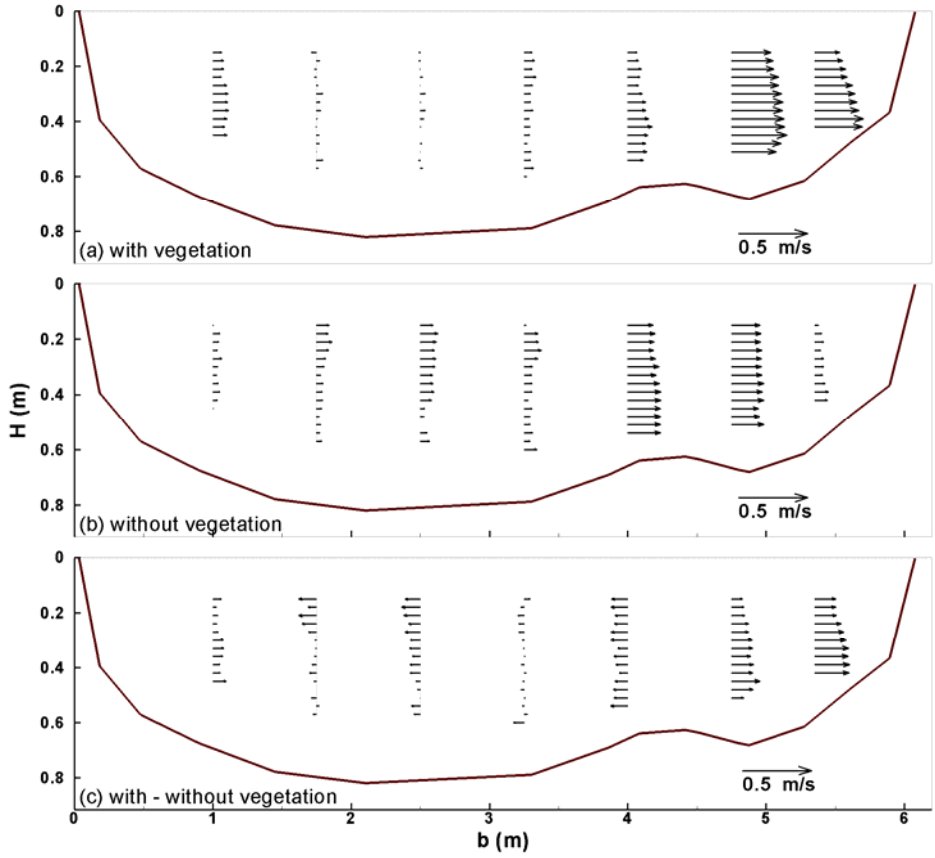

Figure 6.5 Streamwise velocity distribution at CS 2 on 13/6/2008 (plotted sideways).

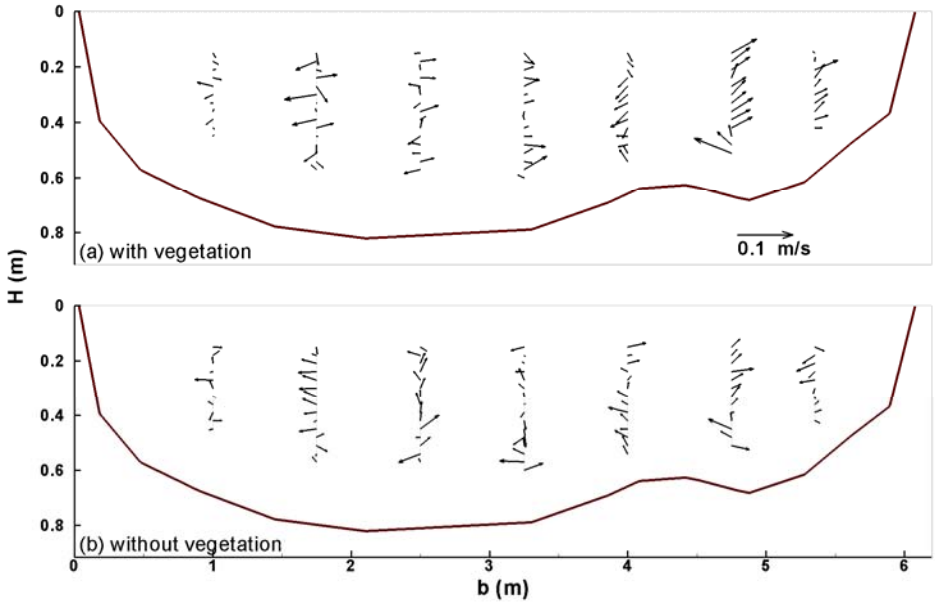

Figure 6.6 Resultants of lateral and vertical velocity vectors at CS 2 (13/6/2008).

The change of conveyance capacity with water depth was analysed using discharge data obtained from the EA gauging station (CS 0) for events between January 2006 and December 2007. This cross section was also chosen since due to the depth of the channel (~ 2m), the flow remained inbank during this period. The 2008 and 2009 discharge data are also available but are excluded from the analysis due to suspected instrument malfunction since June 2008. Figures 6.7. and 6.8. illustrate consecutive 15 minutes-averaged *H v Q* relationship for the years 2006 and 2007 respectively. This dataset has not previously been analysed by other researchers. The water depth in the Figures is based on the depth recorded by the Environment Agency. However, it is not certain whether or not the water depths were measured from the deepest part of the particular cross section. Observations indicated some variation in the river bed elevation over this cross section (Figure 6.9.). Three straight lines (red, blue and green) with gradients of 0.33, 0.67 and 1 were introduced to aid in distinguishing the difference between the monthly rating curves. A linear regression was also applied to each monthly rating curve to quantify the differences in the gradient of the curves. This approach made it easier to distinguish between rating curves, rather than using polynomial or log regression, and fitted the data reasonably well as indicated by the value of the coefficients of determination (R^2), which are discussed later.

The gradient of the *H v Q* curves for the year 2006 (Figure 6.7) appears to be smaller and more linear in winter months than in summer months. The first corresponds to the higher conveyance capacity of the river during winter months. The rating curves for January 2006 – April 2006 are reasonably

aligned with the green line (H = 0.33Q + 0.32). The gradient of the curve becomes steeper and more exponential in May, and reaches its maximum value during the months of June, July and August. The gradient starts to decrease again in September and becomes aligned again to the green line in November.

Throughout the year, the gradients of the rating curves for the year 2007 follow similar patterns to that for the year 2006 (Figures 6.7 and 6.8). It is however acknowledged that some of the 2007 curves are less steep than those for the same months in 2006 (June – August, December). This was initially attributed to the effect of regular maintenance of the reach (i.e. vegetation cutting) which occurred once in March 2007. However, this is not the case since the effect of vegetation cutting on the vegetation extent for the summer months of 2007 was low. This was shown by the similarity in the extent of vegetation in June 2007 and June 2008 (year without vegetation cutting). An example of this similarity is shown in Figure 6.10. Thus, the reasons for the steeper rating curves gradient for some months in 2007 may be due to the yearly variation of vegetation extent.

The *H v Q* rating curves shown in Figures 6.7 and 6.8 follow a loop pattern. Sellin and van Beesten (2002) examined the influence of both non-uniform and unsteady flow on the shape of the rating curve in the same site. They concluded that the unsteady effects were small in comparison to the non-uniform contribution. They also suggest that the effects of downstream obstructions could be observed in the data. However, in their analysis they concluded that such effects were present at a stations located >50m downstream of station 5 shown in Figure 6.1, i.e., there were minimal effects over present in the reach in question. Based on this finding, it may be assumed that the flow during measurements was adequately free of any backwater effects and reasonably steady (Figure 6.2).

The discharge capacity of the channel tends to be greater for a falling river level during summer months (*H v Q* loop is clockwise), referred as case 1 (June/July to October/November). This could be observed using the arrows in Figures 6.7 and 6.8 that represent the sequence of the events. Sellin and van Beesten (2002) suggested that this is attributed to the flattening of vegetation and removal of dead material and detritus that leads to a reduction of the channel resistance. There is no visual evidence recorded for this for the summer floods during the course of the project (2007-2009). However, there is evidence that vegetation on the floodplain were flattened toward the direction of the flow during the flood event on 10/2/2009 (Figure 6.11). Thus it is likely that the tall grass on the floodplain will be flattened during summer flood events with the same extent of that on 10/2/2009.

Less regular shape of the curve in the rising limb, possibly affected by the resistance of the vegetation, is observed for the summer data (Figures 6.7 d-e, 6.8 d). Interestingly, an opposite behaviour is observed for winter months, referred as case 2 (October/November to June/July). It perhaps worth reflecting that even if the difference in magnitude observed between the EA gauge and ADCP measurements was taken into account (see Section 4.8.3), the trends illustrated in Figures 6.7 and 6.8 would not change.

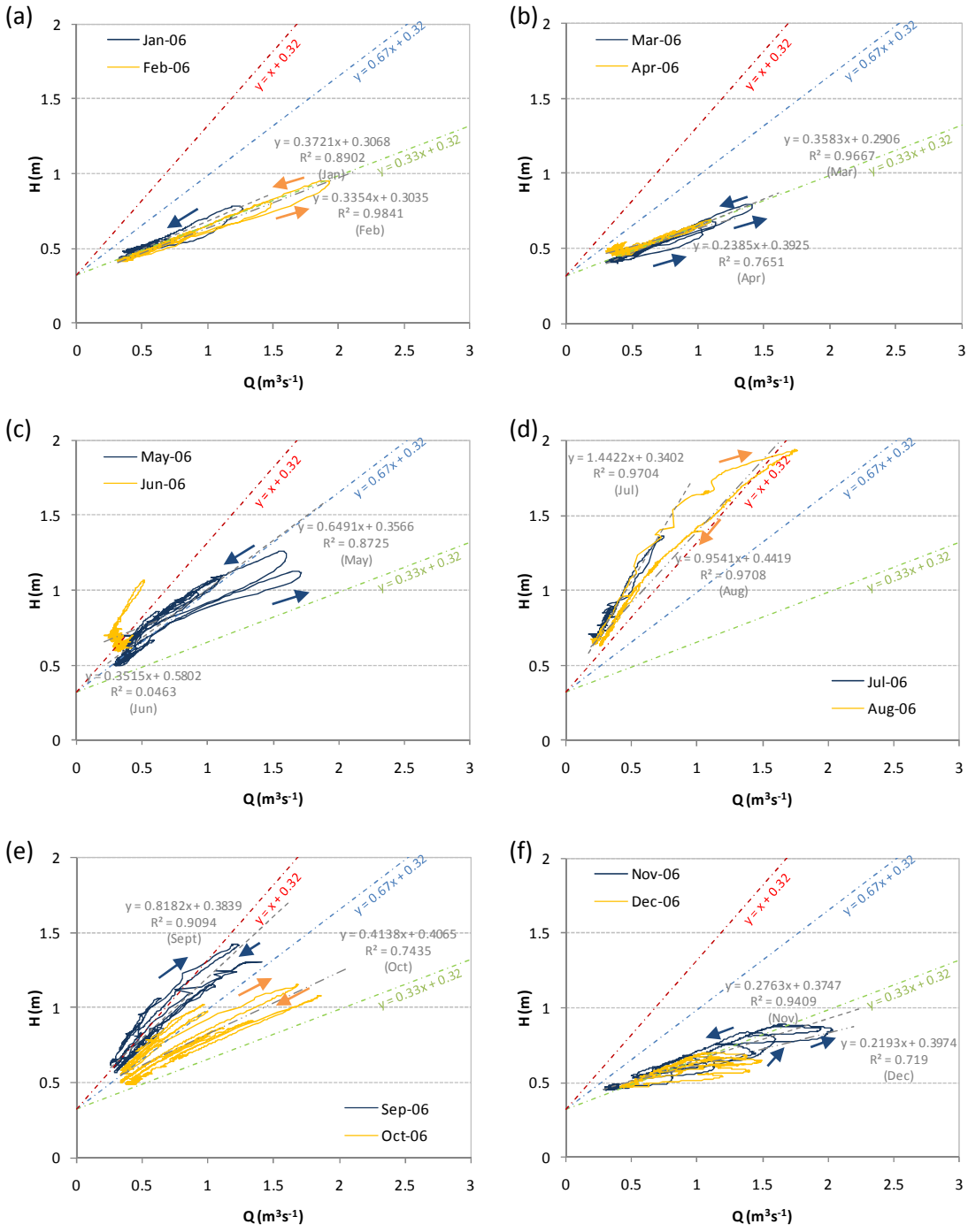

Figure 6.7 Stage discharge relationship at CS 0 for the year 2006.

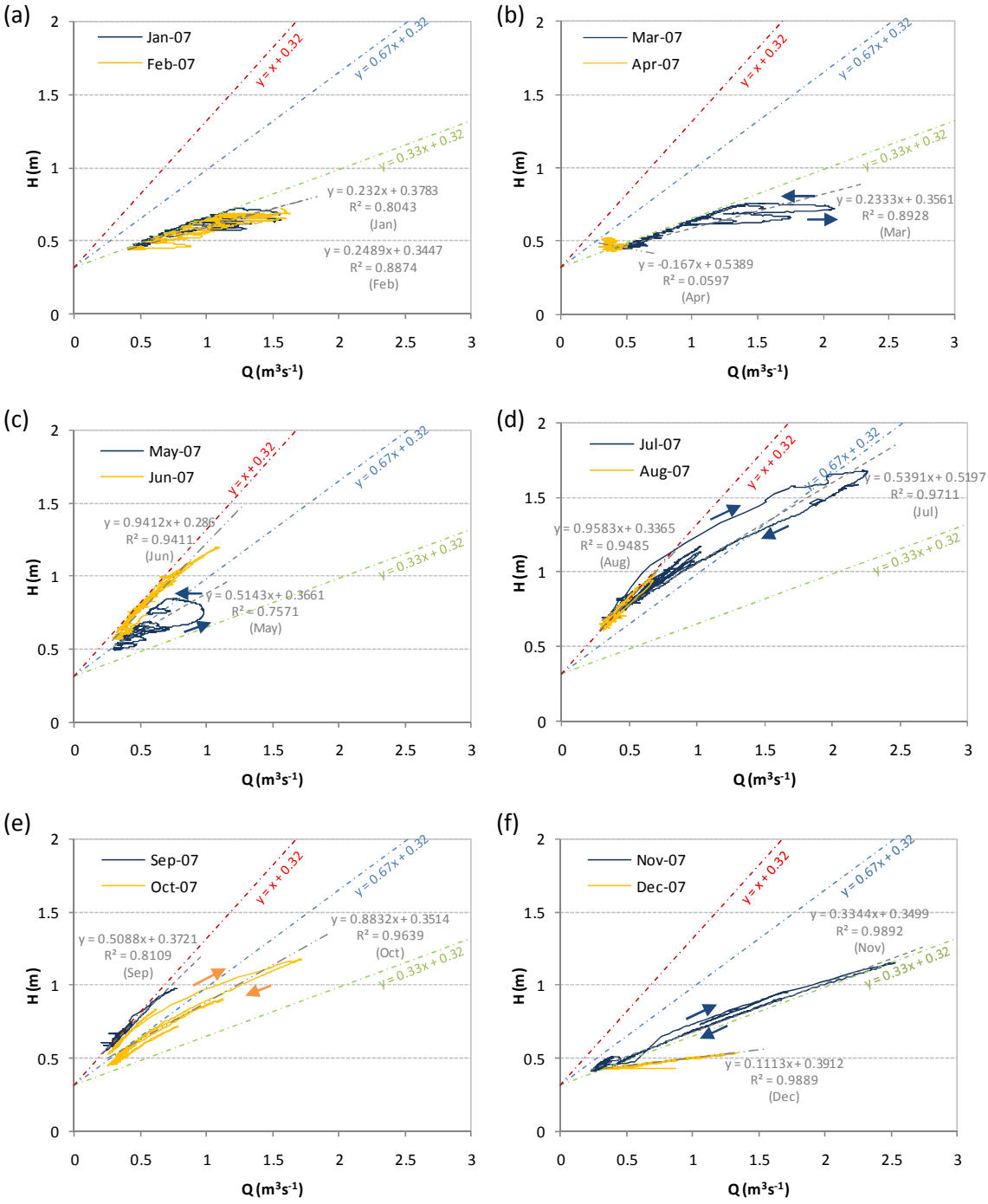

Figure 6.8 Stage discharge relationship at CS 0 for the year 2007.

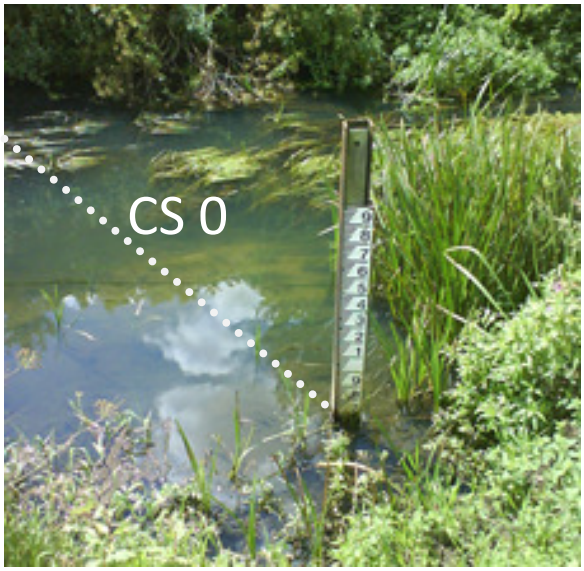

Figure 6.9 Variation of bed elevation at CS 0 as seen through the clear water.

Figure 6.10 Vegetation extent at a location downstream CS2 in June 2007 and June2008.

Figure 6.11 Vegetation flattening at CS4 at 10/2/2009 (red arrows indicate flow direction).

Figures 6.12 and 6.13 show the flood hydrographs for eight storm events in 2006 and 2007. Variations of *H* with respect to time, *dQ*/*dt* and *dH*/*dt* are also shown. Based on these Figures, it can be postulated that:

1. When the *H v Q* loop is anti clockwise (higher discharge capacity in the rising limb - Figures 6.12a, b, d and Figure 6.13a), the maximum discharge (Q_{max}) always occurs earlier than the maximum stage (H_{max}). The time delay in occurrence between Q_{max} and H_{max} lasts for between 1.25 to 30.5 hours.
2. When the *H v Q* loop is clockwise/lower discharge capacity in the rising limb (Figures 6.12c and Figures 6.13b, c, d), the maximum discharge (Q_{max}) always occurs at more or less the same time as the maximum stage (H_{max}). The delay in occurrence between Q_{max} and H_{max}, or vice versa, lasts around 2.75 hours.
3. The changes in water stage are less sensitive to the changes in discharge during the winter months (e.g. Figures 6.12a, d and Figure 6.13a), than during the summer months (e.g. Figures 6.12c and Figure 6.13b). This is because the river has a higher cross sectional area in the winter months, when the vegetation is low.
4. During the peak summer months, i.e. July-August (Figures 6.12c and 6.13b), the shape of the discharge hydrograph is rather interesting, i.e. there is a 'staircase' appearance in the rising limb. Abrupt changes of discharge appear during the rising limb, until the peak discharge is achieved. A distinct change in gradient of both the stage and discharge was also observed. This may be related to the process of flattening of the vegetation mentioned earlier. Another possible explanation may be attributed to the limitations inherent in the measurement instrument, i.e., vegetation on the main channel interfered with the induction process on the electromagnetic gauging station.
5. The lowest discharge capacity of the river occurs in the month of August (Figure 6.12c). This corresponds to the highest value of Manning's *n* over the year, as indicated in Figure 3.30. The maximum stage during the event shown in Figure 6.12c is the highest compared to that for the other events shown in Figures 6.12 and 6.13, although its discharge value is not.
6. It is clearly important that the variation of resistance when occur as a result of changes in vegetation, throughout the year should be considered in engineering design, as it affects greatly the discharge capacity, stage and the shape of the flood hydrograph.

(a) February 2006 (cf. Figure 6.7a).

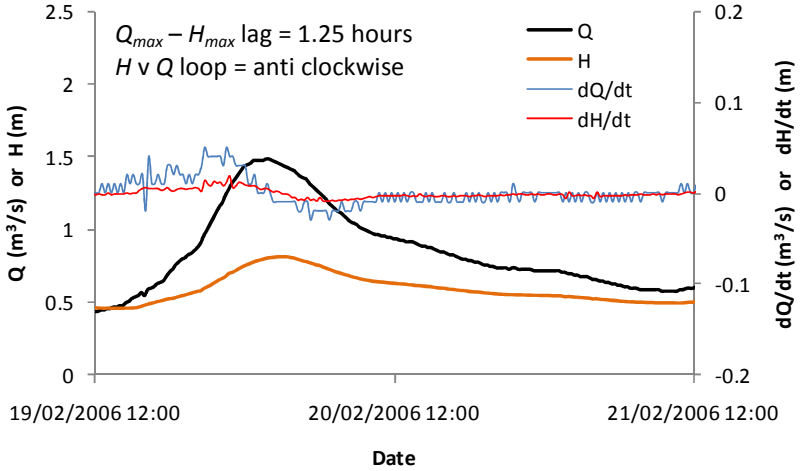

(b) May 2006 (cf. Figure 6.7c).

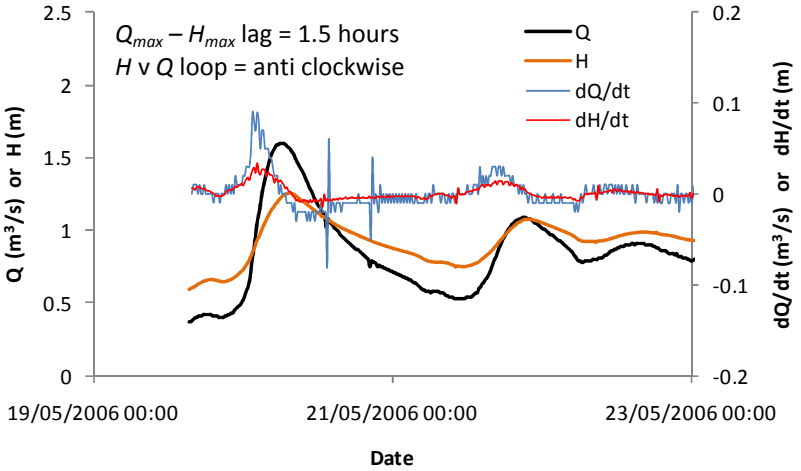

(c) August 2006(cf. Figure 6.7d).

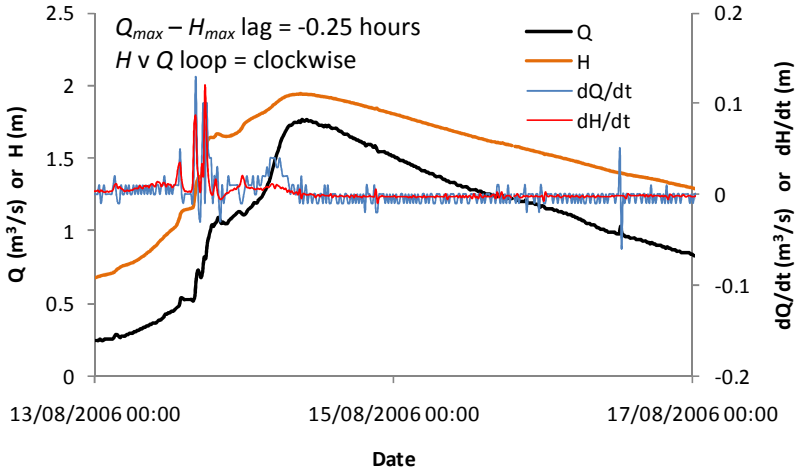

(d) November 2006 (cf. Figure 6.7f).

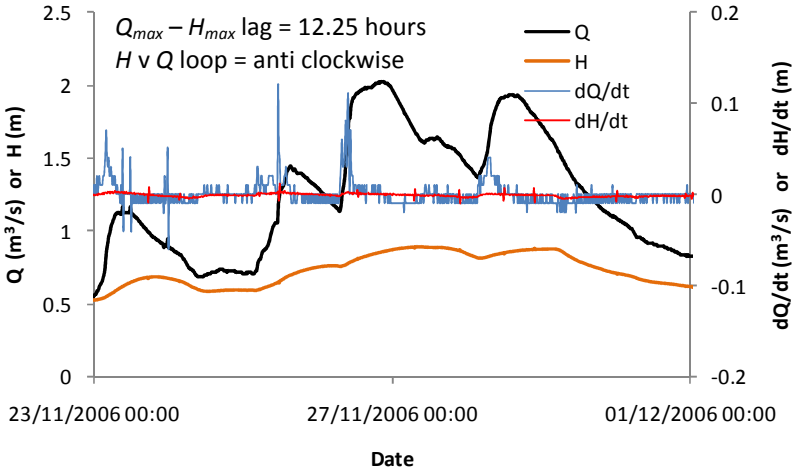

Figure 6.12 Flood hydrographs at CS 0 at four events in 2006.

(a) March 2007 (cf. Figure 6.8b).

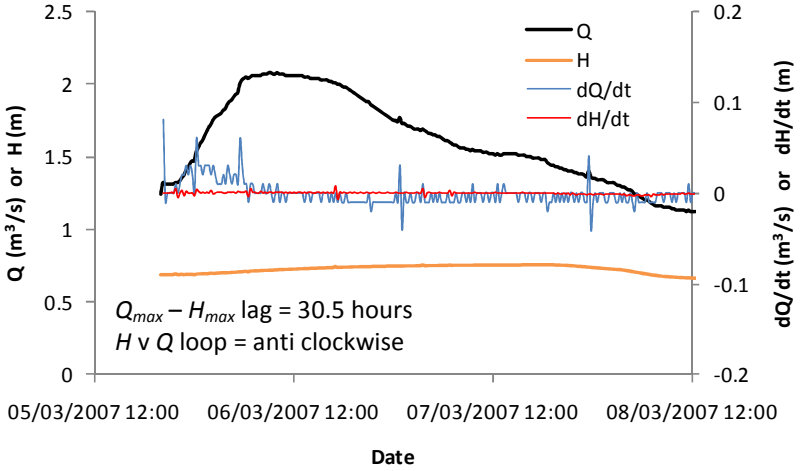

(b) July 2007 (cf. Figure 6.8d).

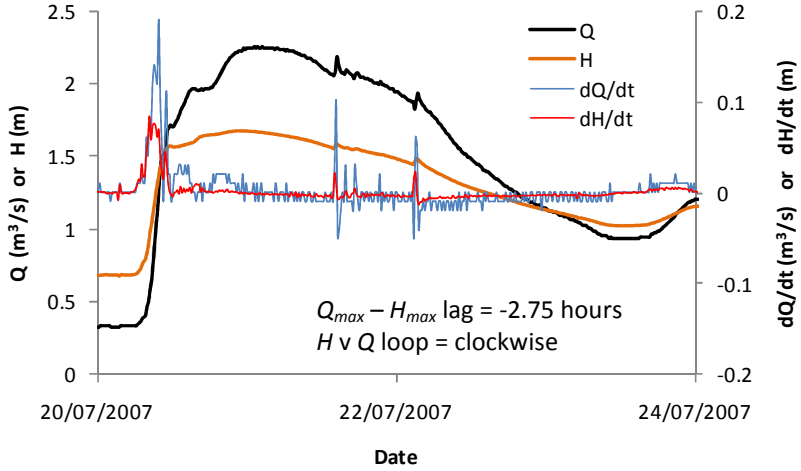

(c) October 2007 (cf. Figure 6.8e).

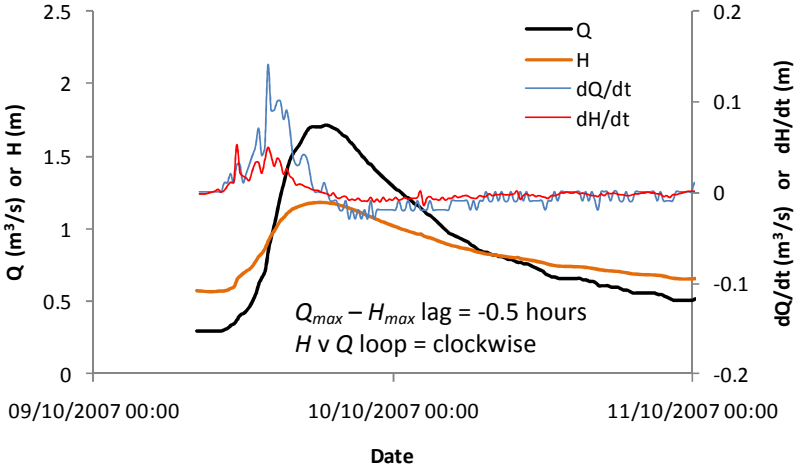

(d) November 2007 (cf. Figure 6.8f).

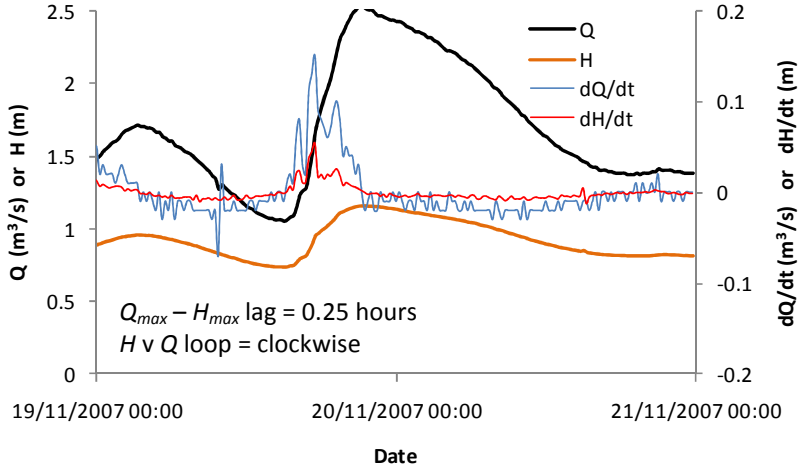

Figure 6.13 Flood hydrographs at CS 0 at four events in 2007.

The coefficients of determination (R^2) were computed in order to assess the accuracy of the linear regression (Figure 6.14) used in the *H v Q* rating curves. Low values of R^2, less than 0.1, occurred for June 2006 and April 2007. This is because most of the data for both months are within a very small range (of *H* and *Q*). Otherwise, the linear regression represents the data reasonably well. This is indicated by the high R^2 values, 0.88 and 0.90 on average for the 2006 and 2007 data respectively (excluding June 2006 and April 2007 data). Furthermore, the variations in the individual-monthly R^2 values are also low, i.e. between 0.72 and 0.99.

The values of the rating curve gradients tend to change in a systematic manner, i.e. low values in winter months and high values in summer months (Figure 6.15). The gradient within the same calendar year could increase up to 7 times (December 2006 and July 2006, Figure 6.15), suggesting that the effect of vegetation on the *H v Q* relationship is very significant. In addition, the gradient for July 2007 is significantly lower than that for July 2006. The cause of this is not clear, but again may be simply due to the yearly variation of vegetation density/height.

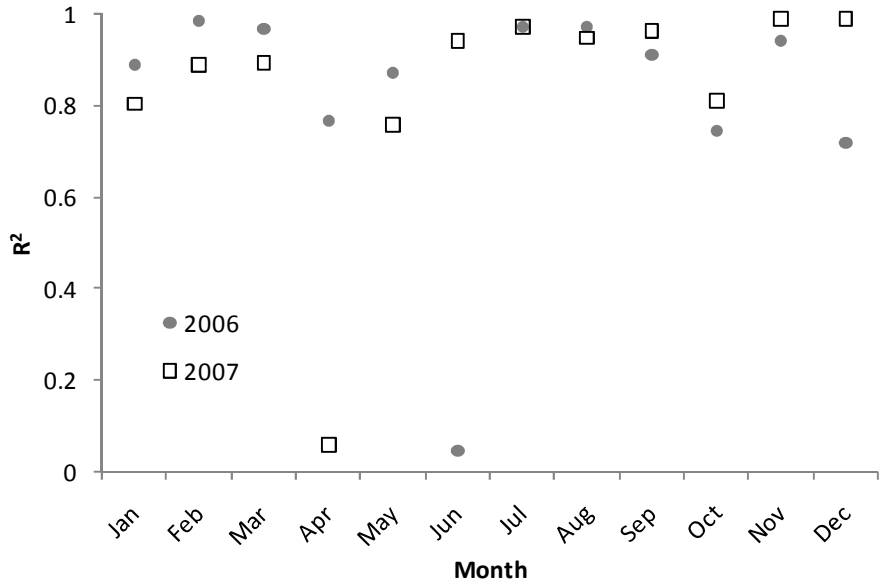

Figure 6.14 The values of R^2 of the monthly *H v Q* rating curve linear fitting *H v Q* distribution at CS 0.

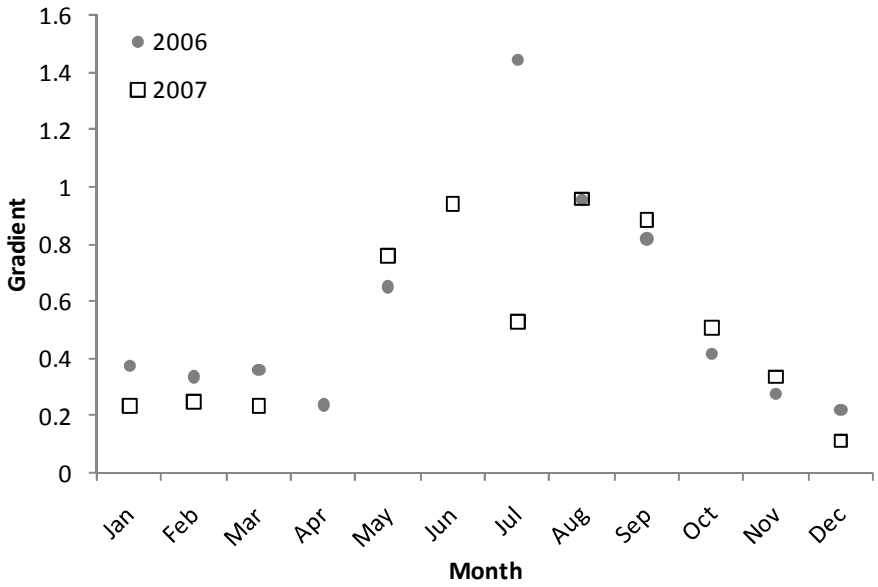

Figure 6.15 Gradients of the monthly *H v Q* rating curve (fitted linearly).

The *H v Q* rating curve at CS 0 constructed using water level data obtained by the Environment Agency and discharge data obtained using ADCP during fieldworks is shown in Figure 6.16. There is a suspected error on the CS 0 water level of the March data as it yields a value 0.5m lower than the water level at a station downstream (CS 1). Therefore, this value was adjusted as the water level of the February data (at CS 0) minus the difference between the March and February data at CS 1, which has been verified by visual observation onsite (Figure 6.17).

The flow for both the March and February data was overbank between cross sections 2 and 4 but was still inbank between cross sections 0 and 1. The higher *H v Q* rating curve gradient for summer months than for winter months that was previously discussed is also present in Figure 6.16. The discharge recorded by the ADCP for higher water level values, i.e. above 1m are significantly higher than that recorded by the Electromagnetic gauge (EG) shown in Figures 6.7 and 6.8. As previously discussed in Section 4.8.3, the EG appears to be less accurate than ADCP in measuring discharge at overbank flow conditions. An example for this is that the EG recorded a similar discharge value of $2.05m^3s^{-1}$ for the 6/3/2007 and 16/1/2008 data whereas further analysis indicates a water level difference of 33% between the former and the latter event (Figure 6.18). It is quite probable that the water depth for such cases exceeded the highest position of the coil on the electromagnetic gauge, which caused the recorded discharge remained at $2.05m^3s^{-1}$ rather than still increasing as in reality.

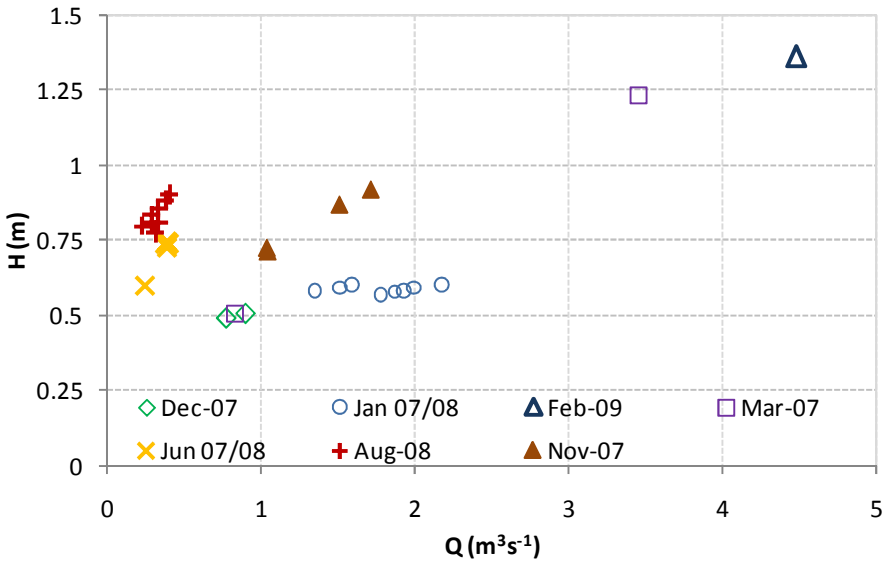

Figure 6.16 Stage-discharge relationship at CS 0 based on ADCP discharge data and staff gauge readings.

Figure 6.17 Gradients of the monthly *H v Q* rating curve (fitted linearly).

Figure 6.18 Water level in the reach as observed on 6/3/2007 and 16/1/2008.

6.3 Analysis of stage-discharge relationship

The *H v Q* rating curves for cross sections 2 and 4 were developed based on the ADCP discharge data and staff gauge readings. From the four available datasets, three were obtained during winter months (January, February and March). The data are shown in Figures 6.18 and 6.19. Various types of regressions methods were applied to the data: 2nd order polynomial, linear, logarithmic, power and exponential. The regressions were applied separately for the winter and summer data since the gradient of the *H v Q* curves for those periods are different (see section 6.2).

The 2nd order polynomial provides a best fit in terms of R^2 value (> 0.999) for the winter data for both cross sections (Figures 6.21 and 6.22, Tables 6.1 and 6.2). The exponential regressions appear to yield a less reasonable fit since *H* increases much quicker than *Q*. Such a condition is not expected since the cross sectional area increases at a greater rate than *H*. The log and the power regressions fit the data better than the exponential regression. Furthermore, the *H v Q* curves for the summer data was extrapolated for overbank condition since only inbank data were available (Figures 6.23 and 6.24). However, the extrapolated results from various regression methods vary greatly, which is not surprising due to the limited availability of data. While the result of polynomial extrapolation for the inbank winter data is reasonably accurate, the result of the same extrapolation method for the inbank summer data appear to be not accurate, i.e. the curve leads to an infinitely increasing *H* with a more or less constant *Q* (Figures 6.23 and 6.24).

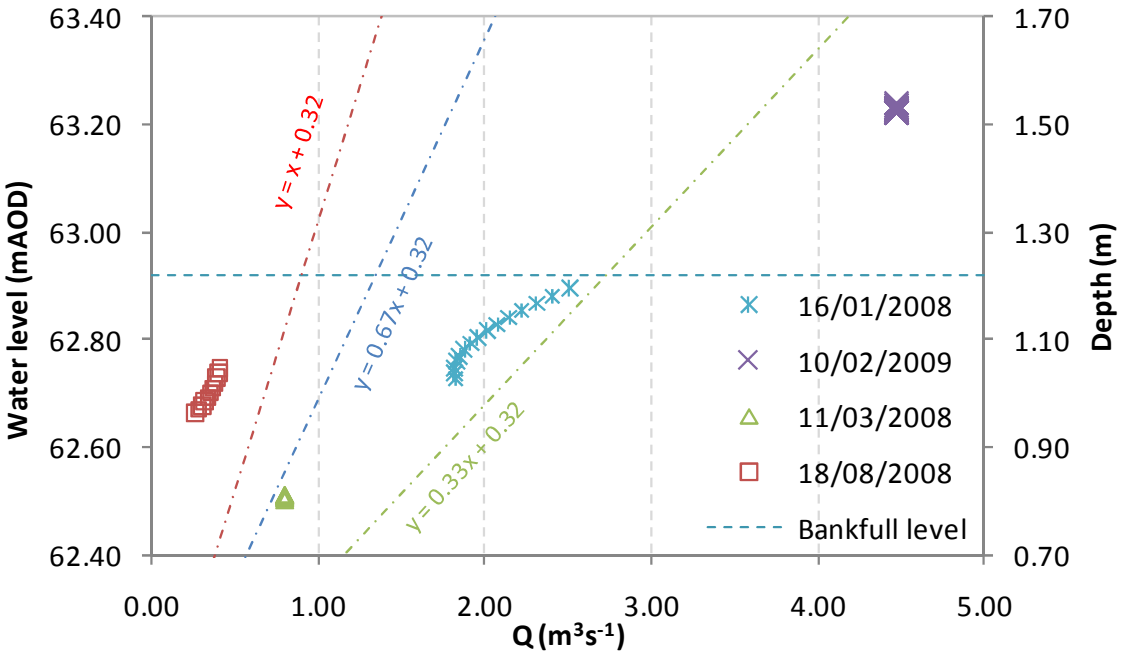

Figure 6.19 Stage discharge rating curve for CS 2.

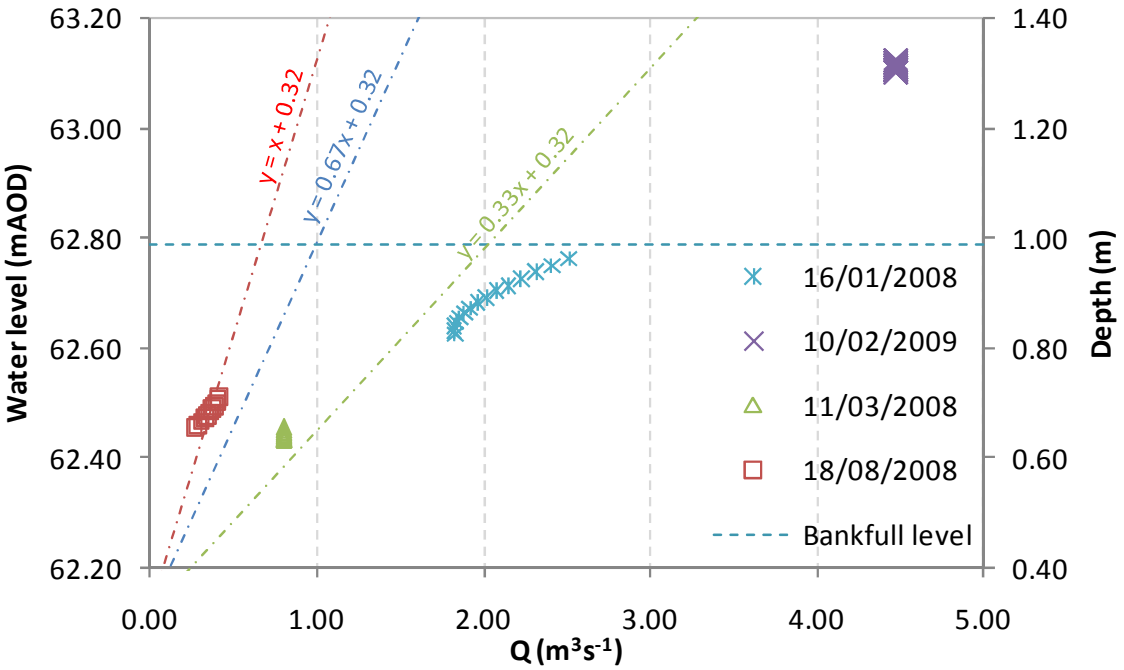

Figure 6.20 Stage discharge rating curve for CS 4.

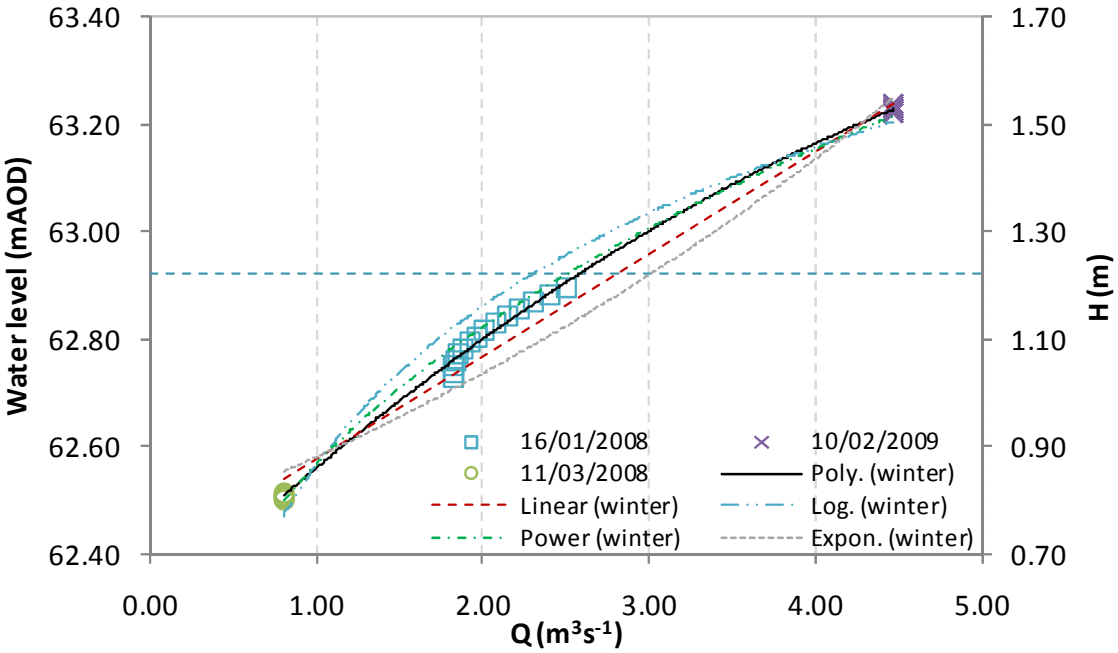

Figure 6.21 Stage discharge rating curve for CS 2 (winter).

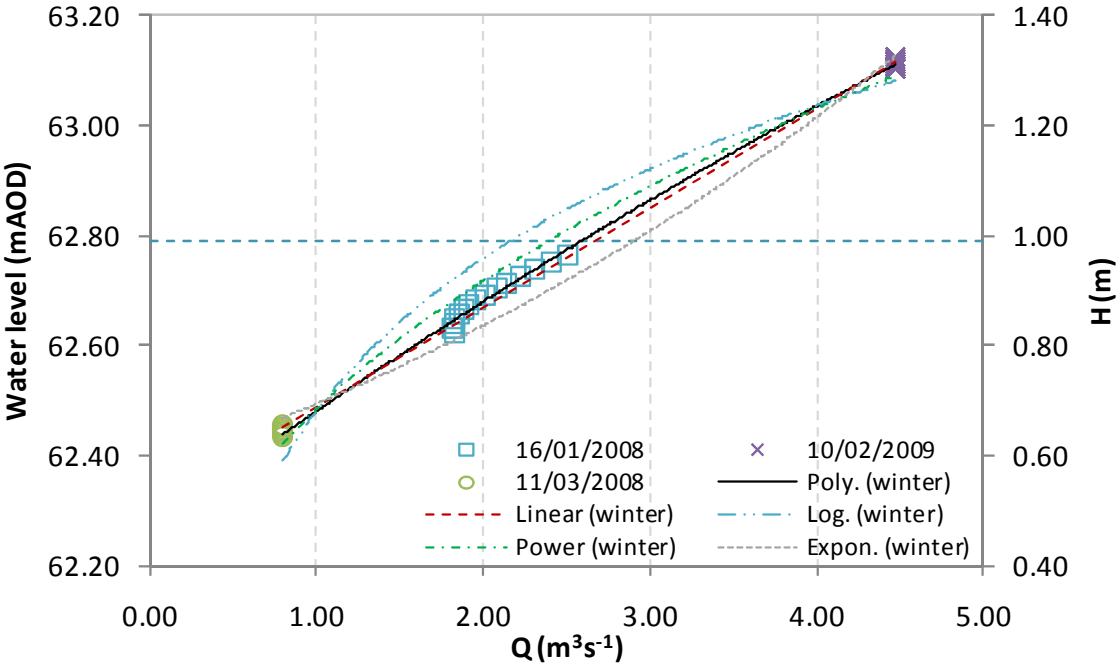

Figure 6.22 Stage discharge rating curve for CS 4 (winter).

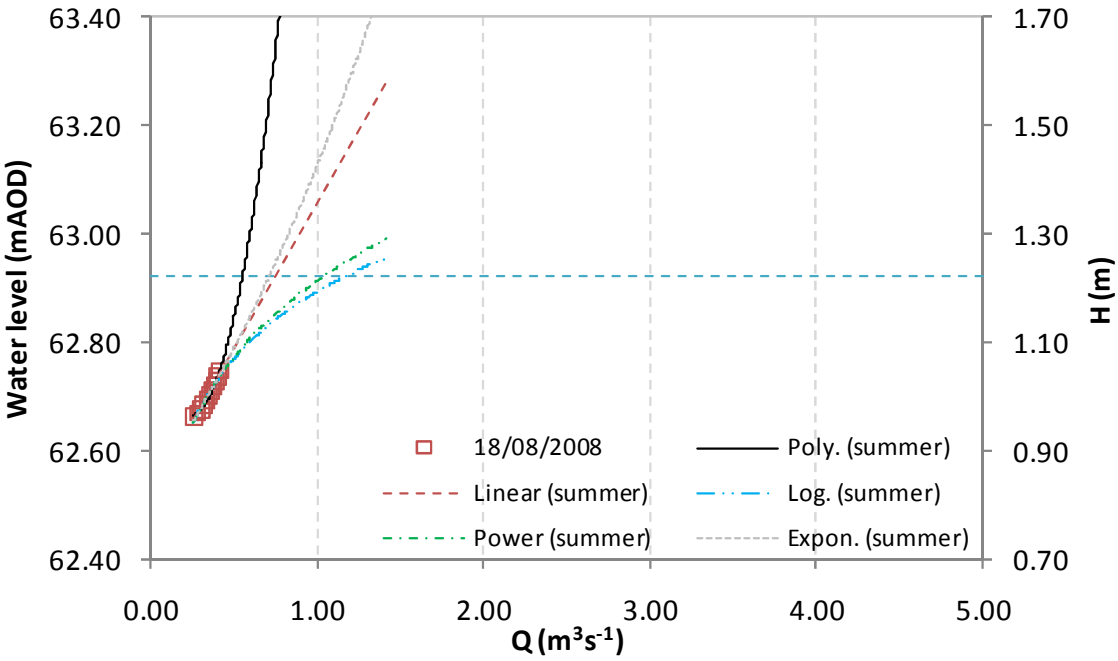

Figure 6.23 Stage discharge rating curve for CS 2 (summer).

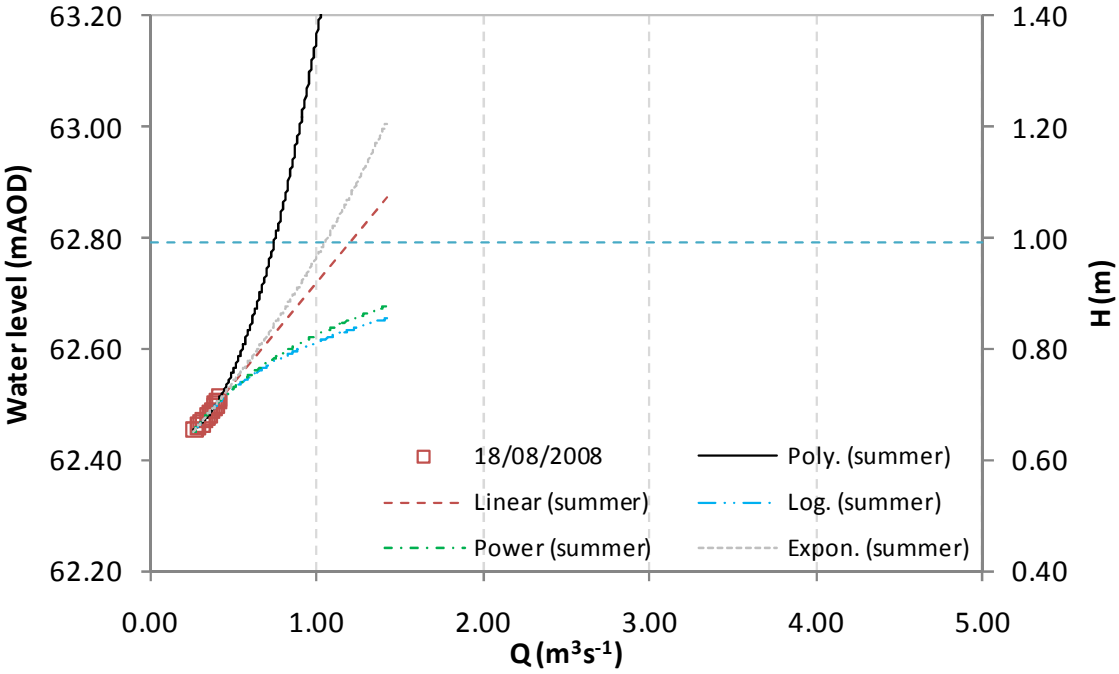

Figure 6.24 Stage discharge rating curve for CS 4 (summer).

	No	Regression type	Regression equation	R^2
Winter	1	inbank & overbank polynomial	$H = -0.0192Q^2 + 0.2973Q + 0.5819$	0.999
	2	inbank & overbank linear	$H = 0.1901Q + 0.6858$	0.992
	3	inbank & overbank log	$H = 0.4272\ln(Q) + 0.8647$	0.980
	4	inbank & overbank power	$H = 0.8664Q^{0.3735}$	0.996
	5	inbank & overbank exponential	$H = 0.7477e^{0.163Q}$	0.970
Summer	6	inbank polynomial	$H = 2.5246Q^2 - 1.1788Q + 1.101$	0.997
	7	inbank linear	$H = 0.5417Q + 0.8141$	0.960
	8	inbank log	$H = 0.1793\ln(Q) + 1.1937$	0.933
	9	inbank power	$H = 1.2128Q^{0.1789}$	0.938
	10	inbank exponential	$H = 0.8305e^{0.5402Q}$	0.964

Table 6.1. Regression equations for CS2.

	No	Regression type	Regression equation	R^2
Winter	1	inbank & overbank polynomial	$H = -0.007Q^2 + 0.2199Q + 0.4676$	0.999
	2	inbank & overbank linear	$H = 0.1807Q + 0.5055$	0.998
	3	inbank & overbank log	$H = 0.4015\ln(Q) + 0.6797$	0.963
	4	inbank & overbank power	$H = 0.6839Q^{0.4237}$	0.989
	5	inbank & overbank exponential	$H = 0.5756e^{0.1867Q}$	0.983
Summer	6	inbank polynomial	$H = 1.0307Q^2 - 0.3385Q + 0.6732$	0.999
	7	inbank linear	$H = 0.3639Q + 0.5561$	0.985
	8	inbank log	$H = 0.1211\ln(Q) + 0.8118$	0.966
	9	inbank power	$H = 0.8248Q^{0.1777}$	0.970
	10	inbank exponential	$H = 0.5668e^{0.5339Q}$	0.988

Table 6.2 Regression equations for CS4.

The extrapolation of an inbank rating curve is often used as a means of predicting the overbank stage-discharge relationship. However, such an approach often results in inaccurate prediction of stage (ISO 1100-2 1998). In order to quantify the error that could arise from such approach, the inbank (winter) data were extrapolated and the extrapolation error were assessed against the overbank data (winter) (Figures 6.25 and 6.26). The five different regressions methods previously used were again adopted.

The results indicate that linear extrapolations for cross sections 2 and 4 over predict the water depth by 10.7 and 4.4% respectively (Tables 6.3 and 6.4). On the other hand, the log and the power extrapolations under predict the water depth by 5.1 to 16% for both cross sections. Polynomial extrapolation provides the best fit to the data as it yields the lowest error compared to other

methods, 0.5 and -3.7% for cross sections 2 and 4 respectively. Furthermore, while the result of the polynomial extrapolation of the inbank data is similar to the result of polynomial interpolation of the inbank and overbank data for CS2 (Figure 6.25), less agreement was observed for the similar case for CS 4 (Figure 6.26). Furthermore, it is acknowledged that the number of available data and the width of the data range play an important part in the accuracy of extrapolation, and hence in predicting the *H v Q* rating curve at overbank conditions.

The rating curve extrapolation undertaken in this section was based on simple curve fitting methods. It is likely that a smooth transition in the rating curve when the flow changes from inbank to overbank flow conditions will not be present in the real conditions in the field, due to abrupt changes in the geometric parameters (*P* and *R*), as well as due to the overall hydraulics (e.g. the existence of a later shear layer) at such the bankfull stage. In order to take these factors into account, a numerical model is used to predict the stage-discharge values for the overbank flow condition in the river. The result of this work is discussed in section 7.4.

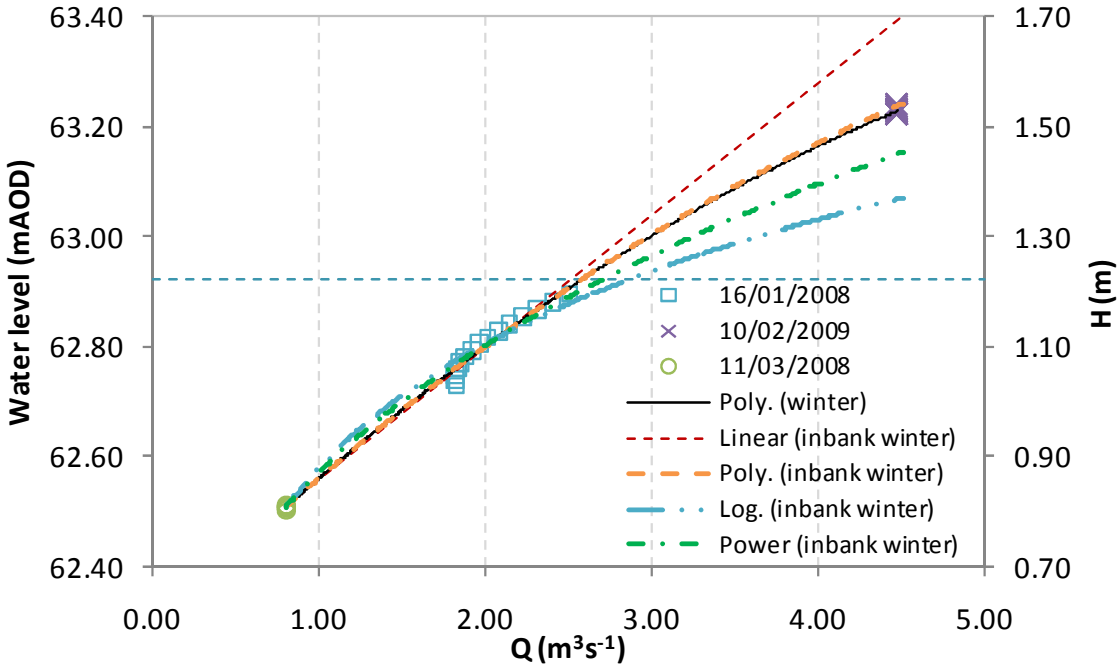

Figure 6.25 Stage discharge rating curve for CS 2 (winter).

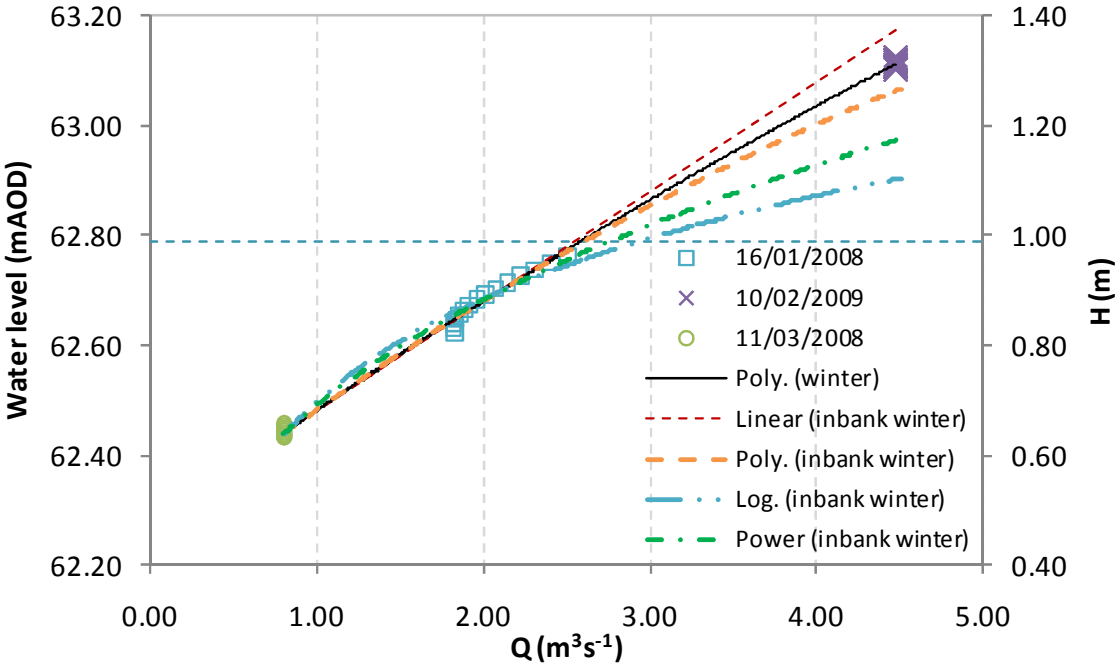

Figure 6.26 Stage discharge rating curve for CS 4 (winter).

No	Regression type	Regression equation	R^2	ΔH (%)
1	inbank polynomial	$y = -0.0182x^2 + 0.2942x + 0.5837$	0.995	0.5
2	inbank linear	$y = 0.2401x + 0.6167$	0.995	10.7
3	inbank log	$y = 0.3266\ln(x) + 0.878$	0.990	-10.5
4	inbank power	$y = 0.8702x^{0.3405}$	0.995	-5.1

Table 6.3 Regression equations for CS2

No	Regression type	Regression equation	R^2	ΔH (%)
1	inbank polynomial	$y = -0.0126x^2 + 0.2364x + 0.4577$	0.995	-3.7
2	inbank linear	$y = 0.1987x + 0.4807$	0.995	4.4
3	inbank log	$y = 0.2702\ln(x) + 0.697$	0.989	-16.0
4	inbank power	$y = 0.6903x^{0.3538}$	0.993	-10.5

Table 6.4 Regression equations for CS2

6.4 Analysis of resistance coefficients

Resistance coefficients in terms of Manning's n, k_s and f were calculated from the field data and compared to the previous findings by Sellin and van Beesten (2002). Furthermore, the resistance coefficient values are used as a basis for numerical modelling calibration in Chapter 7.

6.4.1 Calculation of Manning's *n*

The 1-D global Manning's n values (which are referred to as n in the rest of this thesis) were computed from the ADCP discharge and water surface slope obtained from staff gauges readings using the Manning's equation. Even though the cross section geometry has changed slightly between 2007 and 2009, only a small effect has been observed on the values of parameters A, P and R, e.g. for CS 2 (Figure 6.27). As this effect is small, the parameters A and P from the 2007 data outlined in Chapter 3 were used.

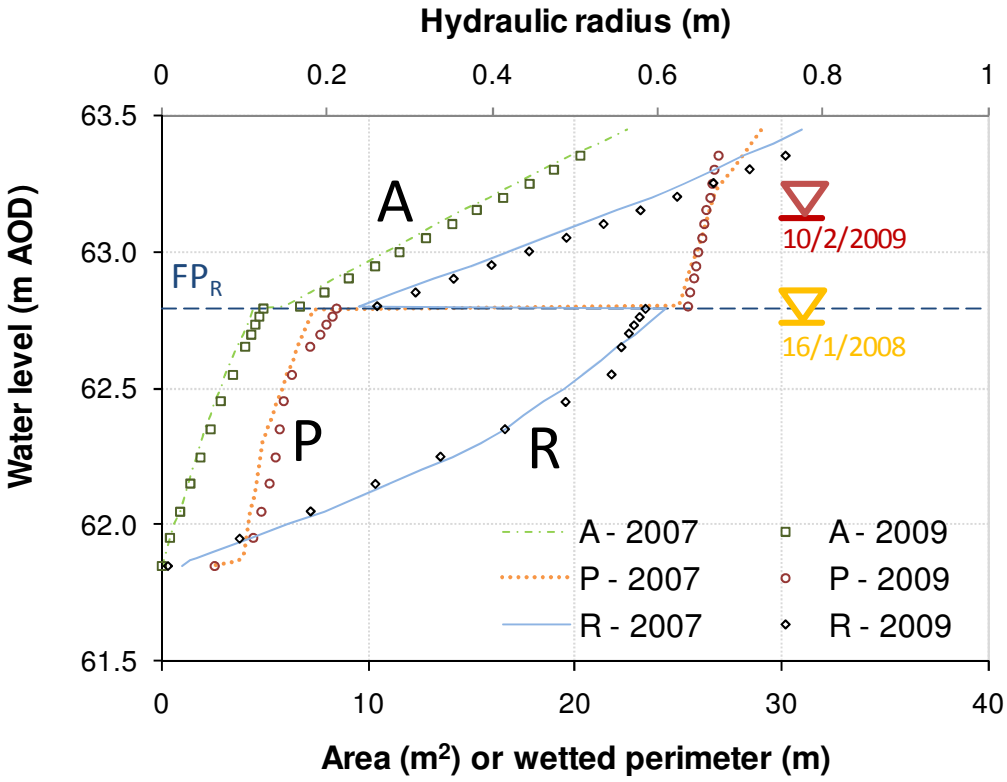

Figure 6.27 Geometric parameters for CS 4

The local water level at stations 2 to 4 and stations 0 to 5 were both used for the calculation of Manning's n for the main channel of cross sections 2 and 4. It is acknowledged that using the slope data between stations 0 to 5 might not be appropriate for design purpose since the man-made section upstream of station 2 was included in the calculation. However, in practice there are often

only a limited number of instruments for measuring water level along river reaches. Hence, in most cases the inclusion of man-made sections, or in sections where the flow may be constricted, in calculating the water slope is difficult to avoid. Notwithstanding that the overall results in Figures 6.28 and 6.29 are reasonably consistent with data from other investigations, see below.

The relationship between *n* values and water levels at cross sections 2 and 4 are shown in Figures 6.28 and 6.29. The *n* values computed using the water slope between station 2 and 4 are on average higher by 17% than the *n* values computed using the water slope between station 0 and 5. Such a variation can be overlooked when undertaking the modelling, due to limited availability of water level monitoring devices in a river. The inbank and overbank *n* values of CS 2 are on average 46% and 32% larger than those for CS 4 (Table 6.5). The variations of *n* values in the streamwise direction over short distances are often neglected as it is convenient to assume that *n* values are similar along a reasonable length of the river course.

The *n* values for the current research are to the same order of magnitude as those reported by Sellin and van Beesten (2002) (Figure 3.30), with the exception of the summer data pertaining to CS 2. In the current research, Manning's *n* values are of the order of 0 - 0.10$m^{-1/3}s$ in January – March and rise to 0.20 in August (CS 4 only). The Manning's *n* for CS 2 in August could reach 0.44-0.60. Such values are attributed to the high vegetation extent and density in the main channel, which could cover the whole cross section and rise one metre above the water surface (such as seen in Figure 6.4).

Furthermore, the cross sectional area at a given time for CS 2 is typically 34% larger than that of CS 4 for winter-inbank flow condition. During the August measurement, the difference increases further to 46%. This resulted in higher *n* values for CS 2 than those of CS 4 for the August data, when the values are back calculated from the Manning's equation. It can also be shown that for CS 2, the water level for the August measurement was at one time the same as the water level for the January measurement (Figure 6.28) (near bankfull). This is not the case for CS 4 (Figure 6.29).

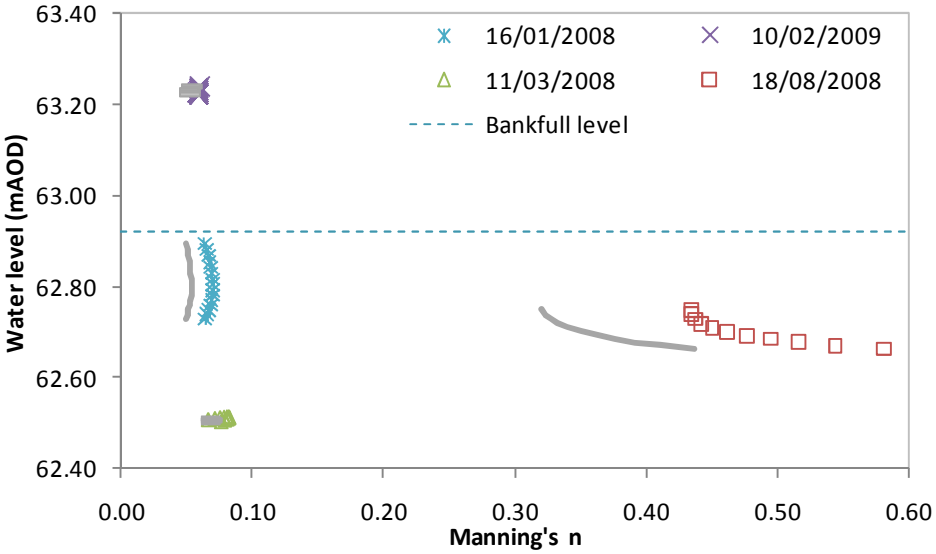

Figure 6.28 Relationship of Manning's *n* and water level for CS 2 (grey line = using the slope of station 0-5).

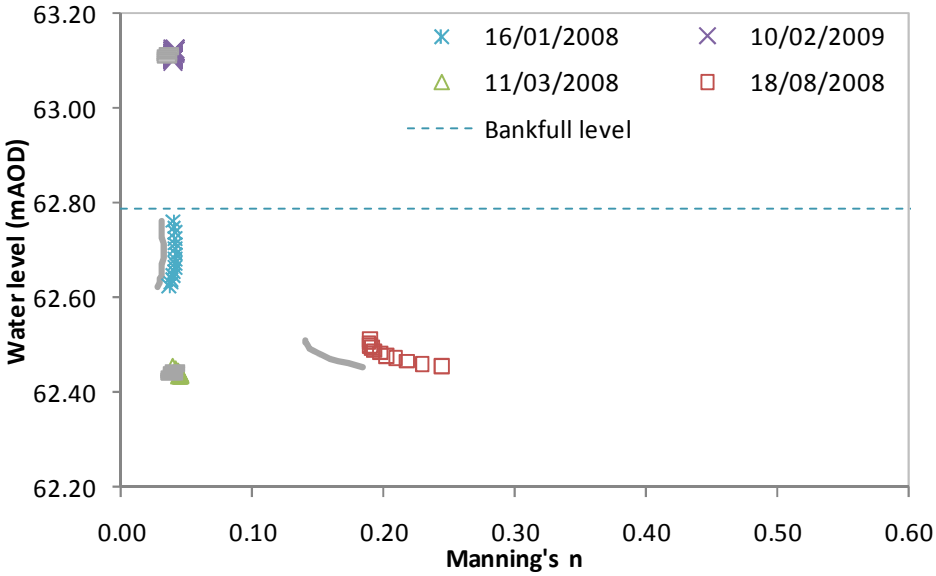

Figure 6.29 Relationship of Manning's *n* and water level for CS 4 (grey line = using the slope of station 0-5).

	Δ n		Δ A	Δ P	Δ R
	slope 0 to 5	slope 2 to 4			
Inbank	46	46	37	20	21
overbank	32	32	32	32	0

Table 6.5 Average difference of parameters *n*, *A*, *P* and *R* between cross sections 2 and 4 (in percent).

6.4.2 Conversion of n to k_s and f

In order to use the resistance coefficient for the SKM calibration, the Manning's n values need to be converted to the Darcy-Weisbach friction factor (f). The following equation is used:

$$f = \frac{8gn^2}{R^{1/3}} \tag{6.1}$$

Equivalent values for Nikuradse equivalent sand roughness size (k_s) were also calculated. Three different conversion methods, mentioned in Morvan, *et al*. (2008), are used:

1. Equation given by Ackers, 1958:

$$k_s = \left(\frac{n}{0.038} \right)^6 \tag{6.2}$$

The equation (6.2) is valid only if $10 < R/k_s < 100$. The parameter k_s is in millimetres.

2. Equation derived by Massey, 1995:

$$k_s = 14.86\, R / \exp_{10}\left(\frac{0.0564\, R^{1/6}}{n} \right) \tag{6.3}$$

3. Equation derived in Chow, 1959:

$$k_s = 12.2\, R / \exp_{10}\left(\frac{0.0457\, R^{1/6}}{n} \right) \tag{6.4}$$

For conversion using equation (6.2), only two sets of data yields R/k_s values within the given limit bounds, i.e. 11/3/2008 (CS2) and 10/2/2009 (CS4) data. The other winter data have R/k_s values in the range of 100 – 3000. The R/k_s values for the summer data are extremely low, 4 to 5 orders of magnitude lower than the lower limit of 10. The equivalent k_s values computed using the three methods are shown in Figures 6.30 and 6.31. Conversion using (6.2) for the valid data yields k_s values in the range of 0.006 and 0.034m. This is one to two orders of magnitude lower than the equivalent

k_s values computed using (6.3) and (6.4). Similar findings were also reported by Morvan, *et al.* (2008) for UK-Flood Channel Facility experiments (Knight and Sellin, 1987), i.e. equation (6.2) yields equivalent k_s values of the order of 10^{-6}m, while (6.3) and (6.4) yield equivalent k_s values of the order of 10^{-4}m. While the equivalent k_s values for the summer data are surprisingly high when compared to some textbook values, such high values were also reported by others, e.g. Knight (1981) reported a k_s value of 8m in a tidal estuary at low depths.

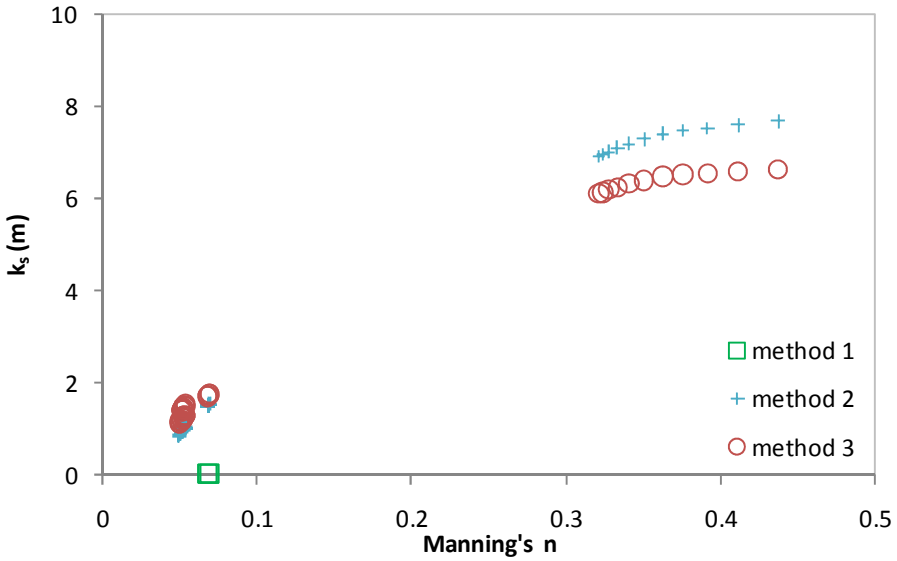

Figure 6.30 k_s as a function of Manning's *n* for CS 2.

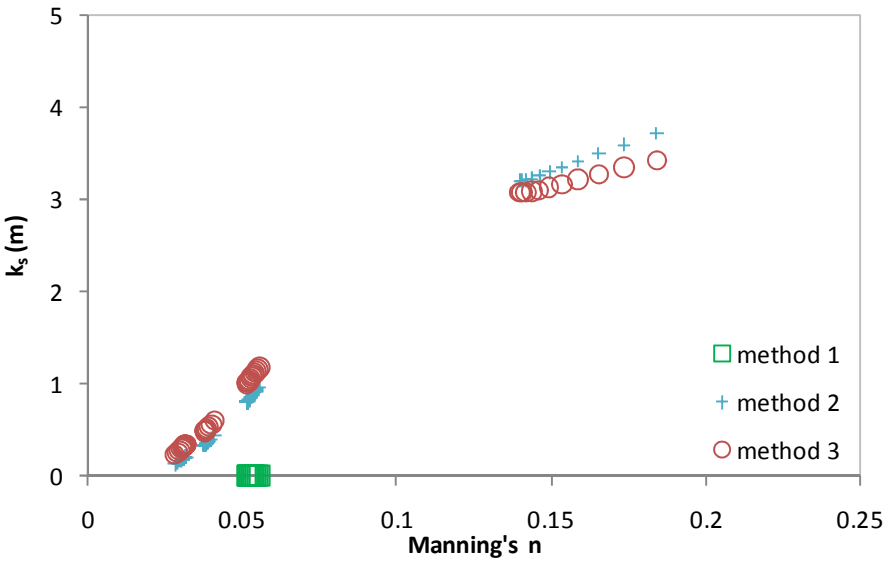

Figure 6.31 k_s as a function of Manning's *n* for CS 4.

6.5 Accuracy of discharge estimation using LS-PIV data

The suitability of using LS-PIV data to estimate discharge was assessed using the ADCP and the LS-PIV data obtained at similar times. In order to estimate discharge using surface velocity, most researchers use an empirical index k_u (= U_d/U_s) (Sun *et al.*, 2009), with U_d and U_s referring to the depth-averaged streamwise velocity (ADCP) and surface velocity (LS-PIV). Such an approach could be reliable if the vertical velocity in the river follows a certain law, e.g. log law, which is often thought to occur in wide rivers. Creutin *et al*. (2003) reported a k_u value of 0.85 from measurements using an ADCP in the River Iowa, i.e. a wide river with discharge values between 50 to 300m^3s^{-1}. This value is close to the value of U_d/U_s for one-seventh power law velocity distribution, i.e. U_d/U_s = 0.875. As previously outlined in Chapter 5, the flow structures in the River Blackwater site are complex and fully three-dimensional. Thus, some variation of the k_u values across the channel is expected.

The values of coefficient k_u were computed from a set of measurements at cross sections 2 and 4 under inbank, bankfull and overbank flow conditions. The values of U_d were obtained from the ADCP data while U_s were obtained from LS-PIV measurements. The coefficient k_u varies from 0 to 2.5 for the CS 2 data (Figure 6.32). For the CS 4 data, the values of k_u could become greater than 5. Such phenomenon occurred at locations near the river banks or where vegetation affects the movement of the LS-PIV seeding (Figure 6.33a). The correlation between U_d and U_s are the highest for the bankfull conditions. This is indicated by a correlation coefficient value of 0.85 for the bankfull conditions for both cross sections (Table 6.6). Low correlation coefficient values were observed for the inbank data of CS 4, i.e. 0.12 and 0.18. The RMSE values between U_d and U_s are surprisingly within similar range for all data, i.e. 0.15 to 0.19ms^{-1} (Table 6.6). Such values are more than 25% of the typical magnitude observed from the data.

The values of k_u for a large proportion of the data shown in Figures 6.32 and 6.33 exceed 1. These values are likely to be a result of poor seeding in the flow domain or as a result of the 3-D nature of the flow in the channel. Thus, when the approach of Creutin *et al.* (2003) (i.e., k_u = 0.85) is used to estimate the discharge from the LS-PIV data, the resulting discharge will underestimate the discharge measured using ADCP. An alternative approach, which assumed that U_s = U_d (i.e. k_u = 1.0) was adopted to attempt to calculate discharge using LS-PIV data. Both U_d and U_s were integrated over the depth to obtain Q_{ADCP} and $Q_{LS\text{-}PIV}$ respectively. The ratio between $Q_{LS\text{-}PIV}$ and Q_{ADCP} was computed for each case to assess the accuracy of the discharge estimation.

The calculation result shows that differences of 10% to 18% were observed between Q_{ADCP} and $Q_{LS\text{-}PIV}$ for the bankfull and overbank conditions. Higher differences of 38% to 51% were observed for the inbank conditions. Furthermore, Q_{ADCP} on five out of seven cases investigated were higher than $Q_{LS\text{-}PIV}$ (Table 6.6). Based on this brief investigation it can be concluded that the accuracy of estimating the discharge using LS-PIV data is at present not sufficient in order to use this approach in practice.

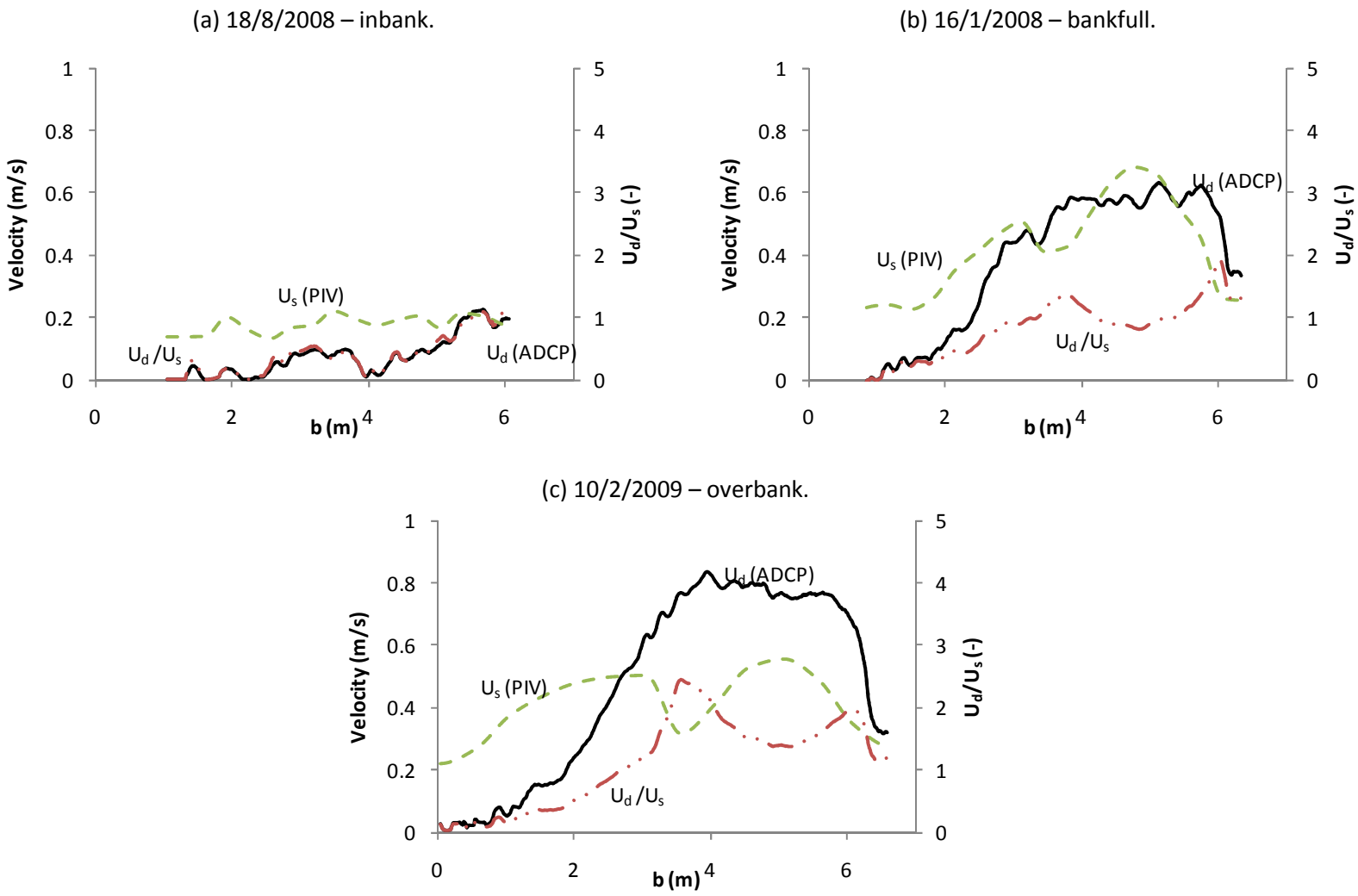

Figure 6.32 Comparison of ADCP streamwise velocity and LS-PIV surface velocity at CS 2.

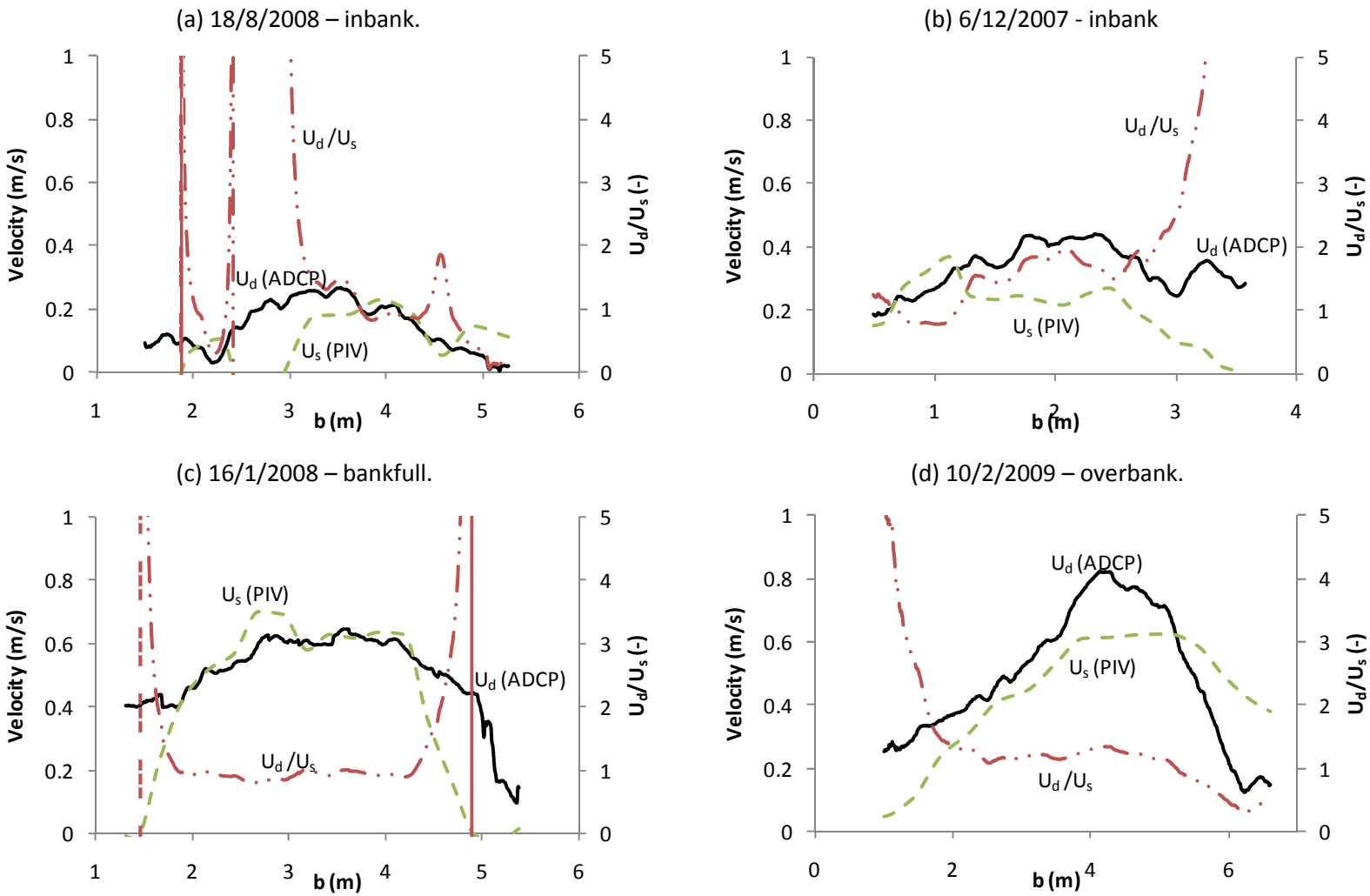

Figure 6.33 Comparison of ADCP streamwise velocity and LS-PIV surface velocity at CS 4.

	Correlation coefficient (between U_d and U_s)			
	Inbank	Inbank	Bankfull	Overbank
	06/12/2007	18/08/2008	16/01/2008	10/02/2009
CS2	-	0.60	0.85	0.50
CS4	0.18	0.12	0.85	0.71
	Root Mean Square Error (between U_d and U_s)			
	Inbank	Inbank	Bankfull	Overbank
	06/12/2007	18/08/2008	16/01/2008	10/02/2009
CS2	-	0.19	0.19	0.19
CS4	0.17	0.17	0.19	0.15
	$Q_{LS\text{-}PIV}/Q_{ADCP}$			
	Inbank	Inbank	Bankfull	Overbank
	06/12/2007	18/08/2008	16/01/2008	10/02/2009
CS2	-	2.38	1.10	0.82
CS4	0.61	0.49	0.83	0.88

Table 6.6 Statistical parameters for the U_d and U_s.

6.6 Closing remarks

An analysis of the stage discharge data leads to the following conclusions:

1. The seasonal variation of vegetation affects the shape of the stage-discharge rating curve significantly. The presence of vegetation in the main channel during the summer months reduces the conveyance capacity of the river. This is shown by the steeper gradient in the stage-discharge rating curves for those periods, reaching to seven times the gradient of the stage-discharge rating curves for winter months (Figure 6.7).
2. The stage-discharge relationship at CS 0 follows a loop or hysteresis pattern (Figures 6.7 and 6.8). The falling limbs of the rating curve have a higher discharge capacity than the rising limbs for summer months (June/July to October/November). Interestingly, the opposite is true for winter months (October/November to June/July).
3. The discharge hydrographs for the month of July and August (Figures 6.12c and 6.13b) indicate abrupt changes of discharge during the rising limb, which was not observed during winter months. This may be caused by the flattening of the vegetation.
4. The variation of the vegetation over the year further highlights the difficulties in undertaking numerical modelling for small rivers. Such variation is clearly important as it affects the discharge capacity, stage and the shape of the flood hydrograph.

5. From five simple extrapolation methods, 2nd order polynomial extrapolation provides the best means for estimating the overbank stage-discharge curve using inbank data (Tables 6.1 and 6.2). However, it is also acknowledged that the number of available data and the size of the data range play an important part in the accuracy of the extrapolation.
6. Variation of water slope between different river sections within the study reach could alter the computed Manning's *n* values by, on average, 17%.
7. The summer *n* values for CS 2 (August 2008) are twice as high as that for CS 4. This is caused by the greater cross sectional area of CS 2 for that particular data.
8. It has been shown that the accuracy of the discharges estimated using the method described in section 6.5 for large-scale PIV data is undesirable. Differences of 10% to 18% were observed between Q_{ADCP} and $Q_{LS\text{-}PIV}$ for the bankfull and overbank cases. Higher differences of 38% to 51% were observed for the inbank cases.

7 NUMERICAL MODELLING OF FLOW IN THE RIVER BLACKWATER

This section of the thesis is concerned with the practical implementation of the measurements into a modelling framework. To that end, a quasi 2-D RANS model, the SKM, is used in order to investigate the conveyance capacity of the reach in question. Data from both the physical simulations and field work are used in order to gain an insight into the calibration of the model.

7.1 Simulating flows in a small-scale physical model of the River Blackwater

The flow in the physical model of the River Blackwater was simulated in order to provide an insight into the values of f, λ and Γ that may be expected for the full scale river. Calibrating the physical model data is theoretically less complex than calibrating the river data as the geometry of the model is more simple and regular than that of the river, and the roughness condition in the model can be easily adjusted, e.g. with the same roughness value for the whole model.

7.1.1 Experimental data

Two configurations of the River Blackwater, referred as configurations C and B in Lambert (1993) were selected for modelling. Three different water depths, 0.162m, 0.187m and 0.237m, were simulated for case C. These will be referred as cases C1, C2 and C3 respectively. Only one overbank case, at H = 0.187m (referred to as case B2), was measured by Lambert (1993). For both configurations the transverse floodplain slope was zero. However, two different roughnesses were used in order to examine the effect of different values of resistance, i.e. 8mm gravel for case C and smooth concrete for case B and (c.f. Table 7.1 for configuration details). Since the bankfull depth is 0.15m, the existence of 8mm gravels on the floodplain left only 4mm of water depth between water surface and the top of gravels for case C1. Measurement at the floodplain was not possible for case C1 since the size of the propeller current meter disc is 10mm (Naish and Sellin, 1996). Due to the low depth of flow on the floodplain, 0.004m, it was not possible to measure the velocity on the floodplain for case C1. Unfortunately, a significant proportion of the velocity data on the floodplain pertaining to case B were not available; the exact reason for this was never ascertained. However, boundary shear stress measurements were available at cross section 2B for case B and are used to verify the SKM results.

Velocity measurements were undertaken on three cross-sections denoted as 2B, 3 and 4 (see Figures 7.1 and 7.2 for details). Flow direction and magnitude along the specified cross-sections were measured using a balanced vane mounted on a rotary potentiometer and a miniature propeller current meter. The boundary shear stress was measured using a 4.05mm diameter Preston tube connected to a differential pressure transducer. The pressure difference was recorded by a PDP 11/73 mini-computer which also calculated the resulting boundary shear stress (Lambert, 1993).

The locations of the velocity measurements at cross-sections 3 and 4 do not follow a straight line (in plan view), i.e. the cross section directions change between the main channel and the floodplain (c.f. Figure 7.2). With such a condition, the boundary conditions between panels in SKM, i.e. $U_d^{(n)} = U_d^{(n+1)}$, will not be valid since the cross section has to be in a straight line in order to be able to be simulated with the SKM. The approach adopted for CS4 was to project its floodplain velocities in the direction of the main channel (51.5^o, see Figure 7.2). Such projection will alter the cross section length. However, as the length change appears to be small, it was decided to retain the floodplain length. The same approach, when applied to CS3, will generate some uncertainties in the data due to the high deviation between floodplains and main channel directions (see Figure 7.2). Thus, it was decided not to use the CS 3 data for SKM modelling.

The stage-discharge relationships for the overbank flow condition (H > 0.15m) for configurations B and C are shown in Figure 7.3. This Figure shows that for a given discharge the stage is always greater in case C than case B. This is not surprising given the difference in floodplain roughness between the two cases.

	Configuration C	Configuration B
Main channel roughness	Design roughness (8mm)	Design roughness (8mm)
Floodplains roughness	8mm	Smooth concrete
Flood plain cross-fall	Horizontal	Horizontal
Discharge at H= 0.187m (m^3/s)	0.084	0.09485

Table 7.1 Description of configurations C and B (after Lambert, 1993).

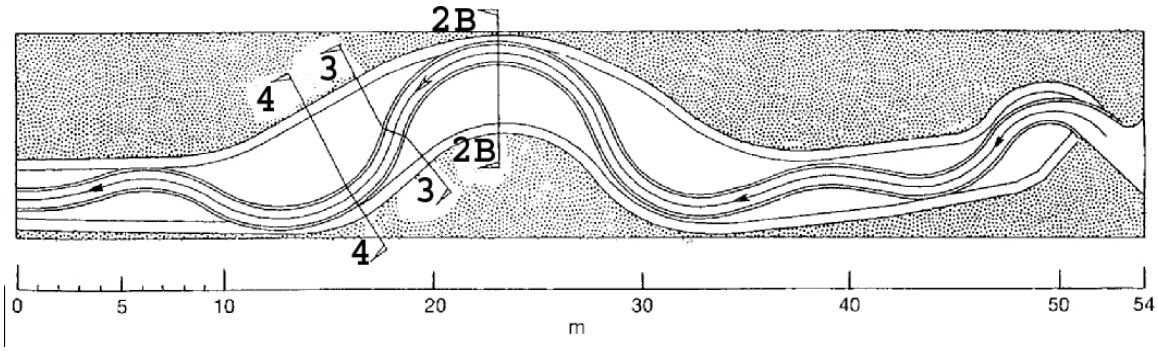

Figure 7.1 Measurement locations in the physical model (after Lambert and Sellin, 1996).

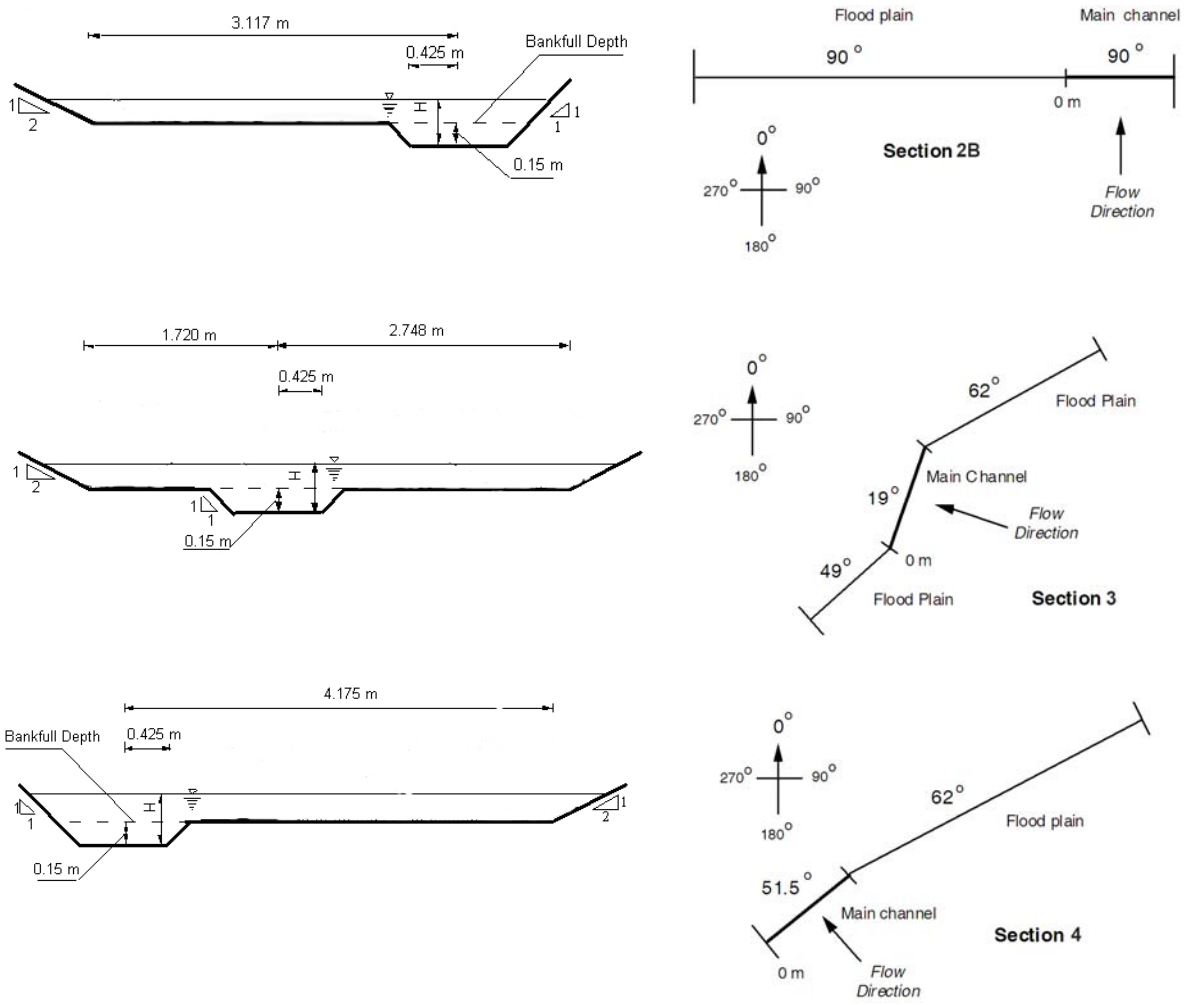

Figure 7.2 Geometry of cross-sections 2B, 3 and 4 on the physical model (after Lambert, 1993).

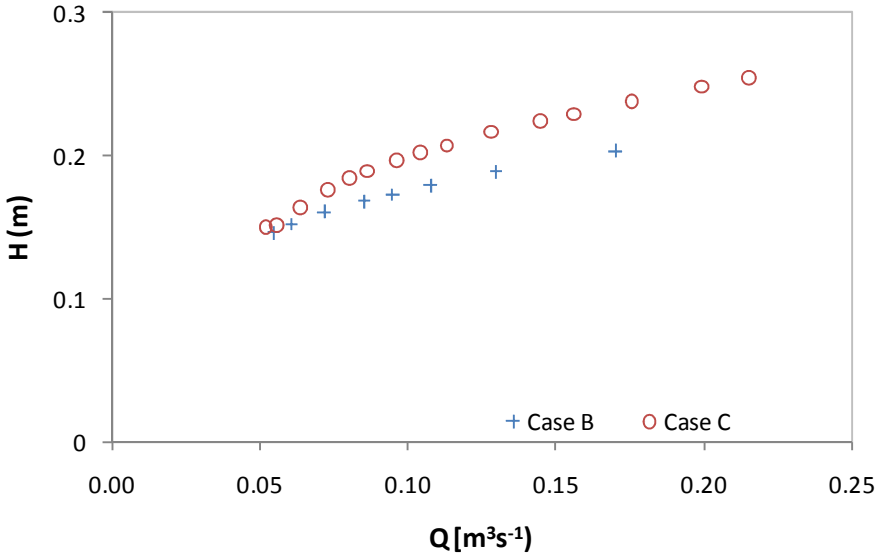

Figure 7.3 Stage-discharge relationship for cases B and C on the physical model (after Lambert, 1993).

7.1.2 Modelling approach

The calibration of the SKM was undertaken by adjusting the values of three coefficients, namely f, λ and Γ. The SKM simulations were undertaken using a 16 panel structure for each cross section. It was felt that this represented a reasonable trade-off between model complexity (which would arise as a result of increasing the number of panels) and the 2-D nature of the model (i.e. the assumptions embodied within the derivation of the SKM). The approach for obtaining these calibration parameters and the details of the 16 panel structure used are described below.

The friction factor, f, is usually assumed to be constant in each panel and often back calculated from the velocity and boundary shear stress data. However, since the boundary shear stress was not measured in most of the experiments, an alternative approach had to be used. Lambert and Sellin (1996) reported that the fully rough turbulent flow equation (7.1) could be used to convert the gravel size (k_s) into f with reasonable accuracy. However, implicit in this is the assumption of a direct relationship between gravel size (roughness) and flow resistance. Notwithstanding this assumption, this approach was adopted, and the parameter f was computed separately for the main channel and floodplain.

$$\frac{1}{\sqrt{f}} = -2.02 \log\left(\frac{k_S}{12.3R}\right) \qquad (7.1)$$

Chlebek (2008) reported that a value of 0.07 is often selected as a constant representing the dimensionless eddy viscosity (λ) as this is the depth-averaged value for a logarithmic velocity profile (Rutherford, 1994). This value has often been adopted in previous studies on different rivers (Knight *et al.*, 2007; Omran, 2005) and shown to yield reasonable results. Furthermore, Tang and Knight (2009) reported that variation of λ has a minor effect on simulations for overbank flows with a wide main channel and floodplain. In order to simplify the work, a constant λ value of 0.07 was adopted for all panels. It is recognised that this is a lower limiting value, and that values as high as 0.5 can be encountered.

The initial secondary flow values, Γ, values were calculated based on the guidelines suggested by Knight and Abril (1996) and Abril and Knight (2004) (equations (7.2) and (7.3)). Adjustment of the Γ values were then made until the Root Mean Square Error (RMSE) value of U_d was equal or less than 0.05ms^{-1} and the difference in discharge between the simulation result and data was within 5%.

$$\Gamma = 0.15\, H\rho g S_o \qquad \text{for main channel region} \qquad (7.2)$$

$$\Gamma = -0.25\, h\rho g S_o \qquad \text{for floodplain region} \qquad (7.3)$$

Furthermore, the sign of the parameter Γ is often used to determine the number of panels required for undertaking SKM (Knight *et al.*, 2007; Tang and Knight, 2009). The magnitude and sign of the term $(UV)_d$ varies depending on the position relative to the secondary flow cell and the rotational sense of the cell. As U is theoretically always positive, with values larger near the free surface than near the bed, and the transverse velocity, V, is only a small fraction of U, then as shown in Figure 7.4 $(UV)_d$ is positive when the rotation is clockwise and negative when the rotation is counter clockwise (Chlebek and Knight, 2006). The variation of $(UV)_d$ with respect to lateral distance gives the secondary term for a constant depth domain, since $\Gamma = dH(\rho UV)_d / dy$.

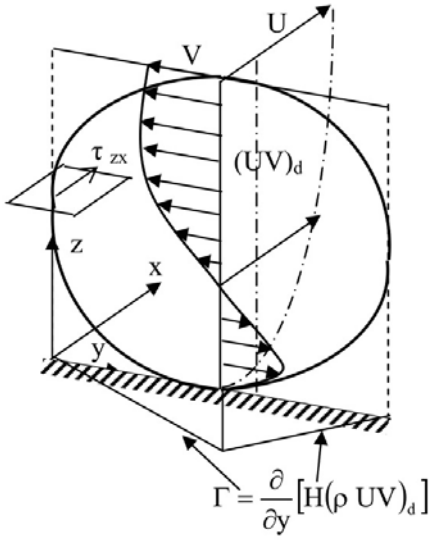

Figure 7.4 Depth-averaged secondary flow term (Chlebek and Knight, 2006).

Knight *et al.* (2007) suggested the physical interpretation of the secondary current term used in SKM using the 3D velocity data measured in a straight trapezoidal channel by Tominaga *et al.* (1989). Tominaga *et al.* (1989) detected three major secondary flow cells in such a channel, as illustrated in Figure 7.5. Knight *et al.* (2007) proposed that the sign of Γ can be obtained using the schematic variation of $(\rho UV)_d$ as shown in Figure 7.5, e.g. the sign of Γ in panel number two (P2a and P2) is negative, since the $(UV)_d$ term changes from a positive value at the right end of panel 3 to a negative value for panel 2, through to a positive value at the left end of panel 1. The SKM is based on using a constant value of Γ for each panel, with the number of panels required based on the sign of Γ. For the example showed in Figure 7.5, a minimum of four panels is required, since the sign of Γ changes three times laterally.

In contrast to the relatively simple distribution of secondary flow cells illustrated in Figure 7.5, a more complex distribution is observed in the UK Flood Channel Facility (FCF) data due to its more complex geometry. An example to the velocity distribution at CS 4 for case C2 is shown in Figures 7.6e and 7.6*f*. Two secondary flow cells one above another, and the depression of the maximum streamwise velocity below the water surface, makes the sign of Γ less predictable, and, thus adds considerable difficulty in determining the location of the panels.

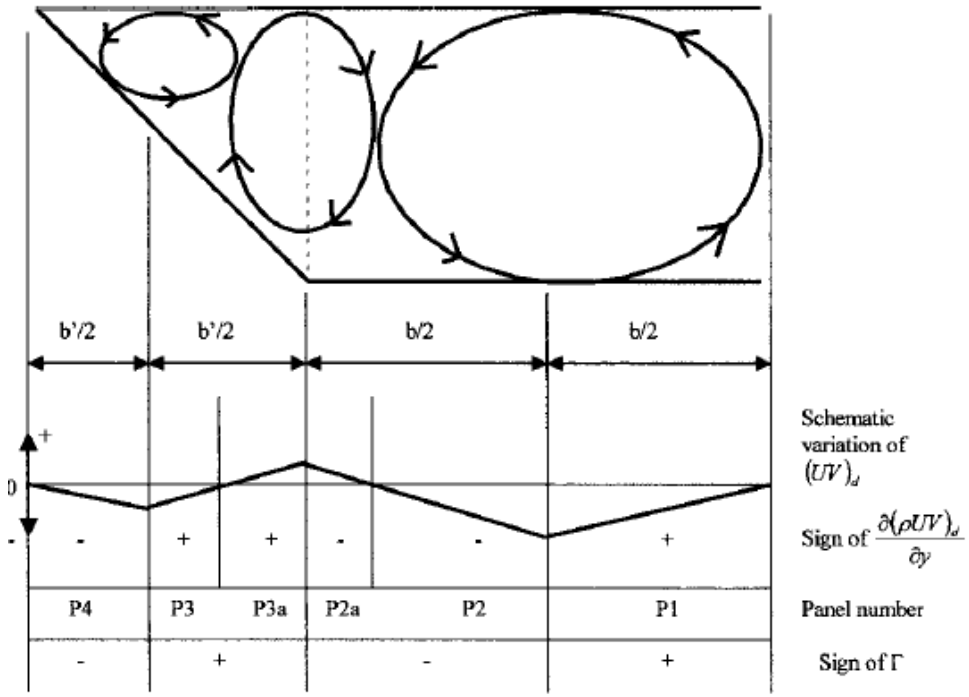

Figure 7.5 Number of panels and sign of secondary current term (Knight *et al.*, 2007).

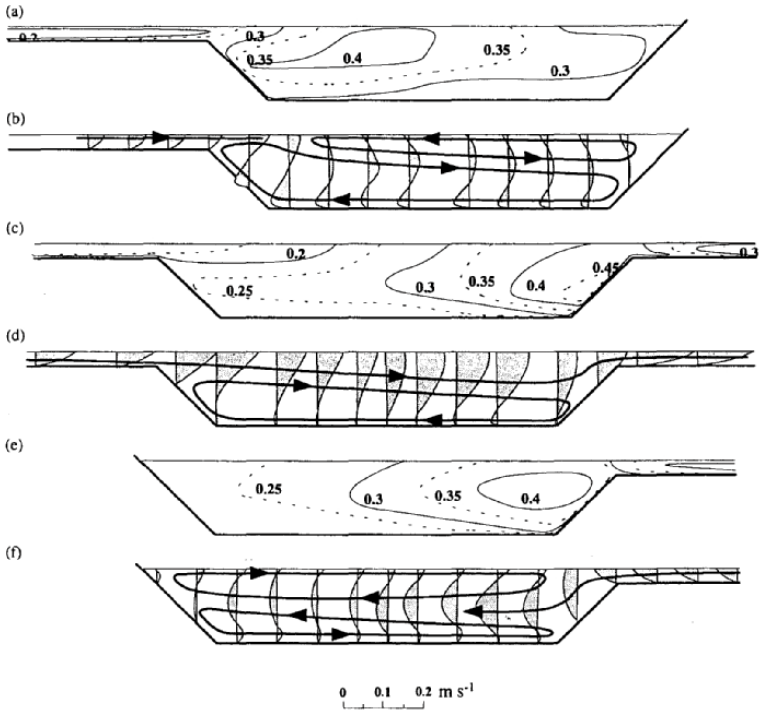

Figure 7.6 Contour of streamwise velocity and transverse velocity profiles for sections 2b (a, b), 3 (c, d) and 4 (e, f) for Case C2 (H = 0.187m) (Naish and Sellin, 1996).

It was decided to use a sixteen panel structure to simulate the flow for all cross-sections. A sixteen panel structure was considered to give the best trade-off between adequately representing the geometry and secondary flow and the amount of work to be undertaken. This panel structure consists of combining panels with flat beds and sloping sides, in order to correctly represent the geometry of the FCF channel (see Figure 7.7). A computer code was written in Visual Basic language within Microsoft Excel to automatically calculate the depth-averaged velocity and boundary shear stress, using SKM, when input parameters are given.

The panel numbers begin with the lowest number (1) on the left most edge of the channel, with the number increasing towards the right hand edge of the channel. Sloping floodplain walls, main channel walls and floodplain beds are represented with two panels each, whereas the main channel bed is represented with four panels. This approach was taken to ensure that an adequate number of panels are available when required, to represent the secondary flow cells distribution in the main channel, as suggested by Knight *et al.* (2007) (Figure 7.5). The flat bed panels located to the side of the main channel, where a floodplain exists, are disabled when appropriate. This is achieved by entering the edge coordinates of the disabled panels with the same value of the right edge coordinate of the previous active panel. For example, if panels 3 and 4 in Figure 7.7 are disabled, the edge coordinates of panels 3 and 4 are used as inputs to the coordinate of the right edge of panel 2, thus the right edge of panel 2 is connected to the left edge of panel 5. Such an adjustment has been proved to not affect the simulation result, e.g. an identical U_d distribution is observed on a trapezoidal channel simulated using a 3 panel structure and 16 panel structure with uneven panel length (Figure 7.8). For the three panel solution, an individual panel was assigned for chainage values of 0 m – 10 m, 10 m – 20 m and 20 m – 30 m, whereas for the 16 panel case the panels were assigned as shown in Figure 7.8. The values of calibration parameters used for the simulations are shown in Table 7.2.

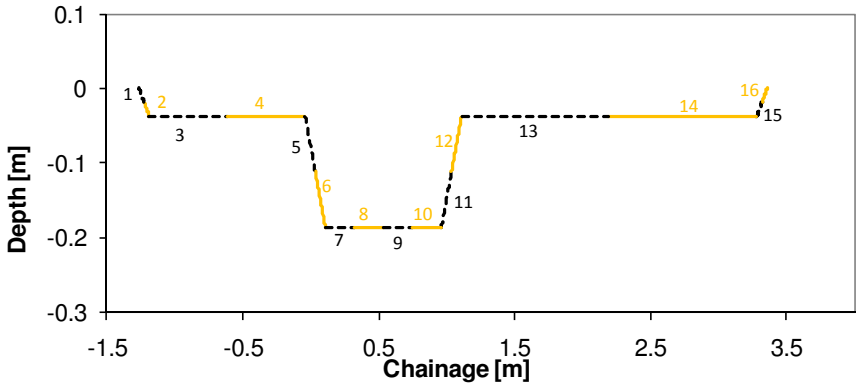

Figure 7.7 Panel numbering of the SKM model with 16 panel structure.

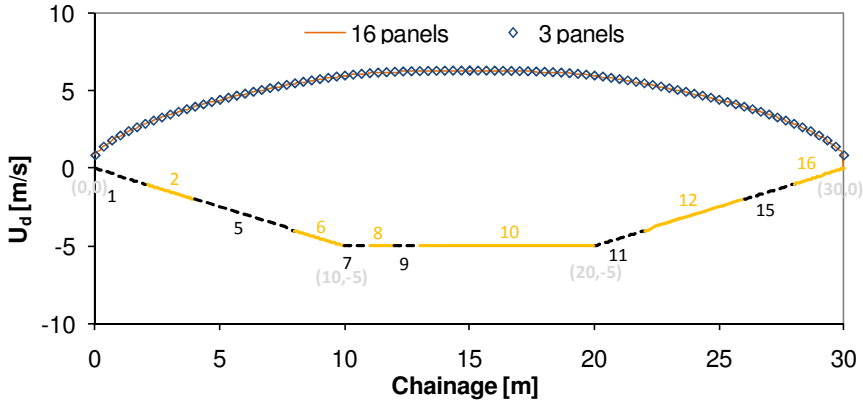

Figure 7.8 Comparison of U_d simulated using 3 panel structure and 16 panel structure with uneven panel length.

Parameter	Value	Unit
ρ	1000	(kgm^{-3})
g	9.81	(ms^{-2})
S_o	0.001	(-)

Parameter	Value	Unit
f	0.01	(-)
λ	0.01	(-)
Γ	-1	($kgm^{-1}s^{-2}$)

Table 7.2 Parameters values for the simulation results shown in Figure 7.8 (for all panels).

In order to determine whether Γ values calculated from the measurement data could be suitable for calibrating SKM, a test was conducted for one of the simulation cases. Figure 7.9 shows the calculated values of Γ for CS 2B case C2. There are typically eight measurement points over the depth of the main channel and two measurement points over the depth of the floodplain (Figure 7.10). The resulting values of $|\bar{\Gamma}|$ are typically larger than 2, with average values of 43.5 and 7.7 for the main channel and floodplain respectively. These are significantly higher than those previously calculated using the equations 7.2 and 7.3 (Table 7.3), as well as those used in the simulations (Tables 7.4 and 7.5), and resulted in unrealistic U_d values when used in the calibration. The extreme values of the calculated Γ are +224.3 and – 145.6. Furthermore, the Γ values vary significantly, with alternating negative and positive signs, at the interface between the floodplain and the main channel (Figure 7.9) and the main channel bank. This may not be surprising since the lateral gradient of the velocities in such locations is generally expected to be high, although the magnitude is not yet known. It is probable that the values of $|\bar{\Gamma}|$ could decrease, closer to the values computed from equations (7.2) and (7.3), if the density of the measurement points is increased, since Γ values are sensitive, especially to the lateral changes of *UV*. Further experimental work is recommended in order to provide an answer to this question.

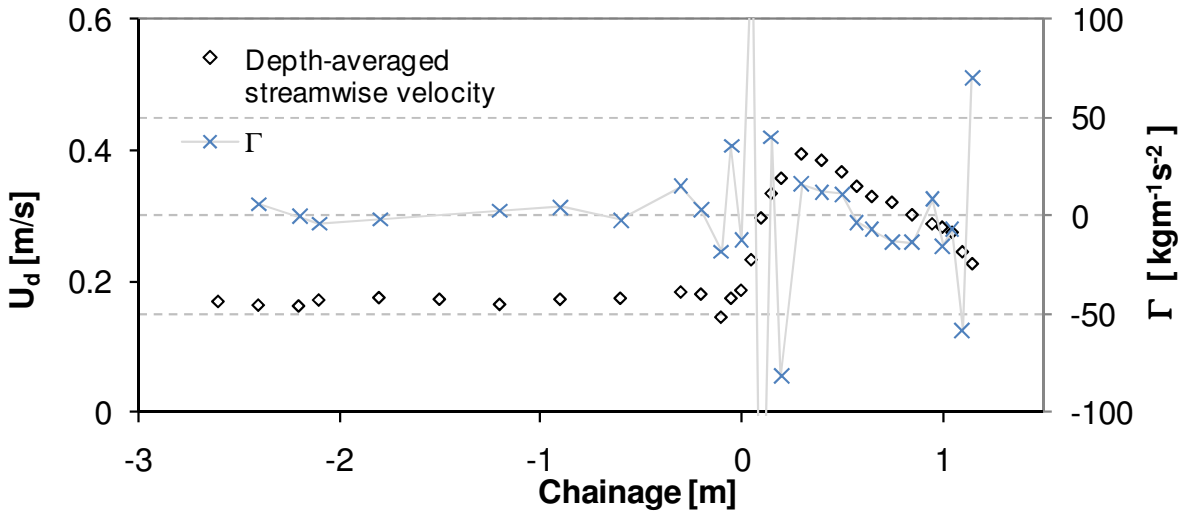

Figure 7.9 Lateral variation of Γ for CS 2B case C2 (physical model).

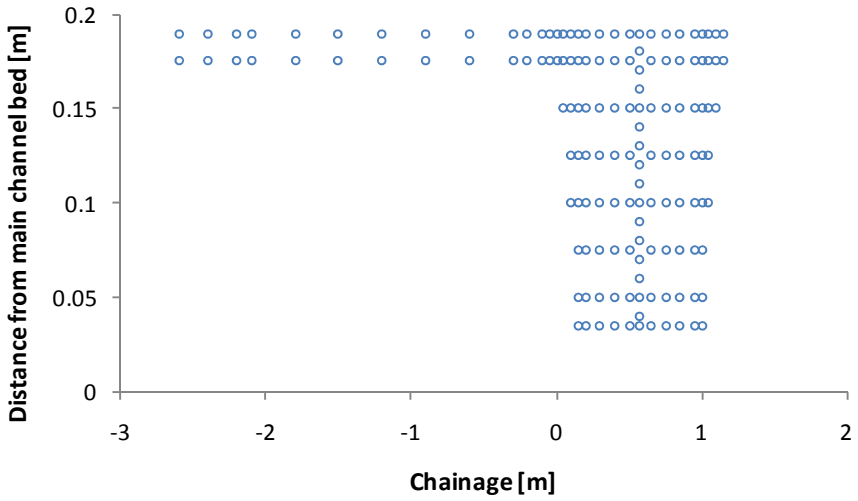

Figure 7.10 Point velocity measurement density for CS 2B case C2 (physical model).

H (m)	Γ- main channel (kgm^{-1}s^{-2})	Γ- floodplain (kgm^{-1}s^{-2})
0.162	0.24	-0.03
0.187	0.28	-0.09
0.237	0.35	-0.21

Table 7.3 The secondary flow term values (physical model CS 2B), calculated using equations 7.2 and 7.3.

7.1.3 Results and discussion

The main points arising from the simulations are:

1. Figures 7.11 and 7.12 show that the SKM is able to predict the trend of the depth-averaged streamwise velocity across the main channel and floodplains quite well (the values of f, λ and Γ used in these simulations are presented in Tables 7.4 and 7.5). This is also supported by the low values of the Root Mean Squared Error (RMSE) between the simulation results and the experimental data, i.e. within 0.05ms^{-1} (Figure 7.13). Furthermore, the maximum value of the lateral distribution of the depth averaged streamwise velocity was also predicted reasonably well.
2. The simulated velocity distribution is well correlated with the experimental data, with values of the correlation coefficient for 7 out of the 8 cases in the region of 0.91 – 0.99 (Figure 7.14). A lower value for the correlation coefficient was achieved for case C1-CS 4 (0.81). This is influenced by the difficulty in modelling the peak velocity because it is located in the middle of the panel. Moving the edge of the panel adjacent to the peak velocity can improve the modelling accuracy. However, this step was not adopted in order to retain the consistency of panel numbering for all cases.
3. The distribution of boundary shear stress data, for the case where shear stress data is available (CS2B case B2), was not predicted accurately (Figure 7.15). The peak of the simulation shear stress was shifted to the right of that of the experimental data.
4. The differences between simulated and measured discharges for all cases are within 5% (Table 7.6). Such agreement is often considered as “good” for engineering applications.
5. Simulated velocity in a long flat bed panel tends to be constant along the panel. Thus, accurate prediction is difficult to achieve when the actual velocity distribution in the panel is irregular. Adding more panels could help to increase the resolution of the result but computationally requires more effort.
6. Figures 7.11b and d indicate for CS 2B that there are higher velocities in the floodplain, in the region adjacent to the main channel, for the smooth floodplain case (case B2, H = 0.187m). The velocity is almost twice that for the rough floodplain case (case C2). Figure 7.11b also shows that the measured velocities on the floodplain for case C2 are almost constant at 0.2ms^{-1}. Unfortunately, velocity data on the floodplain for the case B2 is only available for a small region, i.e. the region adjacent to the main channel. The velocities on the unmeasured region for case B2 were simulated, and retaining the velocities in the unmeasured region at similar value to that

in the region adjacent to the main channel resulted in higher than the desired 5% discharge difference between data and simulation. In order to retain the discharge different within 5% (to be consistent with the other simulations), lower velocities in the unmeasured region are required (Figure 7.11d). It may, therefore, be concluded that if the floodplain is sufficiently smooth (e.g. case B2 – CS 2B), the velocities decrease along the floodplain, from the edge on the main channel to the floodplain bank. This is due to the decreasing influence of the velocity in the main channel. The influence of the main channel flow on the floodplain flow decreases with rising roughness in the floodplain, until it becomes insignificant, e.g. for the 8mm gravel roughness on the floodplain for case C2 at CS 2B. However, it is acknowledged that this also depends on the longitudinal geometry of the channel and the depth ratio of the channel (c.f. point no. 7).

7. Figures 7.11c and 7.12c show that, at a higher depth (e.g. H = 0.237m), higher velocities are observed in the middle of the floodplain, near the floodplain bank. This is because the floodplain flow in a meandering channel tends to be more tangential to the main channel flow with increasing relative depth (c.f. Figure 2.5 and Shiono and Muto, 1998). As for cross sections 2B and 4, the high velocity region on the floodplain tends to move away from the main channel with increasing depth ratio, following the slope of the valley (c.f. Figure 7.1).
8. The velocity distribution in cross sections 2B and 4, for case C2, is similar, i.e. the floodplain velocity remains relatively constant at ~0.2ms^{-1} and the maximum main channel velocity in the inner bend of the meander is ~0.4ms^{-1}. For a higher water depth (case C3), the velocities at CS 4, especially in the main channel, are significantly lower than those at CS 2B. This appears to be caused by the reduction of kinetic energy, due to the shear between the floodplain and main channel flows, which takes place in the cross-over region between CS 2B and CS 4.
9. The values of Γ for the main channel, calculated from equation 7.2, are typically 2 to 5 times lower than those used in the model (c.f. Tables 7.3 and 7.4). Generally, the differences become higher with rising water depth. For the floodplain, equation 7.3 can estimate the Γ values in the floodplain reasonably well (c.f. Tables 7.3 and 7.4). The sign of Γ in most of the panels appear to follow the sign in equations (7.2) and (7.3), i.e. positive in the main channel and negative in the floodplain.

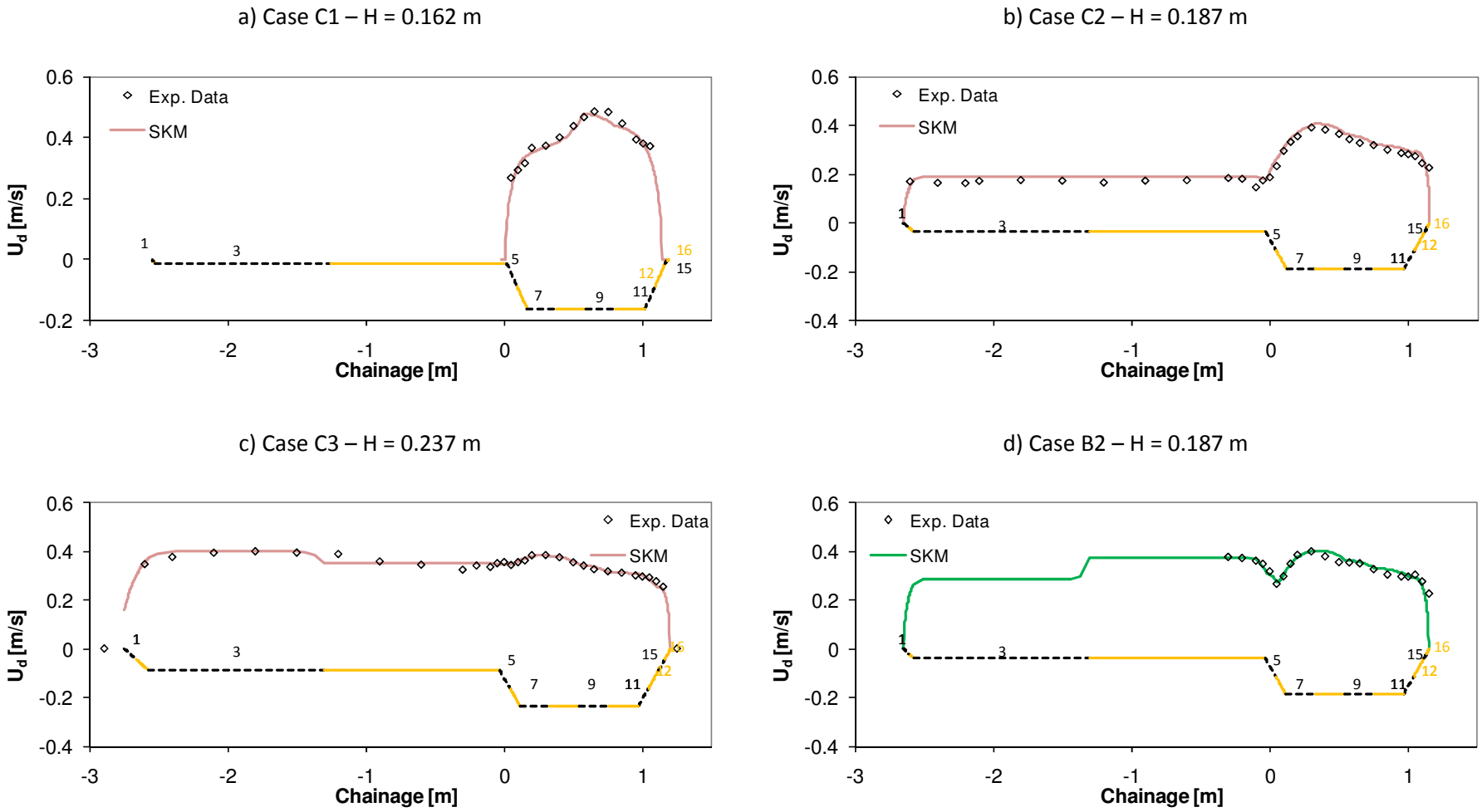

Figure 7.11 Comparison of simulated U_d and data at CS 2B (physical model).

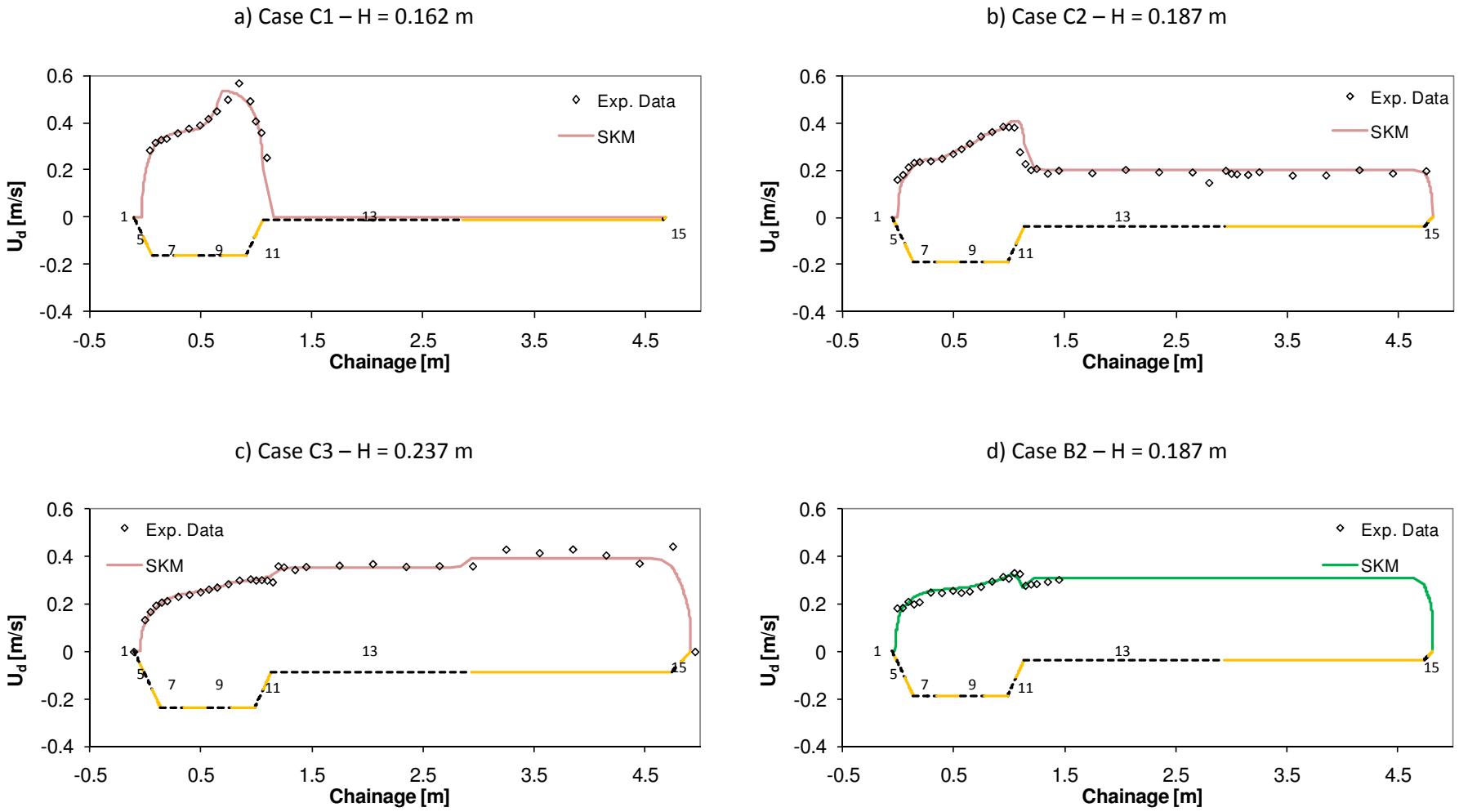

Figure 7.12 Comparison of simulated U_d and data at CS 4 (physical model).

Panel no.	Case C1 H= 0.162 m		Case C2 H= 0.187 m		Case C3 H= 0.237 m		Case B2 H= 0.187 m	
	f	Γ	*f*	Γ	*f*	Γ	*f*	Γ
1	*N/A*	*N/A*	0.08	0	0.055	-0.2	0.035	0
2	*N/A*	*N/A*	0.08	0	0.055	-0.2	0.035	0
3	*N/A*	*N/A*	0.08	0	0.055	-0.25	0.035	0
4	*N/A*	*N/A*	0.08	0	0.055	0	0.035	-0.25
5	0.047	0.4	0.044	0.5	0.041	0.3	0.035	0
6	0.047	0.4	0.044	1.3	0.041	1.5	0.044	1.8
7	0.047	0.8	0.044	0.9	0.041	1.4	0.044	0.8
8	0.047	0.8	0.044	0.8	0.041	1.45	0.044	0.8
9	0.047	0.2	0.044	1.05	0.041	1.65	0.044	1.05
10	0.047	0.3	0.044	1.25	0.041	1.8	0.044	1.2
11	0.047	0.4	0.044	1	0.041	1.2	0.044	1
12	0.047	0.4	0.044	0	0.041	0.9	0.044	0.05
13	*N/A*	*N/A*	*N/A*	*N/A*	*N/A*	*N/A*	*N/A*	*N/A*
14	*N/A*	*N/A*	*N/A*	*N/A*	*N/A*	*N/A*	*N/A*	*N/A*
15	0.047	0.4	0.044	0	0.041	0.1	0.044	0.05
16	0.047	0.4	0.044	0	0.041	0.1	0.044	0.1

Note: double line indicates border between main channel and floodplain.

Table 7.4 Calibration parameter for CS 2B (physical model).

Panel no.	Case C1 H= 0.162 m		Case C2 H= 0.187 m		Case C3 H= 0.237 m		Case B2 H= 0.187 m	
	f	Γ	*f*	Γ	*f*	Γ	*f*	Γ
1	0.047	0.3	0.044	0.6	0.041	0.6	0.044	0.3
2	0.047	0.3	0.044	0.6	0.041	0.6	0.044	0.3
3	*N/A*	*N/A*	*N/A*	*N/A*	*N/A*	*N/A*	*N/A*	*N/A*
4	*N/A*	*N/A*	*N/A*	*N/A*	*N/A*	*N/A*	*N/A*	*N/A*
5	0.047	1	0.044	0.6	0.041	1.1	0.044	0.5
6	0.047	1	0.044	1.4	0.041	1.9	0.044	1.3
7	0.047	0.8	0.044	1.4	0.041	2	0.044	1.45
8	0.047	0.8	0.044	1.5	0.041	2	0.044	1.45
9	0.047	0.9	0.044	1.4	0.041	2	0.044	1.45
10	0.047	-0.2	0.044	1.2	0.041	1.9	0.044	1.4
11	0.047	-0.4	0.044	-0.2	0.041	1.3	0.035	0.55
12	0.047	-0.4	0.044	-0.6	0.041	0.5	0.035	0.3
13	*N/A*	*N/A*	0.08	-0.05	0.055	0	0.035	-0.05
14	*N/A*	*N/A*	0.08	-0.05	0.055	-0.2	0.035	-0.05
15	*N/A*	*N/A*	0.08	-0.05	0.055	-0.1	0.035	0
16	*N/A*	*N/A*	0.08	-0.05	0.055	-0.1	0.035	-0.1

Note: double line indicates border between main channel and floodplain.

Table 7.5 Calibration parameter for CS4 (physical model).

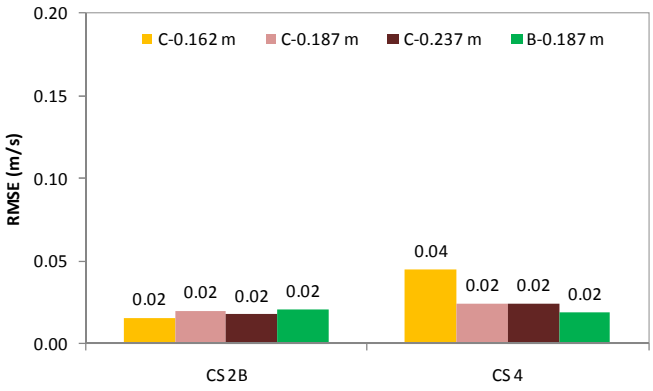

Figure 7.13 RMSE values between SKM simulations and data (physical model).

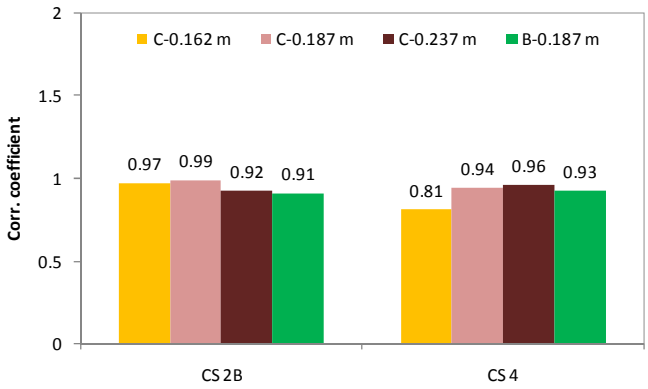

Figure 7.14 Correlation coefficient values between SKM simulations and data (physical model).

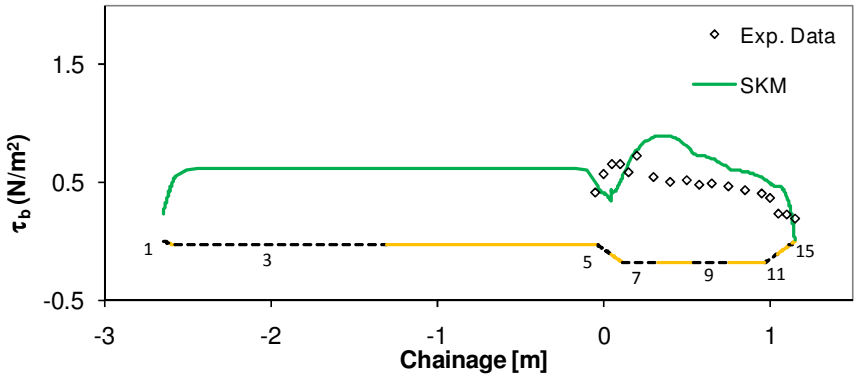

Figure 7.15 Distribution of simulated τ_b at CS 2B for case B 2 (physical model).

	Case C1	Case C2	Case C3	Case B2
H (m)	0.162	0.187	0.237	0.187
Measured *Q* (m^3/s)	0.065	0.084	0.175	0.095
CS 2B	4.6	0.8	0.8	4.4
CS 4	4.4	0.43	0.43	-2.1

Table 7.6 Difference (in percent) between measured and simulated discharge (physical model).

7.2 Simulating flows in the River Blackwater at full scale

The post-processed U_d at cross sections 2 and 4 previously discussed in Chapter 5 were also simulated using the Shiono and Knight Method. Three different cases: inbank, bankfull and overbank are now discussed.

7.2.1 Modelling approach

The geometry of the river for SKM modelling was based on the survey undertaken in 2007 (see Chapter 3). The SKM modelling for all cases were undertaken using a Visual Basic code that can accommodate up to 16 sloping bed panels. Only sloping bed panels were used in the code since the main channel and floodplain beds in the river generally have some degree of irregularity, i.e. the bed and walls slope. The panel numbering used is the same to that for the numerical modelling of the experimental data, with the lowest number (1) on the left most edge of the channel and with the number increasing towards the right hand edge of the channel.

The global f values could be estimated from ADCP measurements using equation (7.4). The minimum and maximum values of f and the corresponding water surface slope (S_w) during the measurement are shown in Table 7.7. It is assumed that S_w is equal to the bed slope (S_o) and, this value was used throughout the modelling (c.f. Table 7.7). The large f values for inbank condition are possibly caused by the very high density of weed in the main channel during the corresponding month (August). For example, it was found that the water level at CS4 during the 18/8/2008 inbank measurement was 6cms higher than that during the 7/12/2007 inbank measurement, even though the discharge for the latter was 90% higher than the discharge for the first (c.f. Table 5.3).

As global, zonal and local friction factors are different concepts in quasi-2D modelling (Morvan, *et.al*, 2008; see also Section 2.4.1), applying the f values in Table 7.7 to each panel on SKM might not be appropriate. When f for each panel (i.e. the zonal friction factor) is computed from the measurement data, the value of the computation result will depend on panel structure and division selected. Furthermore, there is some uncertainty as to how the wetted perimeter for each panel for such a case should be defined. Due to these uncertainties it was decided that f would be calibrated, with the computed global f values used as guidance for the initial f values used in the modelling.

$$f = \frac{8gn^2}{R^{1/3}} \tag{7.4}$$

	18/08/2008 (Inbank)	16/01/2008 (Bankfull)	10/02/2009 (Overbank)
S_w	10^{-3}	$5 \times 10^{-4} - 6 \times 10^{-4}$	$7 \times 10^{-4} - 8 \times 10^{-4}$
min *f* (CS2)	9.19	0.22	0.22
max *f* (CS2)	17.04	0.26	0.24
min *f* (CS4)	1.94	0.08	0.26
max *f* (CS4)	3.43	0.10	0.30

Table 7.7 Measured water surface slope and friction coefficient for inbank, bankfull and overbank cases being investigated.

An attempt to quantify the secondary flow term in the river using ADCP transect averaging data was made in order to get a sense of its scale. Due to technical limitations of the ADCP, the unmeasured area near the water surface and the river bed were not included in the calculation. In order to reduce the noise in the result, a moving-average filter that averages every five consecutive data was introduced. Figures 7.16 and 7. 17 show the computed Γ values for cross sections 2 and 4.

The lateral variation of Γ is complex, with frequent alternation of positive and negative signs. There is a significant increase in the maximum magnitude of Γ when the flow changes from inbank to overbank (see Figures 7.16 and 7.17). The average of absolute secondary flow term ($|\bar{\Gamma}|$) rose from the inbank to the bankfull condition at cross-sections 2 and 4 seven and three times respectively, and further rose eight and six times from the inbank to the overbank flow condition. The maximum magnitudes of Γ in both cross-sections are two orders of magnitude higher than the Γ values that are often used for rivers (e.g. Abril and Knight, 2005; Sharifi, 2009).

In comparison to the Γ values calculated from the physical model (Figure 7.9), the alternating between positive and negative sign in the river are more intense. Furthermore, the values of $|\bar{\Gamma}|$ in the river are higher than those in the physical model, i.e. 45.5 in the model compared to 133 and 175 in the river. This may be due to the more complex flow conditions in the field than in the laboratory, as well as the differences in the measurement devices being used and the differences in the spatial density of the measurement points.

a)Inbank

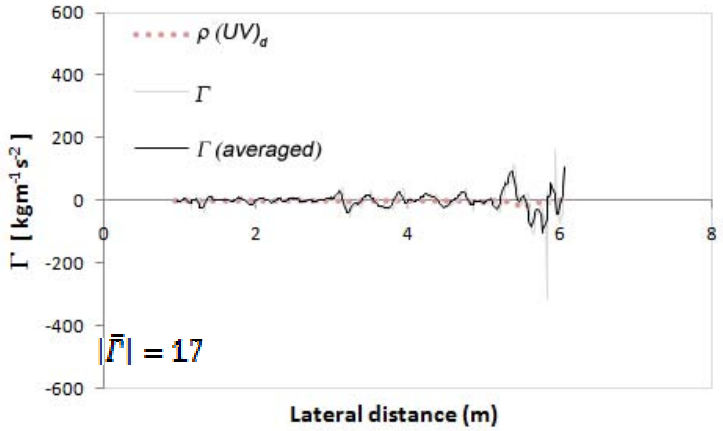

b)Bankfull

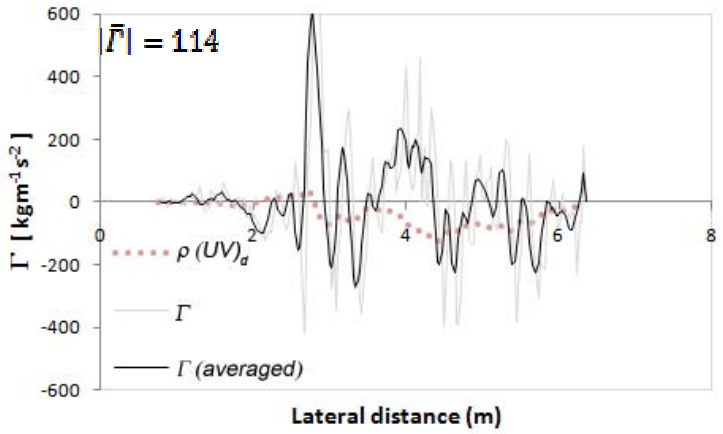

c)Overbank

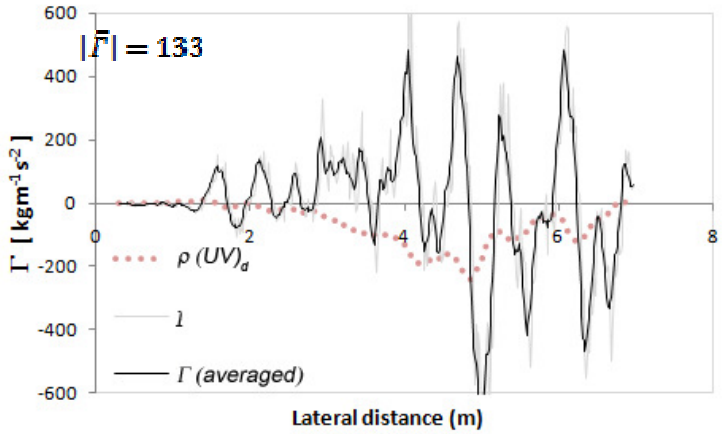

Figure 7.16 Lateral variation of Γ for CS 2 (field data).

a)Inbank

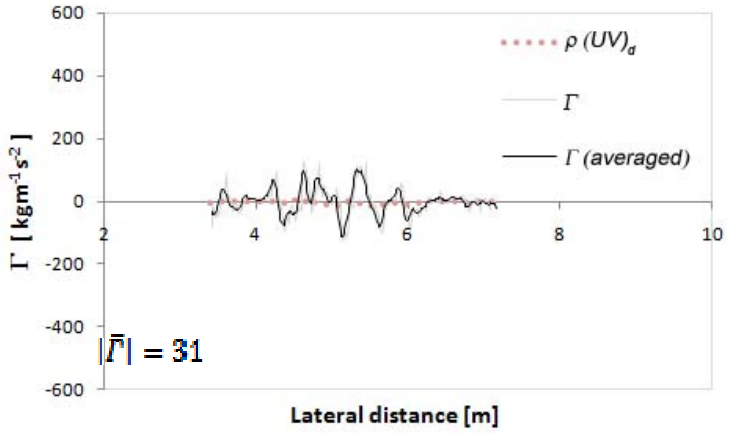

b)Bankfull

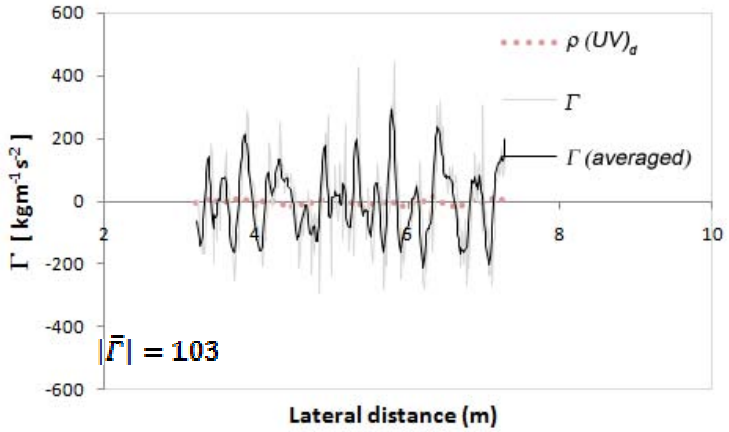

c)Overbank

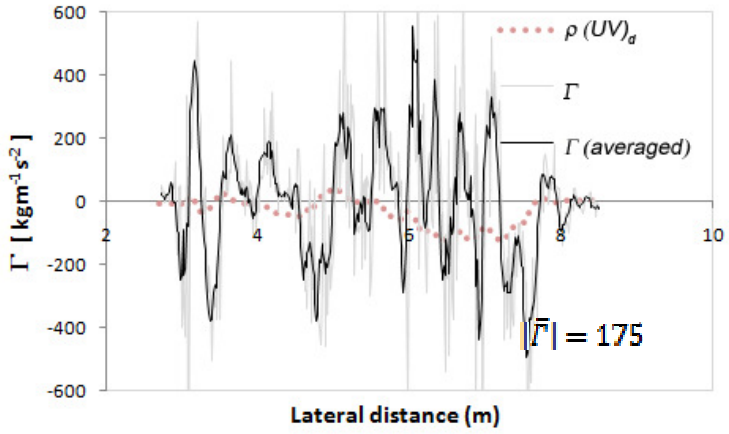

Figure 7.17 Lateral variation of Γ for CS 4 (field data).

Since the SKM incorporates a spatially averaged Γ for each panel, the average for each panel was also computed. The calculated Γ values between panels differ by up to two orders of magnitude (0 ± 140kgm^{-1}s^{-2}). The calculated Γ values, when used in the simulation, yield extremely large or low values of simulated U_d and, therefore, are not able to achieve the required modelling accuracy. It is acknowledged that a different selection of panel structure could alter the average Γ values, but this will not change the value range of the data (up to two orders of magnitude). The Γ values in the modelling will, therefore, be calibrated.

Due to existence of the equifinality problem, where different sets of model parameters can produce equally acceptable results (see Section 2.4.3.2), it was decided that the calibration should be focused on a range of parameter values that produce RMSE ≤ 0.05 ms^{-1} and ΔQ ≤ 5% between simulation and measurement, rather than concentrating on just one set values of f, λ and Γ. In keeping with previous work (Knight, *et al.*, 2007; Omran, 2005) it was also decided that λ should take a constant value of 0.07 for all of the cases, since this parameter has been shown to have a limited impact on the accuracy of the simulated data. A "reasonable" range of f and Γ values that produce reasonably good results was then established from previous research work. The modelling approach adopted to achieve this goal was to initially set Γ to zero for all panels, and then to vary only f to fit the measured data. When RMSE ≤ 0.05 ms^{-1} and ΔQ ≤ 5% have been achieved, new simulations were then conducted with new f values, which were varied by 25% and 50% from the initial f values (for each panel). As the f values for the new simulation were altered from the initial values, the parameter Γ was calibrated in order retain the RMSE and ΔQ thresholds. For the rest of this thesis, the five sets of calibration parameters are referred as cases 100%f (initial f), 50% f, 150% f, 75%f and 125%f.

7.2.2 Results and discussion

The main points arising from these simulations are:

1. Figures 7.18 and 7.19 show that the SKM is able to predict the trends in the depth-averaged streamwise velocity across the main channel and floodplains for cross sections 2 and 4, using five different set of parameters mentioned in section 7.2.1. The simulated results in these Figures indicate that no significant changes in the U_d values occur when the effect of changing f values was compensated by choosing suitable Γ values. This is also supported by the low values

of RMSE (within 0.05 ms^{-1}) and high values of correlation coefficient (>0.86) between simulated and measured U_d (Tables 7.8 and 7.9).

2. A difference of between +16% to +16.6% for simulated and measured discharges was achieved for the CS2 inbank case (Table 7.10) while differences for other cases were generally within 5%. Thus, the CS2 inbank case is excluded from the following discussion points in this section, except where relevant to other issues.
3. It is shown that a good fit between simulated and measured U_d can be obtained by calibrating *f* and setting λ and Γ for each panel to 0.07 and 0. Lowering the initial *f* values by 25% (case 75%*f*) can be compensated by increasing Γ to a certain value for each panel, whereas lowering *f* values by 50% (case 50%*f*) can be compensated by increasing Γ to twice of the value required for case 75%*f* (see Tables 7.11 and 7.12). This relationship is also valid for the 125%*f* and 150%*f* cases. This shows that altering *f* and Γ based on a linear relationship could be used to retain the defined simulation thresholds (RMSE ≤ 0.05 ms^{-1} and ΔQ ≤ 5%). An example of such a relationship is shown in Figure 7.20. Such a simple "trade-off" relationship between *f* and Γ provides an easy approach to calibration for SKM users.
4. While calibrating the SKM is generally not difficult, the values of *f* and Γ should ideally be based on a rational physical interpretation. Guidance for choosing *f* can be sought from textbooks and previous findings (e.g. Knight *et al,* 2010). Chow (1959), for example, provides a Table of Manning's *n* values for natural streams, ranging from 0.025 for a clean and straight channel to 0.15 for a weedy stream. The equivalent *f* values for such *n* values are 0.06 and 2.28, when equation 7.1 is used for converting them using the hydraulic radius for the CS4 inbank case.
5. Not enough is known about the lateral variation of Γ in natural rivers. Values of Γ as low as -4 and as high as 8.63 have been used for calibrating SKM in full-scale rivers (Abril and Knight, 2004; Sharifi, 2009). A sensitivity analysis was undertaken in which the *f* values in all panels were set to 0.01 for the overbank flow cases. The Γ values required to produce an adequate fit between the simulated and measured U_d then were always lower than 10. It is therefore concluded that 10, or lower, is the upper limit of Γ values for any modelled cross-section, since *f* values in natural streams are likely to be higher than 0.010.
6. Most of the *f* and Γ values used in the calibration of the River Blackwater are within the range mentioned in point no.4. A large *f* value is required to correctly model low velocities that often occur on floodplains, caused by dense vegetation, e.g. on the right floodplain of CS-2 overbank case (panel 11). Furthermore, low velocities that require large *f* values for calibration were also present in the left part of the main channel for both cross sections. It is suspected that the

sudden widening of the cross-section (see also Figure 3.18) just upstream CS2 produces a low velocity region on the left part of CS2 main channel. A low velocity region also occurred on the left part of CS4 main channel, as it is located in the outer part of a meander bend. Rameshwaran and Shiono (2007) and Tang and Knight (2009b) introduced an additional momentum sink term into the RANS equation in order to account for the effect of vegetation, rather than including it into the friction factor. Such an approach is yet to be used in the current research, but is recommended for further work.

7. Figures 7.18 and 7.19 show that altering f yields little difference to the simulated U_d. Such differences in f values are not significant in a 1D modelling application such as conveyance estimation, but could be important for 2D/3D applications involving pollution dispersion, sediment transport and fish habitats.
8. Higher f values are required for inbank cases. Typically one or two higher orders of magnitude in f values are required for the inbank cases compared to the bankfull cases. This trend is similar to the values calculated from the measurements (Table 7.7).
9. Modelling the flow in rivers is a complex task, and is not generally as straight forward as most people imagine. The SKM has been shown to be capable of simulating the measured discharge and depth averaged streamwise velocity in the River Blackwater with reasonable accuracy. However, predicting the stage-discharge rating curve for a wider depth range using SKM, and also using other numerical models, is a more difficult process since the values of the calibration parameters are likely to vary with flow depth. Knowledge of these variations is therefore needed prior to calibration. When measurement data at two or more water depths are available, the trend may be estimated by interpolating calibration parameters from the simulations of the measured data.
10. In order to examine the changes in f values with rising water level, used in the calibration (Tables 7.11 and 7.12), the ratio between f at inbank and bankfull and at bankfull and overbank was computed. A similar procedure was undertaken for Γ, but not adopted when the values were equal to zero. The calculated ratios for cases 50%f, 75%f, 125%f and 150% are shown in Tables 7.13 and 7.14. It is acknowledged that the values shown in Tables 7.13 and 7.14 may be different, if different combination of f and Γ are chosen, since there is a "trade-off" relationship between f and Γ(c.f. point no. 3).

a) Inbank

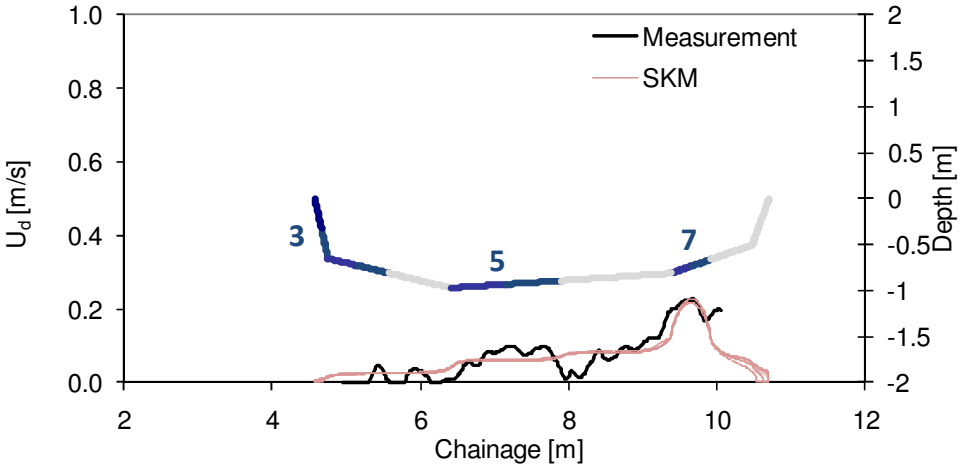

2) Bankfull

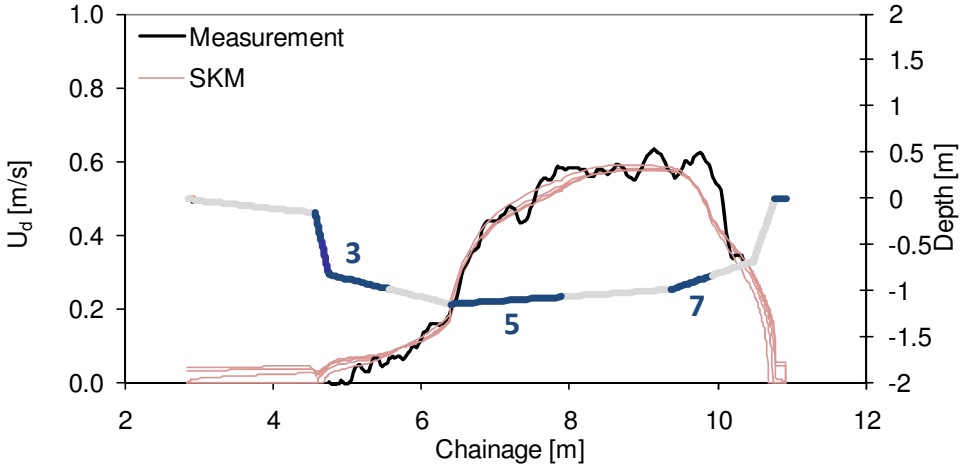

c) Overbank

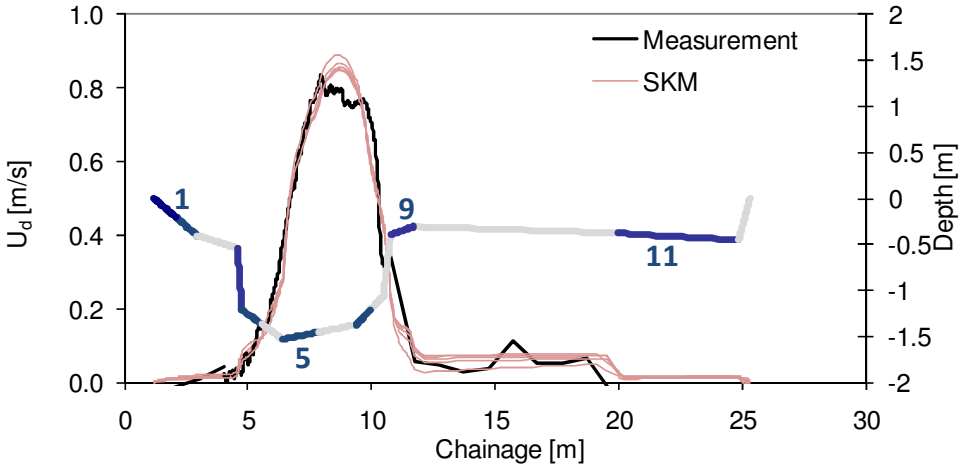

Figure 7.18 Comparison of simulated U_d and measurement at CS 2 for inbank, bankfull and overbank flow conditions (field data).

a) Inbank

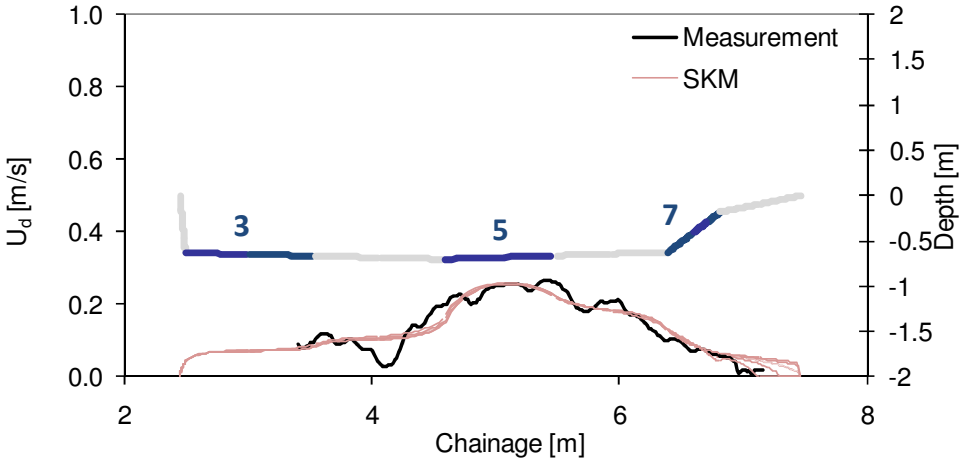

b) Bankfull

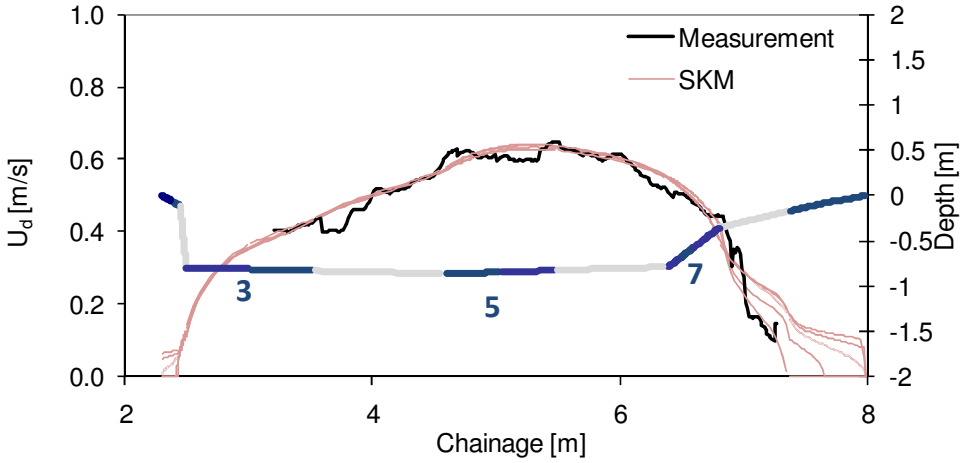

c) Overbank

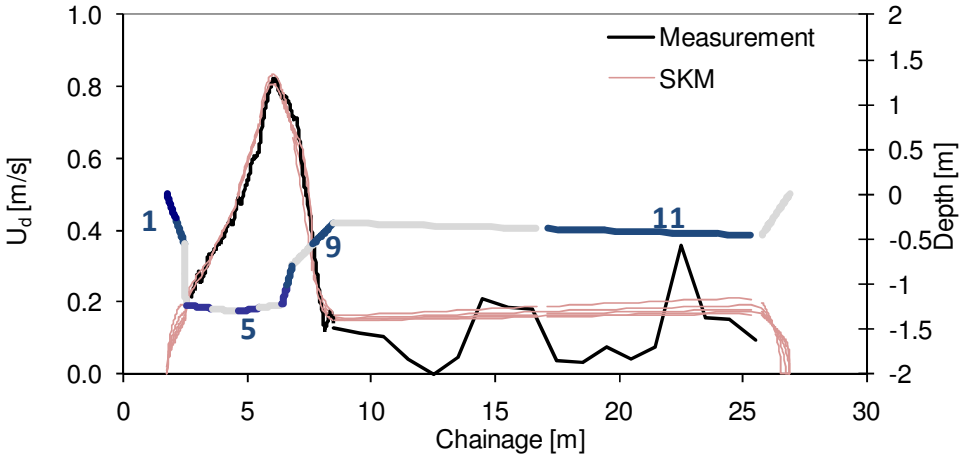

Figure 7.19 Comparison of simulated U_d and measurement at CS 4 for inbank, bankfull and overbank flow conditions (field data).

	50%f	75%f	100%f	125%f	150%f
CS2-inbank	0.03	0.03	0.03	0.03	0.03
CS2-bankfull	0.03	0.04	0.03	0.04	0.03
CS2-overbank	0.04	0.05	0.04	0.05	0.04
CS4-inbank	0.03	0.03	0.03	0.03	0.03
CS4-bankfull	0.03	0.03	0.04	0.04	0.04
CS4-overbank	0.05	0.03	0.03	0.03	0.03

Table 7.8 RMSE value between simulated and measured U_d (ms^{-1}) for field data.

	50%f	75%f	100%f	125%f	150%f
CS2-inbank	0.87	0.86	0.87	0.86	0.87
CS2-bankfull	0.99	0.99	0.99	0.99	0.99
CS2-overbank	0.99	0.98	0.99	0.99	0.99
CS4-inbank	0.94	0.94	0.94	0.94	0.94
CS4-bankfull	0.98	0.97	0.97	0.96	0.96
CS4-overbank	0.98	0.99	0.99	0.99	0.99

Table 7.9 Correlation coefficient value between simulated and measured U_d for field data.

	50%f	75%f	100%f	125%f	150%f
CS2-inbank	16.6	16.1	16.0	16.0	16.1
CS2-bankfull	1.3	0.4	0.0	-0.1	-0.2
CS2-overbank	4.9	4.0	3.5	3.2	3.2
CS4-inbank	0.3	-0.8	-1.3	-1.6	-1.7
CS4-bankfull	-4.0	-3.3	-3.0	-2.7	-2.5
CS4-overbank	0.6	-1.7	-2.8	-3.5	-4.0

Table 7.10 Difference between simulated and measured discharge (in percent) for field data.

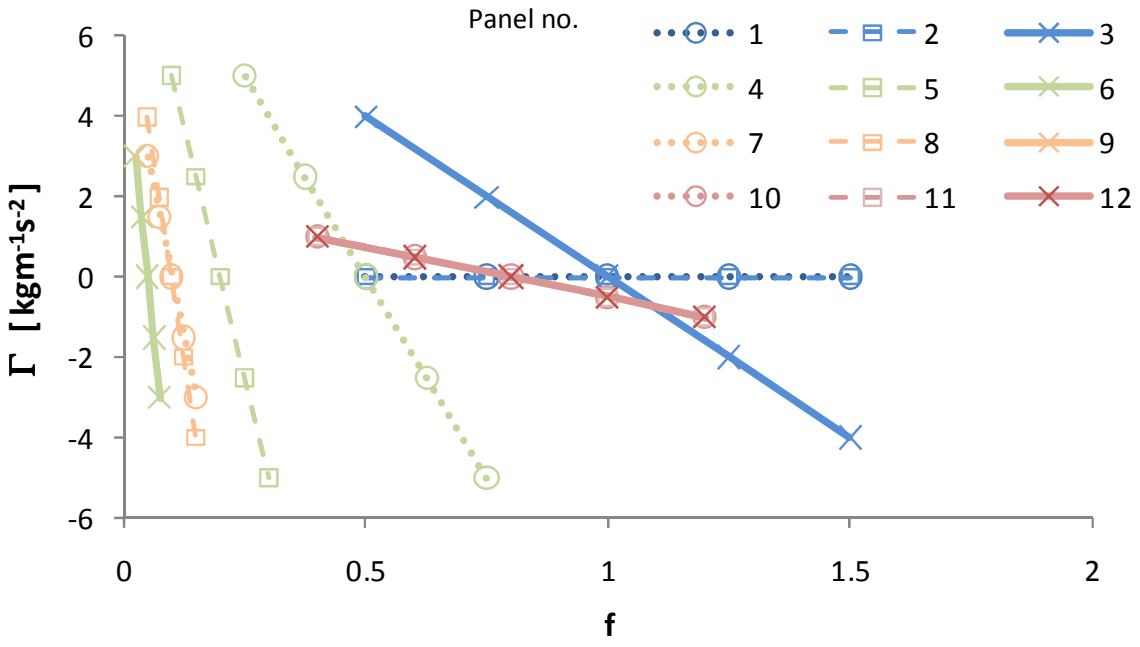

Figure 7.20 Relationship of *f* and Γ used in five different cases (CS 4-overbank case).

	Panel no.	50%f		75%f		100%f		125%f		150%f	
		f	*Γ*	*f*	*Γ*	*f*	*Γ*	*f*	*Γ*	*f*	*Γ*
CS2-Inbank	3	50	4	75	2	100	0	125	-2	150	-4
	4	50	4	75	2	100	0	125	-2	150	-4
	5	10	4	15	2	20	0	25	-2	30	-4
	6	5	4	7.5	2	10	0	12.5	-2	15	-4
	7	0.25	3	0.375	1.5	0.5	0	0.625	-1.5	0.75	-3
	8	5	4	7.5	2	10	0	12.5	-2	15	-4
CS2-Bankfull	2	5	3	7.5	1.5	10	0	12.5	-1.5	15	-3
	3	5	4	7.5	2	10	0	12.5	-2	15	-4
	4	2.5	3	3.75	1.5	5	0	6.25	-1.5	7.5	-3
	5	0.1	2.5	0.15	1.25	0.2	0	0.25	-1.25	0.3	-2.5
	6	0.065	2.7	0.0975	1.35	0.13	0	0.1625	-1.35	0.195	-2.7
	7	0.04	2	0.06	1	0.08	0	0.1	-1	0.12	-2
	8	0.15	2.8	0.225	1.4	0.3	0	0.375	-1.4	0.45	-2.8
	9	2.5	3	3.75	1.5	5	0	6.25	-1.5	7.5	-3
CS2-Overbank	1	50	0	75	0	100	0	125	0	150	0
	2	50	0	75	0	100	0	125	0	150	0
	3	5	1	7.5	0.5	10	0	12.5	-0.5	15	-1
	4	1.5	10	2.25	5	3	0	3.75	-5	4.5	-10
	5	0.08	4	0.12	2	0.16	0	0.2	-2	0.24	-4
	6	0.04	4	0.06	2	0.08	0	0.1	-2	0.12	-4
	7	0.04	4	0.06	2	0.08	0	0.1	-2	0.12	-4
	8	0.15	4	0.225	2	0.3	0	0.375	-2	0.45	-4
	9	0.5	2	0.75	1	1	0	1.25	-1	1.5	-2
	10	2	2	3	1	4	0	5	-1	6	-2
	11	50	2	75	1	100	0	125	-1	100	-2
	12	50	2	75	1	100	0	125	-1	100	-2

Table 7.11 Calibration parameters for CS2 for field data.

	Panel no.	50%f		75%f		100%f		125%f		150%f	
		f	*Γ*	*f*	*Γ*	*f*	*Γ*	*f*	*Γ*	*f*	*Γ*
CS4-Inbank	2	5	3	7.5	1.5	10	0	12.5	-1.5	15	-3
	3	5	3	7.5	1.5	10	0	12.5	-1.5	15	-3
	4	2.5	3	3.75	1.5	5	0	6.25	-1.5	7.5	-3
	5	0.35	3	0.525	1.5	0.7	0	0.875	-1.5	1.05	-3
	6	0.75	3.3	1.125	1.65	1.5	0	1.875	-1.65	2.25	-3.3
	7	1.75	2	2.625	1	3.5	0	4.375	-1	5.25	-2
	8	1.75	1	2.625	0.5	3.5	0	4.375	-0.5	5.25	-1
CS4-Bankfull	1	1	2	1.5	1	2	0	2.5	-1	3	-2
	2	1	2	1.5	1	2	0	2.5	-1	3	-2
	3	0.125	2	0.1875	1	0.25	0	0.3125	-1	0.375	-2
	4	0.075	2.5	0.1125	1.25	0.15	0	0.1875	-1.25	0.225	-2.5
	5	0.04	2.3	0.06	1.15	0.08	0	0.1	-1.15	0.12	-2.3
	6	0.045	2.3	0.0675	1.15	0.09	0	0.1125	-1.15	0.135	-2.3
	7	0.045	1.6	0.0675	0.8	0.09	0	0.1125	-0.8	0.135	-1.6
	8	0.1	1	0.15	0.5	0.2	0	0.25	-0.5	0.3	-1
	9	0.25	1	0.375	0.5	0.5	0	0.625	-0.5	0.75	-1
CS4-Overbank	1	0.5	0	0.75	0	1	0	1.25	0	1.5	0
	2	0.5	0	0.75	0	1	0	1.25	0	1.5	0
	3	0.5	4	0.75	2	1	0	1.25	-2	1.5	-4
	4	0.25	5	0.375	2.5	0.5	0	0.625	-2.5	0.75	-5
	5	0.1	5	0.15	2.5	0.2	0	0.25	-2.5	0.3	-5
	6	0.025	3	0.0375	1.5	0.05	0	0.0625	-1.5	0.075	-3
	7	0.05	3	0.075	1.5	0.1	0	0.125	-1.5	0.15	-3
	8	0.05	4	0.075	2	0.1	0	0.125	-2	0.15	-4
	9	0.4	1	0.6	0.5	0.8	0	1	-0.5	1.2	-1
	10	0.4	1	0.6	0.5	0.8	0	1	-0.5	1.2	-1
	11	0.4	1	0.6	0.5	0.8	0	1	-0.5	1.2	-1
	12	0.4	1	0.6	0.5	0.8	0	1	-0.5	1.2	-1

Table 7.12 Calibration parameters for CS4 for field data.

Panel no.	Inbank : bankfull		Panel no.	Bankfull : overbank	
	f	Γ		f	Γ
			2	0.1	N/A
3	10.0	1.0	3	1.0	4.0
4	20.0	1.3	4	1.7	0.3
5	100.0	1.6	5	1.3	0.6
6	76.9	1.5	6	1.6	0.7
7	6.3	1.5	7	1.0	0.5
8	33.3	1.4	8	1.0	0.7
			9	5.0	1.5
Average	41.08	1.39		1.58	1.19

Table 7.13 Ratio of calibration parameters at CS 2: inbank/bankfull and bankfull/overbank.

Panel no.	Inbank : bankfull		Panel no.	Bankfull : overbank	
	f	Γ		f	Γ
			1	2.0	N/A
2	5.0	1.5	2	2.0	N/A
3	40.0	1.5	3	0.3	0.5
4	33.3	1.2	4	0.3	0.5
5	8.8	1.3	5	0.4	0.5
6	16.7	1.4	6	1.8	0.8
7	38.9	1.3	7	0.9	0.5
8	17.5	1.0	8	2.0	0.3
			9	0.6	1.0
Average	22.88	1.31		1.03	0.57

Table 7.14 Ratio of calibration parameters at CS 4: inbank/bankfull and bankfull/overbank.

7.3 Comparison of calibration parameters obtained from physical model and fieldwork data

Calibration parameters for the physical model and field data are now compared for the cross-section that was modelled in both cases (CS4). However, it is acknowledged that a direct comparison between f and Γ values in the model and those for the river is not straight forward, due to the reasons listed below:

1. The roughness in the river could not be represented accurately in the physical model. There are more roughness variations in the natural river than in the physical model, e.g. only one type of roughness, 8 mm gravel, was used for channel configuration C.
2. There is uncertainty which values of f should be used for the river model since some values within the "correct" f range will only provide adequate results if suitable Γ values are selected.
3. While the velocity in the physical model tended to decrease in the main channel with increasing water level, the opposite behaviour occurred for the full scale natural river.
4. The relative depth, D_r, between the field and physical model data are different.

In order to minimise the effect of the "trade off" behaviour between f and Γ(point 2 above) in the analysis, it was decided to only compare f, while Γwere set to zero in both numerical models. This requires re-calibration of f for the physical model with Γ= 0 for each panel. The values of λ were kept constant at 0.07. Similar to previous simulations, a discharge difference of less than 5% between simulated and experimental values was aimed at in these new simulations. The result of the new simulation is shown in Appendix III. An attempt was made to compare the f values used for

the physical model and river, for two cases which are considered as having the most similar condition:

1. Comparison of physical model with D_r = 0.37 and field data with D_r = 0.39.

Table 7.15 shows the values of *f* used for calibrating both numerical models. The values of *f* on the floodplain bed for the river data are 15 times higher than those in the physical model. The main channel bed *f* values in the prototype for the overbank case (D_r = 0.39) decrease gradually from 1.0 on the most left panel to 0.05 on the most right panel. In contrast to that, the *f* values in the physical model for D_r = 0.37 tend to be more constant, at 0.22 – 0.35. This is consistent with the fact that velocity distribution in the main channel for the river varies more than in the physical model (see Figures 7.12c and 7.19c).

2. Comparison of physical model with D_r = 0.07 and field data at bankfull condition.

The *f* values for the main channel bed in both simulations are within a similar order of magnitude. Three out of four panels of the river have 50% - 130% higher *f* values than in the physical model. However, the velocity magnitude in the river is generally 1.5 times higher than in the physical model (see Figures 7.12a and 7.19b). This is an indication that other factors, e.g. discharge, scale effect and river geometry, play an important role on the magnitude of the velocity.

In conclusion, comparing the calibration parameters used to simulate the flow in the river and its 1:5 scale model is not straightforward. There are differences in the geometry and roughness between the river and physical model that could have more influence on the simulation results than the values of the calibration parameters themselves. It would be more appropriate to investigate the effect of scale on calibration parameter values using only on physical models, with different scales, as the geometry of the channel and roughness can then be made the same between the models. The equifinality problem also made the comparison more difficult.

Physical model				Full-scale river			
	H= 0.162 m D_r = 0.07	H= 0.187 m D_r = 0.20	H= 0.237 m D_r = 0.37		Inbank	Bankfull	Overbank D_r = 0.39
1	0.1	0.2	0.4				
2	0.1	0.2	0.4				
3	0.1	0.2	0.4				
4	0.1	0.2	0.4				
5	0.11	0.2	0.4	1	N/A	2	1
6	0.11	0.2	0.4	2	10	2	1
7	**0.11**	**0.25**	**0.35**	**3**	**10**	**0.25**	**1**
8	**0.1**	**0.25**	**0.33**	**4**	**5**	**0.15**	**0.5**
9	**0.09**	**0.19**	**0.27**	**5**	**0.7**	**0.08**	**0.2**
10	**0.045**	**0.11**	**0.22**	**6**	**1.5**	**0.09**	**0.05**
11	0.04	0.039	0.09	7	3.5	0.09	0.1
12	0.04	0.039	0.09	8	3.5	0.2	0.1
13	*0.08*	*0.08*	*0.055*	*9*	*N/A*	*0.5*	*0.8*
14	*0.08*	*0.08*	*0.045*	*10*	*N/A*	*N/A*	*0.8*
15	0.1	0.08	0.055	*11*	*N/A*	*N/A*	*0.8*
16	0.1	0.08	0.055	12	N/A	N/A	0.8

Main channel and floodplain wall panels are indicated in grey. Bolt and italics letters are indicating main channel panels and floodplain bed panels respectively.

Table 7.15 Friction factor (*f*) values for physical model and river at CS4.

7.4 Stage-discharge rating curve extension using SKM

The SKM was also used to simulate overbank flow conditions at cross sections 2 and 4 for various water depths in order to predict the stage discharge rating curve. The interpolation of stage-discharge values between the bankfull (16/1/2008) and overbank (10/2/2009) data, using a numerical model (SKM) is now compared to the result of the simpler interpolation method (polynomial) discussed earlier in Section 6.3. Seven water depths, distributed to those values recorded during the bankfull and overbank measurements, were simulated. In order to simplify the calibration process, Γ and λ values were set to 0 and 0.07 respectively, the same as those used for the case 100%*f* in Section 7.2. The values of *f* in each panel for each water depth case were obtained from a linear interpolation of the *f* values used for simulating the 16/1/2008 inbank and 10/2/2009 overbank data (Tables 7.11 and 7.12, cases 100%*f*). It is recognised that the *f* values may not change linearly throughout water depth. However, as only overbank cases are simulated, such an assumption may be considered as sufficient, since the changes in hydraulic radius over the depth are

linear (cf. Figures 3.11 and 3.12). Since the interpolation result is not available, i.e. for the dry panels during bankfull conditions, f for such panels is taken from the f values used in the 10/2/2009 overbank case. Two different values of S_o, of the 16/1/2008 (5.7×10^{-4}) and 10/2/2009 (7.3×10^{-4}) measurements, were used in the simulations. The f values used for the simulation are shown in Appendix IV.

The simulation results are shown in Figures 7.21 and 7.22. The simulated U_d for CS 2 increases with water level, with the location of the maximum velocity remaining at relatively the same lateral position (Figure 7.21). The maximum U_d for $S_o = 5.7 \times 10^{-4}$ is 11.35% lower than that for $S_o = 7.3 \times 10^{-4}$. For low overbank depths, the simulations did not converge when the interpolated value of f was used. This appeared to be caused by the 'wetting and drying' problem at panel no. 10 (cf. Figure 7.18c for panel numbering). An attempt was made to obtain a fully converged result by reducing the f values. However, this was only successful when a very low value of f was used, which in return gave an unreasonable magnitude of U_d. Due to this problem, it was decided to disable panel 10 for the simulation. The direct result of this is a reduction in discharge of 4.25% (for both slope values used) for the maximum depth value used in the simulation, i.e. the 10/2/2009 data.

The simulated U_d for CS 4 also increases with water level, but this time the location of the maximum velocity moves toward the inner region of the meander bend with increasing depth value. The maximum U_d for $S_o = 5.7 \times 10^{-4}$ is also 11.35% lower than that for $S_o = 7.3 \times 10^{-4}$. A convergence problem also occurred in the CS 4 simulation, but only for H = 1.01 and 1.09m. In the first case, the floodplain panel was disabled. This is a reasonable assumption, since only 0.02m water was overtopping the main channel bank. For the latter case, a converged result could be obtained by slightly adjusting the f at panel no.10 (cf. Figure 7.23 for panel numbering). This results in slight increase of U_d for the corresponding panel.

The *H v Q* rating curves for cross sections 2 and 4 are shown in Figures 7.23 and 7.24 respectively. It should be noted that the polynomial method interpolates the measured data with different S_o values, i.e. 5.7×10^{-4} for the bankfull data and 7.3×10^{-4} for the overbank data. The trend of the *H v Q* rating curve obtained using SKM for CS 2 is similar to the polynomial interpolation of the data (Figure 7.23). When used for predicting water depth at CS 2, the *H v Q* rating curve obtained using SKM yields results up to 4% different from the *H v Q* rating curve obtained using polynomial interpolation.

The trend in the *H v Q* rating curve obtained using SKM for CS 4 is not similar to the polynomial interpolation of the data. Higher water levels on the *H v Q* rating curve were obtained using SKM, of up to 7.3% and 12.4% for S_o = 5.7 x 10^{-4} and 7.3 x 10^{-4} respectively, as shown in Figure 7.24. It appears that the increment of *f* for panels no. 3 and 4 with rising water depth is the major contribution towards this (cf. Appendix IV). The discharges for the *H v Q* rating curve obtained using SKM for *H* = 1.01m are 24% and 14% lower than the discharge for the *H v Q* rating curve obtained using a polynomial interpolation. It is difficult to determine whether the *f* values in the field for panels no. 3 and 4 are actually lower than the values used for the simulation.

Constructing an accurate stage-discharge rating curve is clearly not a straightforward process. When simple interpolation methods are used, one has to take into account of the effect of using data with different S_o values, as the resulting *H* and *Q* prediction are proven to be sensitive to these values. Furthermore, as previously discussed in Sections 6.1 and 6.4.1, the water surface slope may vary significantly even within a short reach (e.g. 500m of the River Blackwater reach). This provides additional uncertainty in the predicted *H v Q* rating curve, especially since it is a very rare occurrence that a set of water level monitoring devices are available within a short reach. Numerical modelling opens the possibility of predicting the *H v Q* rating curve for each specific value of S_o since S_o values can be set. When a numerical model is used, e.g. SKM, care has to be taken since there are challenges in determining the proper values of calibration parameters, especially for Γ, since its distribution is still largely unknown.

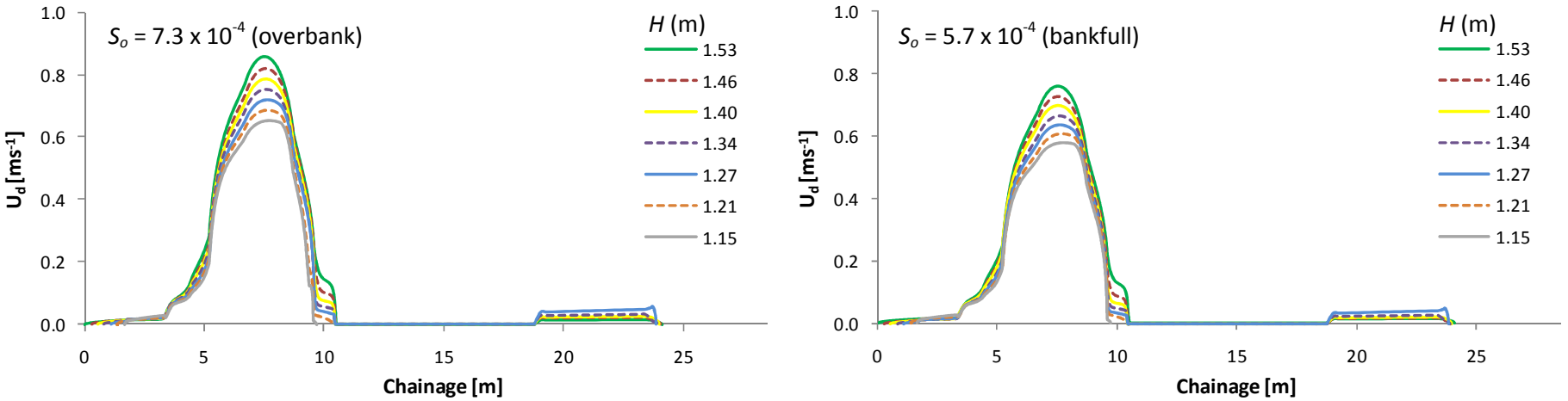

Figure 7.21 Simulated U_d for various water depth and bed slope values at CS 2.

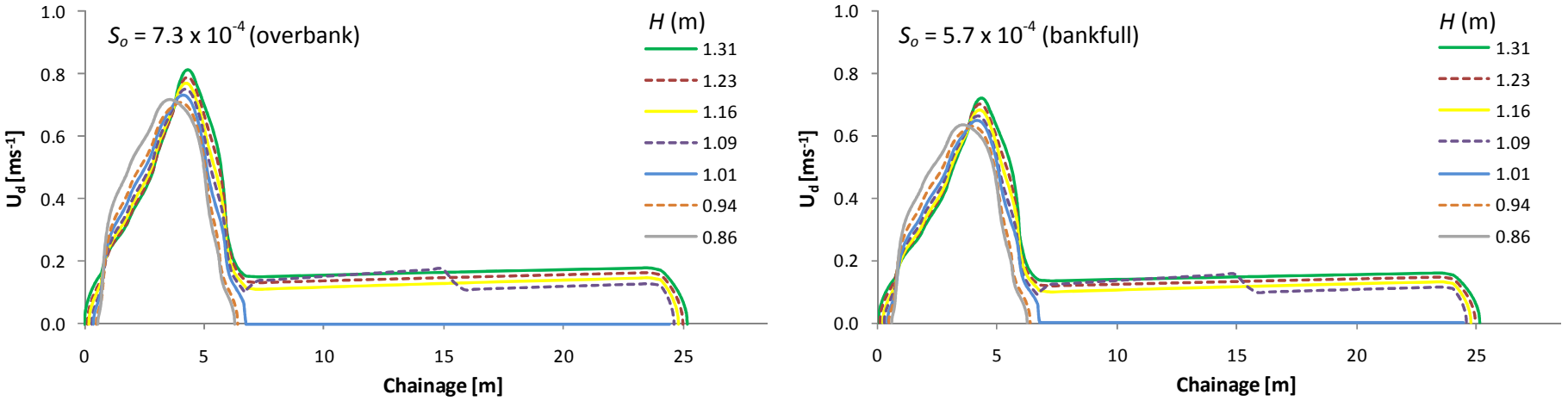

Figure 7.22 Simulated U_d for various water depth and bed slope values at CS 4.

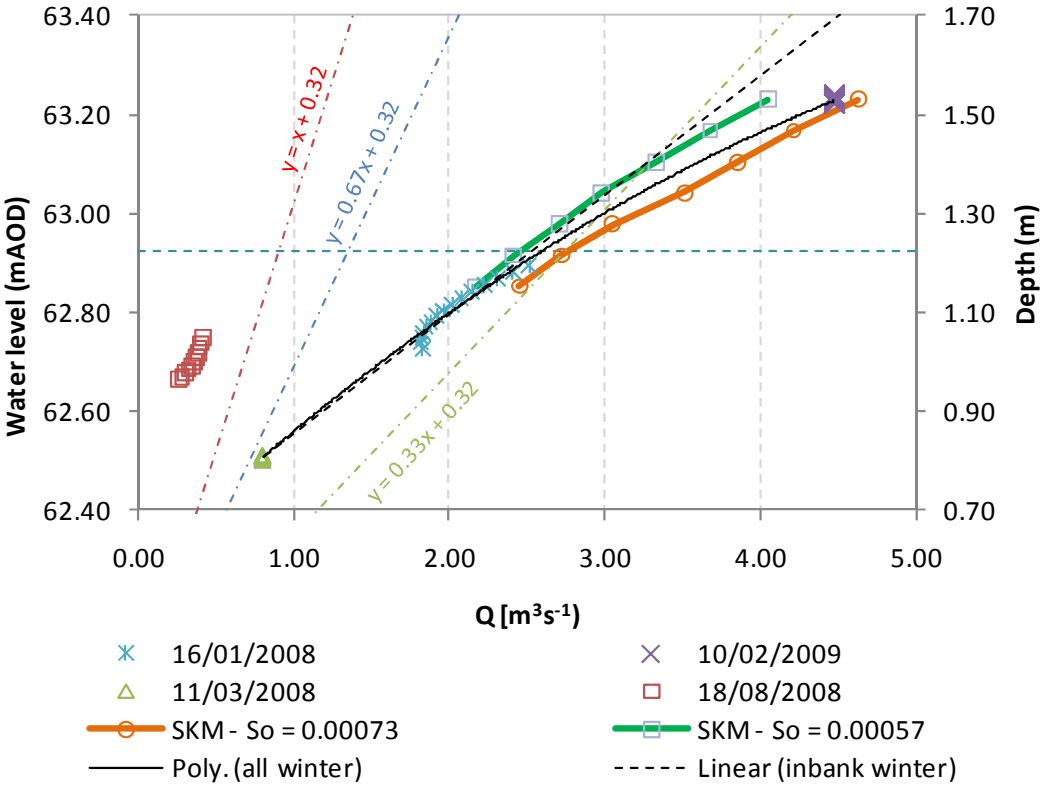

Figure 7.23 Stage-discharge rating curves at CS 2.

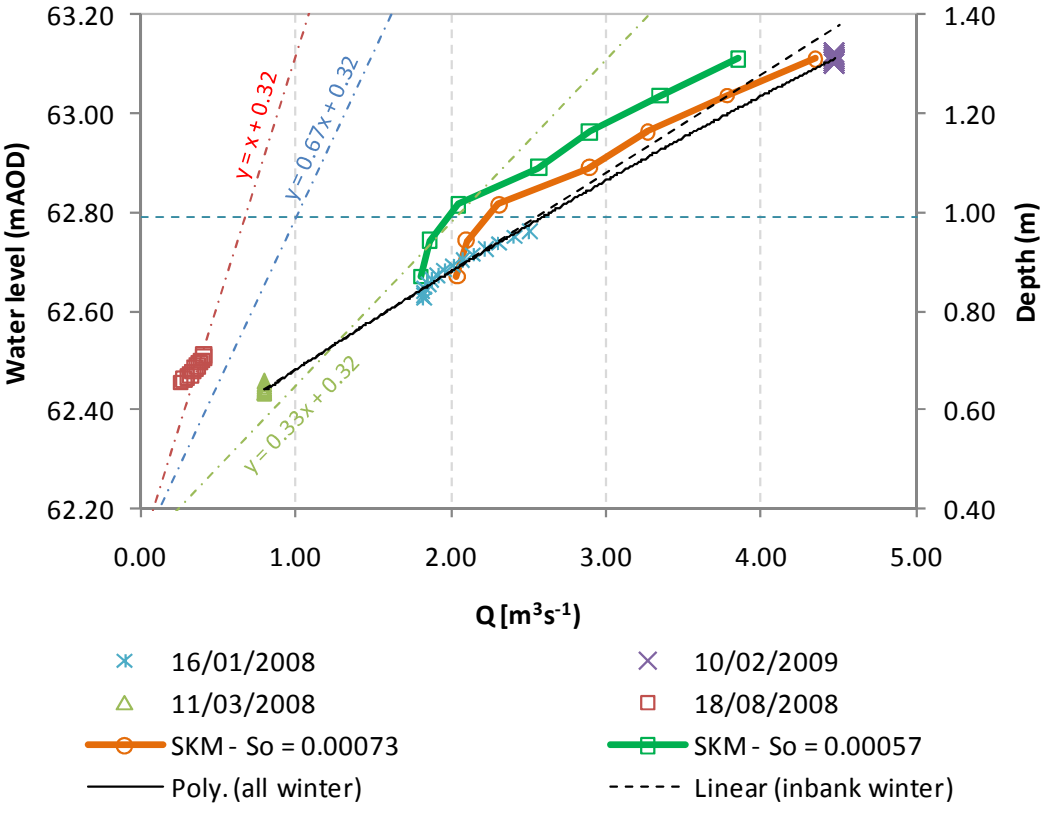

Figure 7.24 Stage-discharge rating curves at CS 4.

8 CONCLUSIONS AND RECOMENDATIONS FOR FURTHER WORK

8.1 Conclusions

The overall aim of this work was to examine the flow characteristics which occur in a small reach of a doubly meandering compound channel during inbank, bankfull and overbank conditions. Underpinning this aim were eight objectives that were mentioned in Section 1.2. These objectives have been fulfilled and the results are addressed in this thesis as following:

1. Objective 1 – Chapter 5.
2. Objective 2 – Sections 4.4 and 4.5.
3. Objective 3 – Sections 5.2.5.
4. Objective 4 – Sections 6.1, 6.3 and 6.4.
5. Objective 5 – Sections 6.2.
6. Objective 6 – Sections 7.1 – 7.3.
7. Objective 7 – Sections 6.3 and 7.4
8. Objective 8 – Sections 6.5.

The main conclusions of this thesis are summarised below.

1. It has been demonstrated that an ADCP can be used successfully to measure velocity in a small river, for inbank, bankfull and overbank flow conditions, providing appropriate care is taken.
2. It has been shown that it is relatively easy to obtain reliable information relating to the discharge. However, if the data are to be interrogated further in order to yield information pertaining to reliable velocity statistics, then the additional level of equipment modification and data post processing required should not be underestimated.
3. The approach of averaging several transect data together, adopted by the author, has successfully reduced the noise in the ADCP velocity data. The processed depth-averaged streamwise velocity data shows good agreement with the depth-averaged streamwise velocity obtained from stationary measurements, typically with a Root Mean Square Value of within $0.054ms^{-1}$. Good agreement is also observed in the bed profiles measured using both methods.

4. Comparison of topographic surveys conducted in the study reach at various times (2007, 2002, 1995 and 1993) shows that the river geometry has changed since 1993 (Figures 3.7 – 3.10, 3.17). The floodplain now tends to slope away from the main channel (Figures 3.4 – 3.6, 3.18), which is opposite to the 'as built' condition and the original design with a floodplain cross-fall of $^{1}/_{30}$. This appears to be caused by deposition of sediment near the edge of the main channel/floodplain, which in some cases has raised the floodplain elevation by 200mm over the intervening period. As a direct result of these changes, the bankfull discharge in the river has now increased significantly from its original value.
5. The high streamwise velocity core at the meandering cross section being studied (CS 4) moved towards the inner meander with rising water level. This was also observed in the physical model (Lambert and Sellin, 1996).
6. The magnitudes of the U_{max} and U_d at CS 4 increase with rising water level, which is opposite to what has been observed in the 1:5 physical model for the cases with a horizontal floodplain. This indicates that in the river there is less interaction between the flow on the floodplain and that in main channel.
7. There is a similarity between the secondary flow pattern in the model and river for the inbank and bankfull cases. A clockwise secondary cell indicated in the model can also be observed in the river for both flow conditions. However, there are also differences, e.g. an additional flow cell near the left bank that was observed in the river for the bankfull case did not appear in the model. Furthermore, the clockwise secondary cell indicated in all overbank cases in the model did not appear in the river.
8. The seasonal variation of vegetation affects the shape of the stage-discharge rating curve significantly. The presence of vegetation in the main channel during the summer months reduces the conveyance capacity of the river. This is shown by the steeper gradient in the stage-discharge rating curves for those periods, reaching to seven times the gradient of the stage-discharge rating curves for winter months.
9. The stage-discharge relationship at CS 0 follows a loop or hysteresis pattern. The falling limbs of the rating curve have a higher discharge capacity than the rising limbs for summer months (June/July to October/November). Interestingly, the opposite is true for winter months (October/November to June/July). The higher discharge in the falling limbs for summer months appears to be caused by the flattening of vegetation that leads to a reduction in the channel resistance.

10. The variation of the vegetation over the year further highlights the difficulties in both engineering design and in undertaking numerical modelling for small rivers. Such variation is clearly important as it affects the discharge capacity, stage and the shape of the flood hydrograph significantly.
11. Manning's *n* values may reach up to 0.60 for low inbank flow conditions during a summer month (August), when there is a high extent of vegetation in the main channel. Typical Manning's *n* values for winter months (January-March), for both inbank and overbank flow conditions, are in between 0.03 to 0.07.
12. SKM is able to predict the trend in the depth-averaged streamwise velocity quite well for the flow in both the prototype and the 1:5 physical model, with typical Root Mean Squared Error (RMSE) between simulated results and the experimental data of within 0.05ms^{-1}.
13. Reducing *f* can be compensated for by increasing Γ in order to obtain a similar result in the simulation. Altering the values of *f* and Γ using a simple linear relationship between them has been shown to produce good result (RMSE ≤ 0.05 ms^{-1} and ΔQ ≤ 5%). Such a simple relationship provides an easy methodology to calibration for SKM users.

8.2 Recommendations for further work

1. To consider the effects of seasonal variation in vegetation on the flow in engineering design projects and in numerical studies of rivers. This variation has been shown to significantly affect the discharge capacity and resistance of the river.
2. To consider the appropriateness of using an ADCP for measuring the 3D velocity field in different rivers over a suitable range of scales and under a variety of flow conditions.
3. To create a standardised procedure for ADCP measurements and data processing.
4. To consider the general degree of uncertainty in numerical modelling results, and the approximations involved in representing the physics of the flow. Since the only effective means of verifying the accuracy of numerical model results is by undertaking field measurements, it is suggested that ADCP technology should be used to obtain further spatial distributions of 3D velocities in rivers. These measured data could then be used to elucidate the relationship between the values of the various calibration parameters and the flow physics.
5. To explore further the extrapolation of stage-discharge rating curve using numerical models in order to determine whether such an approach can provide improvements to the simple extrapolation methods.

REFERENCES

Abril, J.B. and Knight, D.W. (2004) Stage-discharge prediction for rivers in flood applying a depth-averaged model, *Journal of Hydraulic Research*, IAHR, Vol. 42, No. 6, pp 616-629.

Ackers (1958) Hydraulics Research Paper: Resistance of fluids flowing in channel and ducts. HMSO 1, 1-39.

Allen, J. R. L. (1985) Principles of physical sedimentology. George Allen and Unwin.

Amtec Engineering, Inc. (2003) Tecplot user's manual, Version 10. Amtec Engineering, Inc., Bellevue, Washington, USA, 424-426.

ASCE Task Committee on Turbulence Models in Hydraulic Computations (1988a) Turbulence modelling of surface water flow and transport: Part 1. *Journal of Hydraulic Engineering*, ASCE, Vol. 114, No. 9.

ASCE Task Committee on Turbulence Models in Hydraulic Computations (1988b) Turbulence modelling of surface water flow and transport: Part 2. *Journal of Hydraulic Engineering*, Vol. 114, No. 9.

ASCE Task Committee on Turbulence Models in Hydraulic Computations (1988c) Turbulence modelling of surface water flow and transport: Part 3. *Journal of Hydraulic Engineering*, ASCE, Vol. 114, No. 9.

ASCE Task Committee on Turbulence Models in Hydraulic Computations (1988d) Turbulence modelling of surface water flow and transport: Part 4. *Journal of Hydraulic Engineering*, ASCE, Vol. 114, No. 9.

ASCE Task Committee on Turbulence Models in Hydraulic Computations (1988e) Turbulence modelling of surface water flow and transport: Part 5. *Journal of Hydraulic Engineering*, Vol. 114, No. 9.

Babaeyan-Koopaei, K., Ervine, D.A., Carling, P.A., Cao, Z. (2002) Velocity and Turbulence measurements for Two Overbank Flow Events in the River Severn. Proc. ASCE *Journal of Hydraulic Engineering*, ASCE, Vol 128, No 10. pp 891-900.

Barenblatt, G. (1993) Scaling laws for fully developed turbulent shear flows: Part 1. Basic hypothesis and analysis. *Journal of Fluid Mechanics*, Cambridge University Press, 248 513-520.

Barua, D.K. and Rahman, K.H. (1998) Some aspects of turbulent flow structure in large alluvial rivers. *Journal of Hydraulic Research*, IAHR, 36,235–252.

Bathurst, J.C., Benson, I.A., Valentine, E.M. & Nalluri, C. (2002) Overbank sediment deposition patterns for straight and meandering flume channels. *Earth Surface Proc. Landforms. 27, pp 659-665.*

Boiten, W. (2000) Hydrometry, IHE Delft lecture note series. A.A. Balkema. Rotterdam, 2000

Carr, M.L and Rehman, C.R. (2007) Measuring the dispersion coefficient with Acoustic Doppler Curent Profilers*. Journal of Hydraulic Engineering*, ASCE, Vol. 133, No. 8.

CES (2010) Conveyance Estimation System. Available at http://www.river-conveyance.net. Last accessed 28 February 2010.

Chen, C.L. (1991) Unified theory on power laws for flow resistance. *Journal of Hydraulic Engineering*, ASCE, 117 (3): 371-389.

Chiu, C. L. (1987) Entropy and probability concepts in hydraulics. ASCE, *Journal of Hydraulic Engineering*, ASCE, Vol. 113, No. 5, p 583-600..

Chlebek, J. (2009) Modelling of simple prismatic channels with varying roughness using the SKM and a study of flows in smooth non-prismatic channels with skewed floodplains. *PhD thesis*, University of Birmingham, Birmingham, UK.

Chlebek, J. and Knight, D.W. (2006) A new perspective on sidewall correction procedures, based on SKM modelling, *3rd International Symposium on Fluvial Hydraulics, River Flow 2006*, Vol. 1, Editors Ferreira, Alves, Leal & Cardoso, Portugal.

Chow, V.T. (1959) Open-channel hydraulics. McGraw-Hill, New York. Colebrook, C.F., 1939, Turbulent flow in pipes, with particular reference to the transition region between smooth and rough pipe laws, *Journal of the Institute of Civil Engineers*, London.

Christensen, J.L., and Herrick, L.E. (1982) Mississippi River Test, Volume 1. *Final report DCP4400/300, prepared for the U.S. Geological Survey by AMETEK/StrazaDivision*, El Cajon, California, under contract No. 14–08–001–19003, p. A5–A10.

Clarke, A., Hughes, T., Hensler, A. and Jenkin, P. (2007) River Blackwater flood study: *Final flood mapping report, Project Ref: 15945/003*. Peter Brett Associates, Reading.

Coles, D. (1956) The law of the wake in the turbulent boundary layer. *Journal of Fluid Mechanics*, Cambridge University Press, 1: 191-226.

Creutin, J.D., Muste, M., Bradley, A., Kim, S.C and Kruger, A (2003) River gauging using PIV technique: proof of concept experiment on the Iowa River. *Journal of Hydrology* 277, 182-194.

Culbertson, J. K. (1967) Evidence of secondary circulation in an alluvial channel. *Professional Paper* 575 – D, U.S. Geological Survey, 214-216.

Darcy, H., (1857) Recherches experimentales relatives au mouvement de l'eau dans les tuyaux, 2 volumes, Mallet-Bachelier, Paris, pp 1-268 and atlas ("Experimental Research Relating to the Movement of Water in Pipes").

Davidson, P.A. (2004) Turbulence: An introduction for scientists and engineers. Oxford University Press, New York.

Defra/EA (2002) Reducing uncertainty in river flood conveyance: scoping study, *R & D Technical Report*, prepared by Evans, E.P., Pender, G., Samuels, P.G. and Escaremia, M. For the Environment Agency R & D Dissemination Centre, c/o WRc, Swindon, SN5 8YF pp1-124

Dimmock, E. (Hydrometry and Telemetry Officer 1, Environment Agency Frimley) (2009) Discussion on the accuracy of the electromagnetic gauging station operated by the Environment Agency (Personal communication on 26 January 2009).

Dinehart, R.L. & Burau, J.R. (2005a) Averaged indicators of secondary flow in repeated acoustic Doppler current profiler crossings of bends. *Water Resources Research*, Vol. 41.

Dinehart, R.L. & Burau, J.R. (2005b) Repeated surveys by acoustic Doppler current profiler for flow and sediment dynamics in a tidal river. *Journal of Hydrology*, XX 1–21.

Einstein, H.A. and Li, H. (1958) Secondary currents in straight channels. *Transactions of the American Geophysical Union*, Vol. 39, No.6, pp 1085-1088.

Environment Agency (2008a) How to measure river discharge using Acoustic Doppler Current Profilers (ADCP), *Operational instructions* version 2, 381_05, Environment Agency (UK).

Environment Agency (2008b) How to process and validate Acoustic Doppler Current Profilers (ADCP) river discharge measurements. *Operational instructions* draft 1, Environment Agency (UK).

Ervine, D.A, Willets, B.B., Sellin, R.H.J. and Lorena, M. (1993) Factors affecting conveyance in meandering compound channel flow. *Journal of Hydraulic Engineering, ASCE,* Vol. 119, No. 12 December.

Ervine, D. A., Babaeyan-Koopaei, K. and Sellin, R. H. J. (2000). Two-dimensional solution for straightand meandering overbank flows. *Journal of Hydraulic Engineering, ASCE,* Vol. 126.

Everard, N. (Senior hydrometry officer, Environmental Agency Wallingford)(2008) Discussion on practical application of ADCP measurements at the Environment Agency (Personal communication in 18 November 2008)

Flow Database at the University of Birmingham (2009). Available at http://www.flowdata.bham.ac.uk/. Last accessed 28 February 2010.

Foresight (2010) Flood and Coastal Defence. Available at http://www.foresight.gov.uk. Last accessed 28 February 2010.

Fujita, I., Muste, M. & Kruger, A. (1998) Large-scale Particle Image Velocimetry for Flow Analysis in Hydraulic Engineering Applications. *Journal of Hydraulic Research, IAHR,* Vol.36, No.3, 397-414.

Fulford, J.M., Pillon, P.J., Kopaliani, Z., McCurry, P.J., Caponi, C. (2007) Call for collaboration in WMO project for the assessment of the performance of flow measurement instruments and techniques, *Journal of Hydraulic Engineering, ASCE,* Vol.133/12.

Gonzalez-Castro, J.A., Ansar, M. and Kellman, O. (2002) Comparison of discharge estimates from ADCP transect data with estimates from fixed ADCP mean velocity data, in: *Proceedings of the ASCE/IAHR Hydraulic Measurements & Experimental Methods Conference*, Estes Park, CO (CD-ROM).

Gonzalez-Castro, J.A. and Muste, M. (2007) Framework for Estimating Uncertainty of ADCP Measurements from a Moving Boat by Standardized Uncertainty Analysis. *Journal of Hydraulic Engineering, ASCE,* Vol.133/12.

Gordon, R.L. (1989) Acoustic measurement of river discharge. *Journal of Hydraulic Engineering, ASCE,* 115, 925–936.

Gunawan, B., Sun, X., Sterling, M., Knight, D.W., Shiono, K., Chandler, J., Rameshwaran, P., Wright, N.G., Sellin, R.H.J., Tang, X. and Fujita, I. (2008) An integrated and novel approach to estimating the conveyance capacity of the River Blackwater. *Proceedings of the Eight International Conference on Hydro-Science and Engineering*, Nagoya, Japan, September 8–12.

Gunawan, B., Sterling, M. and Knight, D.W. (2009) Using an Acoustic Doppler Current Profiler in a small river. *Water and environment*, CIWEM, Chartered Institution of Water and Environmental Management, UK, (in press for printing, published online on 12/5/2009/DOI: 10.1111/j.1747-6593.2009.00170.x).

Henderson, F.M. (1966) Open channel flow. Macmillan Publishing, New York.

Herschy, R.W. (1995) Streamflow measurement. Elsevier applied science publishers.

Holmes, R.R. & Garcia, M.H. (2002) Velocity and Sediment concentration Measurements over Bedforms in Sand-Bed Rivers. *Proceedings of the ASCE/IAHR Hydraulic Measurements & Experimental Methods Conference*, Estes Park, CO (CD-ROM).

Ikeda, S., Sano, T., Fukumoto, M. And Kawamura, K. (2001) Organised horizontal vortices and lateral sediment transport in compound channel flows, *Journal of JSCE* (accepted).

ISO 1100-2 (1998) Measurement of liquid flow in open channels – Part 2: Determination of stage-discharge relation.

Karcz, I (1966) Secondary currents and the configuration of a natural stream bed. *J. Geophysical Res*., 71, 3109-3116.

Klein, H. (2003) Investigating sediment re-mobilisation due to wave action by means of ADCP echo intensity data field data from the Tromper Wiek, western Baltic Sea Estuarine. *Coastal and Shelf Science* 58 (2003) 467–474

Knight, D.W. (1981) Some field measurements concerned with the behaviour of resistance coefficients in a tidal channel. Est. *Coastal and Shelf Science* 12, 303-322.

Knight, D.W. (1989) Summary of final report for Severn-Trent Water Authority, River channels and floodplains, Severn-Trent Water Authority.

Knight, D.W. (2001) Flow and sediment transport in two-stage channels, Keynote Lecture, Proc. 2nd IAHR Symposium on River. *Coastal and Estuarine Morphodynamics*, September, Obihiro, Japan, 1-20.

Knight, D.W. (2005). River flood hydraulics: theoretical issues and stage-discharge relationships, in River basin modelling for flood risk mitigation [Ed. Knight, D.W. and Shamseldin A.Y.], Taylor & Francis (The Netherlands).

Knight, D.W. (2008) Modelling overbank flows in rivers – data, concepts, models and calibration, Chapter 1 in Numerical Modelling of Hydrodynamics for Water Resources [Eds P Garcia-Navarro & E Playan], Taylor & Francis, 3-23. [B].

Knight, D.W. and Patel, H.S. (1985) Boundary shear in smooth rectangular ducts. *Journal of Hydraulic Engineering, ASCE,* 111 (1): 29-47.

Knight, D.W. and Sellin, R.H.J. (1987) The SERC Flood Channel Facility, Journal of the Institution of *Water and Environmental Management*, Vol. 1, No. 2, October, 198-204.[J]

Knight, D.W., Shiono, K. & Pirt, J. (1989) Prediction of depth mean velocity and discharge in natural rivers with overbank flow, *Proc. Intl. Conf. Hydraulic and Environmental Modelling of Coastal, Estuarine and River Waters*, Bradford, England, 19-21 September.

Knight, D.W. and Abril C., J.B. (1996) Refined calibration of a depth-averaged model for turbulent flow in a compound channel, *Proceedings of the Institution of Civil Engineers, Journal of Water, Maritime and Energy*, Vol. 118, pp 151-159, September, 11017

Knight, D.W. and Shiono, K. (1996) River channel and floodplain hydraulics. In Anderson, M.G., Walling, D.E. & Bates, P.D. (Eds.) Floodplain Processes. J.Wiley & Sons, 139-181.

Knight, D.W., Omran, M. and Tang, X. (2007) Modelling depth-averaged velocity and boundary shear in trapezoidal channels with secondary flows, *Journal of Hydraulic Engineering, ASCE*, Vol. 133, No. 1, January, pp. 39-47

Knight, D.W., Mc Gahey, C., Lamb, R. & Samuels, P.G., 2010, *Practical Channel Hydraulics – Roughness, Conveyance and Afflux*, CRC Press/Taylor & Francis, 1-354.

Knight, D.W., Aya, S., Ikeda, S., Nezu, I and Shiono, K (2009) Flow structure (Chapter 2) in Flow and sediment transport in compound channels, e.d. Ikeda, S and McEwan, I.K. *IAHR Monograph*. IAHR Spain.

Lambert M.F. (1993) Hydraulics of compound channels. *PhD thesis*, The University of Newcastle, Australia, Nov. 1993

Lambert, M. F and Sellin, R. H. J. (1996). Velocity distribution in a large-scale model of a doubly meandering compound channel. *Proc. Instn Civ. Engrs Wat., Marit. & Energy*, 118.

Le Coz, J., Gilles, P., Magali, J. & Andre, P. (2007) Mean vertical velocity profiles from ADCP river discharge measurement datasets. *Proceedings 32nd Congress of International Association of Hydraulic Engineering and Research*, Venice, Italy.

Lemmin, U. & Rolland, T. (1997) Acoustic velocity profiler for laboratory and field studies. *Journal of Hydraulic Engineering*, ASCE, Vol.123/12.

Marsden, R. (2005) StreamPro ADCP Performance Characteristics. *Proceedings of the IEEE/EOS Eight Working Conference on Current Measurement Technology* 2005.

Massey, B.S. (1995) Mechanics of Fluids. Chapman and Hall.

McGahey, C. (2006) A practical approach to estimating the flow capacity of rivers. *PhD thesis*, The Open University, UK.

McGahey, C., Samuels, P.G. and Knight, D.W. (2006) A practical approach to estimating the flow capacity of rivers-Application and analysis. *Proceedings of the International Conference on Fluvial Hydraulics (River Flow 2006)*. [Eds. Ferreira, R.M.L., Alves,E.C.T.L., Leal, J.G.A.B. & Cardoso, A.H.], Lisbon, Portugal, 1: 303-312.

McGahey, C., Samuels, P.G., Knight, D.W. and O'Hare, M.T. (2008) Estimating river flow capacity in practice. *Journal of Flood Risk Management*, Wiley InterScience, 1 (1): 23-33.

Merckelbach, L.M. (2006) A model for high-frequency acoustic Doppler current profiler backscatter from suspended sediment in strong currents*. Continental Shelf Research*, 26/1316–1335.

Morvan, H., Knight, D.W., Wright, N., Tang, X. And Crossley, A. (2008) The concept of roughness in fluvial hydraulics and its formulation in 1D, 2D and 3D numerical simulation models. *Journal of Hydraulic Research*, IAHR, Vol. 46, No. 2, pp. 191 – 208.

Moeller, M. (1883) Studien ueberdie Bewegung des wassers in Fluessen mit Bezugnahme auf die Ausbildung des Flussprofiles. Zeitsharift fuer Bauwesen, 201.

Morlock, S.E. (1996) Evaluation of acoustic Doppler current profiler measurements of river discharge: *U.S. Geological Survey Water-Resources Investigations Report* 95-4218, 37 p.

Mueller, D.S. (2002) Use of Acoustic Doppler Instruments for Measuring Discharge in Streams with Appreciable Sediment Transport. *Proc. Hydraulic Measurements & Experimental Methods 2002* CD-ROM.

Mueller, D.S. (2003) Field Evaluation of boat-mounted Acoustic Doppler instruments used to measure streamflow. *Proc. of the IEEE/OES Seventh Working Conference on Current Measurement Technology*.

Mueller, D.S., Rehmel, M.S. and Wagner, C. (2007) Cause and solution for false upstream boat velocities measured with a StreamPro Acoustic Doppler Current Profiler. *Proceedings of Hydraulic Measurements and Experimental Methods 2007*, American Society of Civil Engineers Conference.

Mueller, D.S., and Wagner, C.R. (2009) Measuring discharge with acoustic Doppler current profilers from a moving boat: U.S. Geological Survey Techniques and Methods 3A-22, 72 p. U.S. Geological Survey (available online at http://pubs.water.usgs.gov/tm3a22. , last accessed: 14 December 2009).

Münchener Rückversicherungs-Gesellschaft (2009), Geo Risk Research, NatCatSERVICE (http://www.munichre.com, last accessed: 14 December 2009).

Murphy, D. (Technical services, field service engineer, Teledyne-RD Instruments) (2009) Discussion on ADCP mode 13 (Personal communication on 28 February 2009).

Muste, M., Yu, K. and Spasojevic, M. (2004a) Practical aspects of ADCP data use for quantification of mean river flow characteristics; Part I: Moving-vessel measurements. *Flow Measurement and Instrumentation*, 15(1), 1-16.

Muste, M., Yu, K., Pratt, T. and Abraham, D. (2004b) Practical aspects of ADCP data use for quantification of mean river flow characteristics; Part II: Fixed-vessel measurements. *Flow Measurement and Instrumentation*, 15(1), 17-28.

Muste, M. (Research Engineer, IIHR- Hydroscience & Engineering, the University of Iowa) (2008) Discussion on the practical operation of ADCPs. (Personal communication on 11 September 2008)

Naish, C. and Sellin, R.H.J. (1996). Flow structure in a large-scale model of a doubly meandering compound river channel, in Coherent Flow Structures in Open Channels [Ed. P.J. Ashworth, S.J.Bennett, J.L.Best and S.J.McLelland], J Wiley, 631-654.

Nezu, I. (2005) Open-channel flow turbulence and its research prospect in the 21st century. *Journal of Hydraulic Engineering*, ASCE 131 (4): 229-246.

Nezu, I. and Nakagawa, H. (1993) Turbulence in open-channel flows. *IAHR Monograph Series*, A. A. Balkema, Rotterdam

Nezu, I. and Rodi, W. (1986) Open channel flow measurements with a laser Doppler anemometer. *J. Hydr. Eng*., ASCE, Vol 112, No 5, pp 335-355.

Nezu, I., Tominaga, A. and Nakagawa, H. (1993). Field measurements of secondary currents in straight rivers. *Journal of Hydraulic Engineering*, ASCE, Vol. 119, No.5. Pp 598-614.

Nikuradse, J. (1933) Translates to: Laws of flow in rough pipes, *Verein deutscher Ingenieure, Forschubgsheft*, No. 361, Berlin.

National Oceanic and Atmospheric Administration (NOAA) (2009) Geomagnetic model. (http://www.ngdc.noaa.gov/geomagmodels/Declination.jsp, last accessed: 14/12/2009).

Nystrom, E.A., Rehmann, C.R., and Oberg, K.A. (2007) Evaluation of mean velocity and turbulence measurements with ADCPs. *Journal of Hydraulic Engineering*, ASCE, Vol.133/12.

Oberg, K.A. (2002) In search of easy-to-use methods for calibrating ADCP's for velocity and discharge measurements. *Proc. Hydraulic Measurements & Experimental Methods 2002* CD-ROM.

Oberg, K. & Mueller, D.S. (2007) Validation of Streamflow Measurements Made with Acoustic Doppler Current Profilers. *Journal of Hydraulic Engineering*, ASCE, Vol.133/12.

Omran, M.N. (2005) Modelling stage-discharge curves, velocity and boundary shear stress distributions in natural and artificial channels using a depth averaged model. *PhD Thesis*, The University of Birmingham

Perkins, H.J. (1970) The formation of streamwise vorticity in turbulent flow. *Journal of Fluid Mechanics*, Cambridge University Press, 44 (04): 721-740.

Pitt, M. (2008) The Pitt Review, Learning the lessons from the 2007 floods, An independent review by Sir Michael Pitt, Cabinet Office, Crown Copyright,

PNI Corp. (2008) TCM3 compass. (http://pnicorp. com/, last accessed August 5, 2008).

Prandtl, L. (1952) Essentials of Fluid Dynamics. London: Blackic.

Rameshwaran, P and Shiono, K. (2007) Quasi two-dimensional model for straight overbank flows through emergent vegetation on floodplains. *Journal of Hydraulic Research*, IAHR, Vol. 45, No. 3, pp. 302-315.

RDI (RD Instruments) (1996) Acoustic Doppler Current Profiler, Principles of Operation, A Practical Primer. RD Instrument. (http://www.rdinstruments.com/mm_papers.html accessed 14 December 2009).

RDI (RD Instruments) (2008) WinRiver 2 User's Guide. RD Instrument.

Rennie, C.D., Millar, R.G. & Church, M.A. (2002) Measurement of bed load velocity using an Acoustic Doppler Current Profiler. *Journal of Hydraulic Engineering*, ASCE, Vol.128/5.

Rennie, C.D. & Church, M. (2007) ADCP shear stress and bedload transport in a large wandering gravel-bed river. *IAHR Venice Congress 2007*.

Rodriguez, J., Vos, F., Below, R. and Guha-Sapir, D. (2009) Annual Disaster Statistical Review 2008: The numbers and trends. Centre for Research on the Epidemiology of Disasters, Belgium.

Rowe, F. and J. Young (1979) An ocean current profiler using Doppler sonar, *Oceans '79 Proceedings*.

Rutherford, J.C. (1994) River mixing, John Wiley and Sons.

Schlichting, H. (1979) Boundary Layer Theory. 7th edition, McGraw-Hill, London.

Schlichting, H and Gersten, K (2000) Boundary layer theory. 8th edition. Springer Verlag Berlin Heidelberg.

Sellin R.H.J. (1964) A laboratory investigation into the interaction between the flow in the channel of a river and that over its floodplain, *La Houille Blanche*, Vol. 19, No. 7, pp 793-801.

Sellin, R.H.J. and van Beesten, D.P. (2004). Conveyance of a managed vegetated two-stage river channel. *Proc. Institution of Civil Engineers, Journal of Water Management*, Vol. 157, WM1, 21-44.

Sellin, R.H.J. and van Beesten, D.P. (2002). Berm vegetation and its effect on flow resistance in a two-stage river channel: an analysis of field data. *Proc. The International Conference on Fluvial Hydraulics*, Belgium, pp.319 - 326.

Sellin, R.H.J., Wilson, C.A.M.E. and Naish, C. (2001). Model and prototype results for a sinuous two-stage river-channel design. *CIWEM, The Journal* volume 15/ No 3.

Sharifi, S. (2009) Application of evolutionary computation to open channel flow modelling. *PhD Thesis*, The University of Birmingham.

Shih, H.H., Payton, C., Sprenke, J. & Mero, T. (2000) Towing basin speed calibration of acoustic Doppler current profiling instruments. *Proc. 2000 Joint Conf. on Water Resources Engineering and Water Resources Planning and Management*, ASCE, Reston, Va.

Shiono, K. and Knight, D.W. (1988) Two-dimensional analytical solution for a compound channel. *Proceedings of the 3rd International Symposium on Refined Flow Modelling and Turbulence Measurements*, Tokyo, Japan, 503-510.

Shiono, K. and Knight, D.W. (1990) Mathematical models of flow in two or multi stage straight channels. *Proceedings of the Conference on River Flood Hydraulics*. [Ed. White, W.R.], Wallingford, 229-238.

Shiono, K. and Knight, D.W. (1991) Turbulent open-channel flows with variable depth across the channel. *Journal of Fluid Mechanics*, Cambridge University Press, 222 617-646.

Shiono, K. and Muto, Y. (1998) Complex flow mechanisms in compound meandering channels with overbank flow. *Jnl. of Fluid Mechanics*, Vol 376, pp 221-261.

Sime, L.C., Ferguson, R.I. & Church, M. (2007) Estimating shear stress from moving boat acoustic Doppler velocity measurements in a large gravel bed river. *Water Resources Research*, Vol. 43.

Simpson, M.R. (2001) Discharge Measurements Using a Broad-Band Acoustic Doppler Current Profiler (USGS. http://pubs.usgs.gov/of/2001/ofr0101/text.pdf , last accessed: 14 December 2009).

Simpson, M. R. and R. N. Oltmann (1990) An acoustic Doppler discharge-measurement system, *Proceedings of the Hydraulic Engineering 1990 National Conference*, 2, 903-908.

Stearns, F.P. (1883). On the current meter, together with a reason why maximum velocity of water flowing open channels is below the surface. *Trans.*, ASCE, 12(216), 331-338.

Sterling, M. (1998) A study of boundary shear stress, flow resistance and the free overfall in open channels with a circular cross-section. *PhD thesis*, University of Birmingham, Birmingham, UK.

Stone, M.C. and Hotchkiss, R.H. (2007) Evaluating velocity measurement techniques in shallow streams. *Journal of Hydraulic Research*, IAHR, Vol. 45, No. 6, pp. 752 – 762.

Sun, X., Shiono, K., Chandler, J.H., Rameshrawan, P., Sellin, R.H.J. and Fujita, I. (2009) Note on discharge estimation in a small river using LSPIV. *Water Management* (submitted).

Szupiany, R.N., Amsler, M.L., Best, J.L. & Parsons, D.R. (2007) Comparison of fixed- and moving-vessel flow measurements with an aDP in a large river. *Journal of Hydraulic Engineering*, ASCE, pp. 1299-1309

Tang and Knight (2009) Analytical models for velocity distributions in open channel flows. *Journal of Hydraulic Research*, IAHR, Vol. 47, No. 4 (2009), pp. 418–428.

Tang and Knight (2009) Lateral distributions of streamwise velocity in compound channels with partially vegetated floodplains. *Science in China Series E: Technological Sciences*, 52(11): 3357-3362.

Tavoularis, S. (2005) Measurement in fluid mechanics. Cambridge University Press.

Tennekes, H and Lumley, J.L. (1982). A first course in turbulence. Eight Printing. The MIT Press, Cambridge, Massachusets and London, England. ISBN no. 0 262 20019 8.

Tominaga, A., Nezu, I., Ezaki, K. and Nakagawa, H., 1989, Three-dimensional turbulent structure in straight open channel flows. *Journal of Hydraulic Research*, IAHR, Vol. 27, No. 1, pp. 149-173

Tsinober, A (2001) An informal introduction to turbulence. Kluwer Academic Publisher, Dordrecht/Boston/London.

Turnipseed, D.P. (2002) Tidal Flux Variation in the Lower Pearl River and Lake Pontchartrain Estuaries of Mississippi and Louisiana. *Proceedings of the Hydraulic Measurements and Experimental Methods Conference 2002*.

Versteeg, H.K. and Malalasekera, W. (1995) An introduction to computational fluid dynamics: The finite volume method approach. Longman Scientific and Technical, Malaysia.

Wagner, C.R. & Mueller, D.S. (2001) Calibration and validation of a two-dimensional hydrodynamic model of the Ohio River, Jefferson County, Kentucky. *U.S. Geological Survey Water-Resources Investigations Rep. 01-4091*, Denver.

Weisbach, J. (1845) Lehrbuch der Ingenieur und Maschinen-Mechanik, Braunschweig

White, F.M. (1999) Fluid mechanics. 4th edition, McGraw-Hill, Boston.

Willetts, B.B. and Rameshwaran, P. (1996) Meandering Overbank Flow Structures. *Coherent Flow Structures in Open Channels, Edited by P.J. Ashworth, S.J. Bennett, J.L. Best and S.J. McLelland, Chapter 29, 609–629*.

WMO (2004) Commission for Hydrology, 12th Session Abridged, Final Rep. with Resolutions and Recommendations, WMO No. 979, Geneva.

Vanoni, V.A. (1946) Transportation of suspended sediment by water. *Trans*., ASCE, 111, 67-133.

APPENDIX I: RESULTS RELATED TO THE ANALYSIS IN SECTION 4.7.3.

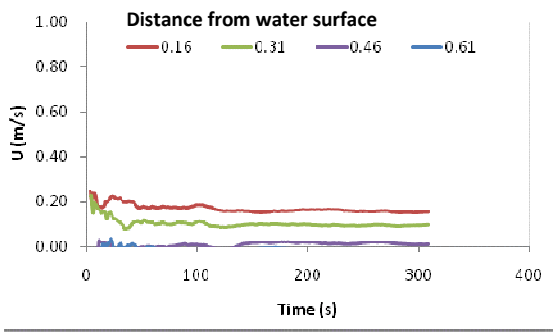

DL = 1.50m (U_d = 0.07ms^{-1})

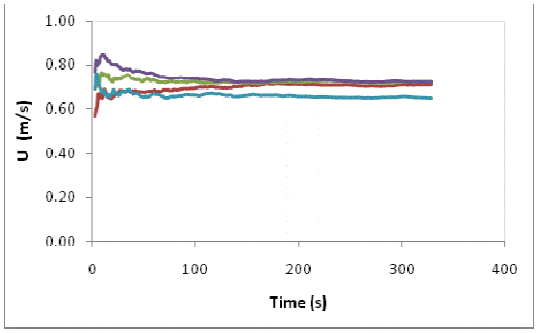

DL = 4.50m (U_d = 0.72ms^{-1})

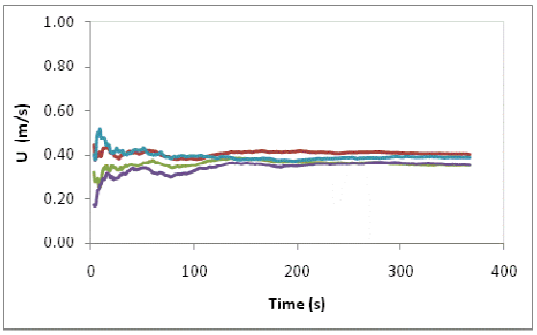

DL = 2.50m (U_d = 0.38ms^{-1})

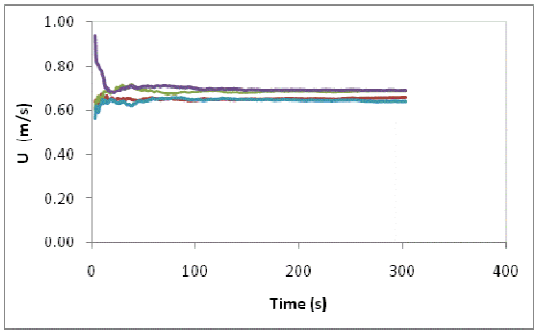

DL = 5.50 m (U_d = 0.69ms^{-1})

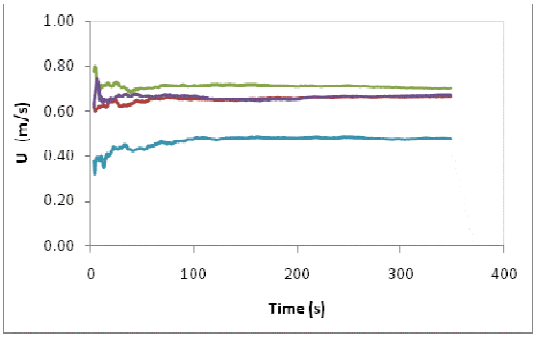

DL = 3.50m (U_d = 0.68ms^{-1})

I-1 Mean streamwise velocity at various depth with respect to averaging time, measured at various distances from left bank at CS 2 (16/01/2008 - bankfull).

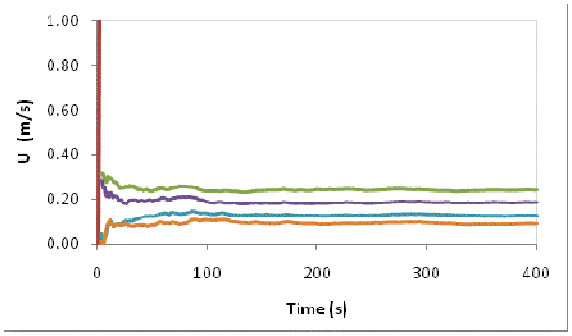

DL = 3.35m (U_d = 0.18ms^{-1})

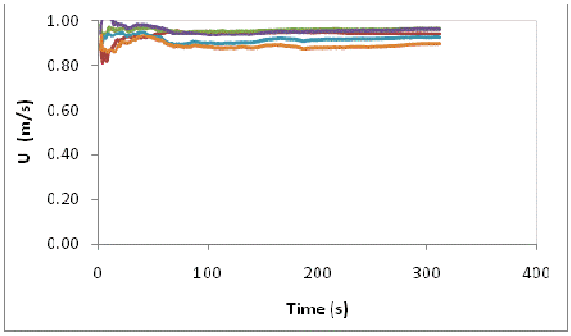

DL = 6.35m (U_d = 0.95ms^{-1})

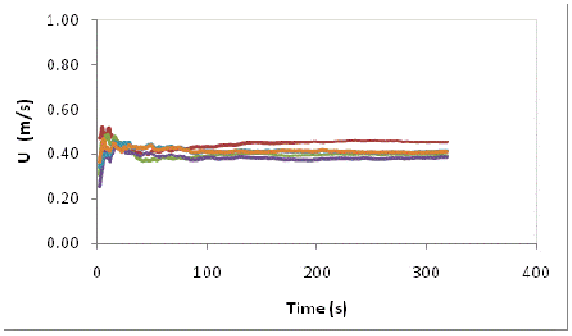

DL = 4.35m (U_d = 0.41ms^{-1})

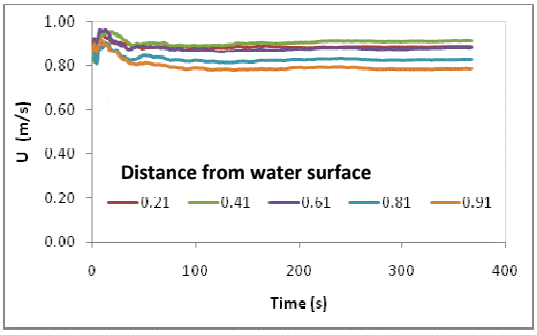

DL =7.35 m (U_d = 0.87ms^{-1})

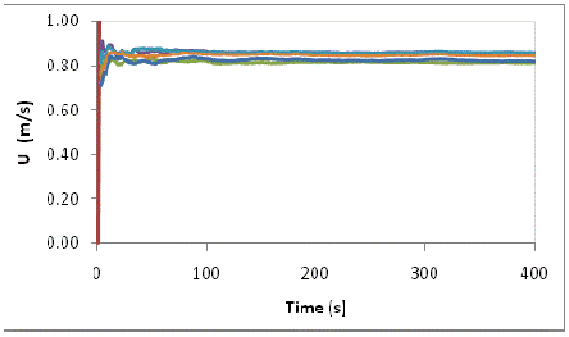

DL = 5.35m (U_d = 0.84ms^{-1})

I-2 Mean streamwise velocity at various depth with respect to averaging time, measured at various distances from left bank at CS 2 (10/2/2009 - overbank).

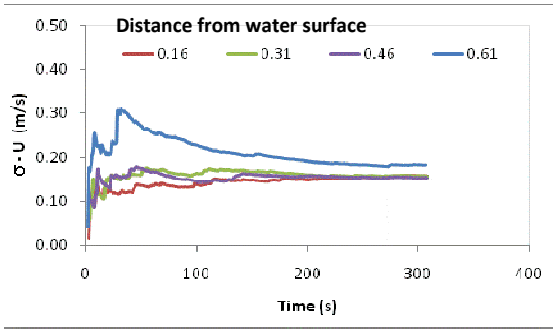

DL = 1.50m (U_d = 0.07ms^{-1})

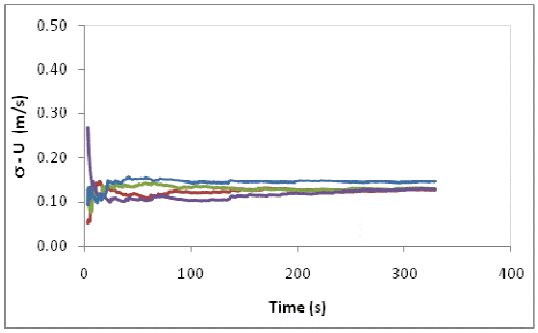

DL = 4.50m (U_d = 0.72ms^{-1})

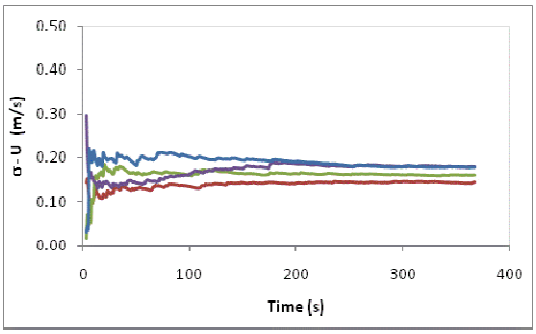

DL = 2.50 m (U_d = 0.38ms^{-1})

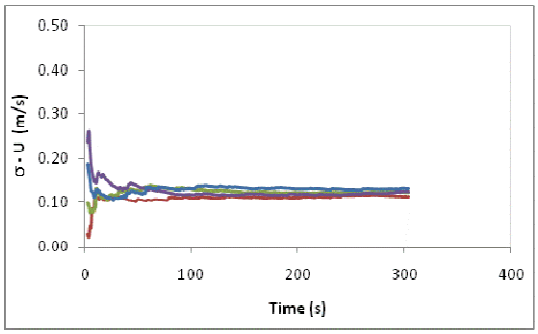

DL = 5.50 m (U_d = 0.69ms^{-1})

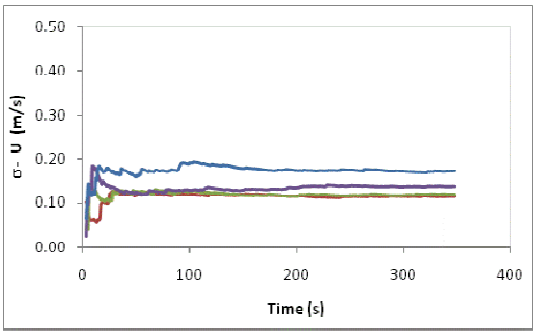

DL = 3.50 m (U_d = 0.68ms^{-1})

I-3 Mean standard deviation of streamwise velocity at various depth with respect to averaging time, measured at various distances from left bank at CS 2 (16/01/2008 - bankfull).

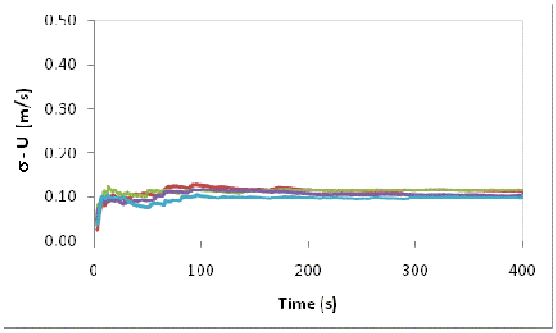

DL = 3.35m (U_d = 0.18ms^{-1})

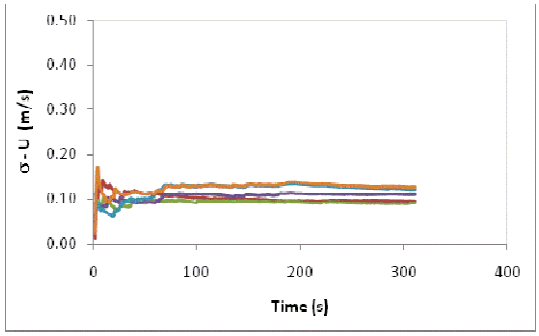

DL = 6.35m (U_d = 0.95ms^{-1})

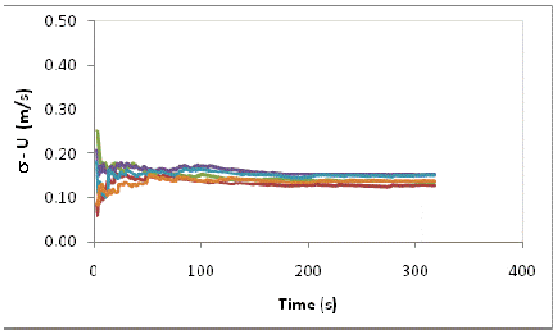

DL = 4.35m (U_d = 0.41ms^{-1})

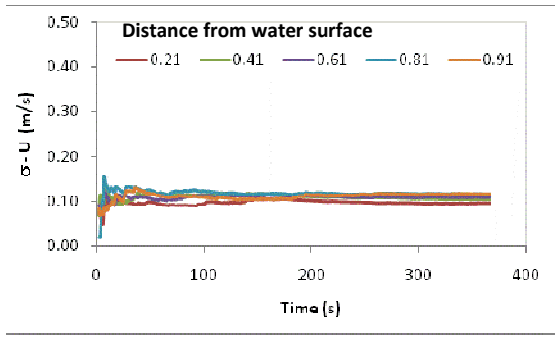

DL = 7.35m (U_d = 0.87ms^{-1})

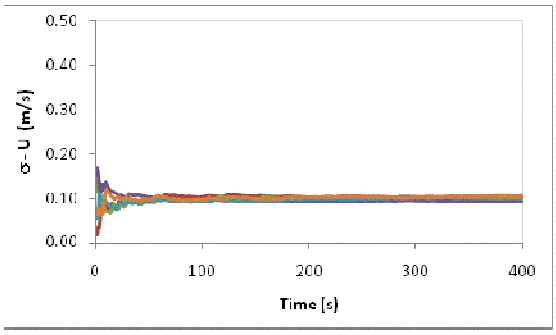

DL = 5.35m (U_d = 0.84ms^{-1})

I-4 Mean standard deviation of streamwise velocity at various depth with respect to averaging time, measured at various distances from left bank at CS 2 (10/2/2009 - overbank).

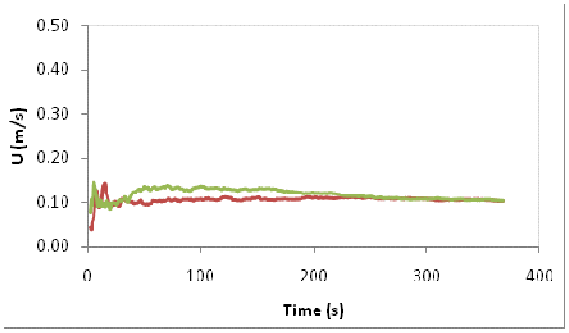

DL = 1.30m (U_d = 0.03ms^{-1})

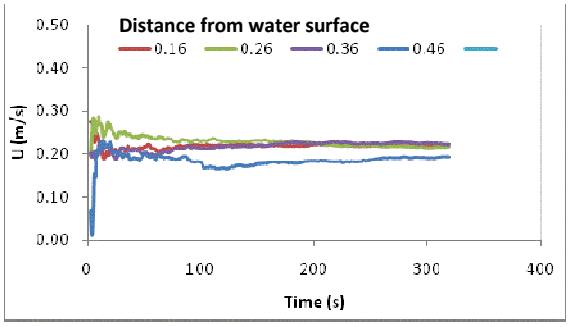

DL = 3.55m (U_d = 0.12ms^{-1})

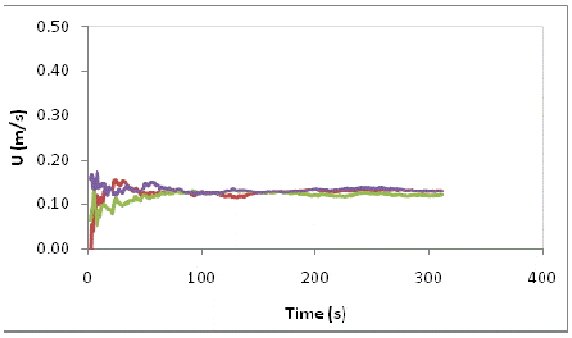

DL = 2.05m (U_d = 0.05ms^{-1})

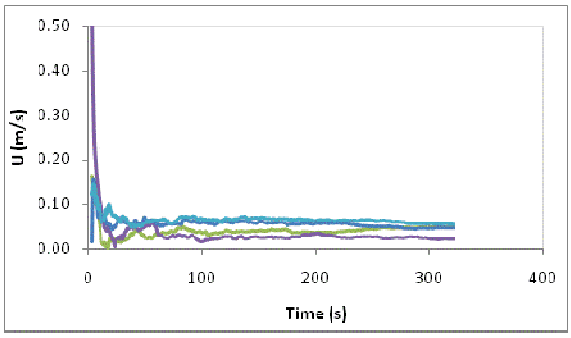

DL = 4.50m (U_d = 0.02ms^{-1})

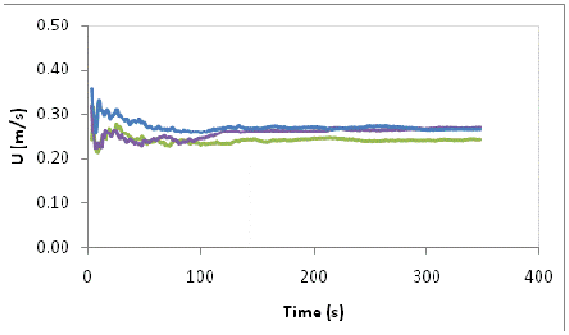

DL = 2.80m (U_d = 0.14ms^{-1})

I-5 Mean streamwise velocity at various depth with respect to averaging time, measured at various distances from left bank at CS 4 (18/08/2008 - inbank).

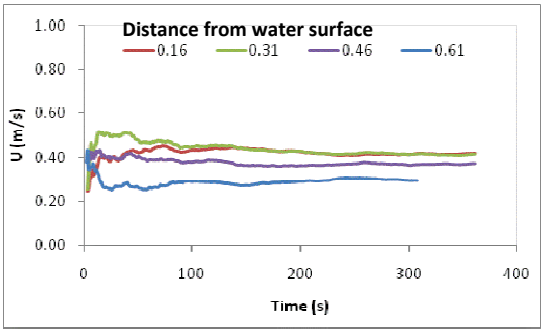

DL = 0.90m (U_d = 0.39ms^{-1})

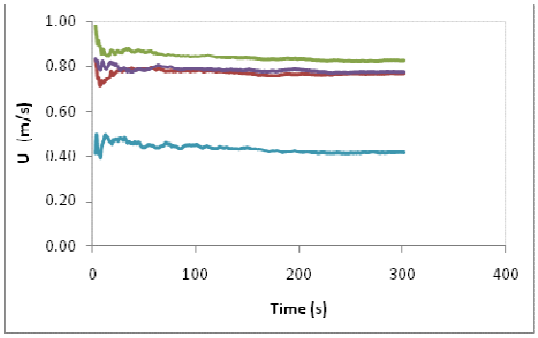

DL = 2.90m (U_d = 0.79ms^{-1})

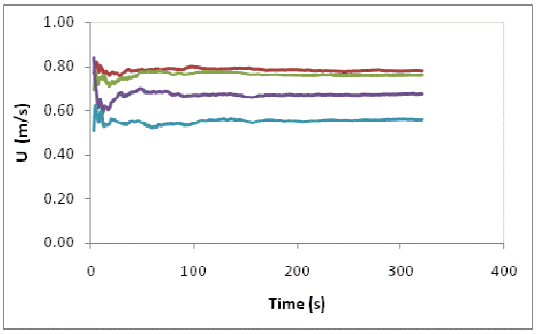

DL = 1.90m (U_d = 0.73ms^{-1})

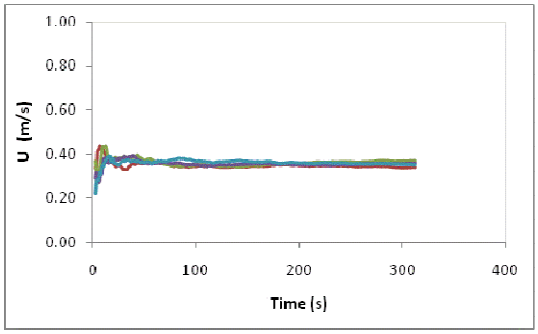

DL = 3.90m (U_d = 0.36ms^{-1})

I-6 Mean streamwise velocity at various depth with respect to averaging time, measured at various distances from left bank at CS 4 (16/01/2008 - bankfull).

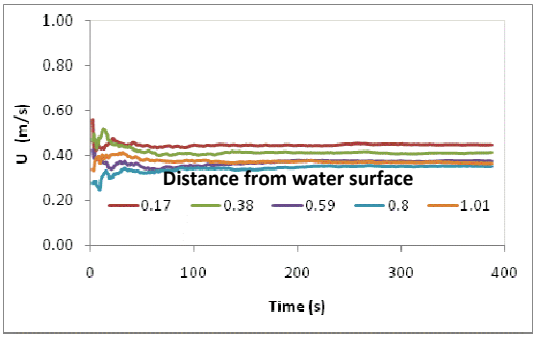

DL = 1.50m (U_d = 0.39ms^{-1})

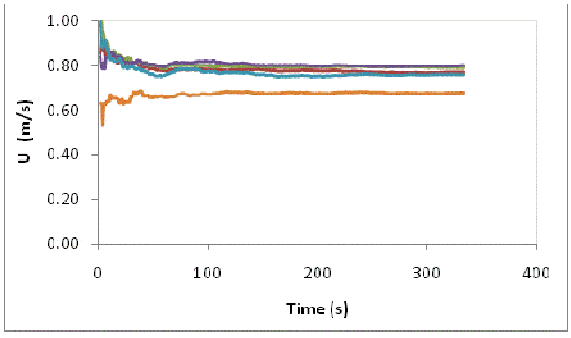

DL = 3.75m (U_d = 0.77ms^{-1})

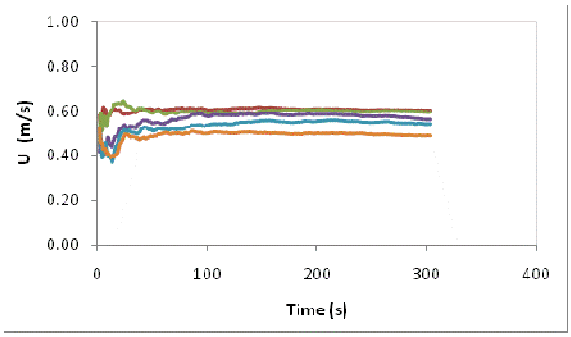

DL = 2.25m (U_d = 0.57ms^{-1})

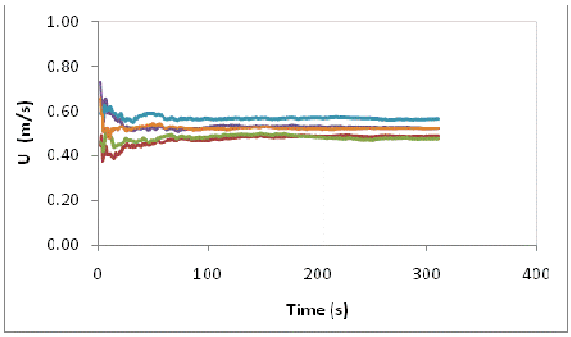

DL = 4.50m (U_d = 0.52ms^{-1})

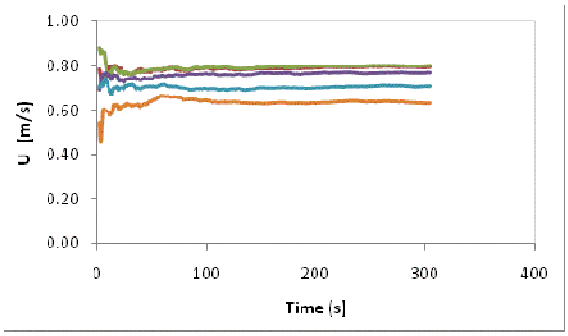

DL = 3.00m (U_d = 0.75ms^{-1})

I-7 Mean streamwise velocity at various depth with respect to averaging time, measured at various distances from left bank at CS 4 (10/2/2009 - overbank).

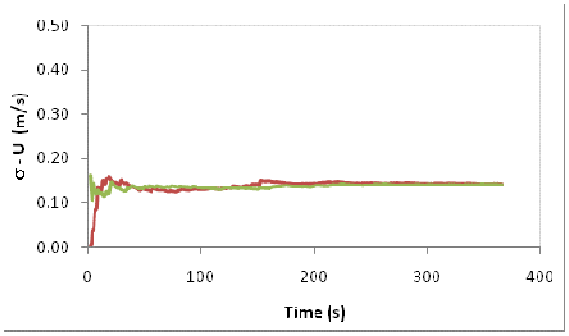

DL = 1.30m (U_d = 0.03ms^{-1})

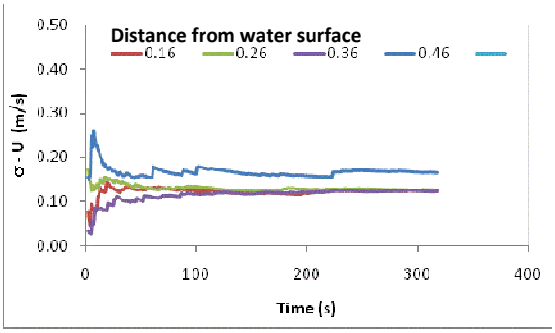

DL = 3.55m (U_d = 0.12ms^{-1})

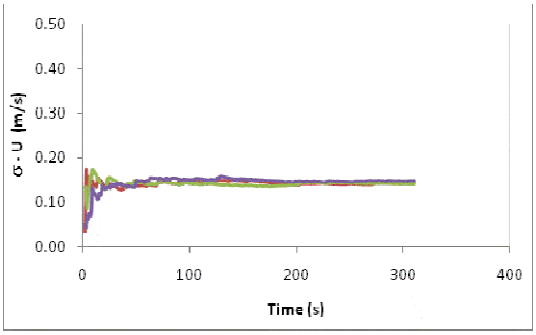

DL = 2.05m (U_d = 0.05ms^{-1})

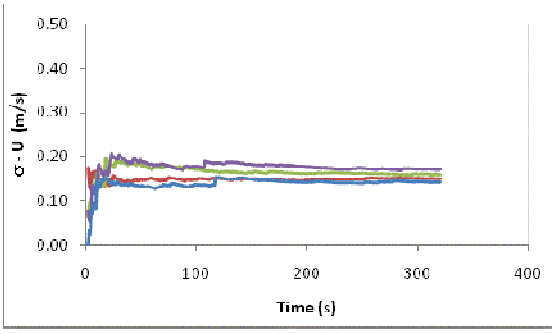

DL = 4.50m (U_d = 0.02ms^{-1})

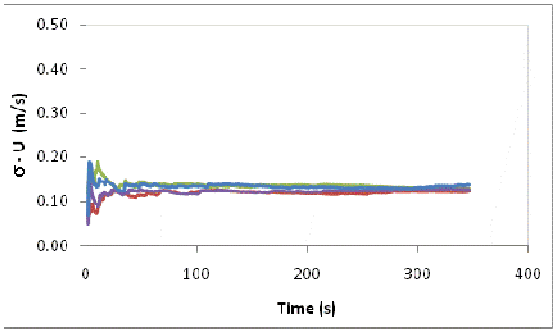

DL = 2.80m (U_d = 0.14ms^{-1})

I-8 Mean standard deviation of streamwise velocity at various depth with respect to averaging time, measured at various distances from left bank at CS 4 (18/08/2008 - inbank).

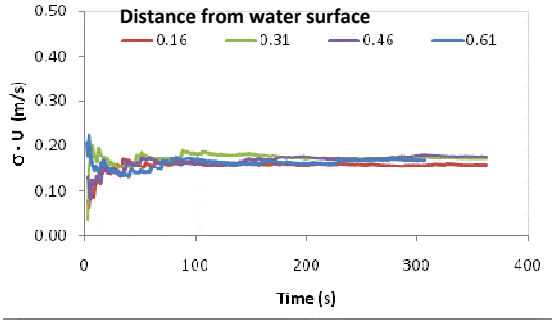

DL = 0.90m (U_d = 0.39ms^{-1})

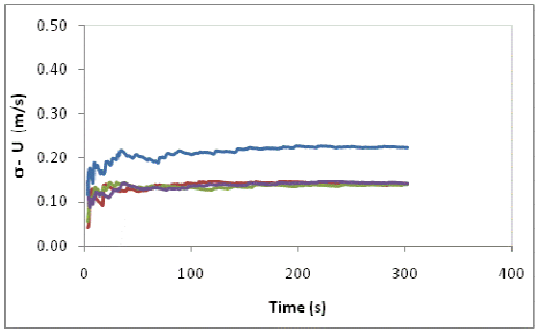

DL = 2.90m (U_d = 0.79ms^{-1})

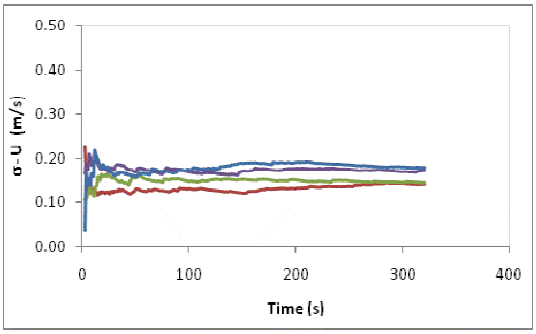

DL = 1.90m (U_d = 0.73ms^{-1})

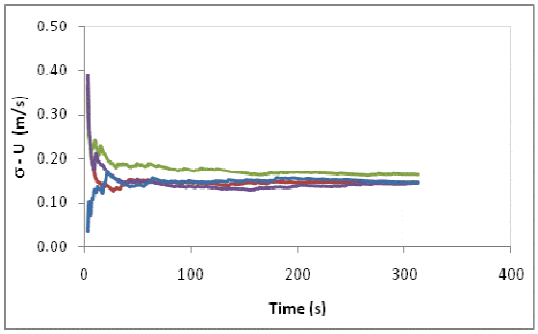

DL = 3.90m (U_d = 0.36ms^{-1})

I-9 Mean standard deviation of streamwise velocity at various depth with respect to averaging time, measured at various distances from left bank at CS 4 (16/01/2008 - bankfull).

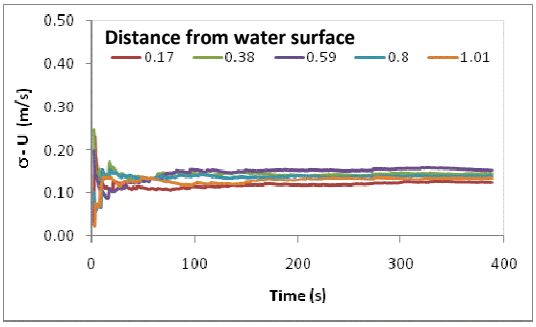

DL = 1.50m (U_d = 0.39ms^{-1})

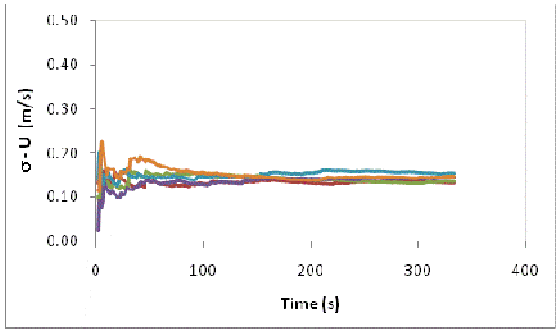

DL = 3.75m (U_d = 0.77ms^{-1})

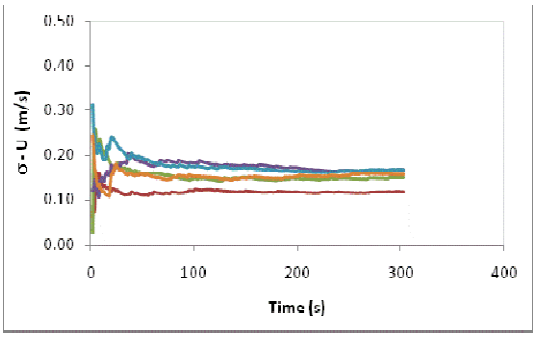

DL = 2.25 m (U_d = 0.57 ms^{-1})

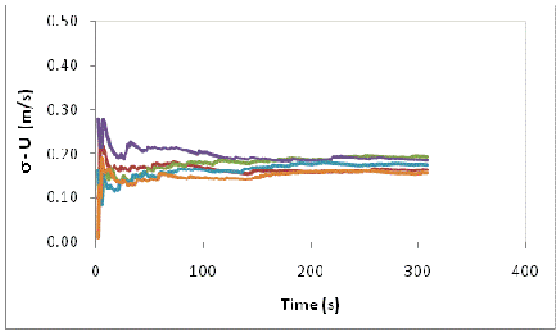

DL = 4.50m (U_d = 0.52ms^{-1})

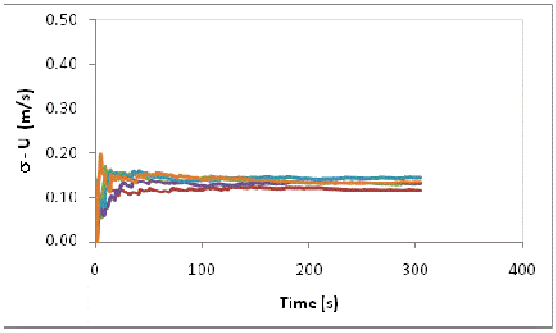

DL = 3.00 m (U_d = 0.75 ms^{-1})

I-10 Mean standard deviation of streamwise velocity at various depth with respect to averaging time, measured at various distances from left bank at CS 4 (10/2/2009 - overbank).

APPENDIX II: RESULTS RELATED TO THE ANALYSIS IN SECTION 4.7.4.

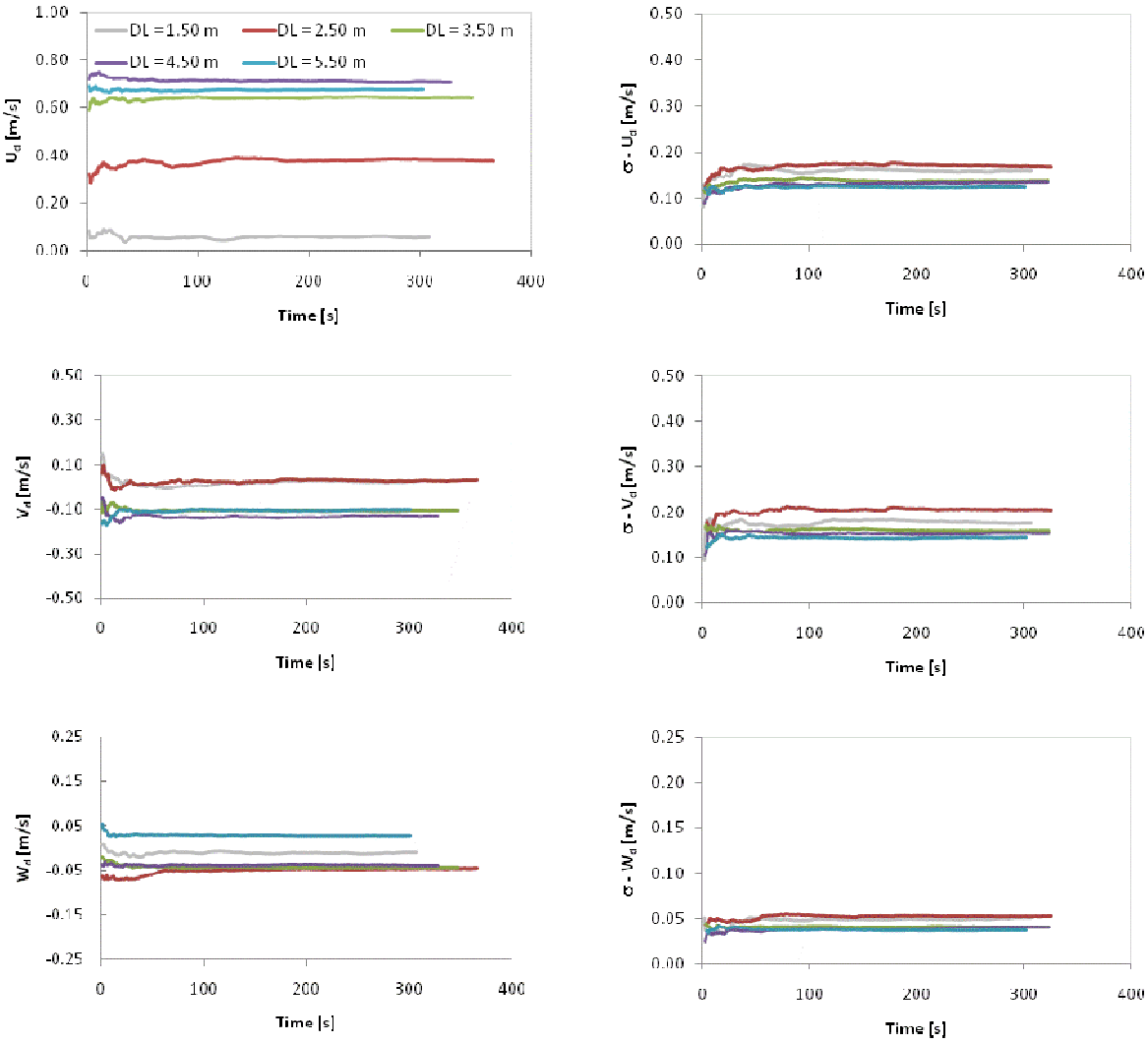

II-1 Mean U_d, V_d and W_d (left) and their standard deviation (right), with respect to averaging time, measured at various distances from left bank at CS 2 (16/01/2008 - bankfull).

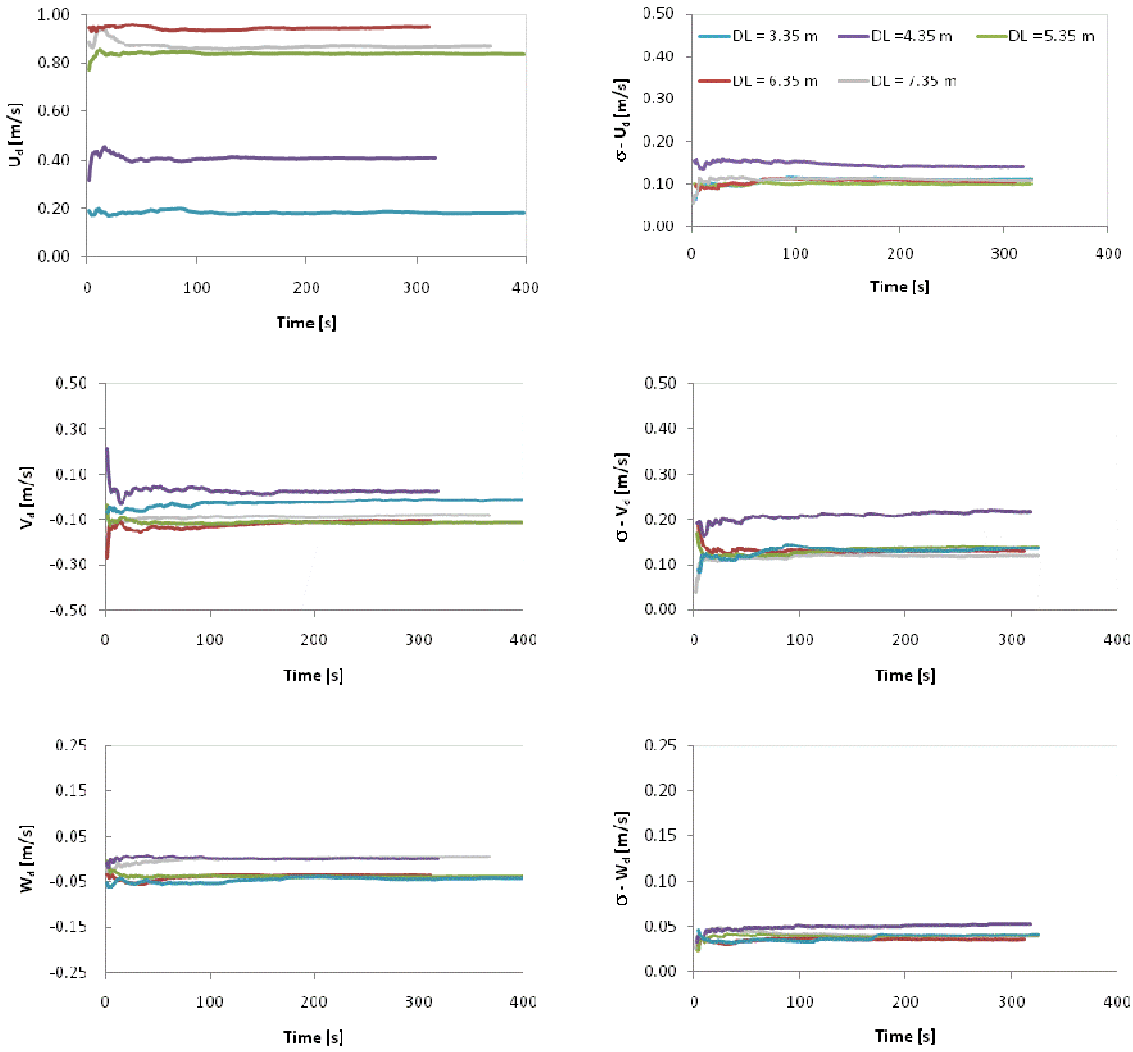

II-2 Mean U_d, V_d and W_d (left) and their standard deviation (right), with respect to averaging time, measured at various distances from left bank at CS 2 (10/2/2009 - overbank).

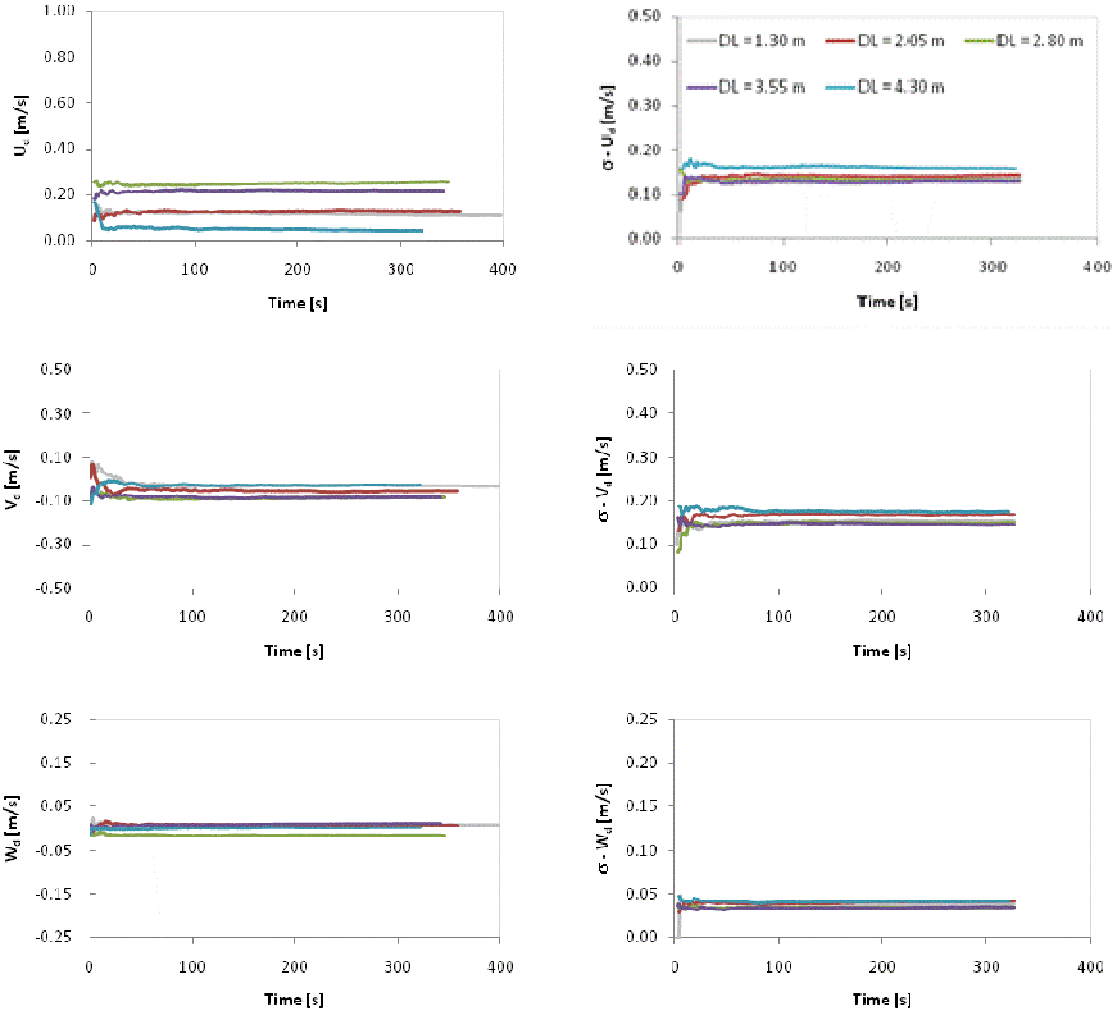

II-3 Mean U_d, V_d and W_d (left) and their standard deviation (right), with respect to averaging time, measured at various distances from left bank at CS 4 (18/08/2008 - inbank).

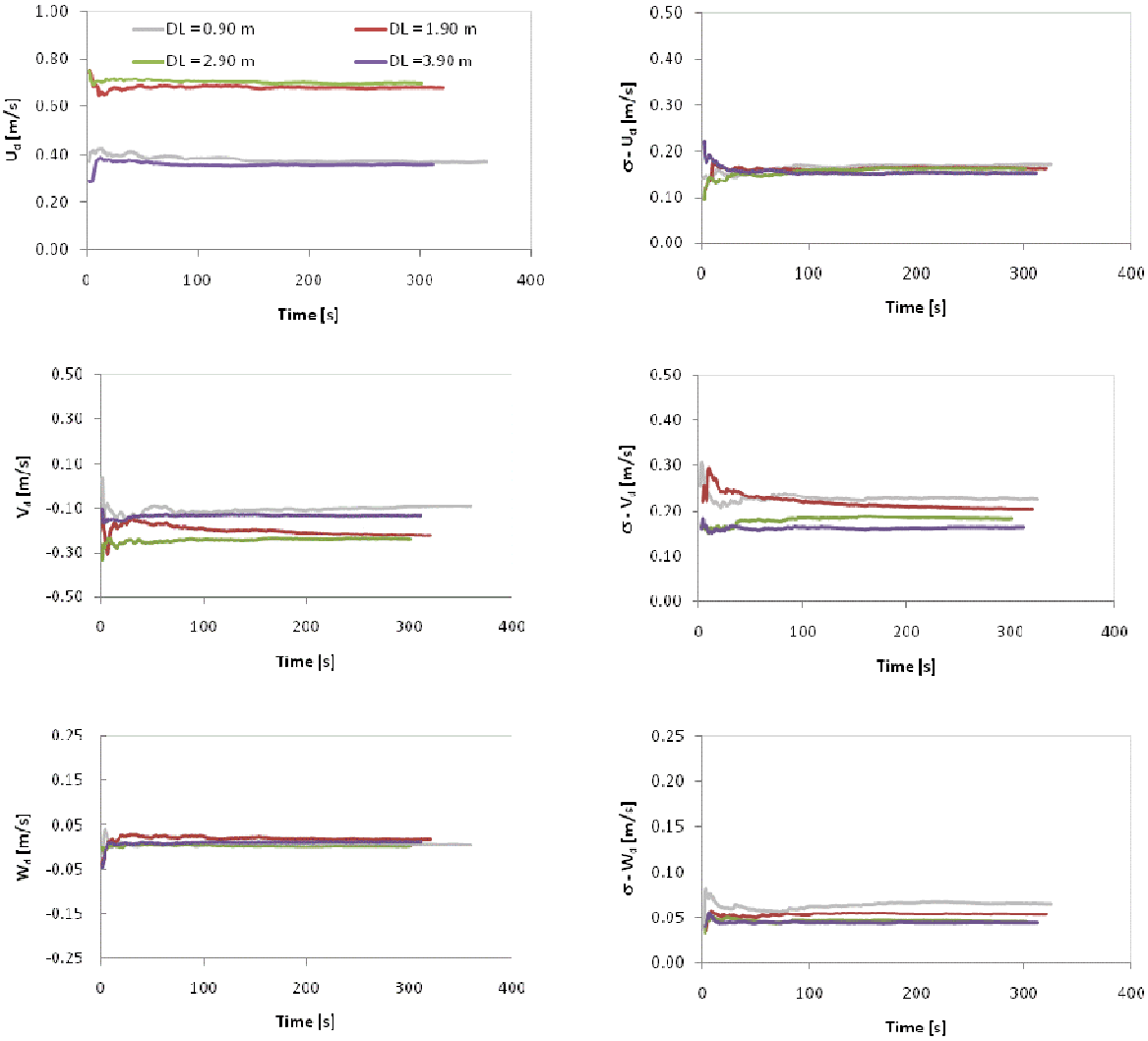

II-4 Mean U_d, V_d and W_d (left) and their standard deviation (right), with respect to averaging time, measured at various distances from left bank at CS 4 (16/01/2008 - bankfull).

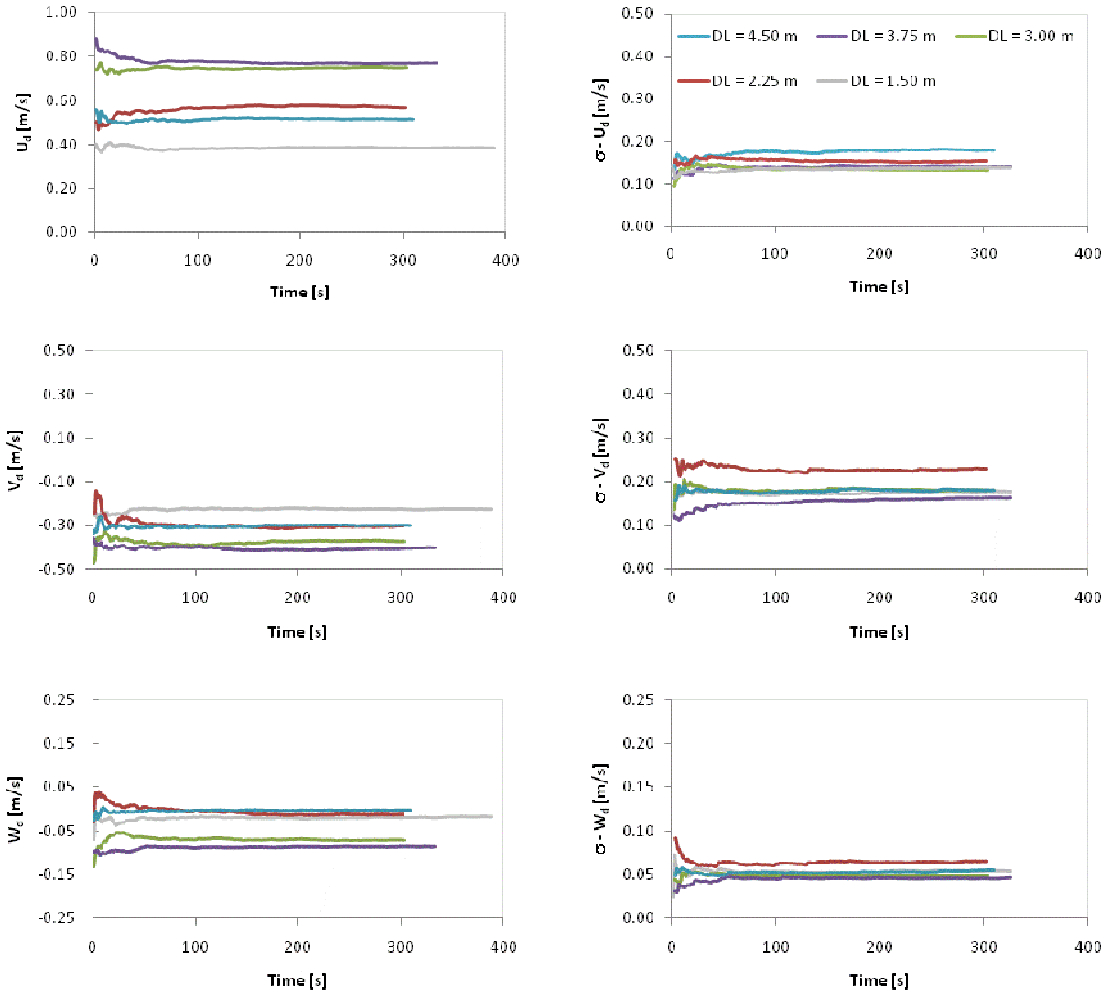

II-5 Mean U_d, V_d and W_d (left) and their standard deviation (right), with respect to averaging time, measured at various distances from left bank at CS 4 (10/2/2009 - overbank).

APPENDIX III: RESULTS RELATED TO THE ANALYSIS IN SECTION 7.3.

a) Case C1 – H = 0.162 m

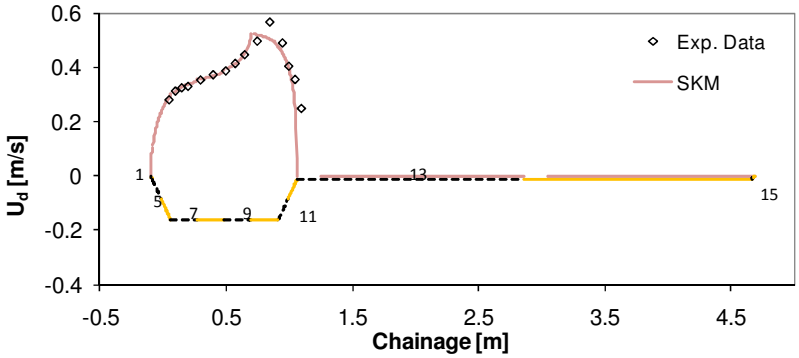

b) Case C1 – H = 0.187 m

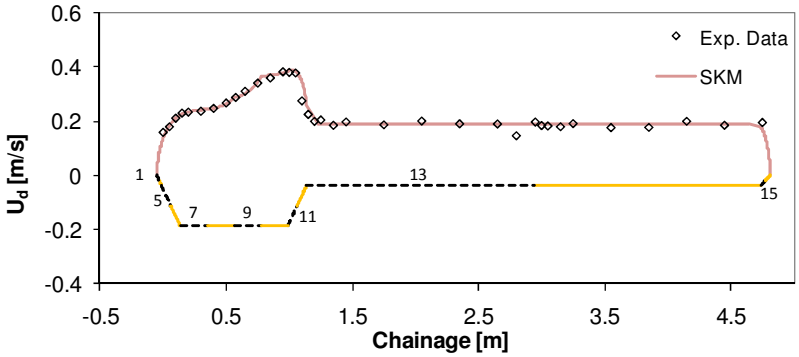

c) Case C1 – H = 0.237 m

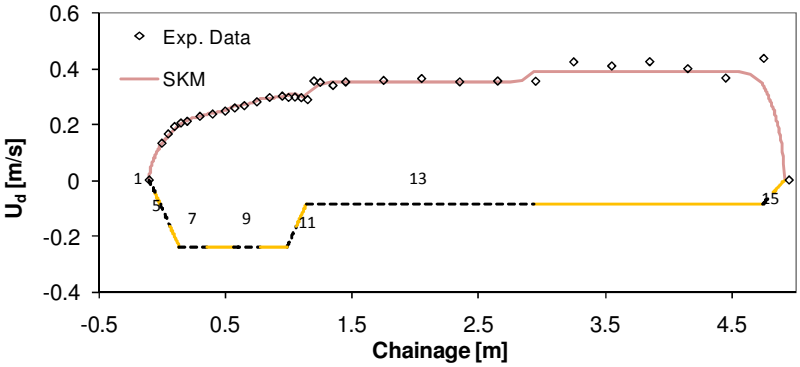

III-1 Comparison of simulated U_d and data at CS 4, with Γ = 0 in all panels (physical model).

	Case C1	Case C2	Case C3
H (m)	0.162	0.187	0.237
Q (measured)	0.065	0.084	0.175
CS 4	4.8	-2.0	4.2

III-2 Difference (in percent) between measured and simulated discharge at CS 4, with Γ = 0 in all panels (physical model).

APPENDIX IV: CALIBRATION PARAMETERS RELATED TO THE ANALYSIS IN SECTION 7.4.

		H=	1.15	m
(1)	(2)	*b* (m)	*h* (m)	*f*
2	1	0.05	0.01	10.00
	2	0.07	0.02	10.00
	3	0.10	0.02	10.00
	4	0.91	0.09	10.00
	5	1.72	0.16	10.00
3	6	1.81	0.49	10.00
	7	1.90	0.83	10.00
	8	2.72	0.99	10.00
4	9	3.55	1.15	5.00
5	10	5.03	1.07	0.20
6	11	6.52	0.99	0.13
7	12	7.07	0.84	0.08
8	13	7.62	0.68	0.30
	14	7.77	0.35	0.30
	15	7.92	0.01	0.30
9	16	8.07	0.00	5.00

		H=	1.21	m
(1)	(2)	*b* (m)	*h* (m)	*f*
1	1	0.00	0.00	100.00
2	2	0.35	0.08	25.00
	3	0.38	0.09	25.00
	4	1.19	0.15	25.00
	5	2.00	0.22	25.00
3	6	2.09	0.56	10.00
	7	2.18	0.89	10.00
	8	3.00	1.05	10.00
4	9	3.83	1.21	4.67
5	10	5.31	1.13	0.19
6	11	6.80	1.05	0.12
7	12	7.35	0.90	0.08
8	13	7.90	0.75	0.30
	14	8.05	0.41	0.30
	15	8.20	0.08	0.30
9	16	9.01	0.00	4.33

		H=	1.27	m
(1)	(2)	*b* (m)	*h* (m)	*f*
1	1	0.33	0.07	100.00
	2	0.65	0.15	100.00
2	3	1.46	0.22	40.00
	4	2.27	0.28	40.00
3	5	2.45	0.95	10.00
	6	3.28	1.11	10.00
4	7	4.10	1.27	4.33
5	8	5.59	1.20	0.19
6	9	7.07	1.12	0.11
7	10	7.62	0.96	0.08
8	11	8.17	0.81	0.30
	12	8.47	0.14	0.30
9	13	9.40	0.05	3.67
10	14	17.66	0.12	0.10
11	15	22.54	0.20	5.00
12	16	22.74	0.00	1.65

		H=	1.34	m
(1)	(2)	*b* (m)	*h* (m)	*f*
1	1	0.46	0.11	100.00
	2	0.93	0.21	100.00
2	3	1.74	0.28	55.00
	4	2.55	0.35	55.00
3	5	2.73	1.02	10.00
	6	3.55	1.18	10.00
4	7	4.38	1.34	4.00
5	8	5.86	1.26	0.18
6	9	7.35	1.18	0.11
7	10	7.90	1.03	0.08
8	11	8.45	0.87	0.30
	12	8.75	0.20	0.30
9	13	9.68	0.12	3.00
10	14	17.94	0.19	0.55
11	15	22.82	0.26	15.00
12	16	23.08	0.00	100.00

(1) = panel number, (2) = sub-panel number.

IV-1. Geometry and friction factor values used for simulating the flow at CS 2 in Section 7.4.

		H=	1.40	m			H=	1.46	m			H=	1.53	m	
(1)	(2)	*b* (m)	*h* (m)	*f*	(1)	(2)	*b* (m)	*h* (m)	*f*	(1)	(2)	*b* (m)	*h* (m)	*f*
1	1	0.60	0.14	100.00	1	1	0.74	0.17	100.00	1	1	0.88	0.20	100.00
	2	1.20	0.27	100.00		2	1.48	0.34	100.00			1.75	0.40	100.00
2	3	2.01	0.34	70.00	2	3	2.29	0.41	85.00	2	2	2.56	0.47	100.00
	4	2.82	0.41	70.00		4	3.10	0.47	85.00			3.37	0.54	100.00
3	5	3.00	1.08	10.00	3	5	3.28	1.14	10.00	3	3	3.55	1.21	10.00
	6	3.83	1.24	10.00		6	4.10	1.30	10.00			4.38	1.37	10.00
4	7	4.65	1.40	3.67	4	7	4.93	1.46	3.33	4	4	5.20	1.53	3.00
5	8	6.14	1.32	0.17	5	8	6.41	1.38	0.17	5	5	6.69	1.45	0.16
6	9	7.62	1.24	0.10	6	9	7.90	1.31	0.09	6	6	8.17	1.37	0.08
7	10	8.17	1.09	0.08	7	10	8.45	1.15	0.08	7	7	8.72	1.21	0.08
8	11	8.72	0.94	0.30	8	11	9.00	1.00	0.30	8	8	9.27	1.06	0.30
	12	9.02	0.27	0.30		12	9.30	0.33	0.30			9.57	0.39	0.30
9	13	9.95	0.18	2.33	9	13	10.23	0.24	1.67	9	9	10.50	0.30	1.00
10	14	18.21	0.25	1.35	10	14	18.49	0.31	3.00	10	10	18.76	0.37	4.00
11	15	23.09	0.32	30.00	11	15	23.37	0.39	50.00	11	11	23.64	0.45	100.00
12	16	23.41	0.00	30.00	12	16	23.75	0.00	100.00	12	12	24.09	0.00	100.00

(1) = panel number, (2) = sub-panel number.

IV-2. Geometry and friction factor values used for simulating the flow at CS 2 in Section 7.4 (continued).

		H=	0.86	m
(1)	(2)	*b* (m)	*h* (m)	*f*
1	1	0.07	0.06	2.00
	2	0.15	0.11	2.00
2	3	0.17	0.45	2.00
	4	0.20	0.79	2.00
3	5	0.72	0.81	0.25
	6	1.25	0.83	0.25
4	7	2.30	0.86	0.15
5	8	2.75	0.84	0.08
	9	3.20	0.82	0.08
6	10	4.10	0.78	0.09
7	11	4.20	0.67	0.09
	12	4.31	0.56	0.09
	13	4.52	0.34	0.09
8	14	5.08	0.17	0.20
9	15	5.35	0.09	0.50
	16	5.69	0.00	0.50

		H=	0.94	m
(1)	(2)	*b* (m)	*h* (m)	*f*
1	1	0.12	0.09	1.83
	2	0.24	0.18	1.83
2	3	0.26	0.52	1.83
	4	0.29	0.86	1.83
3	5	0.81	0.88	0.38
	6	1.34	0.89	0.38
4	7	2.39	0.93	0.21
5	8	2.84	0.91	0.10
	9	3.29	0.89	0.10
6	10	4.19	0.85	0.08
7	11	4.29	0.74	0.09
	12	4.40	0.63	0.09
	13	4.61	0.41	0.09
8	14	5.17	0.23	0.18
9	15	5.44	0.15	0.55
	16	5.92	0.00	0.55

		H=	1.01	m
(1)	(2)	*b* (m)	*h* (m)	*f*
1	1	0.17	0.13	1.67
	2	0.33	0.26	1.67
2	3	0.36	0.60	1.67
	4	0.38	0.94	1.67
3	5	1.43	0.98	0.50
4	6	2.48	1.01	0.27
5	7	3.38	0.97	0.12
6	8	4.28	0.93	0.08
7	9	4.49	0.71	0.09
	10	4.70	0.49	0.09
8	11	5.54	0.26	0.17
9	12	6.37	0.02	0.60
10	13	15.02	0.09	0.30
11	14	23.66	0.16	0.80
12	15	23.86	0.08	0.80
	16	24.06	0.00	0.80

		H=	1.09	m
(1)	(2)	*b* (m)	*h* (m)	*f*
1	1	0.21	0.17	1.50
	2	0.43	0.34	1.50
2	3	0.45	0.68	1.50
	4	0.48	1.02	1.50
3	5	1.53	1.05	0.63
4	6	2.58	1.09	0.33
5	7	3.48	1.05	0.14
6	8	4.38	1.01	0.07
7	9	4.59	0.79	0.10
	10	4.80	0.57	0.10
8	11	5.63	0.33	0.15
9	12	6.47	0.10	0.65
10	13	15.11	0.17	0.30
11	14	23.76	0.24	0.80
12	15	24.31	0.01	0.80
	16	24.33	0.00	0.80

(1) = panel number, (2) = sub-panel number.

IV-3. Geometry and friction factor values used for simulating the flow at CS 4 in Section 7.4.

		H=	1.16	m			H=	1.23	m			H=	1.31	m	
(1)	(2)	*b* (m)	*h* (m)	*f*	(1)	(2)	*b* (m)	*h* (m)	*f*	(1)	(2)	*b* (m)	*h* (m)	*f*
1	1	0.26	0.20	1.33	1	1	0.31	0.24	1.17	1	1	0.35	0.28	1.00
	2	0.52	0.41	1.33		2	0.61	0.48	1.17		2	0.71	0.56	1.00
2	3	0.54	0.75	1.33	2	3	0.64	0.82	1.17	2	3	0.73	0.90	1.00
	4	0.57	1.09	1.33		4	0.66	1.16	1.17		4	0.76	1.24	1.00
3	5	1.62	1.12	0.75	3	5	1.71	1.20	0.88	3	5	1.81	1.27	1.00
4	6	2.67	1.16	0.38	4	6	2.76	1.23	0.44	4	6	2.86	1.31	0.50
5	7	3.57	1.12	0.16	5	7	3.66	1.19	0.18	5	7	3.76	1.27	0.20
6	8	4.47	1.08	0.06	6	8	4.56	1.15	0.06	6	8	4.66	1.23	0.05
7	9	4.68	0.86	0.10	7	9	4.77	0.93	0.10	7	9	4.87	1.01	0.10
	10	4.89	0.64	0.10		10	4.98	0.71	0.10		10	5.08	0.79	0.10
8	11	5.72	0.40	0.13	8	11	5.82	0.48	0.12	8	11	5.91	0.55	0.10
9	12	6.56	0.17	0.70	9	12	6.65	0.24	0.75	9	12	6.75	0.32	0.80
10	13	15.20	0.24	0.80	10	13	15.30	0.31	0.80	10	13	15.39	0.39	0.80
11	14	23.85	0.31	0.80	11	14	23.94	0.38	0.80	11	14	24.04	0.46	0.80
12	15	24.41	0.08	0.80	12	15	24.50	0.15	0.80	12	15	24.59	0.23	0.80
	16	24.61	0.00	0.80		16	24.88	0.00	0.80		16	25.15	0.00	0.80

(1) = panel number, (2) = sub-panel number.

IV-4 Geometry and friction factor values used for simulating the flow at CS 4 in Section 7.4 (continued).

APPENDIX V: AUTHOR'S PUBLICATIONS

Using an Acoustic Doppler Current Profiler in a small river

(CIWEM) Water and Environment Journal (in press for printing, published online on 12/5/2009/DOI: 10.1111/j.1747-6593.2009.00170.x)

Water and Environment Journal. Print ISSN 1747-6585

Using an acoustic Doppler current profiler in a small river

B. Gunawan, M. Sterling & D. W. Knight, MCIWEM

School of Civil Engineering, College of Engineering and Physical Sciences, University of Birmingham, Edgbaston, Birmingham, UK

Keywords
acoustic Doppler; ADCP; discharge; flow measurement; river; velocity.

Correspondence
Budi Gunawan, School of Civil Engineering, College of Engineering and Physical Sciences, University of Birmingham, Edgbaston, Birmingham B15 2TT, UK. Email: BXG640@bham.ac.uk

doi:10.1111/j.1747-6593.2009.00170.x

Abstract

Some practical and theoretical concepts related to the use of an acoustic Doppler current profiler (ADCP) in a small river are examined. The importance of understating the limitations of the measurement equipment and a system for locating the exact position of the ADCP are discussed. Details of a new measurement protocol which is suitable for small rivers are presented. Small samples of data measured in the River Blackwater are used to illustrate the concepts outlined in the paper. It is concluded that ADCPs can be successfully used in small rivers provided sufficient care is taken over their deployment and subsequent data analysis. However, in some cases it is acknowledged that additional modifications to the ADCP may need to be undertaken as illustrated in the paper.

An integrated and novel approach to estimating the conveyance capacity of the River Blackwater

Proceeding of the Eight International Conference on Hydro-science and Engineering, Nagoya, Japan, September 8-12, 2008

AN INTEGRATED AND NOVEL APPROACH TO ESTIMATING THE CONVEYANCE CAPACITY OF THE RIVER BLACKWATER

Gunawan[1], B., Sun[2], X., Sterling[1], M., Knight[1], D.W., Shiono[2], K., Chandler[2], J.H., Rameshwaran[3], P., Wright[4], N.G., Sellin[5], R.H.J., Tang[1], X., and Fujita[6], I.

[1]Department of Civil Engineering, The University of Birmingham, B15 2TT, UK, e-mail: bxg640@bham.ac.uk
[2]Department of Civil Engineering, Loughborough University, LE11 3TU, UK, e-mail: x.sun4@lboro.ac.uk
[3]Centre for Ecology & Hydrology, Wallingford, OX10 8 BB, UK, e-mail: ponr@ceh.ac.uk
[4]UNESCO–IHE, PO Box 3015, 2601 DA, Delft, The Netherlands, e-mail: n.wright@unesco-ihe.org
[5]Department of Civil Engineering, the University of Bristol, BS8 1UP, UK, e-mail: r.h.j.sellin@bristol.ac.uk
[6]Department of Architecture and Civil Engineering, Kobe University, Kobe 657-8501, Japan, e-mail: ifujita@kobe-u.ac.jp

ABSTRACT

This paper presents a number of complex issues associated with the methodology and preliminary analysis of velocity and discharge measurements using various techniques applied to the River Blackwater, UK. An ADCP deployment procedure was adapted in order to take into account the difficulties of using such equipment in small rivers. The velocity profile in the middle of main channel has been measured using both ADCP and ADV, and averaged over a time scale of 800 s and 300 s respectively, to obtain a stable value. A discrepancy of approximately 6.8% was observed in the mean streamwise velocity between both measurements. A good agreement between surface velocity measurements using PIV and ADCP in cross-sections located in straight and meandering reaches of the river was observed. Finally, several numerical models have been benchmarked against a physical scale model of the river.

Keywords: acoustic techniques; comparative studies; flow measurements; rivers